Interplanetary Scintillation Studies of the Large-Scale Structure of the Solar Wind

Mario M. Bisi, MPhys (Hons) (Wales)

Solar System Physics Group

Institute of Mathematical and Physical Sciences

Penglais Campus

University of Wales

Aberystwyth

SY23 3BZ

Dr. A. R. Breen - Supervisor

June 2006

This thesis is submitted in fulfilment of the requirements for the degree of

Doctor of Philosophy of The University of Wales

Declaration

This thesis has not previously been accepted in substance for any degree and is not being concurrently submitted in candidature for any degree.

Signed ..... (candidate)

Date .....

Statement 1

This thesis is the result of my own investigations, except where otherwise stated.
Other sources are acknowledged by footnotes giving explicit references. A bibliography is appended.

Signed ..... (candidate)

Date .....

Statement 2

I hereby give consent for my thesis, if accepted, to be made available for photocopying and for inter-library loan, and for the title and summary to be made available to outside organisations.

Signed ..... (candidate)

Date .....

I don’t believe in mathematics

–Albert Einstein

Acknowledgements

I would like to start by thanking my supervisor, Dr. Andy Breen, for his unwavering support and extreme enthusiasm throughout the whole of my Ph.D.. Many thanks also goes out to my research colleagues, office mates and good friends Dr. Richard Fallows and Richard Jones for their help in improving my understanding of IPS. Other office mates at some point during my Ph.D. and good friends whom I owe thanks to are Bo Li, Gareth Dorrian, and especially Ian O'Neill for bringing his goldfish in as office pets throughout the years, first Tiny (R.I.P.) and then Comet A.K.A. Jimbob (R.I.P.).

I am indebted to the staff of the EISCAT, ESR, and MERLIN research facilities for their help in keeping the receiving systems operational throughout the several IPS observing campaigns for which I have been lucky enough to be a part of. I am also indebted to PPARC for their financial assistance during the period when this work was carried out.

My thanks go out to all my other friends at Aberystwyth (past and present); Mark Burden, Katherine (Kat) Dewis, Richard (Ricky) Sims (especially for the formatting style file for the bibliography of this thesis), Graham Parton, Daniel (Dan) and Leslie (Les) Le Messurier; all those from Aberdance DanceSport (past and present) for without dancing I think my sanity would have been at real threat, especially Stephanie Thorlby, Nichola (Nikki) Colabella, Amée Morris, Clare Hardy, Kathryn (Kate) Williams, Joanne (Jo) Shelton, and Saurabh (Rabh) Pandya; and my current flatmates for this year as Assistant Warden at Tŷ Gwerin, especially Kathryn (Kate) Faulks and Anna Williams. I also want to thank friends from home (Ebbw Vale and the South Wales area) and elsewhere in Great Britain; Michael (Mike) Kelly, Ceri-ann (Cer) Lloyd, Philip (Strandy) Strand, Emma Edwards, Tristan (Tris) Humphreys, Lisa Thomas and Emma Kerswill.

An enormous amount of thanks is due to my loving girlfriend since December 4th 2005, Lisa Hopkinson for the great times we have shared over the final months of this thesis and for helping me to maintain my focus!

Last, but certainly by no means least, I would like to thank my parents (Mark and Avril), sister (Gemma) and Nans (Rosina Bisi - R.I.P. and Joan Reed) for the encouragement, support and help they have given me throughout the whole of my schooling and academic life; I would not be where I am today without them.

Summary

The solar wind is a highly supersonic outflow of coronal plasma flowing in a close to radial direction out from the Sun. Generally, there are two modes of outflow, a fast stream mode with velocities in the range of 750 km s^{-1} to 800 km s^{-1}, and a slow stream mode with velocities in the range of 350 km s^{-1} to 400 km s^{-1}. The method of interplanetary scintillation (IPS) is used to obtain solar wind velocity estimates by observing the "twinkling" of radio waves from distant compact sources caused by density variations in the solar wind. The Aberystwyth IPS group has been conducting IPS observations using the European Incoherent SCATter radar (EISCAT) in northern Scandinavia since 1993 and more recently using the Multi-Element Radio-Linked Interferometer Network (MERLIN) radio telescopes in the United Kingdom.

This thesis investigates the large-scale structure of the solar wind using IPS observations in conjunction with white-light, extreme ultra-violet (EUV) and X-ray Carrington rotation maps from ground-based: Mauna Loa; and space-based: SOlar and Heliospheric Observatory (SOHO) and Yohkoh; as well as in-situ spacecraft observations of solar wind velocity from Wind and Ulysses.

A complete study of EISCAT IPS data from 1994 to 2003 is undertaken looking for detections of interaction in terms of shear layers and co-rotating interaction regions (CIRs) by ballistically mapping the IPS observations out to in-situ distances to see how interaction develops. From this, an investigation was carried out with solar minimum (1994-1997) EISCAT IPS data investigating a possible bi-modal fast solar wind structure. In addition, the technique of extremely long-baseline IPS measurements (developed from 2002) was used to look at the finer structure of solar wind velocity. This technique was also used to investigate the direction of flow which included observations of fast and slow wind, interaction regions, and the passage of a magnetic cloud.

In Loving Memory of "Mam" Rosina Bisi
(Rosa Zeraschi)

Contents

List of Figures

List of Tables

Chapter 1

An introduction to the Sun and the solar wind

1.1 Overview

The Earth is one of what are generally considered to be nine planets in our solar system orbiting the Sun, our star. The planets in order of orbit starting from nearest the Sun and working outward are Mercury, Venus, Earth, Mars, Jupiter, Saturn, Uranus, Neptune, and Pluto. The orbit of Pluto is highly elliptic which causes it to overlap with the orbit of Neptune, which then makes Neptune the outermost planet for two periods during an orbit of Pluto. There are also other objects in the solar system. Between the orbits of Mars and Jupiter there lies a ring of meteors which is thought to be due to a planet failing to form during the formation of the solar system. There lies a disk-shaped region at a distance just passed the orbit of Neptune to about 100 AU (1 AU is defined as the mean distance between the Sun and the Earth, equivalent to approximately 1.5×10^{11} m) which is known as the Kuiper Belt, after Gerard Kuiper who discovered it. At an even greater distance (thousands of AU) away from the Sun lies a cloud of comet-like material. This is known as Oort's cloud which was proposed in the 1950s by Jan Hendrik Oort. Seven of the nine planets have at least one natural satellite orbiting them, the two that are without moons are the innermost two, and also the hottest two, Venus and Mercury. The total

mass of the planets and minor solar system bodies only makes up around 0.2% of the total mass of the solar system, the remaining 98.8% or so is contained within the Sun.

Ground-based measurements of the Sun can only effectively be taken in either the optical or radio wavebands. This is due to the fact that the Earth's atmosphere filters out much of the electromagnetic spectrum by the time it gets to the Earth's surface.

Ground-based observations of the Sun started many years ago when the first observations of sunspots took place using optical telescopes. Observations have taken place at all visible colours and have been used to resolve features that are unseen by the naked eye. One should never look directly at the Sun using any kind of telescope, binoculars, camera or the naked eye unless they have been fitted with the necessary solar filters as doing so can cause permanent damage to eyesight. The safest way is to project an image of the Sun onto a surface and view it from there (an indirect observation).

There are two types of optical telescope, refractor and reflector, both of which can be used and have been used to observe the Sun. The earliest telescopes were refractors where the light coming from the Sun was focused by a lens to the rear of the telescope where it was brought to focus for the viewer. The reflecting telescope uses a large parabolic mirror to collect and focus the light which is then re-directed using mirrors and/or lenses to where the image obtained is to be projected, e.g. Prime focus and Newtonian Focus. Other apparatus such as a coronagraph or spectroheliograph can then be fitted to the telescope to block out the light from the disc of the Sun or to break down the Sun's light and get further information about the Sun from it.

Radio ground-based observations of the Sun have been carried out for decades. You can directly or indirectly take measurements of the Sun and the solar wind using radio telescopes or arrays. The method of observing by radio observations in this thesis was by radio scintillation or interplanetary scintillation (IPS), as described in detail in Chapter

3 of this thesis.

1.2 The Sun, our star

The Sun is a large, rotating, almost perfect sphere of hot plasma (but cool by comparison to larger and/or younger stars), that lies at the centre of our solar system. It is a Main-Sequence G-Type star approximately half-way through its life. It is primarily made up of Hydrogen (H) and Helium (He) but does contain heavier elements such as Carbon (C) and Oxygen (O). By mass, Hydrogen accounts for 70.68 %, Helium accounts for 27.43 %, and all other heavier elements accounting for the remaining 1.89 %, with the total mass of the Sun being approximately 1.99×10^{30} Kg. In terms of the number of particles, Hydrogen accounts for 92.1 % of the particles, Helium accounting for 7.8 %, and all other particles only accounting for 0.1 % by number.

Our Sun is just an ordinary star in our Galaxy, the Milky Way, which is one of many billions of galaxies in our Universe. The Sun is of typical size and luminosity, and of spectral classification G2 as defined from its spectral lines, which are in turn derived from the chemical content of the Sun, its temperature, and the ambient density in the emitting region. The radius of the Sun, $R_{\odot}$, is 6.96×10^8 m or approximately 109 Earth radii, $R_{\otimes}$, where the radius of the Earth, $R_{\otimes}$, is approximately 6.4×10^6 m. The luminosity of the Sun is 3.85×10^{26} W, with an estimated age of around 4.6 Billion Years. This is less than half the age of the Universe itself which is estimated to be between 10 and 15 Billion Years from the latest Hubble constant calculations using measurements obtained from galactic Red-Shift surveys.

The orientation of the Sun is such that its heliographic equator is inclined to the plane of the solar system by 7.25°. As the Sun is not a solid body it has a differential rotation, whereby it rotates at different rates ranging from 25 days at its equator to around 30 days near its poles, with a mean rotation of ~27.2 days, i.e. the Sun rotates faster as you go

from the poles toward the equator.

The Sun is effectively a giant nuclear fusion reactor, where nuclear reactions are its primary source of power. The core temperature where the nuclear fusion reactions take place is around 1.6×10^7 K. The primary process by which these reactions take place is via the proton-proton (p-p) chain where mass is effectively converted into energy. The p-p chain is where two Hydrogen nuclei (protons) collide together and fuse to form a nucleus of Deuterium, sometimes referred to as a Deuteron particle (Heavy Hydrogen), a positron (positive counterpart of the electron), and an electron-neutrino (an almost massless particle that travels at the speed of light when released from the Sun). By the release of the positron and electron-neutrino, the one proton is converted into a neutron when it fuses with another proton leaving a neutron-proton pair, i.e. the Deuterium nucleus. Another proton can then collide with the Deuterium particle which then forms a nucleus that happens to be an isotope of Helium, the ^3He nucleus, and a release of energy in the form of γ-rays (gamma-rays - the highest energy form of electromagnetic radiation). This leaves a nucleus containing two protons and one neutron. If this ^3He nucleus then collides with another ^3He nucleus, another Helium nucleus would be formed (the more abundant isotope that is found on the Earth), the ^4He nucleus along with two Hydrogen nuclei. The ^4He nucleus comprises of two protons and two neutrons. The overall result of this chain is:

$$6^1H \rightarrow^4 He + 2^1H + 2e^+ + 2\nu + 2\gamma \tag{1.1}$$

The 2γ represents the energy released in this reaction. This reaction process is shown schematically in figure 1.1.

The energy released by each p-p chain reaction is equal to the mass loss from the four protons to the one Helium (^4He) nucleus, i.e. from:

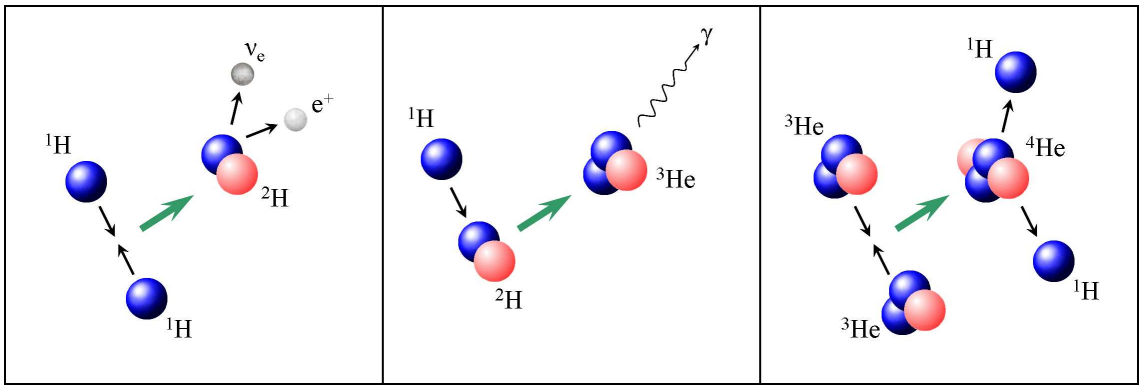

Figure 1.1: The p-p chain.
(Based on Lang, 2001)

$$E = mc^2 \tag{1.2}$$

we get the following:

$$\Delta E = (4m_H - m_{He})c^2 \tag{1.3}$$

and

$$\Delta E = 4.2 \times 10^{-12} \text{ J per reaction} \tag{1.4}$$

where:

$m_H = 1.672 \times 10^{-27}$ kg (mass of a proton);

$m_{He} = 6.664 \times 10^{-27}$ kg (mass of the Helium nucleus);

and $c = 2.997 \times 10^8$ ms^{-1} (the speed of light in a vacuum).

The Sun uses around 5×10^6 tons s^{-1} of its mass[1] to maintain its roughly constant lumi-

[1] 1 ton = 2000 pounds and approximately 2.2 pounds = 1 kg

nosity. This is calculated from the mass loss per reaction multiplied by the number of reactions needed to maintain the Sun's luminosity. The energy created from these nuclear reactions is carried out of the Sun through the different regions/zones of the Sun by various methods such as radiation and convection. The reason why the radiation emitted from the "surface" of the Sun is not in the form of γ-rays is because the photons released in the core are absorbed and re-emitted many times as they follow a "random walk" through the body of the Sun. The effect of this is to convert the initial γ-ray photons produced in the core to a much larger number of lower energy photons by the time they escape into space.

Traditionally, the Sun has been divided into two main regions, the solar interior, and the solar atmosphere; with the "surface" of the Sun (the photosphere) separating the two. As the Sun is a gaseous body of plasma, it has no solid surface, and the traditional divide between the interior and the atmosphere corresponds to the height where the mean-free-path for visible wavelength photons becomes large with respect to the size of the Sun. This takes place over a range of heights which account for the sharply defined appearance of the solar disc.

The solar interior has several main parts to its structure: a core, a radiative zone, and a convective zone; then there is the photosphere, the chromosphere, the transition region, the corona, and the solar wind; all of which are parts of the solar atmosphere. A cutaway diagram of the Sun can be seen in figure 1.2. The temperature gradually decreases throughout the different zones until the chromosphere is reached where it increases, and then through the transition region and into the corona, the temperature rises very, very rapidly to around two million Kelvin at the corona. The density however, continuously decreases as you move outward, and therefore away from the core of the Sun. A diagram of the energy transport can be seen in figure 1.3.

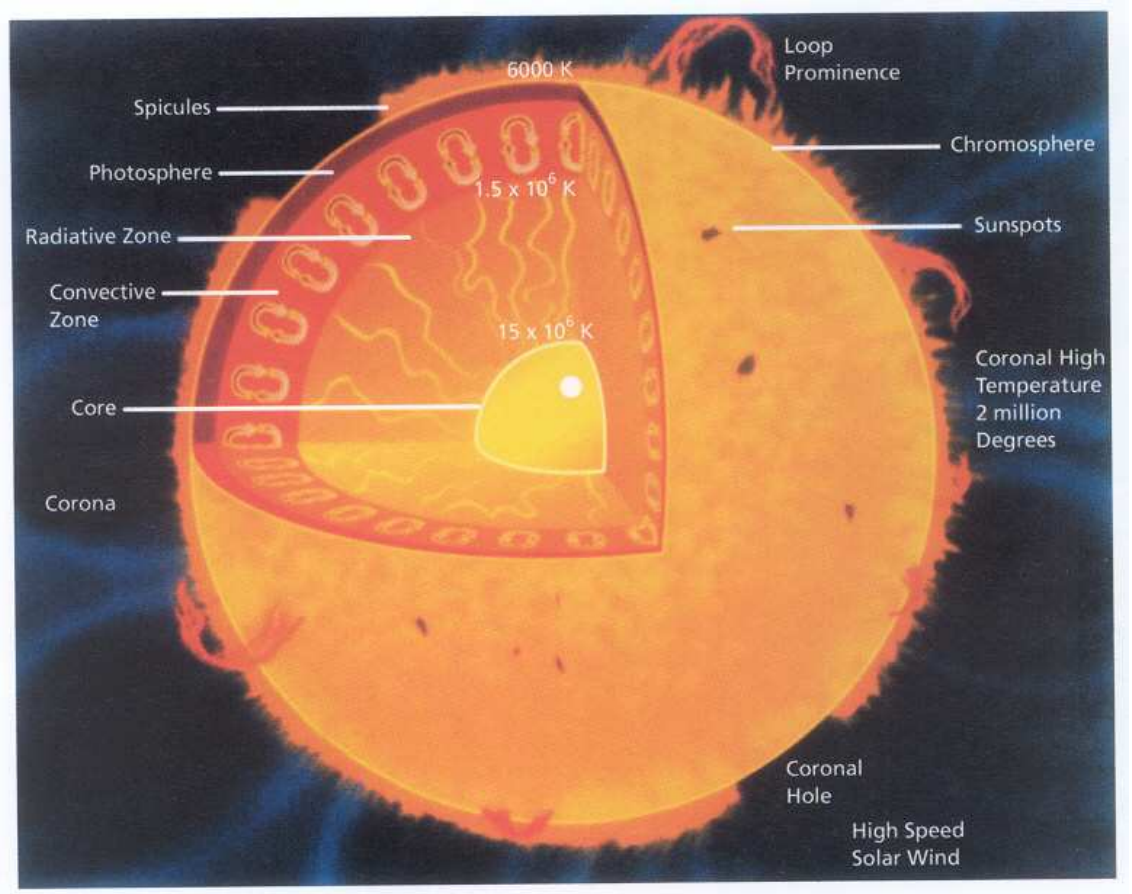

Figure 1.2: A cut-away sketch of the Sun and its interior.
(Lang, 2001)

1.2.1 The solar interior

The solar interior is made up of three parts, the Core, the Radiative Zone, and the Convective Zone, at each stage getting cooler and less dense coming outward from the centre of the Sun.

There are ways in which we can gain information about the interior of the Sun. One is by observing the slow and rhythmic in-and-out motions of the photosphere, otherwise known as helioseismology (Phillips, 1992), and the other is from the neutrinos that can travel unimpeded out through the Sun from where they originate at the core.

Sound waves inside the Sun can cause the visible solar disc to slowly move in and out

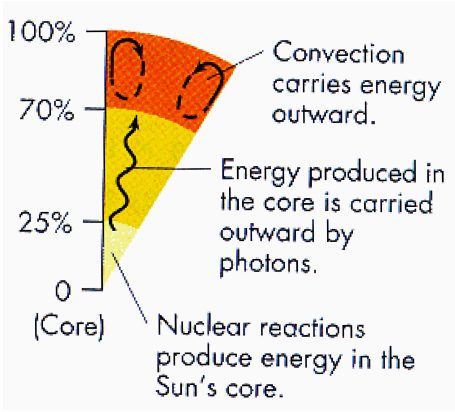

Figure 1.3: Energy transport methods from the centre of the Sun to 1 $R_{\odot}$. (Lang, 2001)

at a frequency of about 3 mHz, i.e. over 5 minutes or more for each period of oscillation. This pulsing of the Sun can be detected in two ways, either by the Doppler shift of a well-defined spectral line, or as minuscule changes in the Sun's total output (Lang, 2001). The tiny fluctuations which have been observed by instruments such as the Michelson Doppler Imager (MDI) on board the SOlar and Heliospheric Observatory (SOHO) spacecraft (Scherer *et al.*, 1995) reflect temperature changes of just 5×10^{-3} K on the Sun over periods of around 5 minutes. An average net change is just 3×10^{-2} K (Lang, 2001).

1.2.1.1 Core

The core of the Sun is its hottest and most dense part, it is the only part of the Sun hot enough to allow nuclear reactions to take place. It is thought that temperatures of around 15 million Kelvin occur here, with a density of about 1.5×10^{5} kg m^{-3} compared with an overall much lower average density of the Sun of around 1.4×10^{3} kg m^{-3}. This average density is just a quarter of the Earth's average density. The core takes up approximately 1.6% of the Sun's volume, in other words the radius of the core is approximately 1.74×10^{8} m, but due to its very high density compared with the rest of the Sun, it accounts for around half the mass of the Sun.

1.2.1.2 Radiative zone

In the inner regions of the Sun, energy is transported by radiative transfer. This is where the energy created in the core is transported by photons via a "Random Walk" method (described earlier) through the radiative zone by constant absorption and re-emission from the particles in the radiative zone. Hence, a constant transfer of energy from particle to particle occurs, but a general decrease in energy of photons as they get absorbed and re-emitted since the emitted photons are of a decreased energy. The radiative zone is still a very hot, but a relatively calm part of the Sun in terms of the movement of the material within the radiative zone. However, it is not dense enough to prevent the flow of the high energy photons outward from the core of the Sun and toward the surface. The temperature gradient is too shallow for convection to occur and is therefore a slow process taking 10^5 years. The radiative zone extends from the core boundary out to about 71.3 % of the Sun's radius, approximately 5×10^8 m. By the end of the radiative zone, the temperature associated with the frequency and wavelength of the photons, and hence this part of the Sun, has dropped to around 1.5×10^6 K.

1.2.1.3 Convective zone

At the convective zone however, the next part of the Sun going outward from its core, the material becomes opaque to the flow of photons because they have lost a lot of energy while travelling through the radiative zone. As temperature decreases, the opacity therefore increases, and radiative transfer becomes much less efficient. Hence this therefore increases the gradient in temperature. By approximately $0.7\,R_\odot$, the temperature gradient is sufficiently steep for convection to occur. Matter (material) in the convective zone is very turbulent. Although radiative transfer still occurs within the convective zone, the bulk flow of energy is due to the constant motion of matter through the zone. This is where the material rises toward the top of the convective zone going away from the radiative zone and core. It does this at speeds of around $50\,m\,s^{-1}$ to $100\,m\,s^{-1}$ (cooling a little while doing so), and moving across the top of the convective zone at speeds of around $200\,m\,s^{-1}$ to $400\,m\,s^{-1}$ where they emit photons and hence cool even more. The

material then sinks back into the convective zone at speeds of around $200\,\mathrm{m\,s^{-1}}$. Energy transport in this region of the Sun is therefore more rapid and takes place on time-scales of the order of 10 days.

The movement of ionised material in the convection zone causes a granulation effect on the Sun as viewed from the Earth, see figure 1.4, with hotter, brighter parts at the centre of the granules, and a darker, cooler outline around the granules. It is thought that these granules are the source of the magnetic originating field from the surface of the Sun. Results from helioseismology have shown substantial changes of the structure of the convective zone over a solar cycle further illustrating the important role that changes in the structure of the convection zone have on the drive mechanisms of the activity cycle. The granules are generally around $1.4 \times 10^6\,\mathrm{m}$ across or smaller, with typical lifetimes of around ten minutes. There is also a much larger cell pattern that forms from the movement of these granules. This is known as supergranulation (Leighton *et al.*, 1962). Supergranulation however, can only be seen in what is known as a dopplergram. This is a detection of the motion of the material at the top of the convective zone. It is believed that supergranulation corresponds to a preferred cell scale size of thermal convection, and is linked in with the Sun's magnetic field whereby the magnetic field lines are dragged across the Sun by the convective flows forming magnetic flux ropes at the boundaries of these supergranules (Galloway & Weiss, 1981). The size of these supergranules can be around $3.5 \times 10^7\,\mathrm{m}$ with lifetimes of one to two days.

Although radiative transfer of energy still occurs within the convection zone (but not through it), most of the energy transport is by method of convection and it can take just 10 days to be transported through the convection zone.

1.2.2 The solar atmosphere

The solar atmosphere is where the mean free path of the photons becomes very large quite abruptly and is made up of five parts, the Photosphere, the Chromosphere, the Transition

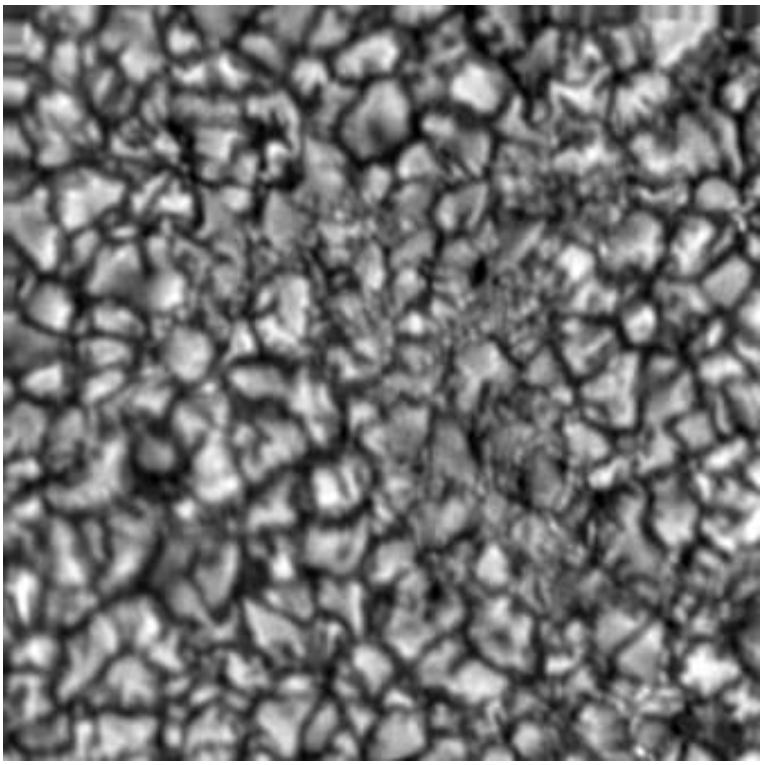

Figure 1.4: A co-spatial and co-temporal G-band 430.5 nm and wide-band 468.6 nm filtergram, taken with the 50 cm Swedish Vacuum Solar Telescope on the Spanish island of La Palma.
(Taken from http://www.solarphysics.kva.se/, January 2005)

Region, the Corona, and the solar wind (which will be talked about in detail later in this chapter).

1.2.2.1 Photosphere

The photosphere of the Sun is so-called due to its meaning of 'sphere of light'. It is the start of the solar atmosphere and is approximately 500 km thick above the convective zone. Its average temperature is measured to be 5780 K. This is a transition where the Sun goes from being opaque to transparent in terms of photons at visible frequencies once more, thus allowing photons to flow out of the Sun again and this time, into the Solar system and beyond. The photosphere is so called because it is the first part of the Sun which we can see and observe, since photons cannot pass through the convective zone, we cannot see directly below the surface of the Sun. It is in the photosphere that sunspots are observed which, depending on how many sunspots there are, relates to how active the

Sun is said to be. Sunspots are discussed further later in this chapter.

1.2.2.2 Chromosphere

Next, just above the photosphere lies a relatively thin layer with an approximate thickness of 2.5×10^6 m. This is known as the chromosphere, from the Greek word for colour, 'chromos'. The red colour of the chromosphere is due to the Hydrogen-Alpha (Hα) emission line at 656.3 nm, so you are seeing an emission line of an electron transition rather than broad-body thermal emission from the disc of the Sun which normally overpowers a single emission line. The intensity of the light from the chromosphere is very faint compared to the photosphere and hence can only be seen by the naked eye during a solar eclipse where the disc of the Sun is blocked out by the moon. It is seen as a faint red outline around the limbs of the Sun for a few seconds just before and just after totality. The temperature in the chromosphere is oddly higher than that of the photosphere, around 1×10^5 K, but there is a very large drop in the density to just one millionth of the density of the photosphere. The reasoning for the increase in temperature is almost certainly due to the dissipation of sound waves in the lower chromosphere heating it; however, these sound waves steepen into shocks too low down to heat the corona which appears above the chromosphere. The chromosphere is approximately 2000-3000 km in thickness. At first sight, this increase in temperature is unusual as both the chromosphere and transition region lies between the cooler photosphere and the tenuous cold gas of interplanetary and interstellar space. The chromosphere is itself a tenuous, incandescent gas which has characteristic spectral lines (e.g. Lang, 2001)

The chromosphere's outer edge is by no means smooth. It has several small jets (spicules) of gas coming out of it that are very dense but short-lived and can be seen when using an Hα filter. These spicules can rise at velocities reaching several thousand m s^{-1} and reach heights of 15×10^6 m. Again, using an Hα filter, it is possible to observe filaments in the chromosphere. These are loop-like structures of cooler denser gas that can stretch across the face of the Sun as dark "ribbons". An example of several filaments can be seen in

figure 1.5. If the limb (edge) of the Sun is also observed using this filter, then the same features can appear now as bright loops emanating from the solar disc. This is because they are now compared to the dark, cooler interplanetary background. In this case, they are known as solar prominences and an example of a large solar prominence can be seen in figure 1.6.

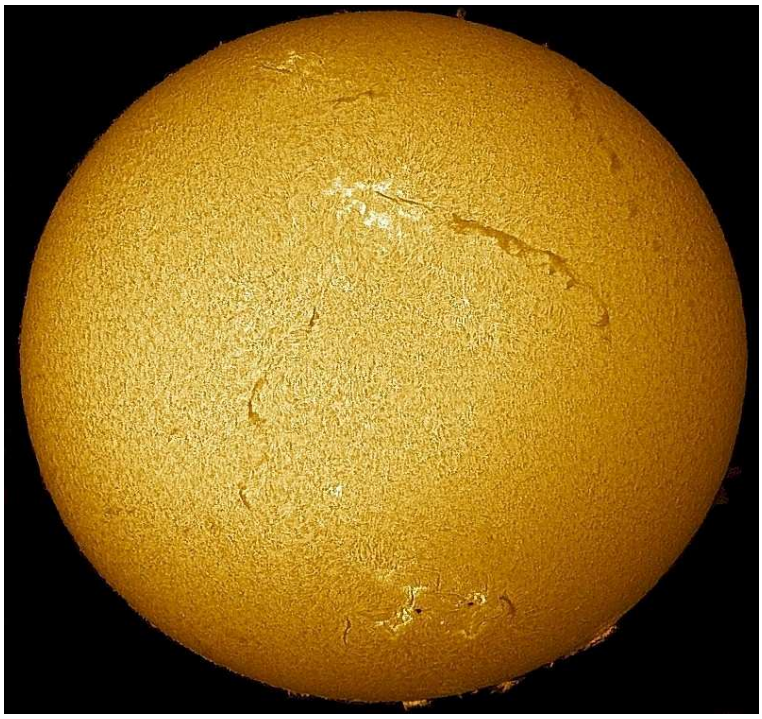

Figure 1.5: An example of solar filaments using the Hα filter. Image was taken on 26 November 2004 at 1800UT in Rockville, Maryland, U.S.A. during Carrington Rotation 2023.
(Courtesy of G. Piepol - http://www.sungazer.net/1126.html, March 2006)

1.2.2.3 The transition region

The transition region lies just at the top of the chromosphere but below the corona. This is where the temperature increases very rapidly up to the corona and the density drops very rapidly, thus the overall gas pressure remains spatially constant. The top of the transition region is where all the particles in the plasma start to regain thermal equilibrium, and henceforth becomes the start of the corona by definition. It is not yet fully understood

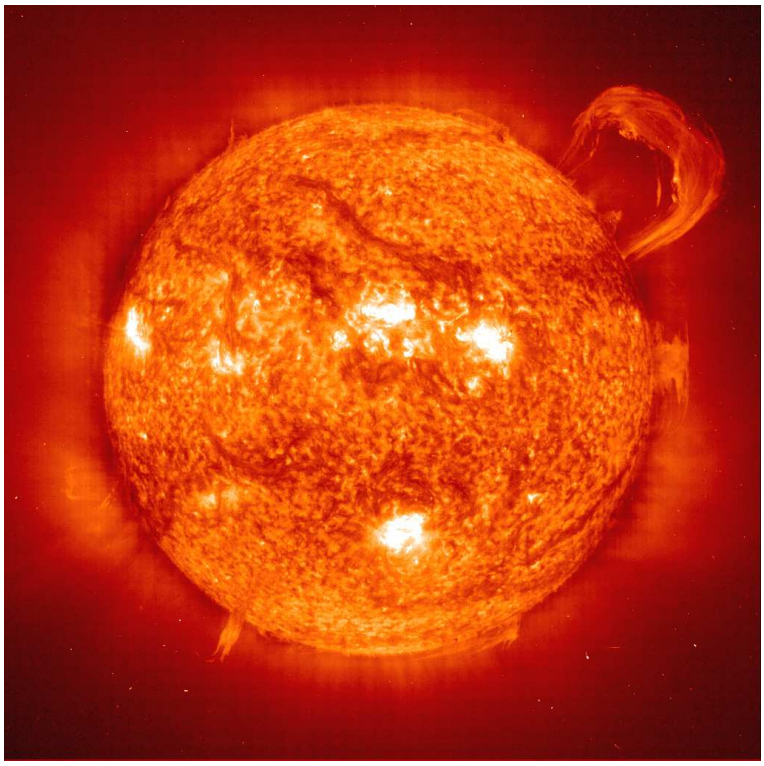

Figure 1.6: An example of a solar prominence using the EIT instrument at 304 Å instrument on board the SOHO spacecraft with the prominence coming off the West limb of the Sun.
(Taken from http://antwrp.gsfc.nasa.gov/apod/ap990923.html, January 2006)

why there is such a large increase in temperature. As a hot region cannot be heated from a cooler one (the photosphere below the chromosphere and transition region), it is obvious that the transition region and chromosphere are not heated by direct radiation from the photosphere, but by some other means (the coronal heating problem).

1.2.2.4 Corona

Finally, just above the transition region lies the solar corona, figure 1.7. This is the hottest part of the solar atmosphere with a temperature of around two million Kelvin. Again, this part of the Sun can only be seen by the naked eye[2] during a solar eclipse, but this time at the point of totality is when it can be viewed most clearly.

There are three parts to the solar corona, the K corona, the F corona, and the E corona.

[2] Advised to be with the use of protective glasses

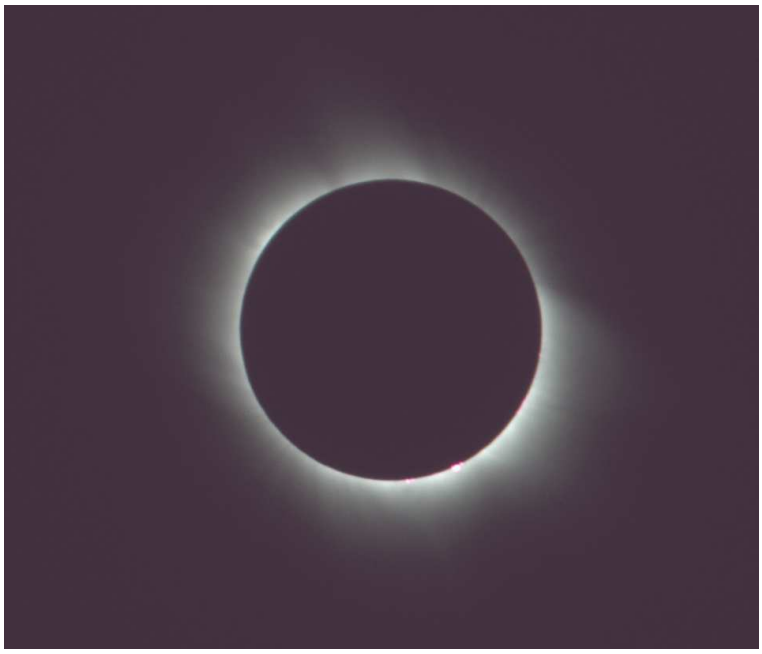

Figure 1.7: The faint glow of the solar corona seen clearly during the 2006 total eclipse of the Sun.

(Courtesy of Dr. Richard Fallows)

The K corona comes from the German word ‘kontinuum’ and is the inner part of the corona. The reason for its name is that the K corona is a continuous spectrum with no absorption lines. It is an electron scattered component of visible sunlight toward the base of the corona where the electron density is around $10^{15}\,\mathrm{m}^{-3}$. This is still a rarefied electron gas where about $10^{15}\,\mathrm{m}^{3}$ would have a mass of just $1\,\mathrm{kg}$. It is now obvious with a one-to-one relationship between protons and electrons (since the corona is overall electrically neutral) that most of the mass is due to protons, with a mass density of about $10^{-12}\,\mathrm{kg\,m}^{-3}$ in the low corona.

The F corona is due to the scattering of sunlight from dust particles in interplanetary space since the whole solar system can be thought of as being in the Sun’s outer atmosphere. It is worth noting though, that both the F and K components of the Sun’s corona decrease in intensity with increasing distance from the Sun. Beyond about two and one-half solar radii, the F component is more intense than the K component, but unlike the K component, the F component contains many Fraunhoffer absorption lines, hence where the F

came from in its naming. Another way of distinguishing between the photons from either corona so far, is from their polarisation. The F corona is not polarised in any preferred direction, but the K corona however, is.

Coming from transitions which can take place only in low density regimes is the E corona. These transitions are known as “forbidden” lines because they cannot occur under normal laboratory conditions, i.e. cannot occur naturally on the Earth. This is because they never live long enough to be de-excited by radiation, they always collide first and thus become de-exciting through collisions and a vacuum high enough to stop this happening cannot be created on Earth in a lab since a low enough density cannot be falsely obtained; the low density means they live long enough to de-excite through photon-emission. These lines remained a major mystery to the astronomical community for many years and were first discovered in 1869 (e.g. Nicolson, 1982). It was assumed for a long time that what we know today as Helium, which at the time had not been discovered on the Earth, was an unknown element that was provisionally called “coronium”, since it did not fit in with any other elements of the periodic table of the day. However, in 1940, it was found that many of the emission lines were transitions that could take place in highly ionised common metals but only where there was a sufficiently high enough temperature and low enough pressure, i.e. the corona of the Sun; hence the inability for them to be man-made with present technology. The green emission line at 530.286 nm was due to Fe-XIV (thirteen times ionised Iron) (Nicolson, 1982). Other lines that feature prominently are those of highly ionised calcium and nickel. This existence of highly ionised ions provided more evidence to the high temperature solar corona.

The corona contains regions of anomalously low density “holes”. These are generally above the poles of the Sun during minimum activity and are known as polar coronal holes. Coronal holes are regions where the magnetic field of the Sun is said to be open. These regions have very little material in them and they generally appear as large dark areas seemingly devoid of radiation at wavelengths of Extreme Ultra-Violet (EUV) and soft X-

rays, with very little emission in the visible spectrum. It should be noted though, at times of high solar activity, coronal holes can appear almost anywhere around the Sun and are not just restricted at the poles. Polar coronal holes at solar minimum are long-lived but at solar maximum, the Sun is dominated by bright and probably closed regions with smaller and shorter lived coronal holes - not necessarily at the poles of the Sun. Coronal holes can also vary in size, which again is dependent on the activity of the Sun, for example, at solar maximum, the polar coronal holes generally decrease in size if not disappear altogether (Phillips, 1992). A schematic of the temperature versus height through the Sun from its photosphere though into its corona can be seen in figure 1.8.

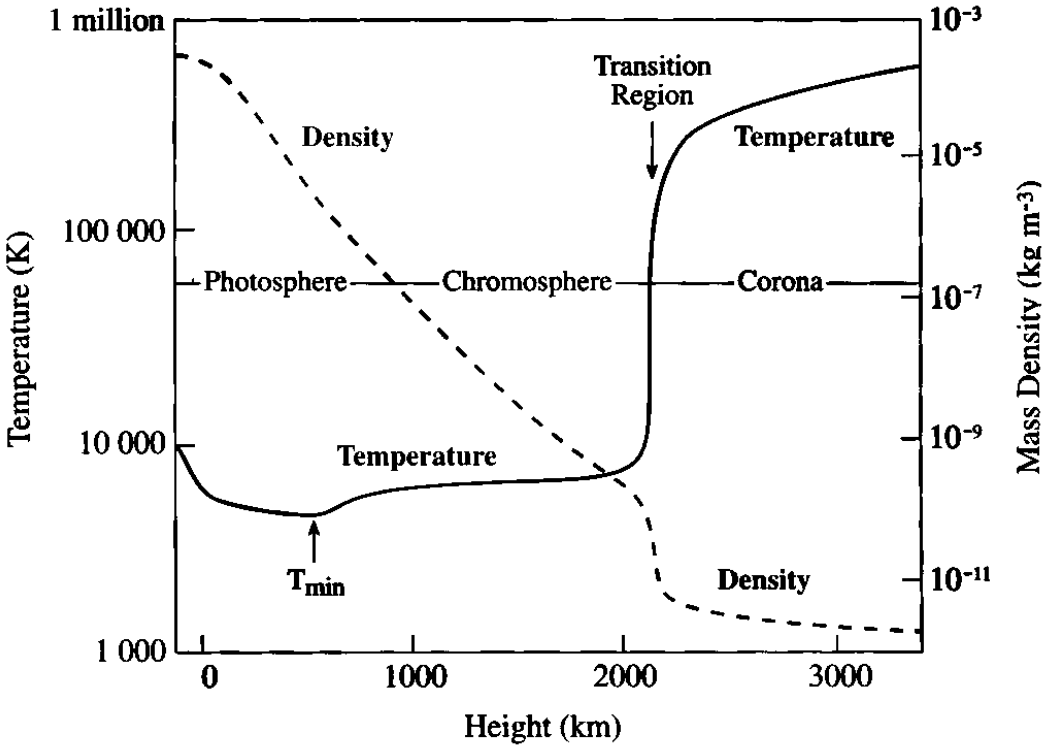

Figure 1.8: Temperature profile of the Sun's atmosphere.
(Lang, 2001)

1.3 Sunspots, the solar cycle and the Sun's magnetic structure

As previously described, sunspots are seen in the photosphere of the Sun. It is a cycle in these sunspots that defines the solar activity cycle. Firstly, what are these so-called sunspots? Sunspots are dark spots or patches on the Sun's surface that can sometimes be seen with an unaided eye when viewing the Sun indirectly. Their centre is the darkest part which is known as the umbra. The umbra is then surrounded by a light filamentary penumbra. If sunspots occur near the centre of the solar disc, they will be about the same width in all directions but if they occur near the edge of the limb of the Sun however, the portion of the sunspot that lies closest to the centre of the disk appears narrower than the part that is closest to the solar limb. This asymmetric distortion of sunspots observed near the solar limb is known as the Wilson effect, after the Scottish astronomer, Alexander Wilson, who was among the first discoverers of it in the eighteenth century.

In the early 1840s, Samuel Henrich Schuabe, a pharmacist and amateur astronomer of Dessau in Germany, was first to suggest the existence of an 11 year cycle in the number of sunspots that were on the surface of the Sun at any one time. He observed the Sun for a total of over forty years. In 1848, a Swiss astronomer from Zurich named Rudolf Wolf introduced the relative sunspot number, R, given by $R = k(10g + s)$. This number helps to distinguish between the number of groups of sunspots, g, counted on a specific day, and the number of actual individual sunspots, s, counted in all the groups on that same day. The k is a factor that is estimated to compensate for the efficiency of the observer and the observer's instruments. (Lang, 2001)

At the start of the sunspot cycle, which is defined as the maximum activity of the solar cycle, explosive flares from the Sun are also at their maximum occurrence and the Sun's magnetic field is in its most complex form with field lines originating and terminating over all parts of the Sun. The belts of activity generally start toward the poles,

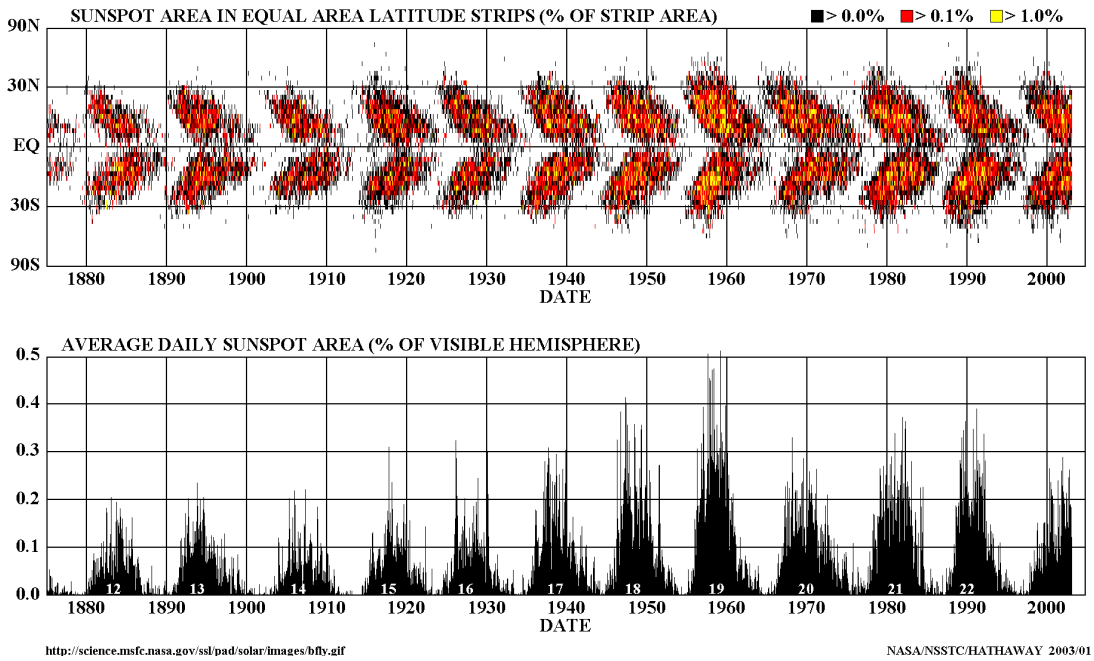

Figure 1.9: Maunder's butterfly diagram of the 11 year sunspot cycle with the maximum Sun coverage of sunspots during each solar maximum.
(http://science.msfc.nasa.gov/ssl/pad/solar/images/bfly.gif accessed March 2005)

about one-third of the way up from the equator, and work their way toward equatorial regions as the cycle progresses toward solar minimum. Sunspots are oriented so that either North or South polarity will be on the leading edge of the sunspot in the northern hemisphere with either the South or North polarity on the trailing edge, and vice versa in the southern hemisphere of the Sun. The tendency for the sunspots to migrate from mid-latitudes toward the equator over a solar cycle can be seen from Maunder's butterfly diagram in figure 1.9. The active regions have a tendency to disappear or "fizzle-out" at sunspot minimum.

As the cycle progresses and old sunspots start to near the end of their lifetime (at or near to the equator toward the end of an 11 year cycle) new ones start to break out at about one-third of the way up, starting again at mid-latitudes. However, this time when they start to form, the magnetic polarities of the sunspots are reversed with North becoming South and

South becoming North. This also happens with the Sun's poles, almost as if the Sun had been turned upside down at the end of the 11 year cycle, the North pole changes polarity to a South orientation and vice-versa for the South pole. The leading polarities in each of the respective hemispheres changes with each 11 year cycle because of the dipolar magnetic field reversal of the Sun meaning that the 11 year cycle is not really so, since after the 11 years, the Sun is not the same as at the start of the next 11 years due to magnetic re-orientation. It is in fact a 22 year (on average) cycle that the Sun tends to follow for it to reach the same point in its dipolar magnetic field configuration and amount of solar activity.

1.4 The explosive Sun

Along with all these features of the Sun that have been so far discussed, there is an explosive aspect of the Sun in various forms; solar flares, erupting prominences, and coronal mass ejections (CMEs) covering a whole range of scales from X-ray bright points, to EUV blinkers, to explosions seen in visible light. All these events are representative of a restructuring of the magnetic field of the Sun with it relaxing into a lower energy state.

A single solar flare explosion has the equivalent energy to the destructive power of one-hundred megatons of TNT (trinitrotoluene) explosive. For a short period, a solar flare can be the hottest place on the Sun, heating approximately Earth-sized active regions to tens of million Kelvin. During a solar flare explosion, the solar system is flooded with fairly intense radiation right across the electromagnetic spectrum from the highest energy in the form of γ-rays to the lowest energy in the form of radio waves. Solar flares tend to occur in close proximity to sunspots.

There are also filaments and prominences as described earlier, and coronal mass ejections. Filaments are masses of relatively cool, dense material suspended above the photosphere in the low corona by the Sun's magnetic field, and prominences are defined as filaments

viewed from the Earth that are on the limb of the Sun. Prominences appear as loops of material coming out of the Sun. Coronal mass ejections are giant magnetic bubbles that rapidly expand in size as they leave the Sun and drag material with them. Further discussion of coronal mass ejections will occur later in this chapter since they are an important feature of the solar wind.

1.5 The solar wind

The solar wind is the extension of the Sun's corona and is the final part of the Sun's "atmosphere". It is best described as a supersonic outflow of coronal plasma into interplanetary space. The Sun's magnetic field is "frozen-in" to the plasma as it travels out into the solar system, thus causing the solar wind to have a magnetic field, and also carries the explosive events of the Sun out into interplanetary space, known as transient events, leading to consequences at the Earth and other planets. The solar wind carries away about 10^{-13} of the Sun's mass per annum.

1.5.1 The discovery of the solar wind

The existence of the solar wind was first thought about back in the early nineteenth century in an effort to explain the phenomenon of the aurora that appeared at mainly high latitudes in the Earth's atmosphere, figure 1.10 is an example of the Aurora Borealis taken from the European Incoherent SCATter radar (EISCAT) Tromsø site on mainland Norway in October 2003. However, there are several possibilities of aurora being documented as far back as 2000 B.C. by the Chinese, around 600 B.C. by the Xenophanes who mentioned moving accumulations of burning clouds, and also in some Greek literature. (Russell, 1995; Grall, 1995)

It was thought that intermittent outflows of material from the Sun were the cause of aurorae from measurements taken with a network of magnetometers of the Earth's changing magnetic field. It was in 1851 that Edward Sabine used the data from these magnetome-

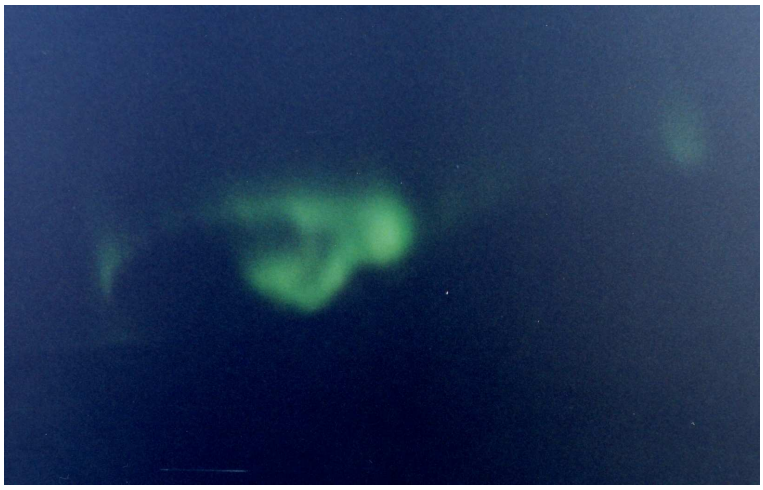

Figure 1.10: A photograph of the Aurora Borealis (Northern Lights) from the EISCAT Tromsø site on mainland Norway, October 2003.
(Taken by M. M. Bisi)

ters to show a correlation in the magnetic storms with the sunspot cycle. Then, in 1859, two independent observers, Hodgson and Carrington, re-affirmed this solar-terrestrial link with sightings of a great white flare from the Sun which caused great aurorae some 18 hours later over both North and South poles, and at lower latitudes. After many investigations and further observations of the aurorae, and hypothesitions as to their causes from scientists such as Becquerel, Goldstein, and Birkeland, it was established that the flow from the Sun was overall electrically neutral, but consisted of ions (mainly protons) and electrons. This was suggested by Lindeman in 1919. (Phillips, 1992; Russell, 1995; Canals, 2002)

After a time from the observations of comets having two tails, one from the dust due to the movement of the comet and always laying behind the comet (usually yellowish or white in colour), and the other from the solar wind plasma, which always points away from the Sun (usually blue in colour), see figure 1.11, it was inferred that the outflow of plasma from the Sun is in fact constant and not intermittent as was first thought. Biermann continued the work of another scientist, Hoffmeister, on comet tails, and proposed that the continuous outflow of plasma from the Sun, continuously in all directions, was solar particle emission, otherwise known as corpuscular radiation (Biermann, 1951, 1957) (cited

in Canals, 2002). A second reason for the continuous outflow from the Sun came from modelling and theoretical work by Chapman, who assumed a static corona and a transfer of energy by conduction alone. However, E. N. Parker, who was not completely satisfied with either Biermann's or Chapman's work, showed in 1958 that the Sun better followed a hydrodynamic model where the material flowed out of the Sun as a result of the much increased temperature within the corona. This is where the solar wind got its name from (e.g. Parker, 1958; Phillips, 1992; Russell, 1995; Neugebauer & von Steiger, 2003).

In later years, from missions like the Russian Lunik III and the American Mariner 2 between 1959 and 1962, it was found that the solar wind did in fact flow out from the Sun continuously. The velocity of the solar wind was measured in the range of 400 km s^{-1} to 700 km s^{-1} (Neugebauer & Snyder, 1962). The speed of sound near the Earth's orbit of 1 AU is around 60 km s^{-1} for material of this density, so there was no further doubt about the existence of a continuous supersonic outflow of material from the solar corona, i.e. the solar wind (e.g. Neugebauer & Snyder, 1966).

1.5.2 Solar wind streams

After many years of observing the solar wind, it is a well established fact that the solar wind contains two components, a slow stream with velocity of around 350 km s^{-1} and a fast stream with velocity of around 750 km s^{-1} (e.g. Schwenn, 1990; Coles, 1996; Moran *et al.*, 1997; Woch *et al.*, 1997; McComas *et al.*, 1998a; Lang, 2001). It is now well established that the faster solar wind emerges from large coronal holes where the magnetic field lines are said to be "open" (e.g. Krieger & Timothy, 1973; Schwenn, 1990; Woch *et al.*, 1997; Breen *et al.*, 1998; Lang, 2001). The slow wind however, is found above bright coronal streamers, but its origin is still uncertain. The very variable nature of the slow wind suggests that it may not have a single origin. A Summary of the various

Figure 1.11: A picture of the comet Hale-Bopp by R. M. Sandy in March 1997 showing the characteristic double tail of comets, one from its movement though the solar system (yellow/white), the other from the solar wind pointing away from the Sun (blue).
(http://www.geol.vt.edu/vesr/astpho/comet/comet.html accessed 14 January 2003)

properties of the different streams within the solar wind can be seen in table 1.1. Near solar minimum, the coronal magnetic field lines have a dipole geometry and an equatorial current sheet which has formed because the magnetic field lines are being pulled out by the slow solar wind around the equator of the Sun. At the polar regions, the fast solar wind escapes along the "open" magnetic field lines.

1.5.3 Solar wind acceleration

The acceleration of the solar wind is still somewhat a mystery however. It is thought that the expansion of the Sun's corona is partly responsible where it starts slowly near the Sun (where gravity is strongest) and then continuously accelerates as it breaks away from the Sun. It eventually reaches an asymptotic limit or terminal velocity, and then continues to travel along at pretty much a continuous speed, unless any interaction occurs between the

Property	Slow Wind	Fast Wind
Speed (v)	$< 400\,\mathrm{km\,s^{-1}}$	$700\,\mathrm{km\,s^{-1}}$ to $900\,\mathrm{km\,s^{-1}}$
Density (n)	$\sim 10\,\mathrm{cm^{-3}}$	$\sim 3\,\mathrm{cm^{-3}}$
Flux (nv)	$\sim 3 \times 10^8\ \mathrm{cm^{-2}\ s^{-1}}$	$\sim 2 \times 10^8\ \mathrm{cm^{-2}\ s^{-1}}$
Magnetic Field (B_r)	~ 2.8 nT	~ 2.8 nT
Temperatures	$T_p \sim 4 \times 10^4$ K $T_e \sim 1.3 \times 10^5$ K $> T_p$	$T_p \sim 2 \times 10^5$ K $T_e \sim 10^5$ K $< T_p$
Coulomb collisions	Important	Negligible
Anisotropies Beams	T_p isotropic None	$T_p(\perp) > T_p(\parallel)$ Fast ion beams + electron "strahl"
Structure	Filamentary, highly variable	Uniform, slow change
Composition	He/H ratio $\sim$ 1% - 30%	He/H ratio $\sim$ 5%
Waves	Both directions	Outward propagation
Minor species	n_i/n_p ratio variable $T_i \sim T_p$ $V_i \sim V_p$	n_i/n_p ratio ~constant $T_i \sim AT_p$ $V_i \sim V_p + V_A$
Associated with	Streamers transiently open field	Coronal holes
Sunspot minimum	$\pm$ 15° from equator	$>$ 30°
Sunspot maximum	Dominant at most latitudes	Less frequent

Table 1.1: Comparison summary of various properties of the slow and fast streams of the solar wind as seen at 1 AU.

(Axford & McKenzie, 1997)

two streams of wind, or if there is some kind of eruption of material from the Sun, other than the standard outward flow of the solar wind.

The fast solar wind has a velocity and mass flux that are too high to be explained by heat transport and classical thermal conduction alone (Lang, 2001). It is thought that the fast solar wind accelerates to its high velocity very close to the sun, within about ten to twenty solar radii. In coronal holes, heavier ions tend to move faster than the lighter ions. The ions are not in thermal equilibrium with each other and do not tend to interact with one another. The reason why the heavier ions move faster is because if they are accelerated by magnetic waves in the coronal holes, then the gyration power given to the heavier ions is greater because there is more power in the lower frequency waves. Another possibility is that Alfvén waves with long wavelength, λ, resonate with the energetic cosmic

rays coming from outside the solar system and oppose their entry into polar regions of the Sun. Alfvén waves change the direction of the magnetic field but not its strength over periods of tens of hours. These Alfvén waves are adding to the heat-driven wind and could potentially provide an extra boost in the acceleration of the solar wind over the coronal holes, i.e. making the flow faster. (Lang, 2001)

1.6 Basic theory of solar wind formation

A little time before the beginning of the space-age, Eugene N. Parker of the University of Chicago, formulated a theory of space being filled with a flow of plasma out from the Sun, which he named the solar wind (Parker, 1958). Parker suggested that the solar wind was a natural consequence of the high temperature at the corona (as described in Brandt, 1970a) and based his first model on force balance between thermal pressure and gravitation in an isothermal corona surrounding a spherically symmetric non-rotating Sun with no magnetic field what-so-ever, seen in equations 1.5 and 1.6 later. Parker was aware of the work being carried out by Chapman on static models of the corona and by Biermann on corpuscular radiation. Chapman's hydrostatic model proposed that at large distances from the Sun, the high temperature of the material was due to conduction from the million degree part of the inner corona and showed a decline in the density of ions or electrons with increasing distance from the Sun. This meant that the gas pressure predicted at the end of the solar system was very much higher than the gas pressure that had been predicted between the stars. (Moran, 1998; Canals, 2002; Neugebauer & von Steiger, 2003)

Parker's proposal was that the inconsistency of these pressures could be explained by taking away the possibility of there being hydrostatic equilibrium and supposing that the Sun's gravity is not strong enough to hold back the pressure force from the high temperature coronal gases and therefore allowing the corona to expand freely into space. This is therefore satisfying the equation of motion (also known as the conservation of momentum equation), equation 1.5, with the assumption that the pressure at an infinite distance

was negligible, and the equation of continuity (also known as the conservation of mass equation), equation 1.6.

$$Nm_H v\frac{dv}{dr} = \frac{d}{dr}(2Nk_BT) - GNm_H M_\odot \frac{1}{r^2} \tag{1.5}$$

$$\frac{d}{dr}(r^2 Nv) = 0 \tag{1.6}$$

Where:

N is the gas density;

T is the kinetic temperature;

v is the radial velocity;

r is the radial distance from the Sun;

m_H is the mass of a single Hydrogen atom;

$M_\odot$ is the mass of the Sun;

k_B is the Boltzmann constant, $1.38 \times 10^{-23}\,\mathrm{J\,K^{-1}}$;

and G is Newton's Gravitational constant, $6.67 \times 10^{-11}\,\mathrm{N\,m^2\,s^{-2}}$.

The left hand side of equation 1.5 represents the change of momentum of the outward flow of the gas from the Sun. The right hand side includes the pressure gradient as the first term and the force of gravity acting inward on the outward-bound gas as the second term.

Parker then went on to solve these equations and hence derive critical distances for different gas temperatures of supersonic speeds as discovered in the Mariner II observations (Neugebauer & Snyder, 1962, 1966). The critical distances were the distances from the Sun where the gravitational and pressure forces balanced on the right hand side of equation 1.5, i.e. the left hand side became equal to zero. Four possible solutions were

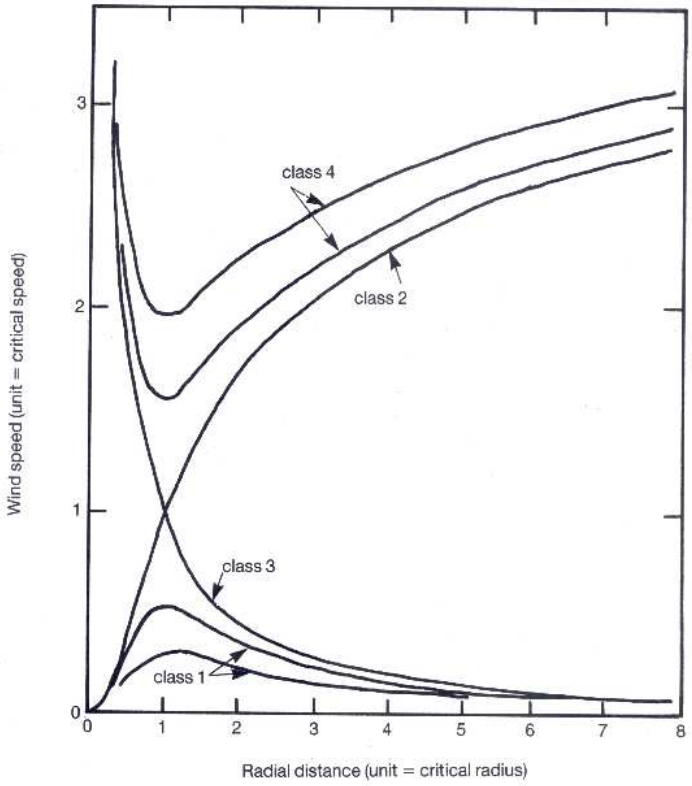

Figure 1.12: The four solutions for the solar wind speed with distance away from the Sun by E. N. Parker, from Phillips (1992).

(After Parker, 1963)

found for the outflow of the solar wind into the interplanetary medium. These can be seen in figure 1.12.

The equations Parker used assume an isothermal corona, spherical symmetry, and single species of particle. The Parker equations show that if the outward pressure is great enough (greater than the Sun's gravity), then it can drive an outflow of material into the interplanetary medium. Out of the four solutions in figure 1.12, three can be dismissed as they do not correctly describe the inner and outer region characteristics of the solar wind accurately. The only solution that correctly predicts the solar wind at very close distances and large distances from the Sun is Class 2. This is because close to the Sun ($R = R_{\odot}$), you see the corona, which means at some point, the velocity is zero (i.e. Class 1 or Class 2 and immediately ruling out Classes 3 and 4). The Class 1 solution never reaches a significant enough velocity to overcome the Sun's gravitational attraction or any

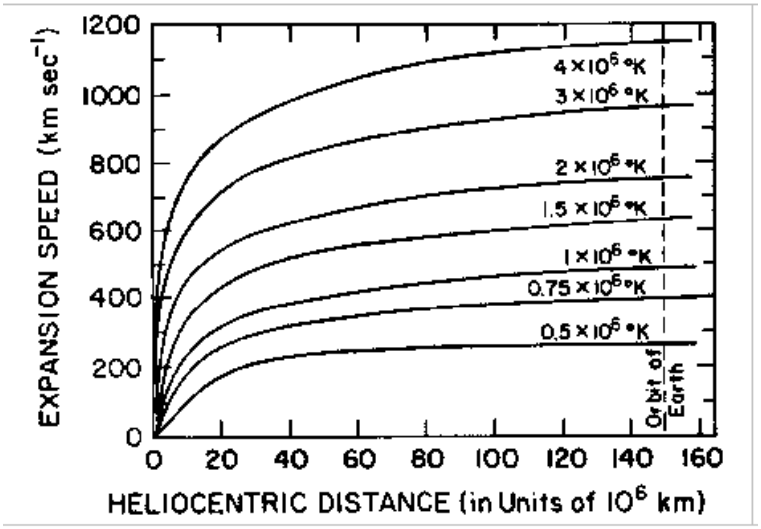

Figure 1.13: The radial expansion speed, u(r), as derived from isothermal coronal-expansion models with coronal temperatures ranging from 5×10^5 K to 4×10^6 K, from Hundhousen (1999). (Adapted from Parker, 1958)

other restraint it may have on it whereas the Class 2 case has a pressure gradient force that is stronger and so continues to accelerate and therefore becomes fast far from the Sun, but still with a positive net acceleration. Parker showed that a variation in solar wind velocities was possible depending on the temperature of the source region of the solar wind, the corona, and this produced a variety of velocity profiles. This can be seen in figure 1.13.

Parker's model predicted the supersonic flow of solar wind at 1 AU, but it was somewhat out for the relationship between the speed of the wind and its kinetic temperature as observations by the Mariner II spacecraft had shown. From these observations, the solar wind speed near the Earth's orbit was about 400 km s^{-1} at a temperature of around 10^5 K. Parker's model however had the same velocity, but at a kinetic temperature in the region of 10^6 K, an order of magnitude higher. This is where the discrepancies between Parker's theory and actual observations start to occur due to the oversimplifications incorporated into his model. Chamberlain in 1961 added to Parker's model by introducing an additional energy conservation equation in an effort to account for the thermal conductivity through the gas into the model (reviewed in Moran, 1998). There have also been other models that include viscosity terms, the magnetic field of the Sun, thermally driven

acceleration models, and also some models considering the propagation of hydrodynamic waves in the solar wind, plus the role of these waves in terms of the acceleration of the solar wind (e.g. Coles & Esser, 1992; McKenzie *et al.*, 1995; Axford & McKenzie, 1997; Ofman & Davila, 1998; Esser *et al.*, 2003; Li, 2004; Jones *et al.*, 2004).

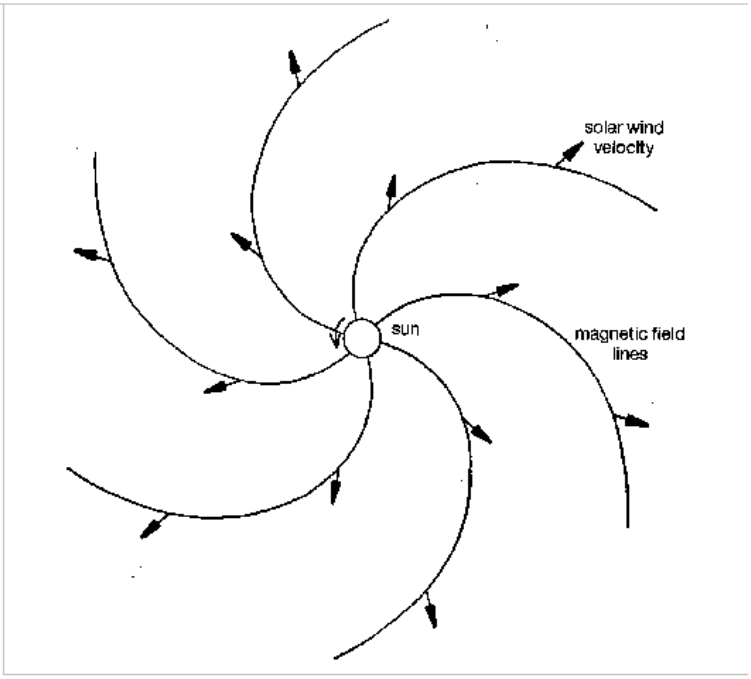

Figure 1.14: The direction of solar wind flow is given by the arrows along with the lines of magnetic field originating from the Sun, which spiral along the interplanetary medium due to the counterclockwise rotation of the Sun as viewed from above the Sun's North pole (Parker spiral pattern).

(Phillips, 1992)

1.7 Co-rotating interaction regions (CIRs)

The angle of magnetic streamlines of solar wind flow to the radial direction - the Archimedes (Parker) spiral angle (ψ) for a given distance from the Sun - can be calculated using the following equations, where r_o in equation 1.7 is one solar radii (1 $R_\odot$):

$$\phi - \phi_o = \Omega t = \Omega \frac{(r_o - r)}{v} \tag{1.7}$$

Where:

Ω is the rotation rate of the Sun;

Ωt is the tangential component of the rotation rate of the Sun;

ϕ is the solar longitude of a point along an Archimedes spiral at a distance r from the Sun;

ϕ_o is the solar longitude at solar surface;

v is solar wind speed;

and t is the time taken for the Sun to rotate through angle ϕ - ϕ_o.

Using Equation 1.7 and figure 1.15, the spiral angle ψ is defined by:

$$tan\,\psi = -\frac{(r - r_o)d\phi}{dr} \tag{1.8}$$

This can be seen schematically in figure 1.15 by considering a single magnetic flux line (or tube) carried by a radial solar wind of velocity v, the angle between the magnetic field line and the radial direction from the Sun at a certain distance is the Archimedes (Parker) spiral angle.

Also from Equation 1.7, the following can be done:

$$\frac{-d\phi}{dr} = \frac{\Omega}{v} \tag{1.9}$$

Therefore we get:

$$tan\,\psi = \frac{(r - r_o)\Omega}{v} \tag{1.10}$$

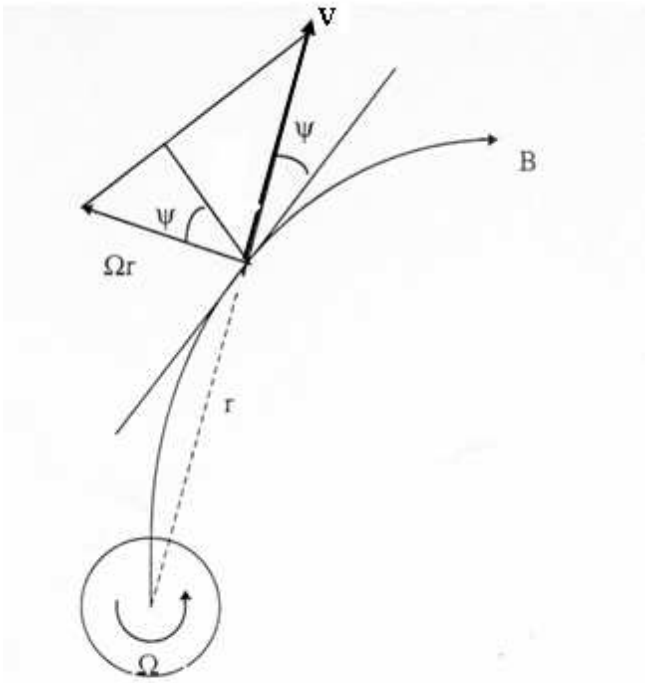

Figure 1.15: Schematic showing the Archimedes spiral pattern of a single flux tube emerging from the Sun and the quantities used to describe it at a distance r, where $\Omega r = v_t$, the tangential velocity. (Adapted from Canals, 2002)

Going back to the theory of the solar wind carrying the Sun's magnetic field within it, this will lead to an Archimedes spiral pattern forming due to the rotation of the Sun since the magnetic field lines are rooted to the Sun's surface, figures 1.14 and 1.15, and equations 1.7 to 1.10. At Earth's orbit, with a solar wind speed of approximately 400 km s^{-1} and also confirmed by in-situ measurements, the angle of the spiral will be roughly 45°.

Co-rotating interaction regions are formed when the rotation of the Sun causes fast and slow streams that are at the same solar latitude (more common at solar maximum) to push into each other, the fast stream in effect catches up with the slow stream. The slow stream has a much tighter spiral than the fast stream since the fast stream travels out from the Sun at higher speeds so does not get spiralled so tightly as seen in figure 1.16.

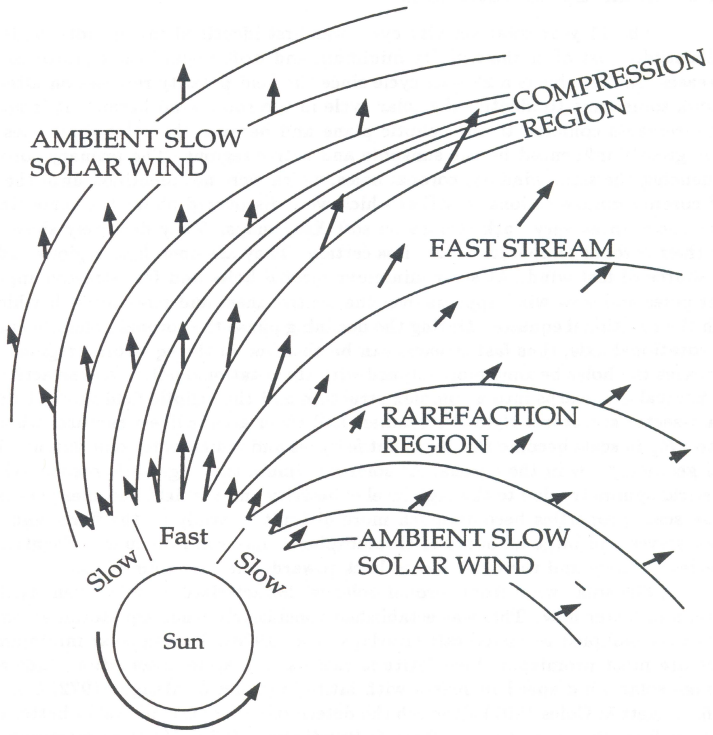

Figure 1.16: A diagram showing the geometry of the fast and slow solar wind in a developing CIR. The longer arrows represent the fast solar wind, the shorter arrows for the slow solar wind. (Taken from Grall, 1995)

As the leading edge of the fast stream catches up with the slow stream, a compression region is formed due to the inability of the magnetic field of each stream to penetrate into the other. It is within this compression region where plasma densities are higher than the densities that are associated with either the fast stream or the slow stream. The magnetic field is also enhanced. The velocity is intermediate compared to the normal fast or slow stream velocities respectively. A forward-propagating wave develops at the leading edge of the compression region which in turn causes the preceding slow wind to accelerate while a backward propagating pressure wave causes the fast stream, which lies behind the region of compression, to slow. The high pressure region which is bounded by the forward and reverse pressure waves is known as the interaction region (Forsyth & Gosling, 2001). The overall net effect of the interaction region is the transfer of momentum from the fast stream to the preceding slow stream. If the velocity difference between the fast and slow streams is sufficiently great, then the pressure waves can cause

a narrowing of the compression region and causes an initial non-linear increase in pressure. This can then cause the forward and reverse propagating pressure waves to steepen into shocks. Once the shocks have formed, they cause the interaction region to expand, since the shock waves can propagate at speeds much greater than that of the fast solar wind speed, therefore most of the acceleration of the slow wind and deceleration of the fast wind takes place discontinuously at the forward and reverse shocks, hence the sharp discontinuities in velocity measurements seen in spacecraft data at forward and reverse shocks (Forsyth & Gosling, 2001). Along with a compression region on the leading edge comes a rarefaction region on the trailing edge of a CIR, as the fast stream pulls away from the slow stream following it. In the rarefaction region, there are again intermediate velocities, but the density drops below that of the slow stream or the fast stream. Compression and rarefaction regions have been detected by spacecraft between 70 $R_\odot$ and about 1100 $R_\odot$ (Schwenn, 1990). CIRs have also been detected in IPS data at distances of less than 30 $R_\odot$ to more than 120 $R_\odot$ from the Sun (e.g. Breen *et al.*, 1998). They are characterised by increased levels of scintillation (e.g. Breen *et al.*, 1997b).

Although more common during the declining phase to solar minimum, CIRs can also occur during solar minimum, particularly when coronal holes sometimes extend down to lower latitudes in an asymmetric manner, but they are even weaker at solar maximum due to the more highly evolving coronal structure. Models have predicted that with CIRs, somewhere beyond the Earth's distance from the Sun if the conditions are right, then the forward and reverse propagating pressure waves can steepen into shocks. The shock fronts will propagate forward as forward shocks and backward as reverse shocks through the plasma from the frame of reference of the flow of the solar wind itself (Gosling *et al.*, 1972). These shock fronts have also been detected at large distances from the Sun by spacecraft (e.g. Forsyth & Gosling, 2001).

CIRs can be mapped inward to the Sun to approximately find the point of origin of the fast and slow streams at a particular latitude in the low corona, or mapped outward to where

spacecraft are taking measurements of the solar wind (Canals, 2002). Ideally, a combination of white-light images, in-situ measurements, and IPS data are needed to trace the full path and origin of a CIR from the Sun, out to the furthest spacecraft to see how far individual CIRs can extend out into the solar system. In addition, with the combination of data from different sources, it is more likely that what is being observed is a CIR and not some other transient effect in the solar wind mistaken for a CIR.

It should be noted that CIRs are not the only cause of intermediate velocities. Coronal mass ejections and other transient effects can also cause intermediate velocities in the solar wind. They can also cause much greater velocity solar wind flow than that of the fast solar wind as well as a variation in density.

1.8 Transients and eruptive events

CMEs have been thought about long before the theories of the solar wind were put together (e.g. Gosling, 1999). These are giant magnetic bubbles that erupt out of the Sun and expand rapidly, occasionally reaching sizes that are comparable to the Sun itself. They carry billions of tons of million-degree gas into interplanetary space at speeds of up to $1200\,\mathrm{km\,s^{-1}}$. The average speed for a CME however is around $400\,\mathrm{km\,s^{-1}}$ taking approximately 4 days to reach Earth distances from the Sun. Their associated shocks tend to propel vast quantities of high-speed particles ahead of the CME itself.

The characteristic detection of a CME while looking at the Sun is by a localised increase in the brightness in the white-light emission of the Sun due to dense features scattering more of the photospheric white-light. CMEs in general contribute to about 5% of the mass flux of the solar wind. Some of the first detections of CMEs were made between December 1971 and February 1972 using the white-light coronagraph on board OSO 7, National Aeronautics and Space Administration's (NASA) seventh orbiting solar observatory. One of the best detectors to date is from SOHO, a joint European Space Agency

(ESA)/NASA spacecraft. Table 1.2 gives a summary of CME properties. (Lang, 2001)

When CMEs erupt out of the Sun, they are self-contained structures of hot material and complex magnetic fields. They are thought to originate from a very rapid large-scale restructuring of the Sun's magnetic field down in the low Corona. During solar maximum, CMEs tend to occur over the whole of the Sun. During solar minimum however, they are generally confined to equatorial regions where the streamer belt lies since the magnetic field is more complex in the streamer than it is in the large coronal holes and surrounding quiet Sun regions which are very often seen around solar minimum conditions. An example of a CME can be seen in figure 1.17 taken with the Large Angle Spectrometric COronagraph (LASCO) C3 instrument on-board SOHO on the 15 May 2000 (20000515) along with the positions of Mercury, Venus, Jupiter, Saturn and the Pleiades star cluster which lie at respective distances of approximately $(18, 110, 780, 1400) \times 10^9$ m and 408 light-years beyond the Sun[3], and the distance from SOHO to the Sun is approximately 150×10^9 m.

In IPS data, CMEs are characterised by the closed field structure in which density irregularities in the solar wind are elongated perpendicular to the flow direction instead of parallel to it as in the normal solar wind. This feature can sometimes help distinguish between features in the solar wind which could suggest a CME or a CIR. (Klinglesmith, 1997)

[3] A light-year is the distance travelled at the speed of light in one year ($\sim 10^{15}$ m)

Characteristic	Value
Average angular width (heliocentric)	45°
Largest mass ejected	5×10^{12} kg to 5×10^{13} kg
Frequency of occurrence during solar maximum	3.5 events per day
Frequency of occurrence during solar minimum	0.8 events per day
Mass flow rate	$\sim 2 \times 10^{8}$ kg s^{-1}
Speed range of leading edge	5×10^{4} m s^{-1} to 1.2×10^{6} m s^{-1}
Average speed of leading edge	4×10^{5} m s^{-1}
Average time to reach Earth distance	$\sim$ 100 hours
Average kinetic energy	Approximately 10^{23} J to 10^{24} J

Table 1.2: Some of the physical properties of a CME which shows that they are generally massive, fast, and very energetic; obtained from spacecraft observations.
(Adapted from Lang, 2001)

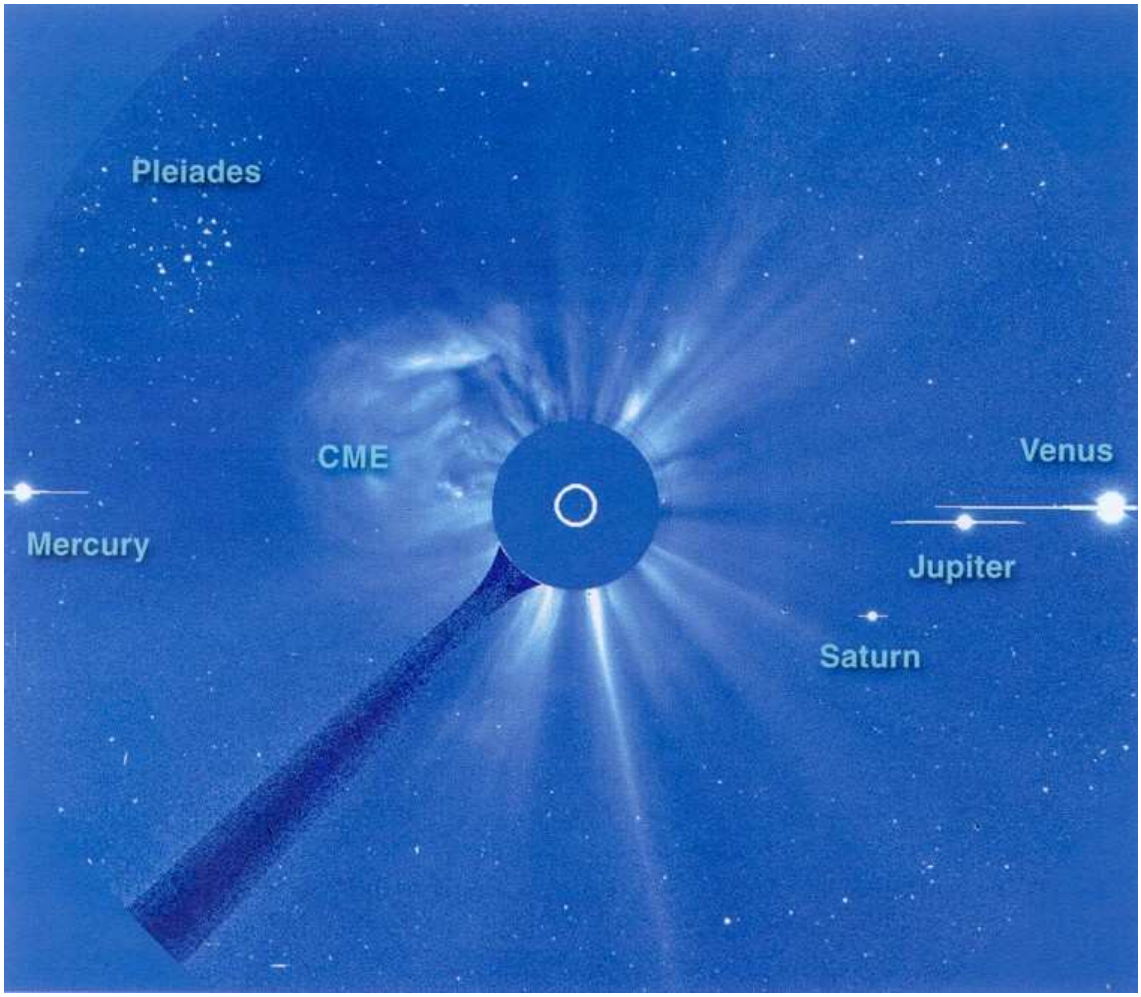

Figure 1.17: A coronal mass ejection, four planets and the bright stars of the Pleiades cluster, 15 May 2000 (20000515) from the LASCO instrument on board SOHO.
(Courtesy of the SOHO|LASCO consortium, taken from Lang, 2001)

Chapter 2

Experimental techniques

There are many techniques that can be employed to study the Sun and the solar wind. There are ground-based and space-based options; ground-based by remote sensing and space-based by either remote sensing or in-situ measurements. Remote sensing observations include radio and visible measurements of the Sun from the ground and measurements in the ultra-violet (UV) and X-ray bands from space along with any other parts of the electromagnetic spectrum. In-situ measurements of solar wind velocity, density, magnetic field and other plasma and field parameters are also important. The density irregularities in the solar wind can also be observed using ground-based or space-based coronagraphs for the inner solar wind as it emerges from the Sun's corona, and by radio measurements of distant radio sources to indirectly observe the solar wind through scintillation in the radio signal received from distant astronomical or artificial radio sources.

An advantage of in-situ measurements is that the physical parameters recorded are measurements of the primary solar wind parameters at that point in time. However, the disadvantage to this is that measurements can only be made at the position of the spacecraft at certain times. For example, in-situ measurements inside of 0.3 AU are non-existent and outside of the ecliptic plane of the solar system, at present, only the Ulysses data-set is available for current and near-past years (described in Chapter 3). Remote sensing observations have the advantage of being able to observe wide areas of the solar wind

over a wide range of heliocentric distances and all heliographic latitudes (i.e. out of the ecliptic plane) and at almost any time. The disadvantage to remote sensing observations is that the primary parameters are not observed but are inferred from other observations, for example, the detection of solar wind velocity from the spectrum of radio scintillation observed by ground-based telescopes which form the main source of information for this thesis.

2.1 Radio measurements

The "great storms" of radio emission from the Sun in February of 1942 was the beginning of the modern development of radio astronomy, even though radio waves themselves had been known since the late 1800s. James Clerk Maxwell (1831-1879) was the first to theoretically predict the existence of electromagnetic waves and hence radio waves by the derivation of his equations that describe mathematically how electric induction occurs from an oscillating magnetic field and showed that they travelled at the speed of light and that light too was another form of electromagnetic radiation (Maxwell, 1873). Although, the original paper on the theory behind his equations was read before the Royal Society on 8 December, 1864. Heinrich Hertz (1847-1894) confirmed during the years 1885 to 1889 that radio waves existed and was the first to send and receive them, thus proving Maxwell's theory and helping along the way to radio communications. In 1901, Gugliemo Marconi was the first to send a radio message across the Atlantic Ocean from England to Canada using the Earth's Ionosphere to reflect the radio waves - although the nature of the reflecting layer was not known at the time. The 1942 detection occurred when British radar stations that were operating at wavelengths of the order of a few metres experienced some form of jamming in late February of that year. An investigation was undertaken by J. S. Hey (Hey, 1983), which lead to the conclusion that radio waves of very high intensity were being emitted from the Sun and were apparently due to a very large presence of Sunspots that were active on the solar disc. This was the first evidence of an outburst of radio waves from any astronomical object. Later that same year, South-

worth (in the USA) discovered that the quiet Sun also emitted solar radio emission, this was the normal solar radio emission from the Sun and was at centimetre wavelengths. (Hey, 1983)

2.1.1 The Sun and radio waves

In 1951, when observations of the outer solar corona were underway, it was noticed that radio waves were coming from the Crab Nebula. These radio waves were refracted due to the electron density irregularities in the solar corona which caused the apparent size of the Crab Nebular to increase as observations of the radio waves moved in closer to the Sun (Hewish, 1955). Interplanetary scintillation of the radio waves from distant compact radio sources produced by density variations in the solar wind were discovered soon afterward by Hewish, Scott and Wills in 1964 (Hewish *et al.*, 1964; Cohen *et al.*, 1967) and have now been in almost constant use in an effort to determine some of the properties of the solar wind and its different streams.

In all, there are three methods of observing the Sun by radio waves; radio emissions from both the Sun itself and from the solar wind, radar echoes of reflected radio waves sent to the Sun off the solar atmosphere, and interplanetary scintillation. Radio emission also occurs from the Sun during flares, these are known as radio bursts. There are four types of radio bursts, Type I, Type II, Type III and Type IV. A diagram of the signatures of Type II and Type III radio bursts can be seen in figure 2.1. Radio bursts can be caused by various Sun-related events such as from blast fronts where you get blast waves moving through the Sun's corona and also emission from shock-fronts moving out through the solar wind and this is usually due to synchrotron emission (Type II and Type III shocks); all of which are related to particle acceleration.

In recent EISCAT and MERLIN IPS observations, a radio burst was detected in the data. A full description of the event can be found in Jones *et al.* (2006a) where a significant enhancement in signal strength was recorded at all sites over a period of ~40 minutes.

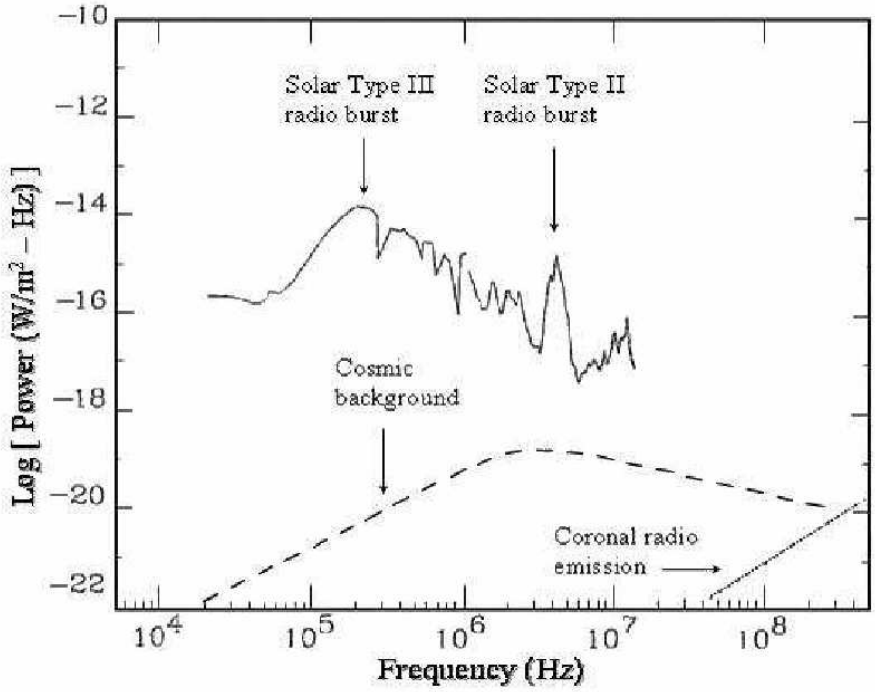

Figure 2.1: A plot showing the level of interplanetary radio burst flux of Type II and Type III radio bursts as compared to the quiet coronal emission and the cosmic background noise. The in-situ plasma frequency can be seen from the low-frequency end of the solid curve and the ionospheric cut-off at the high-frequency end.

(Taken from Gopalswamy, 2004)

2.1.1.1 Type I radio bursts

Type I radio bursts[1] are short bursts of radio emission over a period of seconds for each burst. They are in a narrow band with wavelengths of the order of a metre. The corresponding frequency of this type of radio burst is 50 MHz to 300 MHz. The sources of the bursts may continue for hours to days. Although these radio bursts are the most common type of activity observed on the Sun at these wavelengths, they are not associated with flares. This type of radio burst is attributed to electrons accelerated to energies of a few keV (kiloelectronvolts) inside[2] large-scale magnetic loops connecting active regions to more distance areas of the Sun. (e.g. Lang, 2001)

[1] Also referred to as "Noise Storms"

[2] 1 keV corresponds to 1.602×10^{-16} Joules of energy

2.1.1.2 Type II radio bursts

Type II radios bursts are again a narrow-band emission, but start at high frequencies and migrate to low frequencies over periods of tens of minutes throughout the burst. They typically start at wavelengths of around a metre and finish around decametres in wavelength. Corresponding frequencies of these wavelengths are 300 MHz down to 10 MHz by the end of the bursts with a decrease in frequency of around 1 MHz per second. Type II bursts are thought to be due to shock waves travelling around 1000 $\mathrm{km\,s^{-1}}$ outward from the Sun. These shock waves excite the local plasma frequency. Type II bursts occasionally accompany a large flare. (e.g. Lang, 2001)

2.1.1.3 Type III radio bursts

Type III bursts occur more frequently than Type II bursts and are the most common flare-associated radio burst. These are narrow-band emission like the Type II, but are characterised by their brief duration of seconds and rapid change of wavelengths from decimetres to decametres. This corresponds to a decrease in frequency from around 500 MHz to 5 MHz but have been observed at frequencies as low as 0.1 MHz and as high as 1000 MHz. Type III radio bursts can be attributed to beams of electrons thrown out from the Sun with kinetic energies of 10 keV to 100 keV and speeds of up to around half that of the speed of light. (e.g. Lang, 2001)

2.1.1.4 Type IV radio bursts

Type IV radio bursts are primarily in the metre range of wavelengths with corresponding frequency of 300 MHz to 30 MHz and are a continuum of broad-band emission, hence they are easily distinguished from the other types of radio burst emission. This type of burst is usually associated with major flare events beginning 10 to 20 minutes after a flare reaches its maximum brightness and can last for hours. Magnetically-trapped high-energy electrons may emit a Type IV radio burst. (e.g. Lang, 2001)

2.1.1.5 Radio burst tracking

The radio burst from the solar atmosphere and solar wind display a characteristic fall in frequency with increasing distance from the Sun. This arises from the decreasing density (and thus plasma frequency) of the solar plasma at greater distance as the shock in the plasma moves outward from the Sun and into the interplanetary medium. Observation of the variation of the frequency with time as it decreases will provide a measure of the velocity at which the shock is travelling outward from the Sun. The relationship between the plasma frequency, ν_p and the electron density, N_e can be described by equation 2.1 where the plasma frequency is given in Hertz.

$$\nu_p = \sqrt{\frac{e^2 N_e}{4\pi^2 \epsilon_0 m_e}} \text{ Hz} = \sqrt{81 N_e} \text{ Hz} \quad (2.1)$$

Where:

N_e is the electron number density in m^{-3};

ϵ_0 is the permittivity of free space = 8.854×10^{-12} F m^{-1};

e is the electronic charge of the electron = -1.602×10^{-19} C;

and m_e is the mass if the electron = 9.109×10^{-31} kg.

2.1.2 Direct observations of the Sun

Any radio telescope with a diameter of less than 10 metres can easily observe the whole of the Sun from the Earth. This however gives a very low resolution to the observations and so not a great deal of detail can be obtained by observing the Sun directly with such small radio telescopes. Larger telescopes are needed to observe the Sun in more detail.

Today, single steerable telescopes of up to 100 metres in diameter and fixed dishes of up to 305 metres in diameter are used to observe the Sun in detail, as are arrays of multiple small telescopes. The largest steerable dish is that of 100 metres at Effelsberg in

Germany and the largest fixed dish is that of the Arecibo incoherent scatter radio telescope in Puerto Rico. The Arecibo dish has a diameter of 305 metres and is basically a valley floor covered in metal. It relies on the rotation of the Earth to bring it in to view with objects to be observed in the sky. Although the Effelsberg and Arecibo dishes are sometimes used for solar observations, they are usually used to carry out astronomical observations of the radio Universe. (Lang, 2001)

There is another way of doing direct measurements of the Sun and that is by way of interferometry, where smaller radio telescopes sited at known separations are used to observe. By combing the signal electronically, radio images of the Sun which are just as sharp as optical images can be obtained. The sensitivity to flux of an interferometric array of telescopes is dependent on the combined areas of the individual elements and not the separations between them, but the resolving power depends upon the antenna separation. Many sets of pairs of radio telescopes can be put together to form large interferometer arrays. An example of which is the Very Large Array (VLA) in New Mexico. It is a set of twenty-seven movable 25 metres radio telescopes oriented in a Y-shape giving 351 pair possibilities and thus creating a radio telescope with an effective diameter of 34000 metres when combined using a computer (as described in Lang, 2001). The angular resolution achieved can be less than one arc second. (e.g. Lang, 2001)

2.1.3 Interplanetary scintillation (IPS) observations

Interplanetary scintillation arises from the variation in the apparent intensity of distant compact (point-like) radio sources (e.g. quasars) due to scattering of the radio waves by the interplanetary medium, and hence due to the solar wind. The scattering, and therefore the scintillation, is caused by density inhomogeneities within the solar wind as it flows outward from the Sun and thus casts a drifting scintillation pattern across the Earth while doing so. IPS is a very powerful and unique technique that can be used to probe the inner heliosphere in regions currently inaccessible to any other technique.

2.1.3.1 A history of IPS

In 1951, Vitevitch in Russia, and Machin and Smith at Cambridge, independently suggested that it was possible to study the Sun's outer corona using radio measurements from distant radio sources. This was accomplished through observations of diffraction of the radio waves from sources if the Earth-source line passed close to the Sun. This arose from the observations of the Crab Nebula seeming to make it increase in size in terms of its apparent diameter from the scattering of the radio waves by variations in the coronal electron density (described in Hewish, 1955; Brandt, 1970b; Hey, 1983). The IPS technique was developed by Hewish from 1962 onward (Hewish *et al.*, 1964) following the serendipitous discovery of unusual fluctuations in source signal strength during a programme to accurately map the position of a large number of radio sources. These sources were subsequently determined to be point-like (P. J. S. Williams, private communication to A. R. Breen, 2002, as cited in Canals, 2002). It was hypothesised that these same density irregularities causing the broadening of the Crab Nebula were responsible for the scintillation in the radio waves from the distant point sources and that the solar corona extended out into the interplanetary medium. Ionospheric scintillation had been ruled out as a possible explanation for these fluctuations (Hewish *et al.*, 1964) as it had been shown that ionospheric scintillation intensity fluctuations are smoothed out for the source angular diameters involved and the frequencies the phenomena was being observed at. The intensity fluctations could only have originated in the interplanetary medium and hence they were called interplanetary scintillation (IPS). It was then recognised that IPS could be a powerful tool in probing the solar wind and for measuring the structure of radio sources (Hewish *et al.*, 1964; Hewish & Okoye, 1965).

The first IPS measurements made by Hewish of the solar wind gave wind speed estimates between 200 km s^{-1} and 400 km s^{-1}. Two radio telescopes were used with a baseline of 53 km between them, one located at Cambridge, the other located at Alvedon (both in the UK). They observed at a frequency of 178 MHz. However, later observations used three stations and observed at the lower frequency of 81 MHz. The longest baseline by now

was 85 km. Dennison & Hewish (1967) used the three sites to gain information about the direction of flow of the solar wind. It was IPS that first indicated that the velocity of solar wind was greater coming from above the polar regions than that observed in the plane of the ecliptic since it was capable of observing at all heliographic latitudes (Dennison & Hewish, 1967). This was then confirmed by the Ulysses polar pass many years later (Phillips *et al.*, 1994).

Multi-site observations were extensively undertaken from the early 1970s until 1987 by UCSD (University of California, San Diego) and then described in a series of papers (Armstrong & Coles, 1972a; Armstrong *et al.*, 1972b; Coles & Rickett, 1976; Coles *et al.*, 1980; Rickett & Coles, 1991; Rickett, 1992). Observations were undertaken at a frequency of 74 MHz with a maximum baseline of 94 km using a three-antenna system. The observations provided an overview of changes in the solar wind over the solar cycle covering all heliographic latitudes. The results showed a large change in the nature of the solar wind structure throughout the solar cycle and following the magnetic evolution of the inner corona (Rickett & Coles, 1991). The declining phase, lasting 7 years, saw the high-latitude heliosphere dominated by near-uniform fast flow occupying approximately half of the heliosphere. This was the same during solar minimum itself. The low heliolatitudes were dominated by a slow velocity flow from the current sheet. A latitudinal gradient could be seen at solar minimum which then vanished at solar maximum, with slow flow extending to all latitudes during the period of and around the maximum activity (Coles & Rickett, 1976; Coles *et al.*, 1980). In Japan (over the same period) IPS observations were being made at Toyakawa (Kojima & Kakinuma, 1987). These observations continue today at a frequency of 327 MHz and so probed closer to the Sun than the UCSD system (the reasons for this are discussed later in this Chapter). IPS observations at a higher frequency of 933.5 MHz began in 1982 at the European Incoherent SCATter radar (EISCAT), (Bourgois *et al.*, 1985) allowing measurements of solar wind parameters from around 15 $R_\odot$ to over 70 $R_\odot$.

The resolving ability of the IPS observations was also improved due to the much larger baselines (in the same way as the resolution is improved for interferometry mentioned earlier in this chapter) of up to 390 km. These observations showed two clear solar wind components and again these were later confirmed by Ulysses (Phillips *et al.*, 1994). EISCAT (Rishbeth & Williams, 1985) has been used for IPS regularly since 1985 and more extensively from 1991. There have been a series of summer campaigns since 1991 with more recent years having spring and quite often early-autumn campaigns. A unique opportunity arose in 1994 and 1995 for a comparison with the in-situ observations from 1.4 AU and outward of the Ulysses spacecraft as it passed over the poles of the Sun reaching latitudinal extents of 80.2° North and South. The bi-modal nature of the solar wind was determined with the fast stream of around 800 km s^{-1} and slow stream around 400 km s^{-1} (Breen *et al.*, 1996b,c) and agreed with data taken by Ulysses (Phillips *et al.*, 1994, 1995). Further analysis of these data sets have revealed a possible two-mode structure of the inner fast solar wind (Bisi *et al.*, 2006).

In 2002, 2004, 2005, and recently in 2006, observations have been made using the Multi-Element Radio-Linked Interferometer Network (MERLIN) facility (Thomasson, 1986) with IPS observing frequencies of up to 5 GHz to 6 GHz (Canals (2002) states that in recent years the VLBA has also been used at 22 GHz for IPS observations). There have been combined programmes of MERLIN and EISCAT to probe the acceleration region of the solar wind and also to look in more detail into the large-scale structure of the solar wind and in particular, the direction of flow of the solar wind and the possible two-mode structure of the fast solar wind (as discussed in later chapters of this thesis). The VLBA at 22 GHz has the capability of observing the solar wind as close as 2.5 $R_\odot$ (Klinglesmith, 1997), and MERLIN as close as 5 $R_\odot$ (Canals, 2002) at 5 GHz. IPS observations with MERLIN have been successfully carried out as close as 7 $R_\odot$ (Breen *et al.*, 2000b).

IPS today is still as relevant and as unique as it was when it was first discovered and used, and is probably more important to supporting in-situ measurements of present and

future missions and with linking to other remote-sensing observations as they very often compliment each other (as can be seen from data used along with the IPS observations throughout this thesis). There are active research groups around the world; two in San Diego, USA; Toyakawa/Nagoya, Japan; Ootacamund, India; Aberystwyth, UK; and even new sites in Mexico and Russia, with the first IPS array currently being established as a low frequency array in the southern Hemisphere located in Australia.

2.1.3.2 Scintillation theory

It is density inhomogeneities in the solar wind which cause the radio waves to have phase modulations as an effect of the variations in the local refractive index of the interplanetary medium due to these variations in density. The irregular changes of refraction bend the waves in different directions and thus they reach the observer from different directions resulting in combinations of scattered waves which sometimes give rise to maxima (large amplitude) where they are in phase, or minima (low amplitude) where cancel each other out because they are out of phase. These variations have a characteristic scale size of tens to a few hundreds of kilometres. Scintillation is produced by these phase changes due to the scattering of radio waves by the density fluctuations in the solar wind. The scattered waves then combine with the unscattered waves causing constructive and destructive interference in the form of amplitude variations in the received signal. The frequency of the fluctuations is about 0.5 Hz when detected from the ground (Hewish, 1989) and only if the sources show-up the variations to a sufficient coherence, i.e. the angular diameters have to have less than around 0.5 seconds of arc, will the scattered waves combine to form a diffraction pattern. This pattern then drifts over the ground to give rise to the fluctuations in intensity (Ekers & Little, 1971), i.e. give rise to scintillation (Coles & Harmon, 1978), as can be seen in figure 2.2. A frequency power spectrum of the solar wind as taken by the Advanced Composition Explorer (ACE) spacecraft can be seen in figure 2.3.

The observed signal will vary depending on the interference occurring while the radio waves travel through the solar wind to the receiver on the Earth. The effect is to cause a

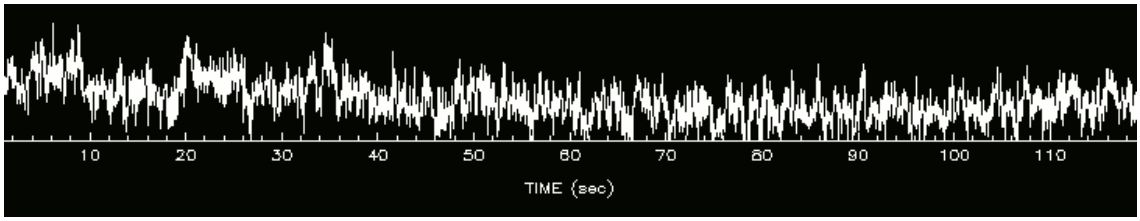

Figure 2.2: Intensity fluctuation seen in an IPS observation using the Sodankylä site during an EISCAT observation on 20040905 of 1256-057.

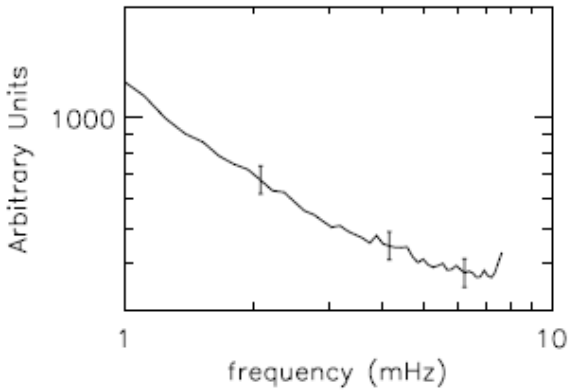

Figure 2.3: This figure shows the power spectrum of the solar wind for June 1999 from ACE. It was taken with a spectral resolution of 0.14 mHz.
(Ford & Menk, 2006)

two-dimensional spatial interference pattern across the Earth's orbit. As the irregularities casting the intensity pattern are moving out in the solar wind, a telescope on Earth will see the apparent intensity of the source varying on time-scales of around 0.1-10 s.

If a source is larger than a certain size, then fluctuations can become smooth due to minima from one part of the source overlapping with minima from another part. A simple formula for working out if a source is too large, is whether or not a source subtends an angle $\geq \frac{L}{D}$ where L is the average size of the "blob" (irregularity) of solar wind, and D is the distance from the observer. If it is, then amplitude fluctuations will be smoothed out.

It is also possible to get ionospheric scintillation (as described earlier), but IPS typical time-scales of 0.5 Hz are significantly faster than that of ionospheric scintillation

and also the diffraction of about 200 km of ionosphere is considerably larger so that high-frequency IPS is not normally confused with any effects that could come from the ionosphere (Hewish, 1989), unless there are very rapid flows in the ionosphere (E. Lucek, private communication to A. R. Breen, 1995, as cited in Canals, 2002) where ionospheric scintillation may rise above a frequency of 0.2 Hz (A. R. Breen, private communication, 2005). In these cases the ionospheric contribution may be seen as an extra bulge in the spectrum close to the low-frequency cut-off end of the spectrum where there is a high-pass filter (IPS analysis is described in greater and more specific detail in Chapter 3 of this thesis). In the work described in this thesis however, observations that exhibit ionospheric contribution to the IPS measurements have been discarded.

Scintillation theory in respect of scattering for the purpose of this thesis relates to figure 2.4, where information is extracted from the distribution of velocities present in the solar wind from measurements such as the example given here. This figure shows a simultaneous time series of two of the EISCAT mainland sites (details on multi-site IPS can be found later in this Chapter) Kiruna and Sodankylä, of the intensity of the radio source 0319+415 recorded on 13 May 2004 (20040513). The recording was taken when the IPS raypath from the radio source to the Earth passed through the solar wind to a point of closest approach (P-Point) of 84.1 $R_{\odot}$. Although the two time series are not identical, there are some very similar features in each of them separated by a time lag. If the pattern of density variations in the solar wind were to move at a uniform velocity, and the baseline between the two IPS observing antennas exactly aligned with the velocity direction, then the two time series would be absolutely identical (in a perfect system). The only exception being a small time lag due to the variations in the solar wind density being detected slightly later at the one site than at the other as the diffraction pattern passes over the Earth's surface as it flows outward from the Sun.

In weak scattering, when the variation between the phase changes is much less than one radian, you can treat the detected scintillation pattern as a linear sum from all the scat-

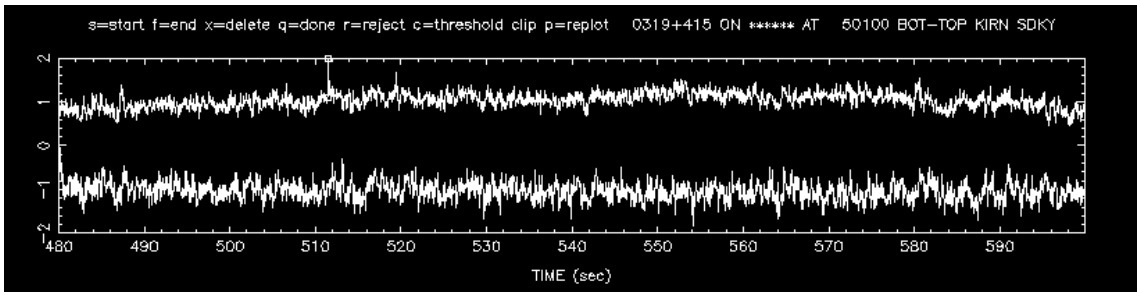

Figure 2.4: The time-series of intensity fluctuations of 0319+415 on 20040513 with the Kiruna and Sodankylä telescopes.

tering events along the raypath from the source to the receiver. Diffraction of the radio waves can be thought of as occurring at a series of "thin screens" and the phase variations that are introduced by diffraction at any single "screen" build up into amplitude variations over a distance which is then dependent on the actual size of the density variations in that particular "screen". Therefore, the final diffraction pattern received at the antenna can be considered to be a combination of the range of density variation scales. In strong scattering however, this is not the case. Although analysis of the results is still possible, the amount of information that can be extracted from the results is reduced. The equation for variation in refractive index (and thus for phase change) is shown by equation 2.9 later. It shows that the variation in phase change will be reduced if the observing frequency is increased and that the transition from weak to strong scattering therefore occurs closer to the Sun at greater observing frequency. (Fallows, 2001; Fallows *et al.*, 2006)

The variations in the local refractive index are directly proportional to the density of electrons if the variation in the electron density is small enough (Hewish, 1989). Using the same notation as Uscinski (1977), the refractive index, $n(x, y, z)$, can be described by equations 2.2 and 2.3.

$$n(x, y, z) = n_0 + n'(x, y, z) \tag{2.2}$$

$$n'(x,y,z) = \mu n_1(x,y,z) \tag{2.3}$$

Where:

n_0 is the mean refractive index;

n'(x,y,z) is the variation of refractive index about the mean (above and below the mean refractive index);

μ is the standard deviation of n'(x,y,z);

and n_1(x,y,z) is the scaled form of n'(x,y,z) with standard deviation of 1.0.

The variation in refractive index is determined by the relative electron permittivity, ϵ, of the medium, i.e. the solar wind in this case. In the absence of particle collisions, and if the magnetic field is of no concern, this can then be represented using equation 2.4.

$$\epsilon = n^2 = 1 - \frac{f_p^2}{f^2} \tag{2.4}$$

Where:

$$f_p^2 = \frac{N_e e^2}{4\pi^2 \epsilon_0 m_e}; \tag{2.5}$$

and

f_p is the plasma frequency in Hertz;

N_e is the electron number density in m^{-3};

ϵ_0 is the permittivity of free space = 8.854×10^{-12} F m^{-1};

e is the electronic charge of the electron = -1.602×10^{-19} C;

m_e is the mass if the electron = 9.109×10^{-31} kg;

and f is the observing frequency of the IPS observation;

Since $f_p \ll f$, the refractive index can now be written as in equation 2.6 using an expansion of the form $(1 + x)^n = 1 + nx^1 + \frac{n(n-1)}{2!}x^2 + ...$, where the x terms of a higher order than x^1 approximate to zero.

$$n = 1 - \frac{1}{2}\frac{f_p^2}{f^2} \tag{2.6}$$

Now $n' = n - n_0$ and substituting for f_p we get equations 2.7 and 2.8 where $\langle N_e \rangle$ is the average electron density at the point of closest approach of the raypath to the Sun.

$$n' = \left[1 - \frac{N_e e^2}{8\pi^2 \epsilon_0 m_e f^2}\right] - \left[1 - \frac{\langle N_e \rangle e^2}{8\pi^2 \epsilon_0 m_e f^2}\right] \tag{2.7}$$

$$n' = \frac{(\langle N_e \rangle - N_e)e^2}{8\pi^2 \epsilon_0 m_e f^2} \tag{2.8}$$

Hence n' can be described using equation 2.9.

$$n' = \frac{\delta N_e e^2}{8\pi^2 \epsilon_0 m_e f^2} \tag{2.9}$$

So, for observations closer-in to the Sun, N_e increases and therefore it is assumed that δN_e is also increased. Hence, n' increases as the strong scattering regime is reached. Since n' is inversely proportional to the observing frequency squared, a higher observing frequency

allows observations in the weak scattering regime to be made closer-in to the Sun than that of a lower observing frequency, as seen in equation 2.9 and figure 2.5. In contrast however, as n' decreases with distance from the Sun, so does the scintillation level (amplitude) of the observation and a point is reached where the interplanetary scintillation signal becomes swamped with noise from the observing system. At higher observing frequencies, this point appears closer to the Sun the higher in frequency you observe. Thus interplanetary scintillation is a capable method of observing the solar wind over a very wide range of distances, especially if multiple-frequencies are at the observers' disposal. If the strong scattering regime is reached, then a sudden drop in the scintillation index occurs as can be seen in figure 2.6 (Fallows, 2001)

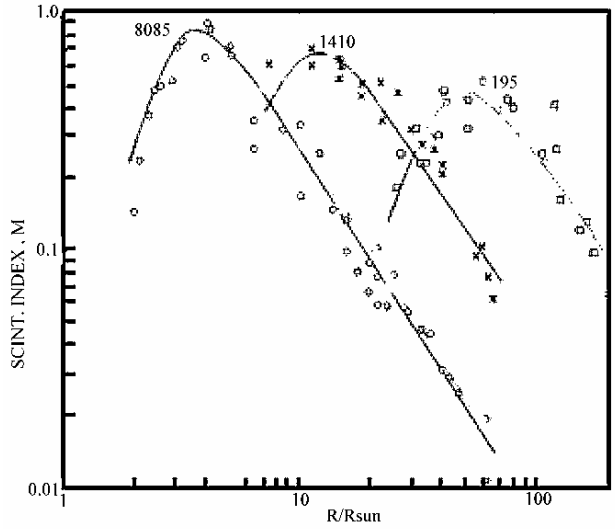

Figure 2.5: A log-log plot comparing the scintillation index (m) with distance from the Sun ($R_\odot$) for three different IPS observing frequencies of 8085 MHz, 1410 MHz, and 195 MHz. Scintillation index is the square of the scintillation power received at the antenna while observing a radio source. As can be seen, the higher the observing frequency, the closer-in to the Sun the peak in the scintillation index, hence higher observing frequencies are able to observe in the weak scattering regime closer-in to the Sun.

(Coles & Harmon, 1978)

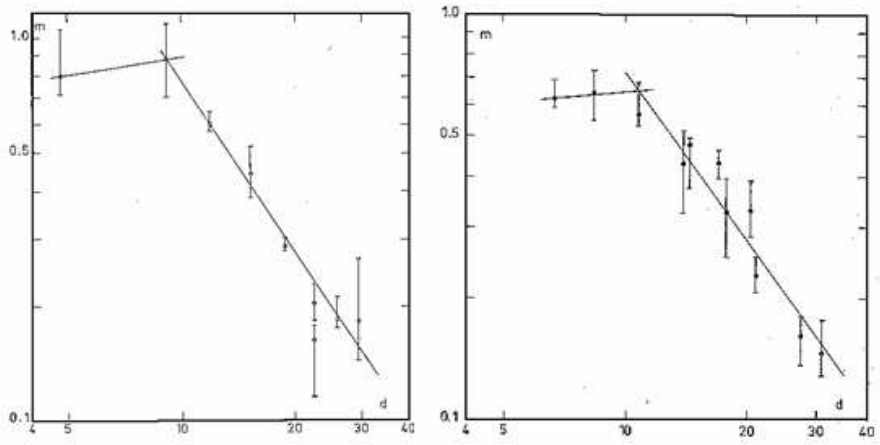

Figure 2.6: A log-log plot of the measurements of the scintillation index (m) with distance from the Sun (d).

(Fallows, 2001)

2.1.3.3 Details of multi-site IPS and further IPS theory

Figures 2.7 and 2.8 show the IPS scintillation potential and observing geometry along the line-of-sight from the Earth to the distant point source. It takes into account the $\cos\theta$ effect as can be seen from the solar wind velocity arrows on the diagrams - it is only the velocity contribution perpendicular to the line-of-sight that IPS is sensitive to, so this is the component of the solar wind velocity that is apparent in the IPS signal. Multi-station IPS is capable of providing a much more accurate measurement of the solar wind in general compared to a single site IPS. However, single-site IPS is generally still used more for IPS observations since it does not require multiple antennas and is therefore more readily achieved.

As previously described, the radio waves scintillate due to the solar wind and cause a 2D pattern and this pattern drifts across the Earth due to the density irregularities in the solar wind moving outward from the Sun. If the alignment of the radio source, solar wind, and telescope is such that the scintillation pattern in the radio signal received at each site is very similar but exhibiting a time lag, and the geometry of the observation is such that the two telescopes lie in the same plane which passes through the centre of the Sun, then this time lag can be used to derive the velocity or velocities (depending on

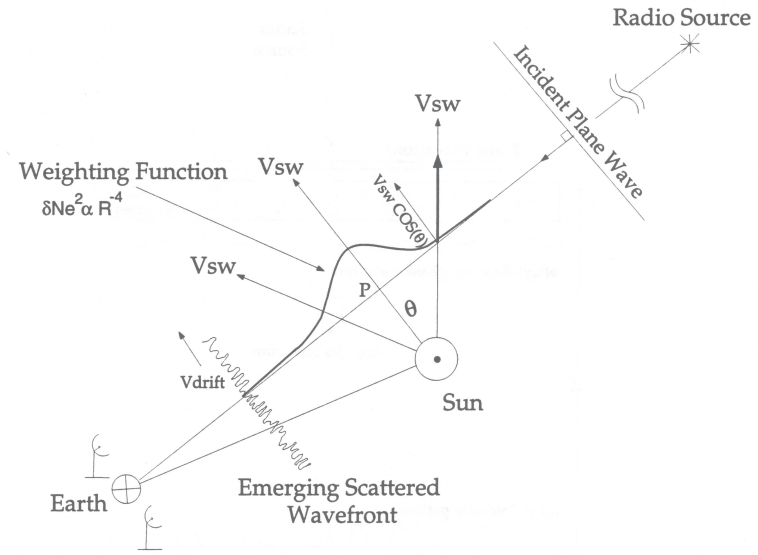

Figure 2.7: A diagram showing the geometry of IPS observations and the weighting of scintillation potential along the line-of-sight from the radio telescopes to the source.
(Taken from Grall, 1995)

whether there are one or more streams in the raypath) along the line of sight. This geometry, seen in figure 2.9, is required for multi-site IPS measurements since the solar wind is assumed to be expanding into the interplanetary medium approximately radially, and therefore the maximum correlation of the two different signals will occur when the two telescopes are in the same plane as the outwardly propagating flow of solar wind. Observations of IPS are henceforth used as a tracer of the solar wind flow, and can be used to study the evolution of the solar wind structure in interplanetary space (e.g. Canals, 2002).

When correlating the two signals, a time lag is seen (as described earlier) due to the solar wind flowing in an outward direction. The time lag, δt, can be used at maximum correlation along with knowing the parallel baseline of an observation to give a first estimate of the velocity of the primary/dominant stream of solar wind in an IPS observation. This is accomplished by using equation 2.10, where the term '*Distance*' in the equation refers to the length of the parallel baseline.

$$V_{SW} = \frac{Distance}{\delta t} \tag{2.10}$$

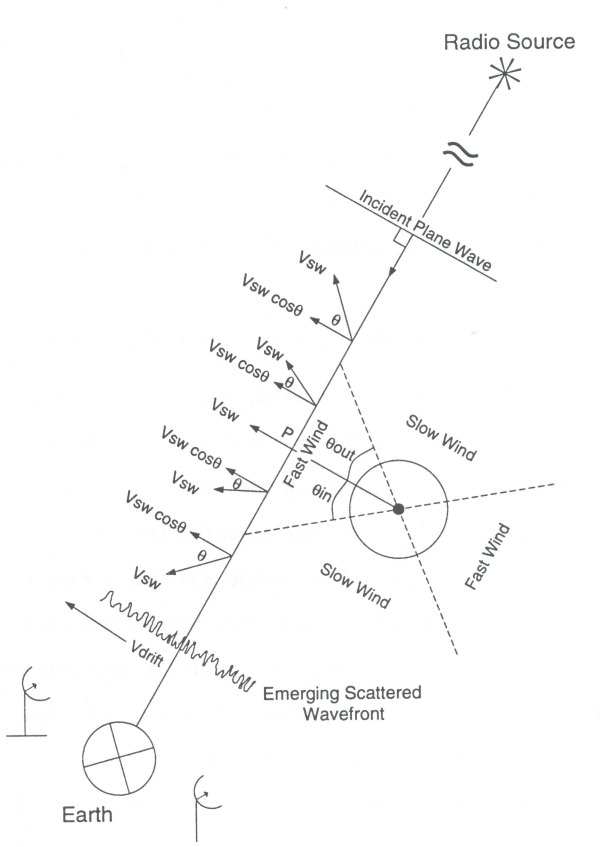

Figure 2.8: A diagram of the geometry of IPS observations showing the direction of solar wind flow across the IPS raypath.

(Taken from Massey, 1998)

The equation can also be used for the time lag of other peaks (if any) that appear in the cross-correlation function of an IPS observation using two sites.

IPS measurements contain contributions from the whole of the raypath (as shown in figure 2.7 and in figure 3.8 in the next chapter) but is sensitive to only the perpendicular component of the solar wind velocity across the IPS raypath as previously described. The $\cos\theta$ effect (calculation of the solar wind component perpendicular to the IPS raypath which is responsible for the scintillation along the raypath) will cause a broadening

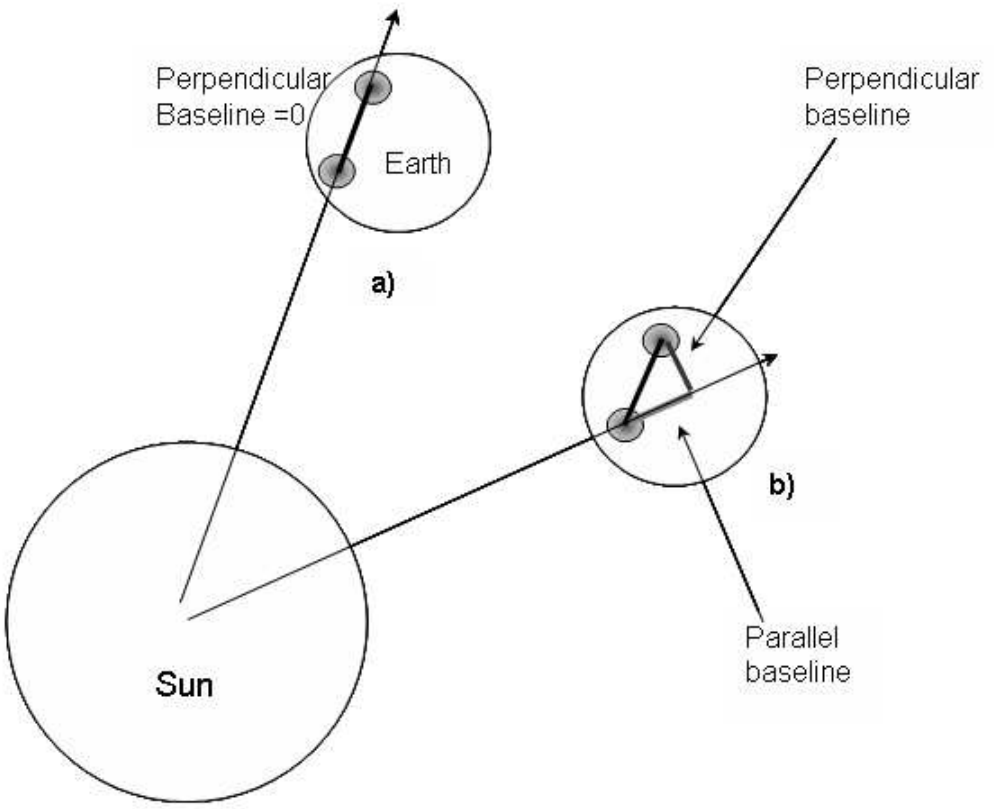

Figure 2.9: Diagram showing two cases of IPS observing alignments as viewed perpendicular to the page as seen from the source. Case a) shows the perpendicular baseline to be zero. The two receiving sites lie in a plane that passes through the centre of the Sun. In case b), the Earth is rotated and therefore moved the baselines relative to the plane that passes through the centre of the Sun and hence introduced a non-zero perpendicular baseline. The effective parallel baseline is shorter than it was with a zero perpendicular baseline (after Moran, 1998).
(Taken from Canals, 2002)

of the cross-correlation function when the signal from the two sites is correlated and this will lead to under-estimation of the velocity of the solar wind stream(s) detected along the raypath. The maximum scattering will occur at the point of closest approach (P-Point) of the raypath to the Sun because the scattering potential of the solar wind decreases with increasing distance from the Sun. To a first approximation, this is $\sim \frac{1}{R^4}$, which shows that the majority of the scattering occurs at the P-Point (where $cos\,\theta \simeq 1$). Hence by a rough correction, the IPS observations can be corrected by a multiplication of 1.18 (Breen *et al.*, 1996c).

Equation 2.11 shows the temporal power spectrum under weak scattering conditions as described in its various forms in Scott *et al.* (1983); Klinglesmith (1997); Moran (1998); Fallows *et al.* (2006) and references therein. It is included in this thesis for the purpose of completeness to the theory, although development of the underlying theory itself is not an aspect of this thesis (which is mostly experimental and related to the technique of IPS itself, not the theory behind it).

$$P(f) = 2\pi r_e^2 \lambda^2 \int_0^{\infty} \frac{2\pi}{v_p(z)} \int_{-\infty}^{\infty} 4sin^2(\frac{q^2 \lambda z}{4\pi})|V(q,z,\theta_0)|^2 q^{-\alpha} exp - (\frac{q}{q_i})^2 R^{-4} dq_y dz \quad (2.11)$$

(e.g. Scott *et al.*, 1983; Klinglesmith, 1997; Moran, 1998; Fallows *et al.*, 2006)

Where:

r_e is the classical electron radius as calculated by equation 2.12;

λ is the observing wavelength;

α is the power law exponent, e.g. Kolmogorov;

v_p is the component of solar wind velocity perpendicular to the line of sight;

q is the 2-dimensional spatial wavenumber (normally in x-y coordinates);

q_i is the inner-scale for turbulence (the scale at which the turbulence dissipates);

z is the distance from Earth to the scattering "screen";

θ_0 is the diameter of the source in radians;

and $V(q, z, \theta_0)$ is the visibility function of a radio source.

$$r_e = \frac{1}{4\pi\epsilon_0} \frac{e^2}{m_e c^2} = 2.818 \times 10^{-15} m \quad (2.12)$$

Where:

ϵ_0 is the permittivity of free space = 8.854×10^{-12} F m^{-1};

e is the electronic charge of the electron = -1.602×10^{-19} C;

m_e is the mass if the electron = 9.109×10^{-31} kg;

and c is the speed of light in a vacuum = 2.998×10^8 m s^{-1}.

The Fresnel filter is described by equation 2.13, which acts as a high-pass filter attenuating wavenumbers below the Fresnel spatial frequency, q_f, given in equation 2.14. The Fresnel filter is necessary as wavefronts need a certain distance to develop into a scintillation pattern - this is known as the Fresnel distance - and is defined as the distance at which these wavefronts are again in phase and the amplitude variations first become fully developed. The diffraction of radio waves that occur very close to the observer (near the Earth) would not have time to fully develop and therefore would not contribute to the overall scintillation pattern received at the Earth from along the IPS raypath. This means that the cause of the scintillation along the raypath is slightly biased to the source side of the P-Point in the raypath and not the Earth side, although the majority of the scintillation comes from around the P-Point. Further details of scintillation potential along the IPS raypath can be found in chapter 3 of this thesis and also in great detail in Fallows (2001).

$$Fresnel\ Filter\ =\ 4sin^2(\frac{q^2 \lambda z}{4\pi}) \tag{2.13}$$

$$q_f\ =\ \sqrt{\frac{4\pi}{\lambda z}} \tag{2.14}$$

Related to the Fresnel frequency is that of the Fresnel radius as defined in equation 2.15. This is the radius of the first Fresnel zone. This gives a maximum scale-size of the irregularities for which amplitude scintillation can be received and is dependent on the observing frequency and the distance to the scattering "screen". Some examples: For an observing wavelength of ~21 cm (1420 MHz), the maximum scale-size of irregularity at a "thin screen" of scattering at 1 AU is ~177 km; for an observing wavelength of ~32 cm (928 MHz), the maximum scale-size of irregularity at a "thin screen" of scattering at 1 AU is ~219 km; and for an observing wavelength of ~60 cm (500 MHz), the maximum scale-

size of irregularity at a “thin screen” of scattering at 1 AU is ~300 km.

$$r_f = \sqrt{\lambda z} \tag{2.15}$$

The $exp - (\frac{q}{q_i})^2$ term from equation 2.11 describes the dissipation. It also attenuates the scintillation power spectrum at wavenumbers higher than q_i. In addition to this, the source visibility function also acts as a low-pass filter attenuating wavenumbers above that given in equation 2.16.

$$q_s = \frac{1}{z\theta_0} \tag{2.16}$$

2.1.3.4 Dual-frequency IPS

Equation 2.11 was for a single observing frequency across both telescopes used in (traditional) multi-station IPS observations. It is only suitable for representing the correlation functions for a single frequency. However, modification can be made to the equation to allow a cross-correlation of two different frequencies, one at each of the sites (Salpeter, 1967; Fallows *et al.*, 2006). It is the terms involving λ^2 (where λ is still the observing wavelength) and split into two single λ terms; λ_1 for the observing wavelength of the first telescope, and λ_2 for the observing wavelength of the second telescope. The result is equation 2.17 where all the symbols are the same as before with the exception of the wavelengths now being different. (Taken from Fallows *et al.*, 2006)

$$P(f) = 8\pi^2 r_e^2 \lambda_1 \lambda_2 \int_0^\infty \frac{2\pi}{v_p(z)} \int_{-\infty}^\infty sin(\frac{q^2\lambda_1 z}{4\pi}) sin(\frac{q^2\lambda_2 z}{4\pi}) |V(q,z,\theta_0)|^2 q^{-\alpha} exp - (\frac{q}{q_i})^2 R^{-4} dq_y dz \tag{2.17}$$

(Fallows *et al.*, 2006)

IPS observations are sensitive to density scales in the order of tens to hundreds of kilometres and these scales overlap when the two observing frequencies are not too far apart. Fallows *et al.* (2006) have shown that IPS at frequencies as far apart as 500 MHz at one receiver and 1420 MHz at another different receiver can still provide meaningful IPS results. The range is more specifically determined by the observing wavelength (or frequency). The higher the observing frequency, the smaller the density scale the measurements are sensitive to, so as the solar wind density increases as you get closer to the Sun, a higher observing frequency can be used to remain in the weak scattering regime for IPS data analysis (as described earlier).

2.1.3.5 Effect of increasing the baseline between two IPS receivers

The effect of increasing the baseline between two IPS receivers (as described earlier) is to increase the sensitivity of the observation to the velocity(s) of the solar wind flowing across the raypath. The ability of the observation to resolve streams of solar wind with different velocities increases as the radial separation in the plane of sky of the raypaths increases. However, the time lag between the two sites is increased by the increase in parallel baseline (B_{Par}) between the two and as the irregularity pattern is evolving in time any increase in parallel baseline will lead to a decrease in the degree of correlation. (Klinglesmith, 1997; Moran *et al.*, 1998)

A plot of this effect can be seen in figure 2.10. As the parallel baseline is increased, the amount of correlation (described in detail in chapter 3) of the signal received at the two sites is decreased at the main peak (the dominant solar wind flow velcity). A second peak (i.e. a second solar wind flow velocity) is resolved as the parallel baseline increases which could not be seen when using the shorter parallel baseline.

Maximum correlation occurs when the projection of the baseline forming the two raypaths is approximately parallel to the solar wind velocity, and completely parallel for a purely radial outflow of solar wind. The larger the parallel baseline, the larger the

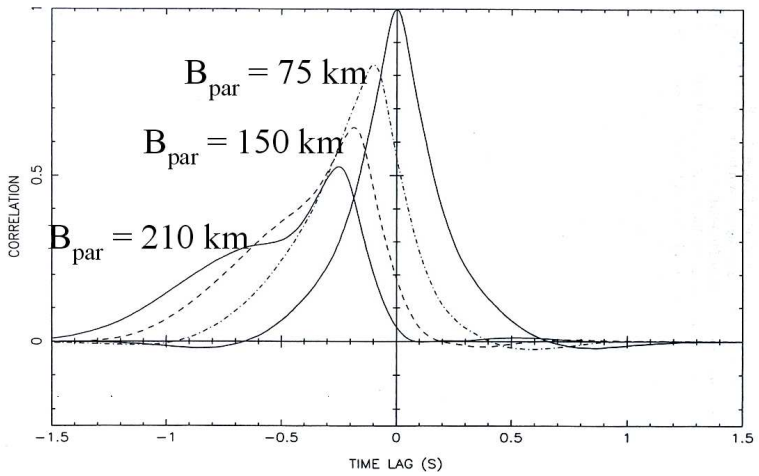

Figure 2.10: Plot showing the effect caused by the increase in the parallel baseline of a multi-site observation (details of what the plot shows can be found in the text).
(Klinglesmith, 1997)

perpendicular baseline (B_{Perp}) for a given angle relative to the solar wind outflow (θ) as described by equation 2.18. In other words, the larger B_{Par} is, the larger B_{Perp} is for a given off-radial angle (θ), and the likelihood of detecting any non-radial flow is increased.

$$tan\,\theta = \frac{B_{Perp}}{B_{Par}} \tag{2.18}$$

2.2 Other electromagnetic spectrum measurements

The techniques of remote sensing can be either ground-based or space-based. These techniques observe at various regions of the electromagnetic spectrum such as optical, UV, X-rays and γ-rays. It should be noted that observations of anything other than optical or radio-wave regions need to be done above the atmosphere of the Earth since these other frequencies are filtered out by the Earth's atmosphere.

The study of the corona first began with the observing of the extended corona during

the moments of totality of solar eclipses. It was in 1930 when the first coronagraph was built by Bérnard Lyot, which allowed people to observe the corona without the need for a solar eclipse, since this instrument blocks out the disc of the Sun and creates an artificial eclipse (see later in this chapter).

2.2.1 X-ray

X-ray observations of the Sun are some of the highest frequency observations that are carried out of the Sun. They enable a view close-in to the Sun from around $1\,R_\odot$ to $1.5\,R_\odot$. X-ray observations can give detailed views of the positioning of the coronal holes, quiet Sun and streamer belts on the surface of the Sun as well as good detail of other, smaller features, such as coronal loops and anything of around 2 million Kelvin and above - depending on what frequency within the X-ray band is being observed. Some of the more common frequencies observed in the X-ray band are those between 3 Å and 60 Å in what is called the soft-X-ray band. There is also a hard-X-ray band (wavelengths of less than 3 Å) at the higher frequencies up to γ-rays.

X-rays were first discovered in 1895 by Konrad Rontgen while doing an experiment with a fluorescent plate and a beam of fast-flowing electrons. It was by accident, as with much of the EM spectrum, that he found the plate to glow even when it was a long way from the electron tube. He was the first person to take an X-ray of a hand, his own hand.

X-ray observations can be carried out on the whole disc of the Sun or of its limbs and then Carrington Rotation maps can be constructed from the data. These are maps of what the Sun looked like at a particular X-ray frequency over a period of a Carrington Rotation.

Telescopes that are designed to observe at either X-ray or UV wavelengths in space do not need to be that large in diameter. For example, an aperture of 0.002 m can be used to achieve an angular resolution of 1 arc second when observing at a soft X-ray wavelength of 10^{-8} m. The Solar Maximum Mission (SMM) achieved excellent images (in

the 1980s) of the hard X-rays emitted during the impulsive phase of solar flares. The hard x-ray sources, which were in two components, were found to be concentrated at the foot-points of the soft X-ray coronal loops. The explanation for this is if the sources of the hard X-ray generation are energetic non-thermal electrons flowing quickly down to both foot-points of a coronal loop into the low corona and dense chromosphere. (Lang, 2001)

An example of an X-ray image of the Sun can be seen in figure 2.11 from July 1993. A description of the Yohkoh spacecraft and the SXT instrument can be found in Chapter 3.

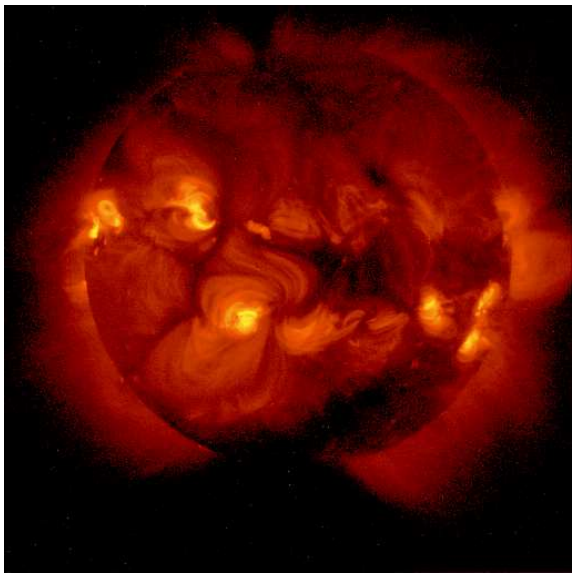

Figure 2.11: An X-ray image of the Sun taken on 27 July 1993 at 11:37:17 UT using the Yohkoh SXT instrument.
(J. F. McKenzie - http://solar.physics.montana.edu/press/sxt/sxt.html accessed 19 March 2006)

2.2.2 Ultra-violet

UV observations of the Sun can also help distinguish where certain features of the Sun are, such as the streamer belt, quiet Sun and coronal holes. UV observations detect anything from around 10 thousand Kelvin up to 2 million Kelvin and are particularly useful

for locating active regions on the Sun as they tend to appear brighter on UV images of the Sun.

UV observations generally take place in the 500-1600 Å band with the most common frequencies in the EUV band for observing the Sun at the iron lines of Fe IX/X at 171 Å, Fe XII at 195 Å and Fe XV at 284 Å, and the helium line He II at 304 Å.

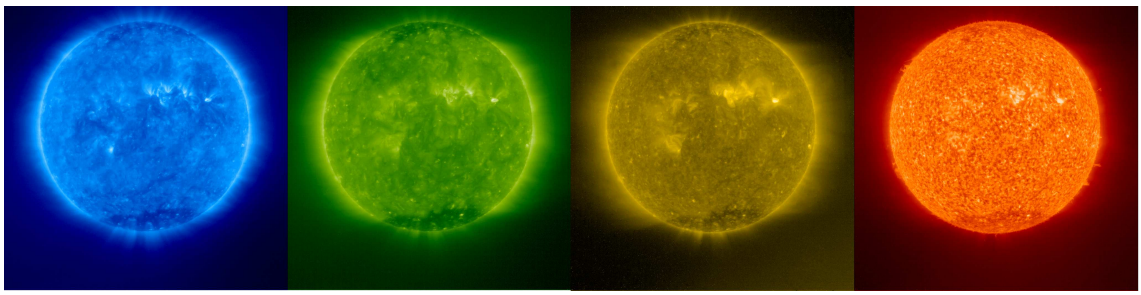

Figure 2.12: EUV comparison full Sun images taken by SOHO|EIT at frequencies from left to right of 171 Å (blue), 195 Å (green), 284 Å (yellow), and 304 Å (orange). The blue image is of the 1 million degree celcius gas of the Sun's plasma in its corona, the green image is of the 1.5 million degree celcius gas of the Sun's plasma in its corona, The yellow image is of the 2-2.5 million degree celcius gas of the Sun's plasma in its corona, and the orange image is of the approximately 60 thousand degree celcius gas of the Sun's chromosphere/lower transition region. (G. Dimitoglou - http://sohowww.nascom.nasa.gov/gallery/EIT/ accessed 18 March 2006)

Images of the disc or the limb of the Sun can be taken in the UV band as well as more detailed higher resolution images of parts of the Sun. Carrington rotation maps of the Sun can be constructed in the same way as those of X-ray observations.

EUV and X-rays produced in the corona are most commonly by Bremsstrahlung emission, often called free-free emission. This is when emission occurs from a free electron that is scattered by a free ion in the corona as seen schematically in figure 2.13. As the electron approaches the ion, due to their opposite charge, a Coulomb field is created between them and this results in the emission of a photon. The photon energy is equivalent to the difference between the kinetic energy of the electron on its in-coming and out-going paths, i.e. the electron loses some of its kinetic energy when it is scattered by the ion in

the form of a photon.

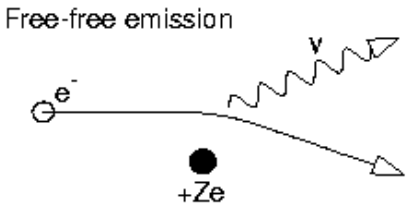

Figure 2.13: Bremsstrahlung emission from the Sun where e^- is an electron, +Ze is an ion, and ν is the photon emitted, either in the X-ray or EUV/UV band of the electromagnetic spectrum. (Aschwanden, 2004)

Bremsstrahlung emission can occur at all wavelengths, as can be seen from equation 2.19. The photon energy and hence wavelength/frequency of the emitted photon is dependent on the amount of kinetic energy lost during the free-free emission interaction between the electron and the ion.

$$e^- + Z^+ = e^{-'} + Z^+ + \nu \tag{2.19}$$

Where:

e^- is the in-coming electron;

$e^{-'}$ is the out-going electron of lowered kinetic energy;

Z^+ is the ion;

and ν represents the quantised energy in the form of a photon.

2.2.3 White-light

White-light observations of scattered photospheric light can be carried out from the ground as well as from spacecraft, since the Earth's atmosphere does not filter-out this wave-band. The white-light corona is light emitted from the photosphere scattered by the coronal material. Dust grains and free electrons in the Sun's corona give rise to the different com-

ponents of the corona as described in Chapter 1. The drift in the structures of material in the corona gives information on the velocity of matter flowing out from the Sun.

Again, as with the X-ray and UV observations, white-light observations of the limbs of the Sun can be used to construct Carrington Rotation maps of each Carrington Rotation of the Sun. These have been done using ground- and space-based optical instruments.

The angular resolution (θ) of a lens or mirror can be obtained using equation 2.20. The smallest linear size that can be resolved on the Sun is given by $L = 725000 \times \theta$ m (Lang, 2001).

$$\theta = \lambda / D \tag{2.20}$$

Where:
θ is the angular resolution of the image obtained in radians;
λ in the wavelength of the radiation being observed;
and D is the diameter of the mirror or lens.

2.2.3.1 Coronagraphs

An instrument quite commonly used when conducting white-light measurements of the Sun is that of a coronagraph. This is an instrument that creates an artificial eclipse to block out the disc of the Sun so that the faint corona can be observed and indeed remotely measured in terms of the outflow velocity of transients. There are two basic types of a coronagraph, an internally occulting coronagraph and an externally occulting coronagraph, both of which were used on the SOHO spacecraft.

Coronagraphs observe the white-light that is scattered by particles of dust and free electrons in the Sun's corona. Coronal emission is split into three sections as described in some detail in the previous chapter; the K-corona - Thomson scattering from free electrons

which dominates out to around $3\,R_{\odot}$; the F-corona - outside of $3\,R_{\odot}$ the dust scattering component is stronger; and the E-corona - emission from the hot gasses within the corona itself. Thomson scattering can be described by equation 2.21 and is shown in figure 2.14.

$$e^{-} + \nu = e^{-} + \nu \tag{2.21}$$

Where:

e^{-} represents a free-electron;

and ν represents the photon being scattered (bent) by the electron.

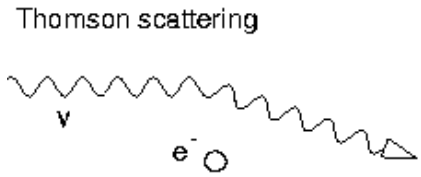

Figure 2.14: Thomson scattering in the Sun's corona, as caused by free electrons. (Aschwanden, 2004)

The first attempt at making a coronagraph was in the late 1890s when the American astronomer, G. E. Hale, creator of the 200 inch Palomar telescope, tried to design and impliment a coronagraph in Colorado on Pike's Peak, but had unconvincing evidence as to the reliability or effectiveness of it. It was the French astronomer, B. Lyot, in the end who solved the technical problem of a false eclipse by designing the internally occulted refracting coronagraph (also known as the Lyot coronagraph) and was awarded the Copley Medal of the Royal Society for his design (Fisher, 1995; Malbet, 1996; Thompson, 2004). A schematic of the Lyot coronagraph can be seen in figure 2.15.

Lyot recognised why the previous attempts at constructing a coronagraph had failed. Some of these were due to the scattering of light within the coronagraph from the edges

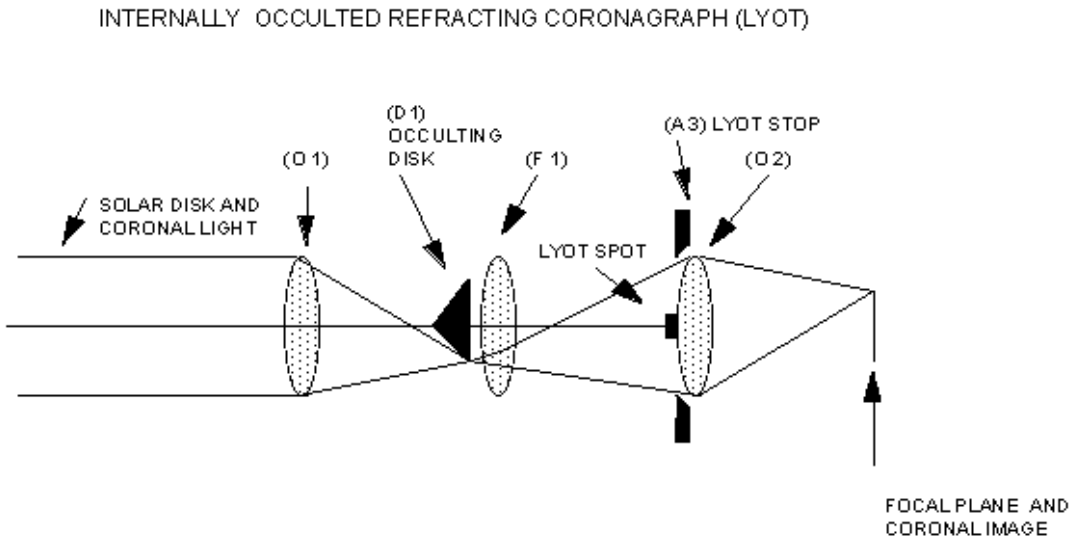

Figure 2.15: The original Lyot coronagraph design. The first objective lens, O1, forms an image of the corona and the solar disc which is then taken out by the internal occulting disk and leaves just the light from the corona. The field lens, F1, forms an image onto the Lyot stop of the objective lens after the disk is removed. The second objective lens, O2, focuses the image of the Sun's corona and the occulting disk of the coronagraph onto the detector.
(Fisher, 1995)

of the optical elements as well as that through the Earth's atmosphere. To avoid as much atmospheric scattering as possible, he located his coronagraph at a relatively high altitude site at a good distance away from urban sources of air pollution. It was the set of specially arranged lenses and baffles to trap the coronal light inside the telescope that then allowed astronomers to view the lower corona on a daily basis from the ground, something that had never been reliably achieved before. (Fisher, 1995)

It was in 1941 on Freemont Pass in central Colorado (only a few miles away from the site where Hale attempted to build his coronagraph) that Walter Orr Roberts, then of Harvard College Observatory, established a working coronagraph that was used by the military at the time to try to predict atmospheric conditions affecting communication capabilities. Then, in 1966, a new design of coronagraph was perfected by Gordon Newkirk of the High Altitude Observatory (HAO) in Boulder, Colorado. His design was to place the occulting disk in front of the first objective lens and hence was known as the exter-

nally occulting coronagraph, see figure 2.16. It was this design of coronagraph that was subsequently used on all American orbital satellites including Skylab, OSO-7 and Solar Maximum Mission (SMM). This design is much improved as it provides a significant reduction in scattered light by not allowing direct sunlight from the solar disc to fall into the first objective lens. (Fisher, 1995)

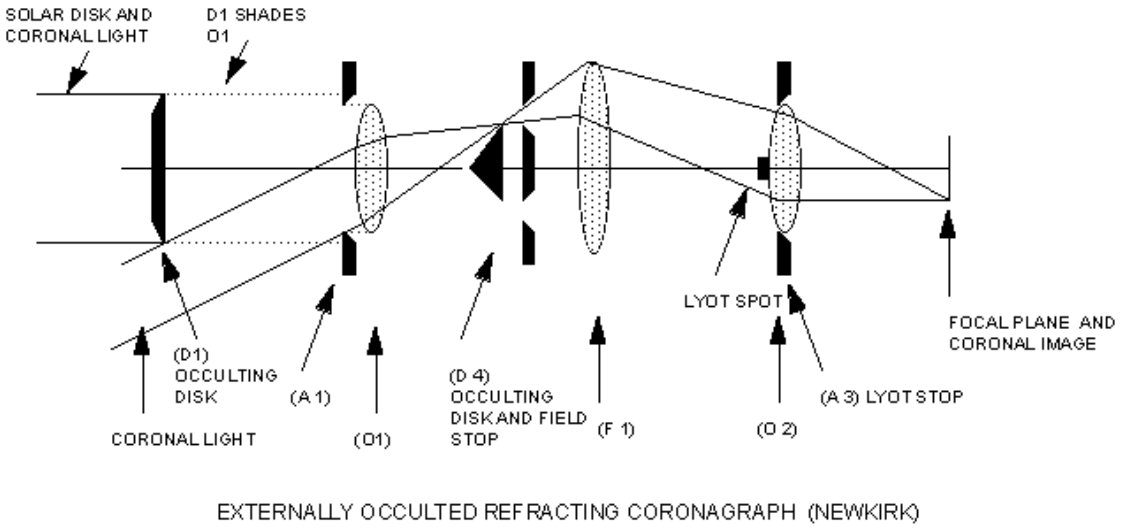

Figure 2.16: A schematic of the Newkirk (externally occulted) coronagraph. The first objective lens is a doublet lens used to colour correct the image of the corona which is obtained from this type of coronagraph. The occulting disk, D1, is superpolished and serrated to help reduce light diffraction.

(Fisher, 1995)

2.2.3.2 Wide-field imagers

White-light observations can also take place with the use of imagers covering a wide field-of-view such as the SMEI instrument on board the Coriolis spacecraft (Eyles *et al.*, 2003) and also the photometers on board the much earlier Helios A and Helios B spacecraft (e.g. Jackson, 1986). The Helios photometers made observations of scattered white-light away from the Sun in the late 1980s (Jackson, 1986). Such wide-field instruments measure the intensity of the scattered photospheric light by free electrons down to several

orders of magnitude below that of the galactic background (zodiacal light). Successful results are obtained by sophisticated software subtraction of the background light to provide the image of the scattered photospheric light from the Sun (e.g. Jackson *et al.*, 2005). Wide-field imagers are a powerful tool for observing the large-scale structures in the solar wind and as such the Solar TErrestrial RElations Observatory (STEREO) mission (described very briefly at the end of this chapter), (Kaiser, 2005) which is scheduled to fly in September/October 2006 will have two Heliospheric Imagers (HIs), (Harrison *et al.*, 2005) aboard each of the two spacecraft.

2.3 In-situ measurements

Instruments on spacecraft can measure many parameters over extended periods of time such as the measurements of ion concentrations with certain energies or within certain energy ranges, measurements of particles of dust in the solar wind with certain masses or ranges of masses, measurements of the overall composition of the solar wind and measurements of the mean speed of the solar wind. Other in-situ measurements that are taken are the electron density and energy and therefore temperature of the solar wind, the magnetic field of the solar wind and also the electric field of the solar wind.

At present, there are no in-situ observations being made inside the L_1-Point, however there have been in the past and there are missions planned for the future to do this. In-situ observations at the L_1-Point and out beyond Earth's orbit are taking place on several spacecraft, but only one of which is completely outside the ecliptic plane of the solar system. An important past mission was that of Helios A (1975-1990) and Helios B (1976-1980) which went inside 1 AU and partly out of the ecliptic (Schwenn, 1974). The Helios spacecraft were the first stereo mission in the way in which they complimented each other. However, the only true out-of-ecliptic measurements of the interplanetary medium are those taken by Ulysses and these are outside of 1.4 AU.

In-situ measurements first started fully in 1962 by the launch of the Mariner 2 spacecraft while it was on its journey to Venus (Snyder & Neugebauer, 1965). It was capable of measuring the density and temperature of the protons in the solar wind and the overall mean speed of the solar wind. However, there were earlier Russian missions in the Lunik-Series (1960-1961) that provided in-situ measurements of the solar wind (previously described in chapter 1), but they were not outside the Earth's magnetosphere long enough for unambiguous measurements. Later spacecraft followed in the form of Pioneer 10, Pioneer 11, Voyager 1 and Voyager 2. These spacecraft provided the early knowledge of the solar wind and the interplanetary medium, while Voyager 1 and Voyager 2 are now journeying out of the heliosphere and into the interstellar medium (IsM) and send back data which will then allow us to get a better idea of, among other things, the pressure, composition and density of the IsM. A picture of the distance scale of the solar system can be seen on a log AU distance in figure 2.17.

The Helios mission (as mentioned earlier) was the first stereo mission to study the solar wind. The spacecraft carried particle instruments, magnetic field instruments, and photometers to look at the white-light intensity of scattered photospheric light, as well as providing the first comprehensive in-situ study of the solar wind in the inner solar system inside of 1 AU. The Helios measurements were not only the first in-situ out of the ecliptic measurements of the solar wind and thus was the first to study the uninterrupted pure fast wind, recognised by R. Schwenn as the fundamental mode of the solar wind, but they also still represent, even today, the closest in-situ solar wind measurements to the Sun. The Helios spacraft observed as close-in as just 60 $R_{\odot}$. These measurements provided us with one of the initial indications of solar wind rapid acceleration. This is the only data set from the same region of space as that which IPS provides us with.

The Helios fast wind results were highly influential in the development of the later Ulysses (Phillips *et al.*, 1994, 1995) mission to study the solar wind over the poles of the Sun. Ulysses (described in more detail in Chapter 3 of this thesis) differs however in that it

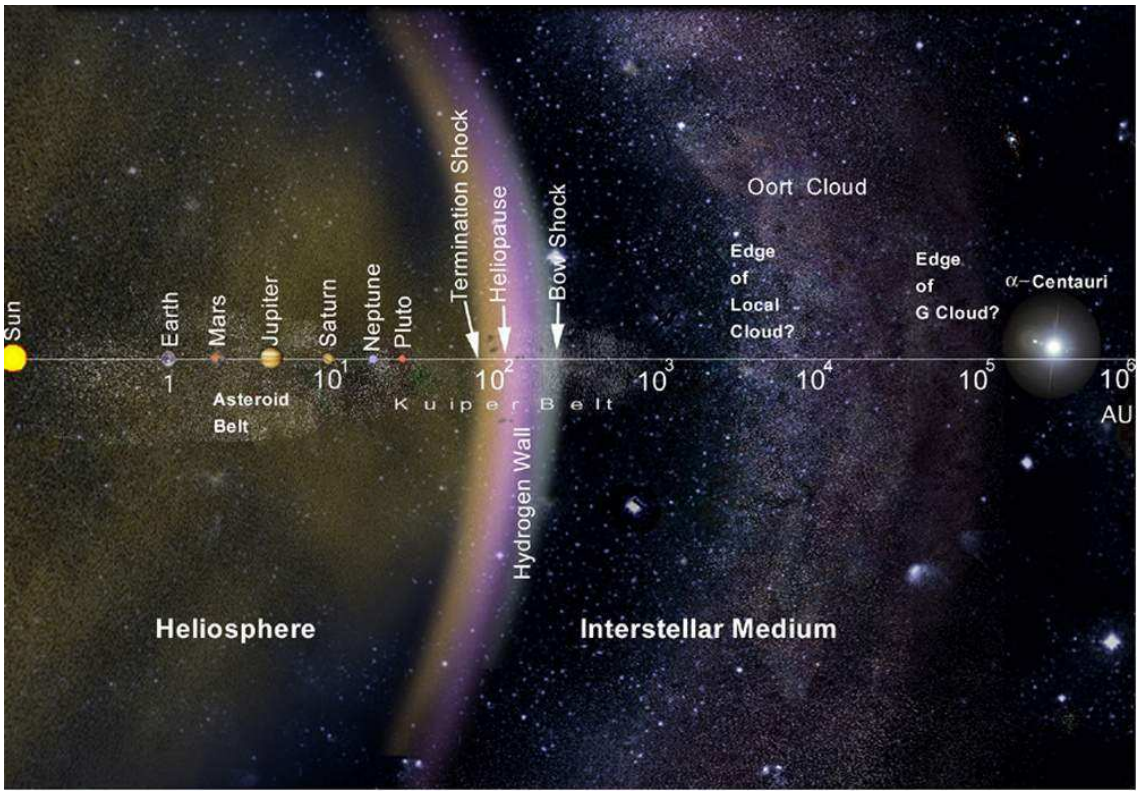

Figure 2.17: A figure showing the scale of the solar system in terms of the log of the distance from the Sun.
(http://voyager.jpl.nasa.gov/mission/images/ZankSolarSystem-big.jpg accessed May 2006)

is just a single spacecraft mission carrying no imaging equipment; it is solely an in-situ measurements mission. It was launched in 1990 and orbited over the poles of the Sun at distances from 1.3 AU to 5.4 AU with an approximate distance of 2.3 AU from the South pole, and 2.0 AU from the North pole of the Sun (Lang, 2001). A picture of the Ulysses spacecraft after its deployment from the shuttle discovery can be seen in figure 2.18, in orbit around the Earth before it began its journey to Jupiter, and then back toward the Sun on its polar orbits. Ulysses has provided fundamental information into the structure of the solar wind both at solar minimum and solar maximum of the solar cycle. Its magnetic field instruments have revealed the first indications of assymetries between the solar cycle in the northern and southern hemispheres of the Sun (e.g. Forsyth & Gosling, 2001; Forsyth *et al.*, 2002a,b).

Other more recent spacecraft that carry out in-situ measurements include: Advanced Composition Explorer (ACE); Polar; Cluster II; and some instruments aboard SOHO that carry out further measurements of the solar wind and interplanetary medium by in-situ measurements.

Figure 2.18: The Ulysses spacecraft with the Earth's surface below drifting against the blackness of space after deployment from the space-shuttle Discovery's payload bay.
(Taken from http://helio.estec.esa.nl/ulysses/Deployment.htm, January 2003)

An important future mission (due to launch September/October 2006) for further in-situ and also remote sensing measurements will be that of the two STEREO spacecraft. STEREO will be two completely separate spacecraft, one preceding away from the Earth at the Earth's orbit, the other accelerating ahead of the Earth at the Earth's orbit. Among other things, they will be making in-situ measurements of particles and CME transients as well as remote sensing with a dual view of CMEs exploding from the Sun. Other future missions that are currently planned for solar wind measurements/solar observations include Solar Orbiter and Solar B.

Chapter 3

Sources of data

Most of the data used in this thesis comes from observations of Interplanetary Scintillation (IPS) from the European Incoherent SCATter radar (EISCAT), (Rishbeth & Williams, 1985) and the Multi-Element Radio Linked Interferometer Network (MERLIN), (Thomasson, 1986). The 32 metre steerable dish, which is part of the EISCAT Svalbard Radar (ESR), (Wannberg *et al.*, 1997) near Longyearbyen was also used for observations during this thesis, but none of these data are included in the investigations undertaken within this thesis. Supporting information also came from other data sources. In this Chapter, a more detailed description of the specific instrumentation and techniques used in this thesis is undertaken.

3.1 IPS data systems and data analysis

This section will describe the systems that were used in this thesis in more detail. For IPS observations, an antenna with a low-noise receiver capable of absolute power measurements, filtering/processing equipment is needed to enable recording of the data, and ability of fast sampling of a radio signal from a distant point source scintillating through the solar wind. IPS requires frequency detection up to 50 Hz (typically 30 Hz to 45 Hz is used for background noise calculation, but this is sometimes changed dependent on there being any "spikes" in that region of the data) so using the Nyquist theorem, as seen in equation 3.1,

a sampling rate of at least 100 Hz is necessary. In addition, for estimates of velocity to be obtained, multiple sites are needed to provide information for cross-correlation and cross-spectral analysis of the recorded radio scintillation. IPS measurements are presently those of amplitude scintillation, but phase scintillation is also possible. However, in this thesis, only amplitude scintillation is investigated. All three systems, MERLIN, ESR and EISCAT Ultra-High Frequency (UHF), have multiple high quality antennas and receiving systems. The EISCAT UHF telescopes and the steerable ESR telescope are all equipped with synchronised clocks to Universal Time (UT), thus enabling cross-correlations and cross-spectral analysis between each of the sites. The MERLIN system works on a master (atomic) clock at Jodrell Bank which transmits pulses to each of the other MERLIN sites to enable precise timing for when astronomical signals are being combined.

$$f_{max} = \frac{f_{sampling}}{2} \tag{3.1}$$

3.1.1 EISCAT UHF

The EISCAT facility (at the time of writing this thesis) is a joint operation by the research councils of Germany, Finland, France, Japan, Norway, Sweden and the United Kingdom. Its primary purpose is for observing the Earth's ionosphere, but since 1982 it has also been used for making interplanetary scintillation measurements of the solar wind (Bourgois *et al.*, 1985). There are four sites in total, three on the northern European mainland and one on the islands of Svalbard; all of which are located inside the arctic circle. The three UHF radar stations that have been used in the past for IPS measurements are located on the mainland, Ramfjordmoen (near Tromsø and always referred to as the Tromsø site) in Norway (also home to the VHF system operating at 224 MHz, which is not used for IPS observations) Kiruna in Sweden and Sodankylä in Finland, centred on frequencies around 928 MHz or 1420 MHz (Wannberg *et al.*, 2002) (with the exception of the Tromsø site which is only capable of measurements around 928 MHz); but some experimental observations have been made recently using the ESR telescope and further observations with the ESR are planned for future campaigns by the Aberystwyth group.

The ESR telescope data are not included in this thesis and the antenna operates around a centred frequency of 500 MHz.

The EISCAT sites in respect of northern Scandinavia can be seen in figures 3.1 and 3.2. They consist of a 32 metre steerable parabolic radio dish at each of the sites and details of the geographic locations can be found in table 3.1. A picture of all the four EISCAT telescope sites can be seen in figure 3.3.

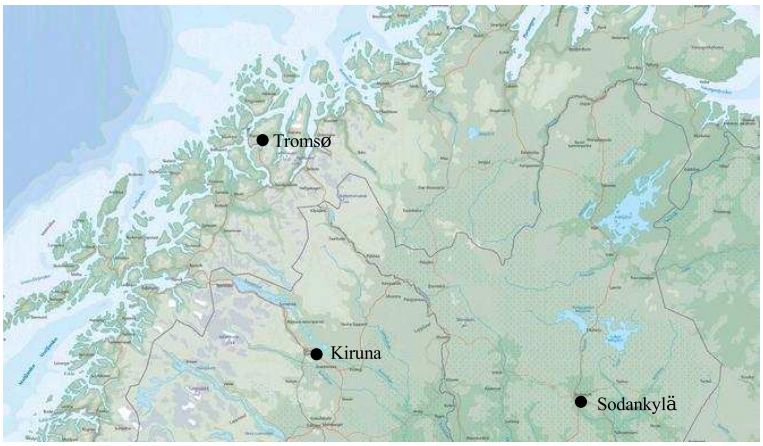

Figure 3.1: A map of the locations of the EISCAT system throughout northern Scandinavia.

Figure 3.2: A map of the locations of the ESR telescopes in relation to the EISCAT system.

The original operating frequency for EISCAT IPS measurements was in a 10 MHz band

Figure 3.3: A picture showing the four EISCAT sites - starting from the left: Tromsø (http://www.deviantart.com/view/5994945/ by M. M. Bisi, October 2003), Kiruna (http://users.aber.ac.uk/mmb02/work/pictures/kiruna_01.jpg by M. M. Bisi, May 2003), Sodankylä (taken from http://www.eiscat.com/sodan.html, May 2003), and the ESR 42 m in the foreground and steerable 32 m in the background along with the site building (http://users.aber.ac.uk/mmb02/pics/various_pics/svalbard/pages/100_1936.html by M. M. Bisi, May 2005).

EISCAT Site	Geographic Latitude	Geographic Longitude	Altitude
Tromsø	69.58470° N	19.2194° E	86.28 metres
Kiruna	67.86066° N	20.43522° E	417.62 metres
Sodankylä	67.36369° N	26.62707° E	197.03 metres
Longyearbyen (32 metre dish)	78.153° N	16.029° E	438 metres

Table 3.1: Table showing the locations of the EISCAT telescopes.
(Adapted from http://www.eiscat.com/locations.html, January 2005)

centred on 933.5 MHz (Rishbeth & Williams, 1985) with all three antennas. Over the years, the frequency has been reduced due to other effects creeping-in to the EISCAT bandwidth such as GSM mobile phone transmissions in Finland. Now we observe at both 928 MHz and 1420 MHz (Wannberg *et al.*, 2002) at which only the Sodankylä and Kiruna remote sites can measure (the 1420 MHz observations have a slight change in beam width and collecting area from the 928 MHz observations since the telescopes were originally designed for measurements around 930 MHz). There is hope to upgrade the Tromsø receiver in the near future to receive at 1420 MHz but due to complications with its ionospheric transmitter, this may or may not be a possibility (the remote sites are receivers only). A detailed listing of the respective operating frequencies of the three mainland UHF sites over the years can be found in table 3.2.

There has been conclusive evidence from recent IPS campaigns that a mixture of 928 MHz

Site	Year(s)	Centre Frequency	Bandwidth
Tromsø	Before 1996	933.5 MHz	10 MHz
	1996-2001	931.5 MHz	8 MHz
	2002	928.5 MHz	6 MHz
	2003-2006 (present)	928 MHz	6 MHz
Kiruna	Before 1996	933.5 MHz	10 MHz
	1996-2001	931.5 MHz	8 MHz
	2002	928.5 MHz	6 MHz
	2003-2006 (present)	928 MHz	6 MHz
Sodankylä	Before 1996	933.5 MHz	10 MHz
	1996-2001	931.5 MHz	8 MHz
	2002	928.5 MHz	6 MHz
	2003-2006 (present)	928 MHz	6 MHz
Kiruna	2002	1400 MHz-1420 MHz	7 MHz
	2003-2006 (Present)	1420 MHz	7 MHz
Sodankylä	2002	1400 MHz-1420 MHz	7 MHz
	2003-2006 (Present)	1420 MHz	7 MHz

Table 3.2: Table showing the observing frequencies of the EISCAT mainland telescopes during their usage for IPS.

and 1420 MHz (as well as 500 MHz from the steerable ESR) can be used and still obtain meaningful results (Fallows *et al.*, 2006), thus allowing longer baselines across frequencies, and very long-baselines if you incorporate the ESR. It is also possible for extremely long-baseline observations to be undertaken when the EISCAT and MERLIN observations co-incide and observe the same sources simultaneously, provided the geometry is such that a suitable baseline through the solar wind can be obtained - further details on this appear later in this chapter.

There are several reasons that make EISCAT a good set of radio telescopes for which to make IPS observations. EISCAT has three steerable antennas, any of which can be used to take measurements at any one time. The two observing frequencies allow a good

range of distances from the Sun to be observed with cross-overs between the different frequencies. At 928 MHz, observations as close as approximately 20 $R_\odot$ can be achieved out to approximately 120 $R_\odot$ with those at 1420 MHz having a smaller range of distance, but allowing closer observations into around 15 $R_\odot$. The actual range depends on the density of the solar wind plasma being observed at the time and therefore gives slightly different ranges of each frequency for each of the modes of solar wind outflow. Another reason why EISCAT is a good choice for IPS observations is its high timing accuracy with all sites being synchronised to UT (as described earlier). The other reason as to why EISCAT is good for IPS observations is that it has three possible baselines between its mainland antennas (six if you include the ESR) and it is possible to have baselines up to approximately 390 km with the mainland sites alone (approximately 900 km if you include the ESR). A Diagram showing baseline orientation can be seen in figure 2.9 in the previous Chapter. A detailed description of the antenna/receiver is covered in Rishbeth & Williams (1985). There are various upgrades and technical changes that have been carried out on the EISCAT telescopes since that paper was written and these are covered in some detail in the theses of Moran (1998); Fallows (2001); Canals (2002).

3.1.1.1 Antennas

The antennas used for IPS from EISCAT are the UHF 32 metre parabolic dishes operating with a Cassegrain feed. An antenna requires as high an illumination as possible along its collecting area out to reflector's edge thus maximising the total amount of signal that can be collected - which is one of the problems with designing an antenna. The Cassegrain feed unfortunately blocks part of this due to the positioning of the secondary reflector, however in the EISCAT antennas, this is a very small obscuration factor due to their advanced design. A Cassegrain system has a secondary hyperbolic reflector directly in front of the prime focus to converge (focus) the beam into the horn of the antenna (in the case of the EISCAT dishes). Another factor that is needed is a low-level spill-over at the edge of the reflector to ensure that ground noise, or as much as possible, is prevented from raising the system noise and thus degrading the signal. A sharp cut-off is required between full

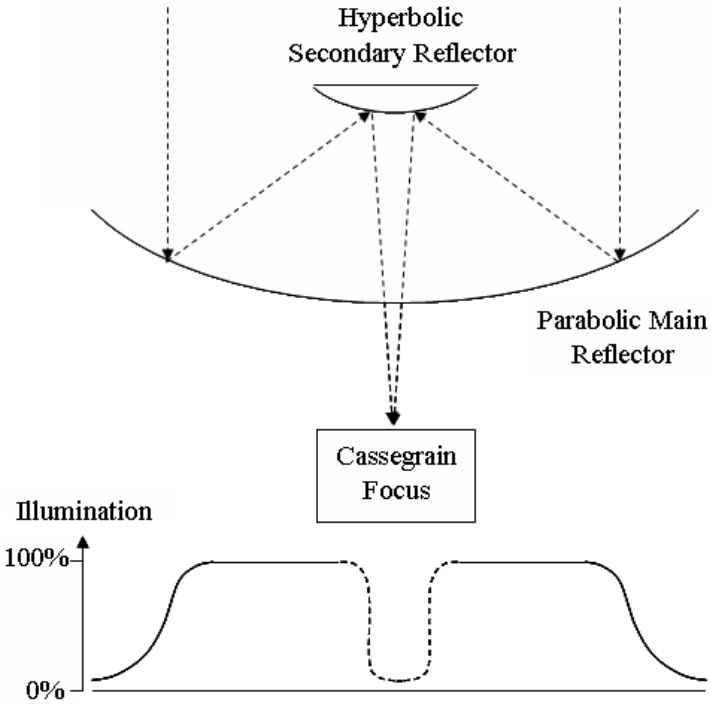

Figure 3.4: A diagram to show the parabolic antenna with Cassegrain feed as used at the EISCAT sites. The illumination across the main reflector can also be seen in the diagram.
(Adapted from Fallows, 2001)

and zero illumination to prevent ground-noise and this can be done by increasing the size of the secondary reflector - but this then blocks more of the incoming signal. A diagram of this can be seen in figure 3.4. Computer modelling of the secondary reflector shape has helped to optimise the shape and thus provide a compromise between the amount of illumination to which the reflector is exposed to and the cut-off at the edge of the dish.

The EISCAT mainland dishes have an efficiency of 71% at 930 MHz and this has been improved upon with the ESR having a value of 75% for observations at 500 MHz. However, at observing frequencies ~1420 MHz for the Kiruna and Sodankylä sites, the efficiency is in the 65% range (Wannberg *et al.*, 2002). A figure of the 933 MHz beam can be seen in figure 3.5 with a half-power beamwidth (HPBM) value of 0.6°, but there is no such diagram for the ~1420 MHz frequency other than a few basic runs of drift measurements in 2002 that have been completed by Assar Westman and Gudmund Wannberg at EIS-

CAT, which were never converted into an ordinary plot with degrees along the X-axis and where the data were never properly digitised. An example of such a plot can be seen in figure 3.6 with a 0.3° offset in elevation. The HPBM value for ~1420 MHz observations is 0.44° (Wannberg *et al.*, 2002).

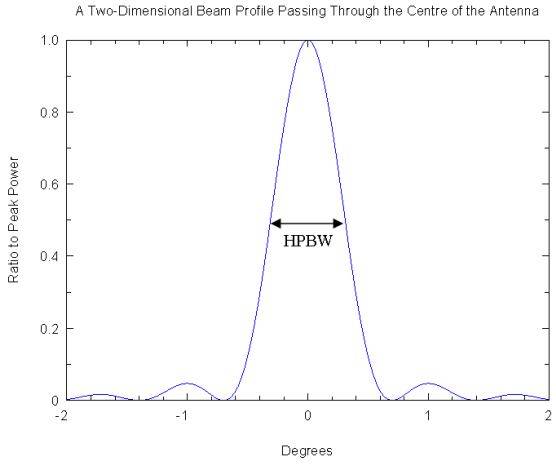

Figure 3.5: A diagram to show the half-power beamwidth (HPBM) of the EISCAT telescopes at 933 MHz.

(Adapted from Moran, 1998)

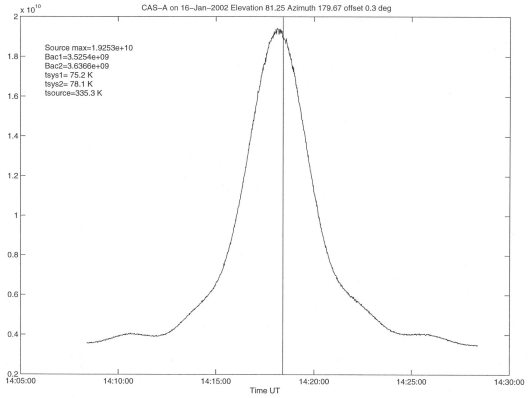

Figure 3.6: A diagram to show roughly the beam shape of the EISCAT telescopes at 1420 MHz. The plot is courtesy of Assar Westman at EISCAT Headquarters in Kiruna, Sweden.

The side lobes are an unfortunate aspect of the beam profiles of any telescope and must be carefully considered when making any observations. In the 933 MHz beam profile, the first side lobe is seen around ± 1° from the central axis. For the EISCAT antennas,

the level of this first lobe is ≤ -16 dB from the peak (~-17 dB for 1420 MHz observations). This is small enough for observations, but special care has to be taken for low elevations, weak sources, strong sources and those that lie very close to the Sun since these effects can “creep-in” to the antennas side lobes.

3.1.1.2 Receiver system and signal processing up to 2000

The radio signal received by each antenna went through various stages of signal processing prior to storage after digitisation. This was accomplished by two sets of electronics to be found in the cabin room behind the dish and also in the antenna aerial room. Details of this can be found in Moran (1998) where there is a full description of the system while operating at a central frequency of 933.5 MHz with a bandwidth of 10 MHz. A full description of the changes in operating frequencies and of the intermediate system in 2001 can be found in Appendix D of Canals (2002). A key part of the electronics used was a specially designed IPS receiver card. This produced an output voltage that was directly proportional to the received power at the antenna, i.e. the output showed the variation in the power received due to all the scattering events along the line-of-sight from the source to the antenna.

The output from the receiver card was converted into a digital format by the use of a single 16-bit analogue-to-digital converter enabling the signal to have 65536 (2^{16}) different values, providing an accuracy that was more than sufficient for subsequent data analysis. The sampling of the output was undertaken at intervals of 10 μs. For recording, 950 of these samples are used for each 0.01s, i.e. averaging for each data point, and then these data are “dumped” to the correlator memory format. The missing 0.5 ms was used when the correlator switched between real and imaginary values. Even though IPS data has no imaginary values as it is a measurement of power, the correlator could utilise both real and imaginary values. The correlator dumped the data to memory every 20 ms, where 3000 of these values (each containing two data points) were dumped every minute to disk. The system was controlled by minicomputers designed by Norsk Data

(ND) and these data were held on the ND560 system. It was later transferred to a SUN workstation in the control room where the first stages of the processing of these data were carried out (Canals, 2002). Detailed descriptions of the antenna movement, control and acquisition of data before 2000 can be found in Rishbeth & Williams (1985), Moran (1998) and Fallows (2001). These outputted data were converted using a program on the ND system (written by Jussi Markkanen at the Sodankylä site) with a 12026 bytes record length in a .dat binary integer format with the 26 bytes being used for the header file; ready for analysis on the Sun machines.

3.1.1.3 Receiver system and signal processing following the upgrades

On 12 September 2000, the system began its upgrades. The system upgrade had been planned for several years but was precipitated by the failure of the ND560 computer at Tromsø. Since there were no spare parts for this machine available any longer, a complete re-design of the receiving system was the only solution. A description of the intermediate system (very similar to that system described here) of 2001 can be found in Appendix D of Canals (2002). During 2001, the data were sampled in three frequency bands (approximately 1.35 MHz in width) and thus produced three time series for each frequency. Each frequency channel was sampled at 10^4 Hz and then integrated to give a 100 Hz sample rate for the three channels. An output file (in matrix form with 3 columns, one for each channel) was written every minute in binary form. The outputted data were then read using a Matlab routine and later saved as .dat files which were then partially analysed on-site to check the quality of data and also transferred to Aberystwyth for full analysis.

The 1.4 GHz receiving system of the two remote sites of Sodankylä and Kiruna was first used in the May 2002 IPS campaign. The change in observing frequency was caused by the encroachment of several communications services into the 930 MHz to 935 MHz band until a peak was reached at the Sodankylä when it was only possible to use a band of 929 MHz to 930.5 MHz due to new GSM antennae in the local area of the site. Therefore the decision to move to the protected bandwidth of 1400 MHz to 1427 MHz was

undertaken. It is unfortunate that due to complications with the transmitter aspect of the Tromsø site that this site could not be upgraded at the same time.

The benefits of moving to around 1.4 GHz were as follows:

- Interference greatly reduced from local GSM networks;
- There are high resolution maps of the radio sources used in IPS at 1.4 GHz thus allowing a better understanding of the variation in the scintillation during an observation as the source structure is better known;
- The higher frequency allows for observations to be made closer-in to the Sun;
- The combined observations between EISCAT and SOHO|LASCO have been improved because of the ability of EISCAT to observe more in the inner regions of the acceleration region of the solar wind.

The EISCAT antennas were designed to work at frequencies around 930 MHz and not around 1.4 GHz. However, it was found that the main reflector illumination was still acceptable at this alternate frequency and hence the same feedhorn was still able to be used for these increased frequency observations. There were modifications that had to be made however. These included several pieces of the lower frequency observing apparatus and the designing of a two-section circular waveguide Chebyshev transformer covering 1300 MHz to 1450 MHz. The new transformer bolted straight onto the feedhorn flange and feeds into the circular waveguide. Exact details of this can be found in Wannberg *et al.* (2002).

The processing of the signal at 1.4 GHz is very similar to that of the 928 MHz system and the signal that is received at (usually) 1420 MHz goes through a series of mixers and bandpass units which then downshift the frequency to around 11.2 MHz and enables the signal to be processed further by computer systems in the EISCAT control rooms and then further using the IPS analysis packages that are described later in this chapter. The fol-

lowing description is for the 928 MHz observing system (after the 2000/2001 upgrades).

Once the signal has been received, the unwanted noise has to be removed and this is accomplished in three stages. The first stage is by the use of pre-amplifiers where the signal is amplified by two cascaded GaAsFET pre-amplifier stages with a bandpass filter between them. To keep the system temperature at a minimum, the first pre-amplifier is kept in a closed circuit cryosystem. The signal then passes through a 925.1 MHz to 932.9 MHz bandpass filter which is used to attenuate the GSM signals that occur above 930 MHz by at least -30 dB. It is followed by the frequency conversion stage. This is where the output signal from the second pre-amplifier feeds into the mixer units and is then converted downward from the 925.1 MHz to 932.9 MHz frequency range to an intermediate frequency range and then finally to a digitised signal centred on 11.5 MHz by a Pentek 6420 dual-channel, 14-bit, analogue-to-digital converter clocking at 15 MHz.

3.1.2 MERLIN IPS

MERLIN is operated by the Jodrell Bank Observatory near Manchester, Great Britain, and is part of the University of Manchester. It is an array of radio telescopes distributed around Great Britain with 6 sites at Jodrell Bank, Cambridge, Defford, Knockin, Darnhall, and Tabley (also known as Pickmere). Figure 3.7 shows a map of these locations. The maximum baseline between telescopes of up to 217 km, is obtainable when using the Knockin and Cambridge sites, with the smallest baseline being around 11.2 km when using the Jodrell Bank and Tabley sites. MERLIN operates on several frequency bands ranging from 151 MHz to 22 GHz. The main sites used for IPS observations are Jodrell Bank, Cambridge and Knockin. A list of the different observing bands can be seen in table 3.3. (Information taken from
http://www.merlin.ac.uk/user_guide/OnlineMUG/newch0-node62.html, January 2005).

The IPS frequency bands used are the C-Band (5 GHz and 6 GHz) and the L-Band (1.4 GHz

Figure 3.7: A map of the locations of the MERLIN system throughout Great Britain. (Taken from http://www.merlin.ac.uk/about/layman/merlin.html, June 2006)

BAND	FREQUENCY(S)
UHF-Band	151 MHz
P-Band	408 MHz
L-Band	1.4 GHz and 1.6 GHz
C-Band	5 GHz and 6 GHz
K-Band	22 GHz

Table 3.3: Table showing the bands at which the MERLIN System is capable of observing at and to which frequency(s) each of the bands relate to.

and 1.6 GHz), but only the L-Band is used in this thesis centred on 1420 MHz with a bandwidth of 10 MHz. The C-Band IPS observations are made much closer-in to the Sun, as close as 5 $R_{\odot}$-6 $R_{\odot}$.

3.1.2.1 Antennas

The radio dishes that make up the MERLIN System vary in size quite considerably. Their exact geographic locations can be seen in table 3.4. The smallest of the dishes used are

the parabolic 25 m diameter dishes and are known as E-system telescopes (same design as those used for the VLA) at Knockin, Tabley and Darnhall. Another 25 m dish is located at Defford which is a mesh parabolic dish. At the Cambridge site, there is a 32 m diameter parabolic radio telescope, and at the main site of Jodrell bank, there are two further large dishes. These are the MkII and the Lovell (MkIa). The MkII is a $37\,\mathrm{m} \times 25\,\mathrm{m}$ concrete elliptical dish and the Lovell telescope (formerly known as the MkIa Telescope and re-named after the astronomer, Professor Sir Bernard Lovell who was the creator of the telescope) is a 76.2 m parabolic radio telescope.
(Information taken from http://www.jb.man.ac.uk/public/story/mk2.html and http://www.jb.man.ac.uk/booklet/Merlin.html, January 2005)

MERLIN Site	Geographic Latitude	Geographic Longitude
Defford	52.091003° N	2.136006° W
Cambridge	52.168467° N	0.039792° E
Knockin	52.778008° N	3.010986° W
Darnhall	53.144000° N	2.545992° W
MkII	53.231006° N	2.309489° W
Lovell (MkIa)	53.236250° N	2.307150° W
Tabley	53.279006° N	2.444994° W

Table 3.4: Table showing the locations of the MERLIN System radio telescopes. (Information taken from http://www.merlin.ac.uk/user_guide/OnlineMUG/newch0-node62.html accessed 30 October 2005)

3.1.2.2 Receiver system and data acquisition

The remote sites are connected to Jodrell Bank via three types of connection: A telephone line; a microwave link; and an L-Band link. The telephone link is used for the transmission of control signals to the remote sites from the Jodrell Bank control room. The microwave link is used to transmit data back to Jodrell Bank from all the remote sites. This can be done using either AM (amplitude modulation) or FM (frequency modulation). The AM link has a higher bandwidth than the FM link, and using the AM link would allow Jodrell Bank to receive both polarisations from the remote sites. Unfortunately, the

AM system includes automatic gain control which would remove information on signal amplitude. This makes the AM link unsuitable for IPS observations for this reason as IPS requires the measurement of signal power. In the IPS experiment on MERLIN, the data are transferred back to Jodrell Bank using the older FM link, which at the high data rates required for IPS, only has sufficient bandwidth for one polarisation to be transmitted back. The radio link is used to keep all the sites at UT time by the transmission of pulses from the Jodrell Bank site. All of the sites are in continuous communication with one another allowing the Jodrell Bank control centre complete and continuous control over the remote sites, as well as the local telescopes and can correct any problems that may occur during, before or after observations.

The first IPS observations to take place using the MERLIN System with baselines up to 127 km were in 1989 at 1660 MHz (Rickett, 1992). There are now three frequencies at which IPS is carried out, 1420 MHz, 5 GHz and 6 GHz - the 5 GHz and 6 GHz observations taking place closer in to the Sun than the 1420 MHz observations. For this thesis, observations from four of the telescopes at three of the sites were used. At the Jodrell Bank site, observations were taken using the Lovell radio telescope and the MkII radio telescope. The remote sites used were Cambridge and Knockin.

The MERLIN system uses voltage to frequency converters and integrating counters to carry out the analogue-to-digital conversion and these counters are susceptible to "rolling over" should the signal not be attenuated correctly or when there is a large increase in the amount of signal received. An example of this is discussed in Jones *et al.* (2006a) during an observation of a radio burst in both MERLIN and EISCAT IPS data. The "rolling over" of the counters causes them to start counting from zero again, thus making the signal look like it is rapidly fluctuating from very high to very low values if it is at the approximate level of the "roll over". This problem is not experienced at EISCAT because the signal attenuation is set automatically before the observations take place to be sure that the receivers do not saturate and cannot be modified in the new EISCAT system by

the user. At MERLIN, the attenuation is set after the observation commences depending on the average strength of signal received.

MERLIN is also heavily susceptible to background noise interference. It is a particular problem at the Cambridge site probably due to the local U.S.A. military base radar systems.

3.1.3 Comparison of the EISCAT and MERLIN systems

MERLIN is capable of observing closer-in to the Sun (observation of the solar wind acceleration region is possible) since it can go to higher frequencies for observation and hence remain in the weak scattering regime which the analysis programs (discussed later) used in this thesis require. However, EISCAT is more capable of resolving streams within the raypath that are close in velocity since its larger baseline capabilities allow for the better resolution of velocities. EISCAT observations are started and stopped automatically by computer control so have an exact UT start/stop time whereas the MERLIN observations are stopped and started manually so usually are started earlier than EISCAT and finished later than EISCAT for the EISCAT-MERLIN combined observations to be sure that both systems were observing the same sources simultaneously. (Bisi *et al.*, 2005; Breen *et al.*, 2006)

Another difference between EISCAT and MERLIN is in the quality of the data recorded. EISCAT samples the data at 10 kHz (and so is over-sampled) and subsequently integrated to give 100 samples s^{-1}. MERLIN however, samples the data at 100 Hz, the minimum required for IPS (as discussed earlier). This means that MERLIN has more noise in its data than that of EISCAT which is of an extremely high quality.

3.1.4 IPS analysis routines

The initial raw data that is received by both EISCAT and MERLIN systems needs to undergo several stages of analysis to obtain the results from the observations. The background noise is removed from the data and a cross- and auto-correlation function is obtained for each useful baseline either within each system or in the case of the extremely long-baseline observations, between the systems. This is accomplished by time-matching the data-files together to be sure that the same time-period of observation is being cross-correlated from each of the receivers. This initial processing gives a first estimate of the solar wind velocity(s) along the IPS raypath. The term "velocity" is used to stay consistent with current and past nomenclature in the field, although it sometimes refers to a scalar "speed". After this, a more accurate measure of the solar wind velocity(s) in the raypath can be obtained by use of a weak scattering model (Grall, 1995; Coles, 1996; Klinglesmith, 1997; Massey, 1998) in the frequency domain of the IPS measurements written by W. A. Coles, R. R. Grall and M. Klinglesmith (University of California, San Diego - UCSD) and subsequently modified and developed (Fallows, 2001) by R. A. Fallows (University of Wales, Aberystwyth - UWA) for the uses as required by the the Aberystwyth group.

3.1.4.1 The first stages of data processing

The analysis of the IPS data to obtain estimates of the solar wind velocity and other measurements such as random velocities follows some initial processing of the data. This is necessary to remove from these data sources of noise such as lightening, variations in system temperature, internal interference within the system, mobile phones, 'leaking' ignition systems from cars at the sites, welding equipment (in the case of the workshop at the EISCAT Tromsø site), and other local interference sources. The total noise can be described by equation 3.2 and these data are viewed where the spikes can be removed or even sections of data when there is a large amount of noise.

$$Total = Background\ Noise + Receiver\ Variation\left(\frac{1}{f}\right) + IPS \text{ (Scintillation Spectra)} \tag{3.2}$$

The next stage is to obtain the first power spectrum by performing a fast fourier transform on the data. Low- and high-pass filters are applied so that the cross- and auto-correlation functions can be obtained. The low-pass filter is used at the high frequencies to remove random variations in the background noise from the power spectrum in frequency-space; and the high-pass filter is applied to the low frequencies where the power rises rapidly and is approximately proportional to 1/f noise. The values of both the filters can be altered for each of the sites and for each seperate observation. Typical values are 0.05 Hz to 0.25 Hz for the high-pass filter and 1.00 Hz to 20.00 Hz for the low-pass filter. The lower frequencies in the spectrum relate to slower moving irregularities whilst the higher frequencies relate to faster moving irregularities, so great care has to be taken while filtering the data as valuable information could be inadvertently removed from the data during this filtering process. White-noise which is present at all frequencies is also removed by background subtraction, but frequency-dependent noise can still cause problems. A more detailed treatment of the filtering process can be found in Moran (1998). An individual set of correlation functions for each part of the raypath is illustrated in figure 3.8.

The low-pass filter is applied to remove the background noise where the spectrum rises above 2σ over the background noise. This is a recent introduction as prior to this it was conducted manually in the program by the user. The key parameters of the spectrum are its position in frequency space, in particular the position where the frequency spectrum starts to flatten-out (this varies with solar wind velocity), and the second is the height of the spectrum which in-turn depends on the density of electrons through the IPS raypath. Application of the low- and high-pass filters as well as the measure of the white-noise is illustrated in figure 3.9.

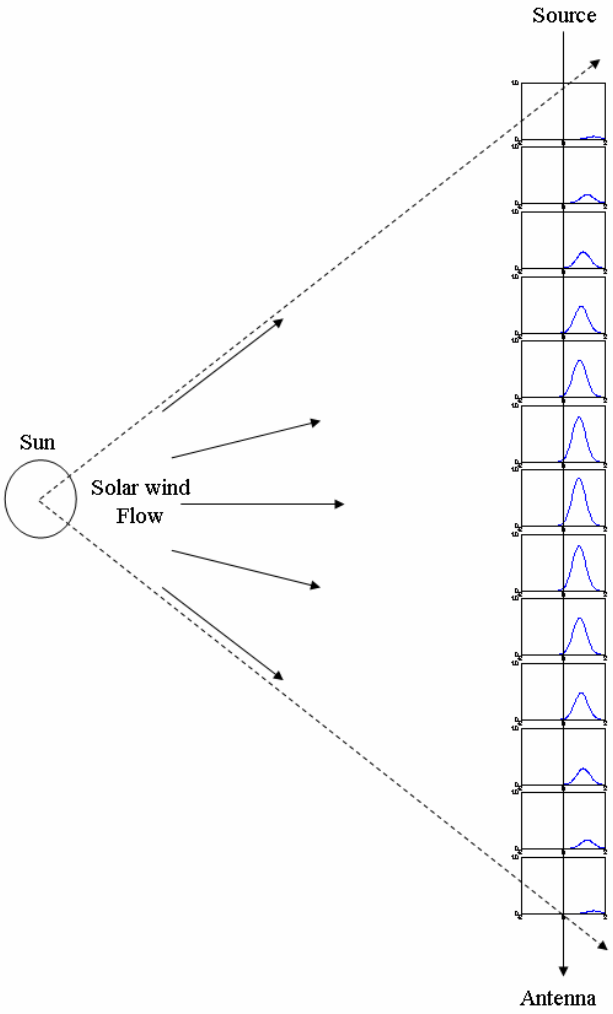

Figure 3.8: A diagram to illustrate the individual correlation functions from along the line-of-sight from the source to the telescope that sum in a linear fashion to give the overall IPS frequency spectrum.

(Adapted from Fallows, 2001)

The manipulation of the power spectrum in this manner ensures the optimum use of data. A figure of the obtained frequency power spectrum and the two auto- and one cross-correlation functions can be seen in figure 3.10 along with the high- and low-pass filters. It is from the time lag of the cross-correlation function that the initial estimate of solar wind velocity across the IPS raypath can be made. This can be done by various methods, one is by relating the time lag of the peak of the cross-correlation function and relating this to the parallel baseline of the observations and another is the point of intersection between the auto- and cross-correlation functions; this can be used to give a measure of

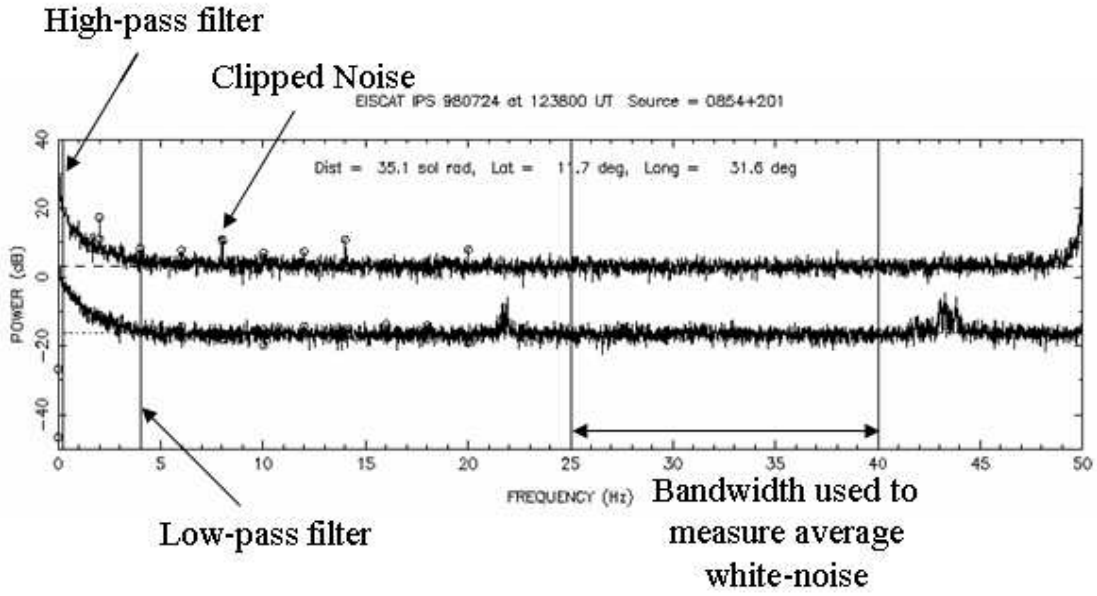

Figure 3.9: The power spectrum in frequency space taken from a typical IPS observation. The level of the power of one of the signals has been lowered by 20 dB to enable both sets of data to be viewed easily on the same plot. At this point any harmonics (0.5s harmonics at 2Hz, 4Hz, etc.) created by the cycle in the cryogenic cooling system for the pre-amplifiers at the EISCAT antennas, are tagged with circles and are clipped from the observation thus cleaning the IPS signal further.

(Adapted from Fallows, 2001)

the mean solar wind velocity across the IPS raypath. A more detailed description of how the solar wind velocity can be directly obtained from the correlation functions can be seen in Grall (1995) and Breen *et al.* (1996b).

The length of the IPS observations varies somewhat from 15 minute observations to observations lasting over 6 hours. Generally, for observations lasting over 15 minutes, the analysis is undertaken in 15 minute intervals, but it is sometimes carried out in 10 minute or 20 minute intervals depending on the speed of the evolution of the solar wind across the IPS raypath at the time and also on the quality of signal received. For example, it is usual for MERLIN data to be treated in 20 minute intervals, EISCAT/ESR data in 15 minute intervals, but EISCAT-MERLIN data in either 10, 15, or 20 minute intervals. Extended observations (more than 15 minutes) have taken place in campaigns since 1994 and give an in-sight into two aspects of the evolution of the solar wind; spatial structure of the solar

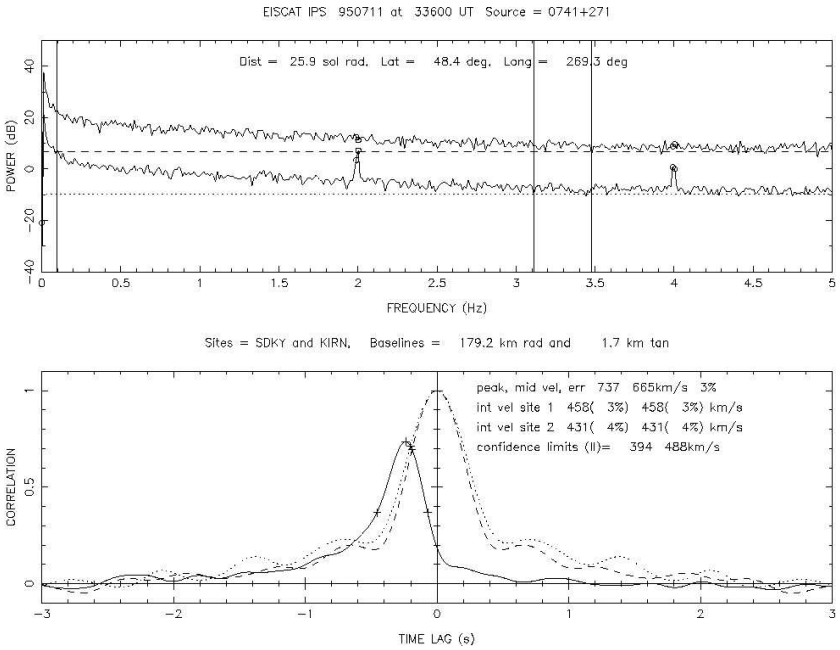

Figure 3.10: The upper section of the image shows the power spectrum in frequency space with both the high and low pass filters in place. The lower section shows the correlation functions that are derived from the power spectrum, the auto-correlation functions at zero-lag and the cross-correlation function of the two sites at a negative time lag.

wind where the solar wind properties remain static, but the observing geometry changes; and in the campaigns that usually take place later-on in the year (as opposed to May), where the geometry only changes very slowly and any changes in the solar wind can be seen.

3.1.4.2 Use of synoptic maps to constrain fitting

During analysis of the IPS data, it is necessary to be able to estimate where the different streams of solar wind lie in the IPS raypath. Synoptic “Carrington” maps derived from coronal limb data (as discussed in more detail later in this chapter) were used from the Mauna Loa MkII coronagraph, the SOHO|LASCO C2 coronagraph, the Yohkoh|SXT instrument and the SOHO|EIT instrument can be used for this purpose.

There is good correlation between the presence of coronal holes and observations of fast solar wind. For the white-light Carrington maps, dark regions of the Carrington maps are

coronal holes where the fast wind has been shown to originate (Krieger & Timothy, 1973; Neupert & Pizzo, 1974; Nolte *et al.*, 1976; Breen *et al.*, 1996b,c). This therefore makes it possible to use maps of white-light intensity in the upper corona (or EUV/X-ray maps of lower heights) to determine whether a given region will be made up of fast or slow solar wind. The slow wind is assumed to lie above the bright regions of the Carrington maps. Construction of such maps can be found later in this chapter. To use these maps to constrain fitting, it is necessary to map the IPS observation of the solar wind in interplanetary space down to relevant coronal heights. In this thesis at this stage, the solar wind flow is assumed to be purely radial and each stream travelling at a constant velocity. The IPS raypath from the source to the antenna is ballistically mapped down the Parker spiral appropriate to the chosen velocity (as discussed later along with the construction of the synoptic maps).

During the periods of minimum activity of the Sun, coronal holes and the streamer belt are clearly defined, so that contributions to the IPS observations from the fast and slow streams can be reasonably well defined. During solar maximum however, the activity of the Sun increases somewhat and so the distinction between coronal holes and streamer belts is much less clear as the streamer belt is not confined to the Sun's equatorial region alone and coronal holes are found to appear at all latitudes and are not just confined to the polar regions. The regions of the IPS raypath in different modes of wind can be related back to the Sun in terms of an angle as can be seen in figure 3.12 later in this chapter, and the projection of the raypath as discussed later in this chapter can be seen in figure 3.11 of a case using a SOHO|LASCO white-light map. The line-of-sight (IPS raypath) is divided into 5° segments (shown by diamonds), and symbols mark the Earth (*) and the P-Point on the line-of-sight (+). It should be noted that for the Mauna Loa MkIII cases, the line-of-sight is split into 10° segments.

Angles along the raypath are measured from the point of closest approach (P-Point) to the Sun at zero degrees (0°) with negative angles toward the Earth and positive angles to-

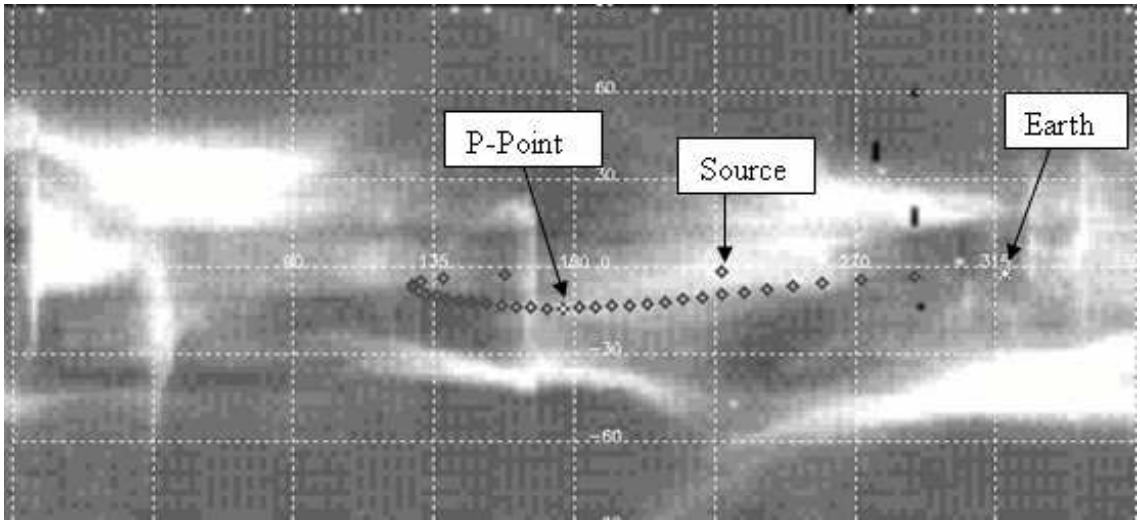

Figure 3.11: Figure showing and example of an IPS raypath ballistically mapped onto a SOHO|LASCO white-light Carrington rotation map.
(Canals, 2002)

ward the source. At the start of attempting to fit an observation (the fitting is undertaken using a weak scattering model described in the next part of this thesis), the IPS raypath is normally mapped back toward the corona at velocities of 350 km s^{-1} and 700 km s^{-1} corresponding to typical values for slow and fast solar wind respectively and is dependent on which stream is dominant to the IPS observation (if indeed there is more than one stream passing across the IPS raypath). The information regarding the position of the slow and fast streams in the IPS raypath is then used to constrain the fitting of the observation and after fitting, this mapping process is repeated using the fitted velocity of the dominant stream (in the case of more than one stream in the IPS raypath). It is then refitted using the new angles and if indeed they are changed by mapping at the first fitted velocity rather than at the typical stream speeds.

3.1.4.3 Fitting data in the frequency domain - the sfit model

The fitting of the data in the frequency domain is carried out by a weak scattering model, sfit, written in Fortran-77. It was first developed by W. A. Coles and later improved upon by R. R. Grall and M. Klinglesmith (all at UCSD at the time) and modified further by R. A. Fallows (from UWA) as stated earlier. The main purpose of the model is to give

more accurate velocity estimates of the solar wind stream velocity(s) flow across the IPS raypath. The model is also capable of providing other terms with respect to the bulk solar wind flow across the raypath such as variations parallel to the flow and those perpendicular to the flow (Coles, 1996). A summary of all the parameters for which the weak scattering model can calculate or provide, or be set as constant, can be seen in table 3.5.

The model includes assumptions based on previous work of the spatial spectrum of electron density, the effects of Alfvén waves, the super-radial expansion of the corona close to the Sun, the line-of-sight integration and the spiral orientation of the magnetic field from the Sun. A theoretical model is fitted to the observed spectra that is based on weak scattering. After initial parameter estimates are made, the model uses a non-linear least-squares minimisation to reach final values to parameters being fitted. A full description of the model and the algorithms used by sfit for parameter estimation can be found in Klinglesmith (1997) and Massey (1998).

The sfit model, as can be seen from table 3.5, can be used for fitting velocity values to up to two modes of solar wind flow across the IPS raypath. The analysis assumes either a single stream of either fast or slow along the raypath or fast flanked by slow or slow flanked by fast. The boundary of each of the streams is obtained by using synoptic maps (as described earlier in this chapter) and related as an angle in terms of θ_{in} and θ_{out} as seen in figure 3.12. These two parameters describe the part of the line-of-sight where a different mode of solar wind may exist as compared to the remaining part of the spectrum. For example, the figure shows the two θ-values describing a fast mode of solar wind in the central part of the IPS line-of-sight flanked by the slow mode of solar wind on either side. Generally speaking, θ_{in} is given as a negative angle and lies the Earth-side of the P-Point (but not always) and θ_{out} is given as a positive angle and lies the source-side of the P-point (but not always). The P-Point is at 0°. However, θ_{in} is always on the Earth side of the IPS raypath and θ_{out} is always on the source-side of the IPS raypath.

Parameter	Parameter Definition	Comments Relating to the Parameter
vfast vslow	Radial bulk flow velocity of the fast and/or slow stream across the IPS raypath	Most easily estimated parameters. Not strictly limited to typical fast and slow velocities, but as labelled as such to enable ease of determining between two streams of different velocity if there are indeed two streams in the observation
thin thout	Boundaries for fast and slow wind set by θ_{in} and θ_{out} as can be seen from figure 3.12	Both θ_{in} and θ_{out} are obtained by using synoptic maps
rmsvf rmsvs	Root mean square deviation in perpendicular velocity, $RMS - V_{perp}$ for both fast and slow winds	A detailed description of how rmsvs and rmsvf vary with distance away from the Sun can be found in Canals (2002), e.g. Wave effects, but more difficult to distinguish from other sources of de-correlation
dvparf dvpars	Systematic variation in radial velocity dV_{par} for both the fast and slow winds	Dominated by real variation in solar wind speed of a stream and is a measure of the spread of the bulk velocity of the stream
wtslow	Ratio of scattering volumes along line of sight in each of the fast and slow streams	= 5.3 (Fallows, 2001) when fast flow flanked by slow flow (Now noted to be an under-estimate however) = 1/5.3 when slow flow is flanked by fast flow either side
arf ars	Axial ratio is the mean scale size both parallel and perpendicular to the flow	Usually, axial ratio > 1 but can be < 1 during a CME passage
alpha	Exponent of the spectrum of electron density	Alpha is know to lie in the range $2.7 \leq \alpha \leq 3.3$ (Coles & Harmon, 1989)
iscale	The inner scale of the spectrum of electron density, where the power drops off (κ_c)	A detailed description of iscale can be found in Appendix A of Canals (2002)
gamma	Tilt angle used to describe the orientation of the magnetic field near the Sun (γ) measured in degrees	Magnetic field close to the Sun modelled with azimuthally symmetric model in which the field tilts equator-ward off-radial by an angle $\gamma_R = \gamma^{R/\gamma_L}$ (Klinglesmith, 1997)
gamma_L	Scale height of the tilt angle (γ_L)	As above for gamma
valfvenf valfvens	Alfvén wave velocity for the fast and slow winds	Velocities are estimated by using the empirical formulae Valfvenf (R) = 9000/R and Valfvens (R) = 4500/R (Massey, 1998)

Table 3.5: A table showing the parameters that are provided and can be fitted/used in the IPS weak scattering model sfit.

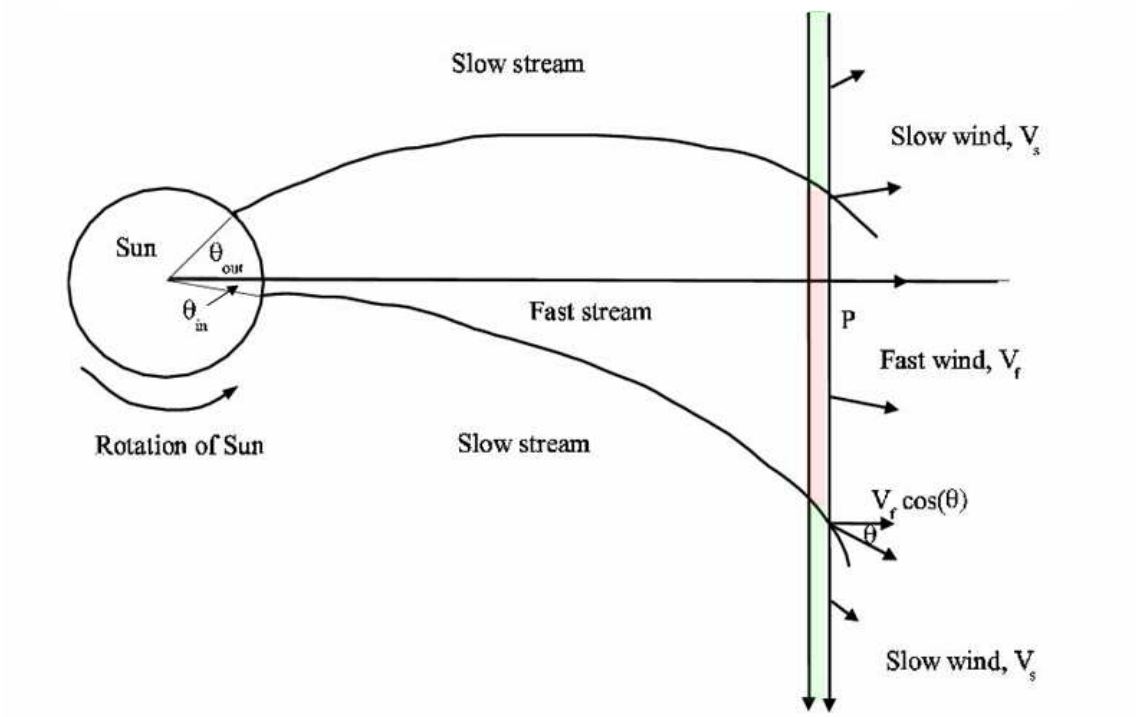

Figure 3.12: Schematic diagram showing how to describe the width of the central stream in the IPS raypath as an angle relative to the centre of the Sun. This schematic is shown as if looking down on the North pole of the Sun with angles toward the Earth from the P-Point (θ_{in}) defined as negative and angles away from the P-Point toward the source (θ_{out}) defined as positive. The fast stream need to be the middle stream, it need not be strictly fast and slow streams, and the central stream need not be centred at the P-Point.

(Adapted from Breen *et al.*, 2002c)

As can be seen from the table of the sfit parameters, which are many in number, some can be set to constrain the data and others can be fitted to improve the model fit of the auto- and cross-correlation functions created by the model (depending on the value of the parameters set/being fitted) and that of the real data obtained from the initial IPS data analysis described in the previous sub-section. The quality of fit obtained is given as an error and is the reduced-χ^2 (χ^2_ν). (Reiff, 1983)

Generally, for the first stage of fitting, only the theta-values are entered manually into the weak scattering model. The main parameters of interest are the solar wind velocities, fast (vfast) and slow (vslow) but can fit for one or both; the random perpendicular velocity of each of these streams (rmsvf and rmsvs respectively); the systematic variations in the

bulk velocity parallel to the flow for each of the streams (dvparf and dvpars respectively); the ratio of the weighting of the slow wind to the fast wind when fitting for more than one stream (wtslow); and the axial ratio of the solar wind (arf and ars respectively). Parameters which are generally not altered include those associated with the modelling of the spatial spectrum of electron density fluctuations, further details can be found in Canals (2002). These parameters include the exponent of the spectrum of electron density (alpha); and the inner scale of the solar wind (iscale). There are also those associated with the large-scale magnetic field of the solar wind which include the non-radial flow angle (gamma); and the scale height (gamma_L). Alfvén wave velocities in the fast and slow wind are also taken account of (valfvenf and valfvens respectively). Description of the parameters in more detail can be found in Klinglesmith (1997) and Massey (1998) and the summary of these parameters as stated earlier can be found in table 3.5.

Correlation functions in the time domain can be viewed in sfit (also referred to as the "stacked correlation" plot as seen in figure 3.13) which helps in the initial setting of parameters, but the program fits the data in the spectral domain. The idea of changing parameters before the program starts fitting is to give the program a better starting point on which to fit the model spectra to the observed spectra. The following description refers to a fitting of an observation that is dominated by a single stream, but a similar procedure is carried out for an observation containing two streams.

The first parameter to be determined is the axial ratio (AR). This is estimated from the zero-lag value. The "stacked correlation" plot is viewed to do this as seen in figure 3.13. In this figure, the model is represented by the dashed lines and the data by the solid lines. The model is drawn as a $\pm 1\sigma$ error model. Changing the AR value can make the modelled cross-correlation function cross the time = 0 axis at the same place as the observed cross-correlation function. The AR is a measure of the anisotropy of the irregularity. A description of how changing the AR can alter the zero-lag value can be found in Chapter 3 of Canals (2002). It should be noted however, that there are negative side lobes in

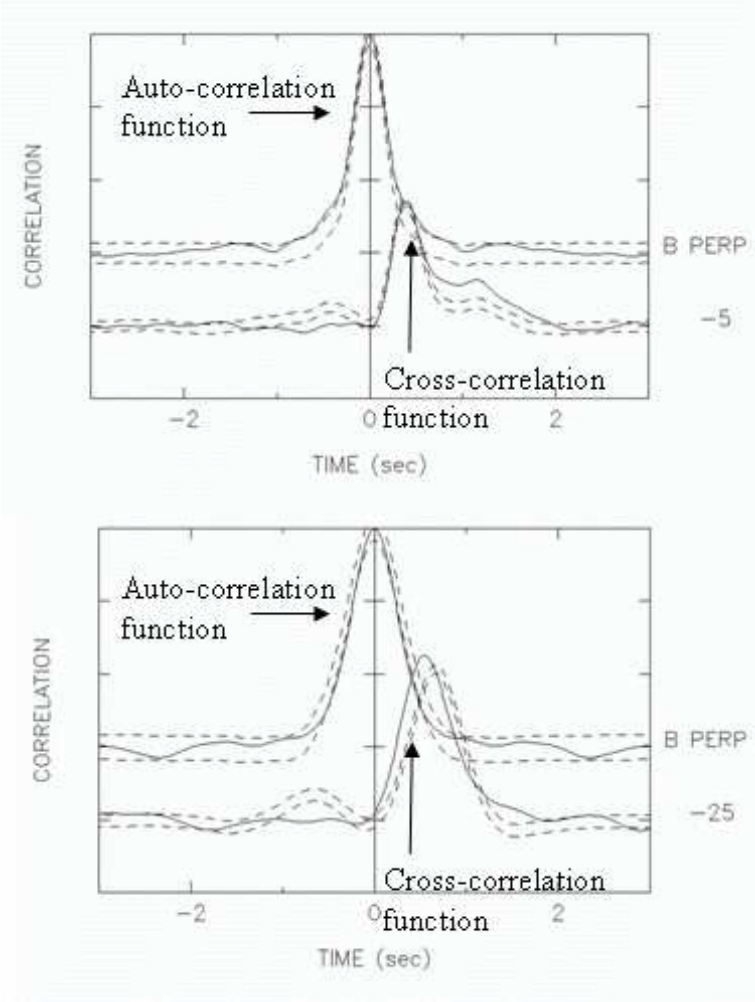

Figure 3.13: The figure shows an example of stacked correlation function plots (auto- and cross-) as can be seen from the weak scattering model. The bottom shows a case where the observation was dominated by a single stream and the top shows a case where the observation has both fast and slow streams crossing the line-of-sight (a double peak in the cross-correlation function). The dashed-lines are the model functions and the solid lines represent the data.

weak scattering models even when AR = 1. As the AR is increased, the lobes become deeper in the perpendicular direction. Since the temporal cross-correlations are simply cuts through this pattern, if the transverse baseline is sufficiently large, negative regions will be sampled and a significant undershoot in the temporal cross-correlation function will occur. It should be noted however that observations are generally centred around a perpendicular baseline that is close to being zero. Negative lobes in the cross-correlation functions can also occur as a result of a transient passing through the line-of-sight such as a coronal mass ejection (CME) usually when the AR is set to a value of one or less. In

the case of a CME, the negative lobe is positioned so that as the pattern drifts passed the two observing sites, it is sampled. Hence, if you decrease the AR in the weak scattering model, you will lower the zero-lag value; and increasing the AR will cause a higher zero-lag value.

If you were to have multiple baseline fits from extended observations where the observation is divided into set-time segments (usually 10, 15, or 20 minutes in length) in the initial analysis, then this is carried-out differently. The zero-lag plot is utilised in this case, an example of which can be seen in figure 3.14. For an extended observation, the baselines are capable of changing quite dramatically, especially in the case of the extremely long-baseline observations as described in Chapter 6 of this thesis. The observations in the figure are shown with 2σ errors where the open circles are the zero-lag cross-correlation values from the model and are connected with a spline. Changing the axial ratio(s) and the non-radial flow angle (gamma) will make the line go through the observation points. This then helps to constrain the AR and gamma values.

The next step in fitting using sfit is to get the peak (or peaks) of the model in the same or similar place as those of the data. This is carried-out by inputting "better" values for the solar wind velocity(s) (vfast and vslow respectively). The shorter time lags are implied by faster velocities and vice-versa for longer time lags. The de-correlation of the correlation functions can be compensated for by changing the random perpendicular (rmsv) and systematic (dvpar) variations in the bulk flow. Both rmsv and dvpar change the diffraction pattern that drifts past the two sites observing, and therefore changes the de-correlation in the temporal cross-correlation function. A more detailed study on the effects of rmsv is carried-out and discussed in chapter 4 of Canals (2002).

The next stage is the fitting of the model to the data. An example of the output from sfit of fitting the model for a single 15 minute observation can be seen in figure 3.15. It is best to fit linked parameters such as vslow and rmsvs rather than, say, fitting four un-

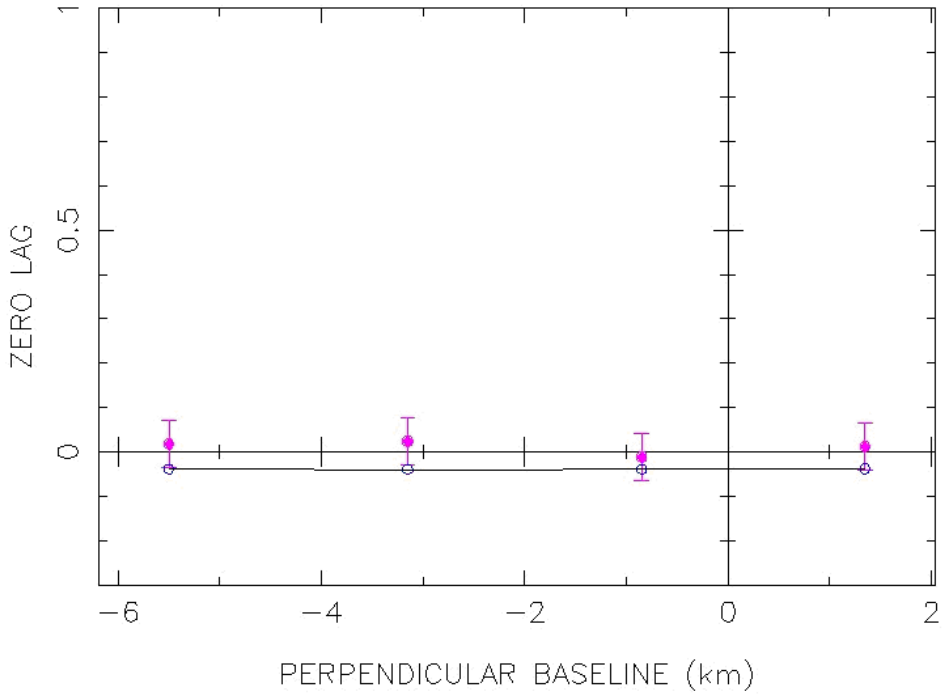

Figure 3.14: Figure showing a zero-lag plot for multiple baselines in the weak scattering model. The observations are shown with 2σ errors where the open black circles are the zero-lag cross-correlation values from the model. They are connected with a spline.

linked parameters at random. The estimates reached by the fitting procedure are given a goodness of fit figure (χ^2_ν) but great care must be taken with this as it can sometimes be very heavily weighted in describing the fit of the auto-correlation function rather than the cross-correlation function. Careful inspection of the data and modelled spectra and correlation function can lead to a more accurate judgement of the quality of fit as well as taking the χ^2_ν value.

The top panel (1) of figure 3.15 gives the magnitude of the auto- and cross-power-spectra. The un-smoothed spectra are shown in red and blue respectively for each site. The cross-spectra is shifted down 5 dB to avoid an overlap when viewing the data. The white dots are the smoothed spectral points which are the points to which the model is fitted. The second panel down (2) gives the phase of the cross-spectra, smoothed and un-smoothed. The third panel down (3) gives the auto- and cross-correlation functions. Then, in the final panel at the bottom (4), the real and imaginary parts of the cross-spectrum are dis-

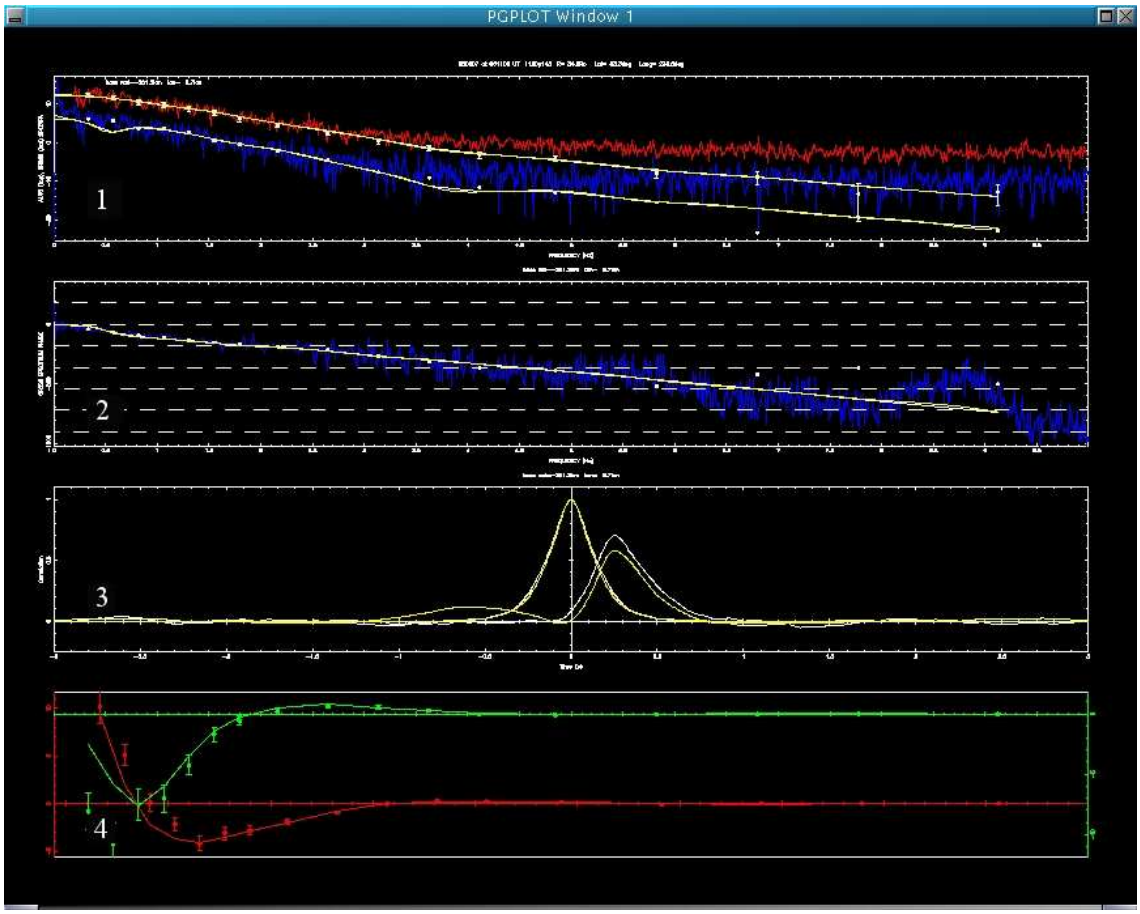

Figure 3.15: A figure showing the four plots 1, 2, 3 and 4, in the weak scattering model of the EISCAT IPS observation of source 1120+143 on 19950707 using the Tromsø and Sodankylä telescopes. This is just one of the displays capable of being shown by sfit. A detailed description of what each panel represents can be found in the text.

played. The yellow lines are representative of the weak scattering model in each of the panels.

This display in the fitting model is useful since it allows small changes to be made to the model spectra by changing the values of the parameters gamma, iscale and alpha. Alpha, as can be seen from table 3.5, usually takes a value of between 2.7 and 3.3 and changing this can rise or lower the model spectra in the top plot (1) of figure 3.15. Changing of the gamma and iscale parameter values can also help match the spectra better. The third plot (3) in figure 3.15 can give a better and more detailed view of the fit (and is similar to the "stacked correlations" view), thus making it easier to make an initial decision whether or

not a fit is good.

The wtslow parameter is used to set the relative weight between the fast and slow wind along the line-of-sight as described in table 3.5. The weighting factor is given by $dN^2_{e\,(slow)}/dN^2_{e\,(fast)}$. The slow wind has a higher electron density, N_e, than that of the fast wind. In the model originally developed at UCSD, wtslow was set between 10 and 15, since there was evidence that close-in to the Sun the electron density variance, dN^2_e, is a factor of 10 to 15 times lower in polar coronal holes (Grall, 1995). Since then, work on scintillation levels carried-out at Aberystwyth, appear to suggest values as low as $(2)^2$ are possible. Further analysis lead to a corrected ratio of 5.3 (Fallows, 2001), which was adopted as a starting point for fitting until it was discovered to be under-estimated. For the purpose of observations where fast wind is flanked by slow wind (as in the majority of observations used in this thesis), a value of $\sim(3.5)^2$ was set as a starting point for the wtslow parameter.

The above description of the use of the model highlights the importance of constraining as many parameters as possible before fitting is undertaken. This then reduces the number of unknowns in the calculations that the program has to perform in fitting the theoretical function to the observed function. (e.g. Canals, 2002)

3.2 Coronal data

There are a large number of instruments available on a selection of spacecraft that are capable of remote-sensing the Sun at various wavelengths. The spacecraft that have such instruments and data which were incorporated into this thesis are those of the Yohkoh and SOHO spacecraft.

3.2.1 Yohkoh - SXT

Yohkoh was launched on 30 August 1991 by Institute of Space and Astronautical Science (ISAS) in Japan from the Kogoshima Space Centre in Japan in a Mu-IIIs-V rocket. A picture of this can be seen in figure 3.16 It was initially named Solar-A, but was renamed Yohkoh, which means Sunbeam in English, after its launch.

Figure 3.16: The launch of the Yohkoh spacecraft at the southern tip of Japan's southern-most main island, Kyushu, at the village of Uchinoura on the Ohsumi peninsula, a view of the Pacific Ocean can be seen in the background of the picture.
(Taken from http://isass1.solar.isas.ac.jp/yohkoh/yohkoh_background.html, January 2003)

The Soft X-ray Telescope (SXT) on board Yohkoh recorded images in the X-ray region of the electromagnetic spectrum from 0.25 keV to 4.00 keV. The way in which it restricted its energy range is by using metallic filters. The SXT used glancing incidence mirrors in order to form soft X-ray images of the Sun on its CCD sensor of 1024×1024 pixels. The SXT had a maximum resolution of 2.5 arc seconds and it could observe and obtain information regarding temperature and density of the plasma emitting the X-ray radiation by comparing images acquired using different filters. An example of an SXT image ob-

tained from the Yohkoh spacecraft can be seen in figure 2.11 in the previous Chapter. A thorough explanation of the Yohkoh spacecraft and its specific instruments can be found in Ogawara *et al.* (1991).

Synoptic maps of the limb of the Sun created from SXT images were used in this thesis to constrain streams of solar wind in the IPS raypath when mapped back onto the synoptic maps as described earlier in this chapter. The maps were used in the investigation into possible internal structure of the fast solar wind in Chapter 5 of this thesis.

3.2.2 SOHO

The SOHO spacecraft, pictured in figure 3.17, is a 1350 kg unit costing ~0.8 billion EUR and is a joint ESA/NASA venture. It was launched from Cape Canaveral in Florida on 2 December 1995 on board a two-stage Atlas/Centaur rocket. It reached its permanent position at the L_1 point (approximately 1.6×10^6 km from the Earth along the Sun-Earth line - it is the inner Lagrange point where the gravitational pull of the Sun is equal to the gravitational pull of the Earth) on the 14 February 1996, and thus orbits the Sun in the same time period as it takes the Earth to orbit the Sun. A major advantage of this orbit is that the instruments remain in a thermally constant environment and are not subjected to the large variations in temperature that can be experienced by Earth-orbit spacecraft due to eclipsing of the spacecraft when it would enter the night parts of its orbit and would no longer be in direct sunlight. However, a downside to this orbit is the limited bandwidth of data which can be sent back to the Earth. This limits the data transmission rate, so it is not possible for all of the instruments to work at their maximum cadence at the same time. Each instrument can have a high cadence campaign provided all or many of the other instruments are shut-down to allow for the prioritised data transfer of the high cadence observation(s). A full description of the SOHO spacecraft can he found in Domingo *et al.* (1995).

SOHO has a total of 12 instruments on board that take measurements 24 hours a day, a

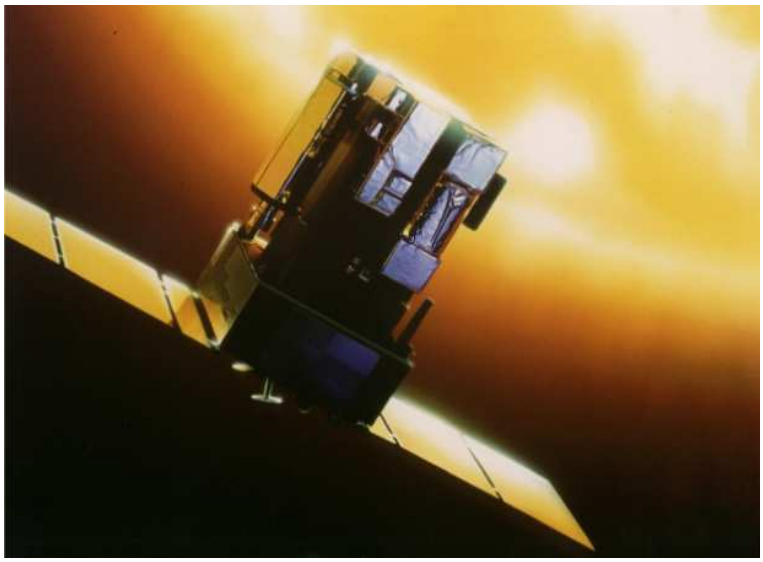

Figure 3.17: An artist's impression of the SOHO spacecraft in space.
(Taken from http://www.esa.int/esaSC/SEM0VZWO4HD_index_1.html, March 2004)

mixture of both in-situ and remote sensing instruments. The two instruments used in this thesis are the Large-Angle and Spectrometric COronagraph (LASCO) and the Extreme ultra-violet Imaging Telescope (EIT) instruments. The two operational coronagraphs for LASCO are the C2 and C3 coronagraphs. C2 measures from 1.5 $R_\odot$ to 6 $R_\odot$ and C3 measures from 3 $R_\odot$ out to 32 $R_\odot$.

3.2.2.1 SOHO - EIT

The Extreme ultra-violet Imaging Telescope (EIT) instrument on board SOHO is a normal-incidence, multilayer telescope of novel design. It is capable of imaging the solar transition region and inner corona with four different bandpasses within the EUV part of the EM spectrum. The four bandpasses are 171 Å (the Fe IX/X line), 195 Å (the Fe XII line), 284 Å (the Fe XV line) and 304 Å (the He II line). EIT is used to make movies, images and Carrington Rotation maps (centred or limb as discussed later in this chapter) of the Sun. Some examples of EIT images can be seen in figure 2.12 in the previous Chapter of this thesis. The four different observing frequencies provide a wide field of viewing of the Sun out to approximately 1.5 $R_\odot$. Each different frequency has a peak temperature associated with it as can be seen in table 3.6.

Observing Wavelength	Peak Temperature Observed	Part of the Sun Observed
171 Å	1.3×10^6 K	Corona/Transition Region Boundary
195 Å	1.6×10^6 K	Quiet Corona
284 Å	2.0×10^6 K	Active Regions
304 Å	8.0×10^4 K	Chromospheric Network

Table 3.6: Table showing the EIT peak observing temperature with respect to each of its observing frequencies and the region of the Sun's "atmosphere" these correspond to.
(Adapted from Delaboudiniere *et al.*, 1995)

Each of the frequencies correspond to different observing heights in the lower corona (as seen in table 3.6). This enables the observer to monitor the evolution of structures through the first 20 $R_\odot$ to 30 $R_\odot$ if used in conjunction with the LASCO instrument.

The EIT instrument has a spatial resolution of 2.6 arc seconds and a 45 arc minutes square field-of-view. A detailed description of the EIT instrument can be found in Delaboudiniere *et al.* (1995).

3.2.2.2 SOHO - LASCO

The Large-Angle and Spectrometric COronagraph (LASCO) instrument originally started out as three coronagraphs, C1, C2 and C3, each observing further ranges out from the Sun between 1.1 $R_\odot$ and 30 $R_\odot$. Unfortunately, the C1 coronagraph was lost when contact with the spacecraft was temporarily lost in June 1998 - only the C2 and C3 instruments were still in operation when contact with the spacecraft was re-established. LASCO is used to observe the Sun in white-light and is capable, like EIT, of making movies, images and Carrington rotation maps of the Sun (as discussed later in this chapter). See table 3.7 for properties of the LASCO coronagraphs.

The resolution of the inner edge of the LASCO telescopes is poor, so overlapping of the images from different coronagraphs allows for the areas which would normally have

	Field of view ($R_\odot$)	Occulter type	Spectral Bandpass	Objective Element	Pixel Size	Brightness Range $B_\odot$
C1	1.1 - 3.0	Internal	Fabry-Perot	Mirror	5.6”	2×10^{-5} - 2×10^{-8}
C2	2.0 - 6.0	External	Broadband	Lens	11.4”	2×10^{-7} - 5×10^{-10}
C3	3.7 - 30	External	Broadband	Lens	56.0”	3×10^{-9} - 1×10^{-11}

Table 3.7: The specifications of the LASCO C1, C2 and C3 coronagraphs, although C1 was not used in this thesis, it is here for completeness.
(Brueckner, 1995)

poor resolution to have improved resolution since the outer edge of the images usually achieves full resolution.

A full description of the LASCO instrument can be found in Brueckner (1995).

3.2.3 Mauna Loa Solar Observatory MkIII coronameter

Based in Hawaii, the Mauna Loa Solar Observatory (MLSO) principal instrument was the Mark III K-coronameter (MkIII) which observed the solar corona from 1.12 to 2.72 $R_\odot$ in white-light. It had been in operation since 1980 and provided a consistent and unique dataset of low coronal white-light observations. The instrument ran for approximately six hours a day and could generate around 20 images per hour making it a useful tool for detecting CMEs as they erupt from the Sun (Worster, 1998). MkIII data were used in this thesis to construct synoptic maps of the white-light corona. The IPS observations were then mapped onto these synoptic maps so that estimates of where multiple streams detected in the IPS observations lay along their respective raypaths could be ascertained (as previously described in this chapter). The MkIII was decomissioned on 30 September 1999.

3.2.4 Synoptic maps

Synoptic (“Carrington”) maps are an effective way of presenting an overview of activity and evolution in the corona over a solar rotation (a little over 27 days). In terms of the

LASCO instrument (although constructed in similar ways with the SXT, EIT and Mauna Loa MkIII instruments), they are constructed from many individual C2 or C3 images (around 340 per rotation) by extracting from each image a slice of each of the limbs of the Sun at a set distance (either the East or the West limb and typically at $5\,R_\odot$ from disc centre using the C2 coronagraph for this thesis). The slices are then assembled into a time-reversed sequence. For each of the slices, 181 values of brightness can be assigned and the slices are inserted as columns in a 360×181 or 720×181 array. If one or more of the columns are skipped, then there is interpolation from the last column.

At solar minimum, the picture is quite clear as structures are relatively long lived. Streamer belts and coronal holes can be easily identified, as seen in figure 3.18, an example of solar minimum of LASCO C2 East and West limbs at $2.5\,R_\odot$, $3.0\,R_\odot$ and $4.5\,R_\odot$. The wispy arc-like features on the white-light maps are projection effects whereby individual structures move to higher or lower apparent latitudes as they rotate away from or toward the plane of the sky. Discontinuities in the streamer belts are caused by longitudinal variations in the features themselves.

An example of LASCO C2 East and West limbs at $2.5\,R_\odot$, $3.0\,R_\odot$ and $4.5\,R_\odot$, can be seen in figure 3.19 during solar maximum.

The important features to note with regards to these maps is that the time-frame moves from right-to-left and covers 27.3 days which is the time of one Carrington rotation of the Sun's equator as viewed from the Earth/L_1-Point. White bars at the top of the map are an indication of missing data. Horizontal streaks may be due to interpolation and occurs when a column in the construction of the map is completely missing. In addition, data gaps over 1.5 days long are filled with a constant value. Coronal Mass Ejections (CMEs) can also be identified on the maps as discontinuities and/or vertical stripes. However, it is important to note that small CMEs may not be obvious in the Carrington maps. When looking at streamer structure, the same features are often apparent on both limbs but they

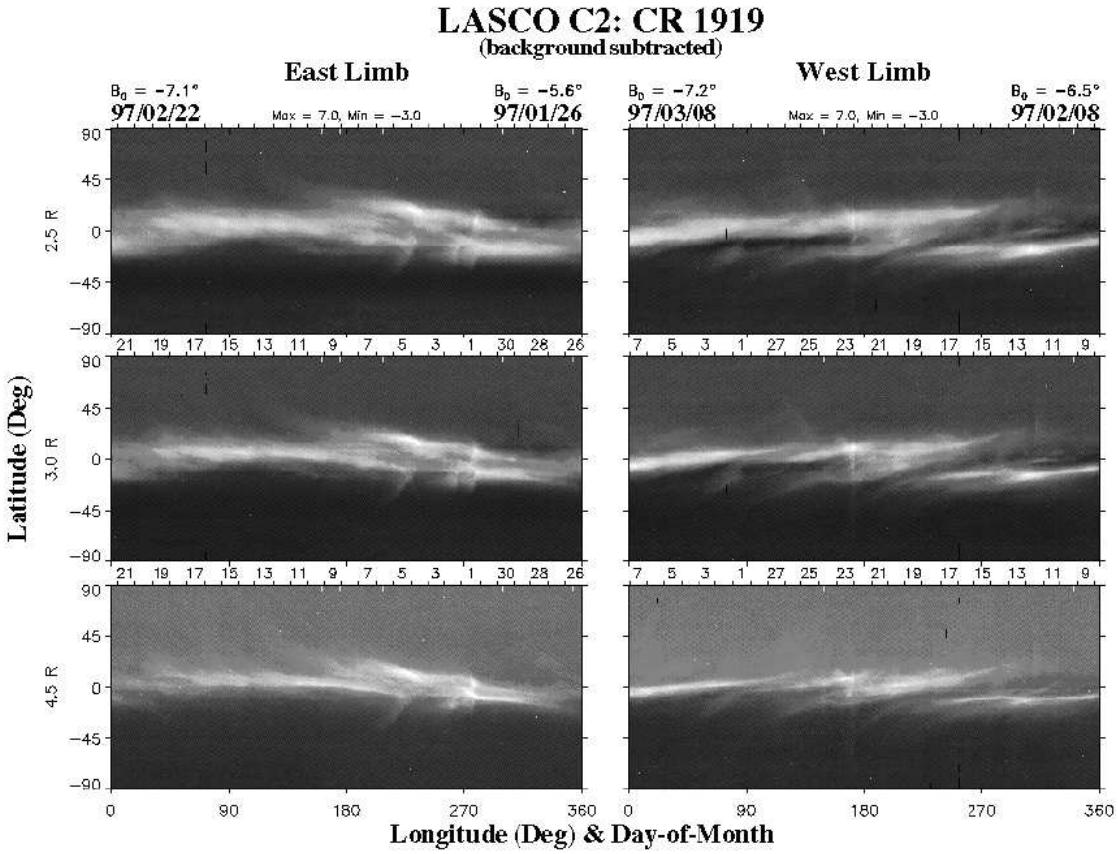

Figure 3.18: Figure showing an example of LASCO C2 synoptic ("Carrington") maps taken from Carrington rotation 1919 of the East and West limbs at $2.5\,R_\odot$, $3.0\,R_\odot$ and $4.5\,R_\odot$, during solar minimum. Figure is courtesy of the SOHO|LASCO Consortium, http://lasco-www.nrl.navy.mil/carr_maps.

also often evolve on time scales less than the approximate 14 days, half a solar rotation as viewed from the L_1-point, between the East and West limb images. At solar maximum, the coronal structure changes on timescales less than 27 days making meaningful reconstruction much more difficult.

Further information on the construction of these maps an their limitations can be found in Wang *et al.* (1997) and at http://lasco-www.nrl.navy.mil/carr_map/agu2000.htm where there is also a poster about synoptic maps from the LASCO and EIT instruments. The white-light maps can be obtained from http://lasco-www.nrl.navy.mil/carr_maps.

A Fortran-77 mapping program created by W. A. Coles, R. R. Grall and M. Klingle-

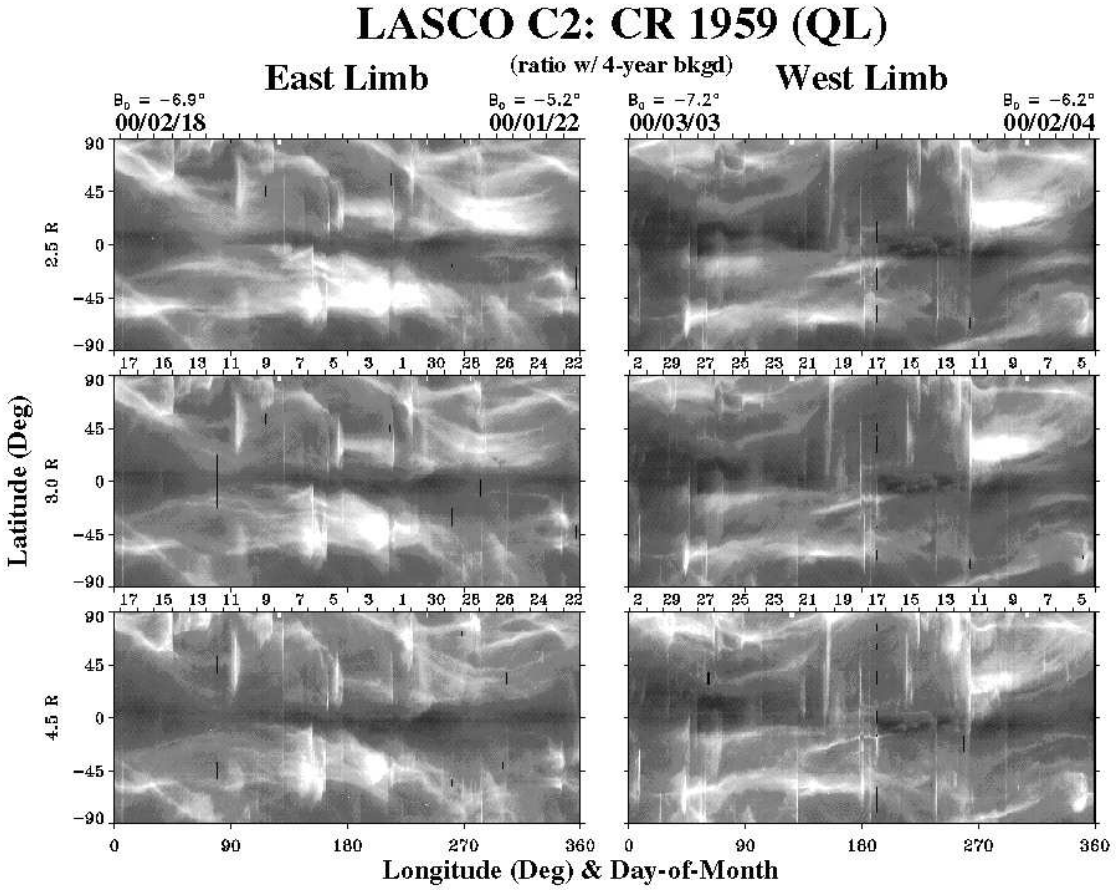

Figure 3.19: Figure showing an example of LASCO C2 synoptic ("Carrington") maps taken from Carrington rotation 1959 of the East and West limbs at $2.5\,R_{\odot}$, $3.0\,R_{\odot}$ and $4.5\,R_{\odot}$, during solar maximum. Figure is courtesy of the SOHO|LASCO Consortium, http://lasco-www.nrl.navy.mil/carr_maps.

smith of UCSD (and subsequently modified at UWA), and an IDL visualisation routine (Canals, 2002) are used to map back the IPS line-of-sight onto the synoptic map at a specified distance (with the exception of Mauna Loa MkIII data which was incorporated into the Fortran-77 program and the raypaths mapped to $1.7\,R_{\odot}$ for the purpose of this thesis), usually the height at which the synoptic map was taken, e.g. $5.0\,R_{\odot}$ in the case of SOHO|LASCO data in this thesis. These are then used to identify the contributions toward the observation from slow and fast wind flow. In the weak scattering model discussed earlier, a region of fast flow flanked by slow flow can be modelled or vice-versa. During solar minimum, the first scenario is quite often the case as the ends of the IPS raypath are often mapped back to the streamer belt at the equator, and the P-Point and

surrounding 70° or so of the raypath have solar wind originating from the polar coronal holes passing through it. The two angles, θ_{in} and θ_{out} (defined earlier), are obtained from this mapping back of the IPS raypath. The angle θ_{in} is defined as the angle between the point of closest approach and the edge of the cone of fast flow toward the Earth, and θ_{out} is defined as the angle between the point of closest approach and edge of fast flow cone away from the Earth - again as previously discussed. Angles toward the Earth are defined as being negative, and angles away from earth are defined as being positive. The angles obtained are then used in the analysis program, which has been described previously in this chapter. It is desirable to use white-light synoptic maps further out from the Sun than those of the Mauna Loa MkIII coronagraph since the solar wind and inner corona show evidence of changes in structure close-in to the Sun so the SOHO|LASCO C2 maps at $5.0R_{\odot}$ were used preferentially when available.

3.3 In-situ measurements

There are a large number of instruments available on spacecraft around 1 AU and outward from the Sun that are currently capable of taking in-situ measurements of the interplanetary medium and thus the solar wind. The spacecraft that have been used at some point during this thesis that are capable of recording in-situ measurements are Wind and Ulysses. The Advanced Composition Explorer (ACE) spacecraft data were also looked at, but never incorporated into this thesis.

3.3.1 Wind - SWE

The Wind spacecraft was the first of two NASA spacecraft in the Global Geospace Science and is part of the International Solar-Terrestrial Physics (ISTP) initiative. It was launched on 1 November 1994 and was positioned sun-ward in a multiple double-lunar swing-by orbit that had a maximum apogee of around 250 R_{Earth} during the first two years of its operation, followed by petal orbits from April 1998 to April 1999. It then proceeded out to a halo orbit around the L_1 point in February 2003. The instruments on

board Wind are used for in-situ measurements.

The Solar Wind Experiment (SWE) instrument consists of five integrated sensor boxes and is used to measure ions and electrons in the solar wind and the foreshock regions (particles whose energies are in the keV range). Using these measurements, one can deduce values for the solar wind velocity, density, temperature and heat flux. Measurements made in the foreshock region will contribute to understanding the structure of the bow shock. Also, measurements of ions and electrons with their velocity distributions can help reveal the vital role they have in the transfer of mass, energy and momentum from the Sun to 1 AU. (Taken from http://www-istp.gsfc.nasa.gov/istp/wind/wind_inst.html, January 2005)

These data were used in making comparisons with IPS data mapped out to around 1 AU. It was the hourly averaged solar wind velocity data that were used. These data were used as a point of comparison with the detected IPS velocity estimates for the study of looking at interaction regions in the solar wind in chapter 4 of this thesis.

3.3.2 Ulysses - SWOOPS

The Ulysses spacecraft (a picture of which can be seen while in Earth orbit in figure 2.18 in chapter 2 of this thesis), as previously mentioned, weighing 367 kg, is used for in-situ measurements of the solar wind in a large orbit over the poles of the Sun as can be seen in figure 3.20 which shows where the Ulysses spacecraft was during its first polar orbit. The spacecraft was launched on 6 October 1990, by NASA's Space Shuttle Discovery. It reached Jupiter on 8 February 1992 and used Jupiter's high gravity to cancel the excess momentum acquired from the Earth and to accelerate, re-orient, and then transfer its orbit to the polar orbit under the Sun with a period of 6.2 years. Ulysses passed beneath the Sun for the first time on 13 September 1994 and due to the nature of a Keplerian orbit, is came up passed the Sun's equator and then over the North pole on 31 July 1995.

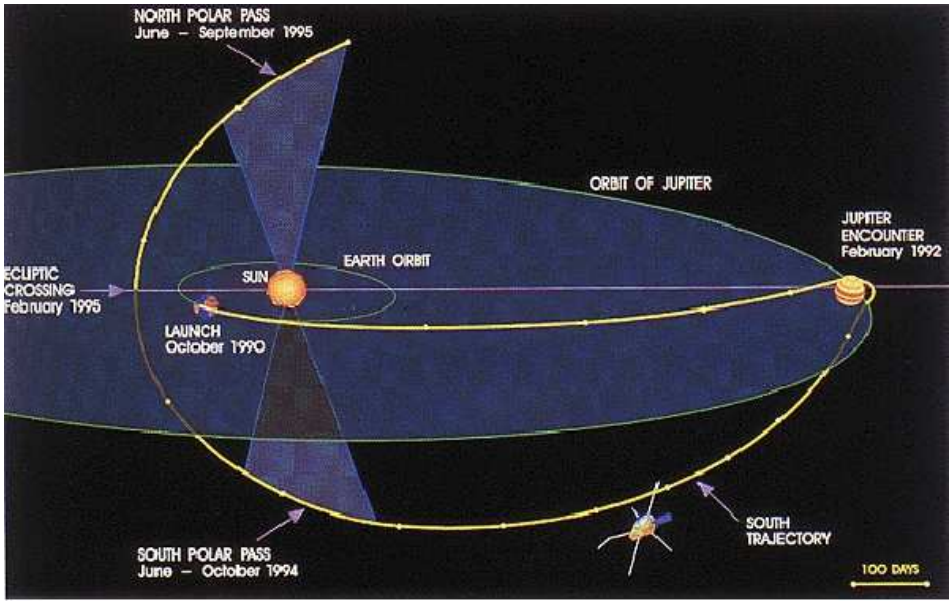

Figure 3.20: The Ulysses spacecraft first polar orbit showing the dates of where it was throughout its first pass over the poles of the Sun.
(Taken from http://www.astro.uni-bonn.de/~mbird/ULS_public_html/sce_uls_frame.html, May 2006)

Ulysses' primary objective is to ascertain a three-dimensional (3D) overall picture of the heliosphere. The instruments on board make measurements of fundamental parameters as a function of distance from the Sun and solar latitude. These parameters include measurements of the solar wind speed, the magnetic field of the solar wind, the composition of the solar wind, and the amount of cosmic rays in the solar wind with the variation of the solar cycle (Lang, 2001). A more detailed discussion of Ulysses and its instruments can be found in Wenzel *et al.* (1992).

The Solar Wind Observations Over the Poles of the Sun (SWOOPS) instrument was designed to investigate the bulk flow parameters and internal structure of the solar wind with changing solar latitude. It investigated the gradients in velocity of the solar wind, particularly the fast solar wind and also the inter-changeability of the solar wind at the interface between fast and slow streams. SWOOPS showed that there was a gradient in fast solar wind velocity over the poles of the Sun (e.g. McComas *et al.*, 2000).

These data were used in making comparisons with IPS data mapped out to the distance at which Ulysses was at during the IPS observation. It was the hourly averaged solar wind ion velocity data that was used. These data were used as a point of comparison with the detected IPS velocity estimates for the study of looking at interaction regions in the solar wind in chapter 4 of this thesis, and also for looking at the large-scale structure of the fast solar wind (since Ulysses is unique in that it provides the only out-of-ecliptic in-situ measurements) in chapter 5 of this thesis.

Chapter 4

Boundary regions between fast and slow streams in the solar wind

This chapter builds on the preliminary work on interaction regions carried out by Canals (2002). It looks at the detection of compression/rarefaction regions and shears that can be seen in IPS data and uses these with Wind and Ulysses hourly averaged velocity data. The study involved the mapping of IPS data down onto white-light maps of the Sun's corona at $5\,R_{\odot}$ to obtain the stream boundaries along the IPS raypath (as described in chapter 3 of this thesis). Mapping, by use of any method, introduces some uncertainties into the new positioning of an observation. The most serious of these uncertainties being tracing measurements made at large heliocentric distances back to a reference point or IPS distance as had been done in the past (e.g. Breen *et al.*, 1998, 2002c). Solar wind streams of different outflow velocities can interact while travelling through the interplanetary medium and therefore evidence of the original streams gets smoothed out by the time they reach such large distances from the Sun. The improved upon mapping method from this was initially looked at by Canals (2002). This was to map the IPS raypath out to in-situ distances of the Wind and Ulysses spacecraft respectively, since the solar wind flows outward, so it is better to track with the flow than trying to track what may be highly evolved structure back to the Sun, in order to look to see if interaction develops. This method was first suggested by T. Hoeksema, private communication, 2001; cited

in Canals (2002). The parts of the raypath were mapped at fast and slow velocities of the fitted fast and slow estimates from the weak scattering model (described in chapter 3 of this thesis) out to in-situ distances along their respective Parker spirals. This was done to look for overlap (and the type of overlap - if any) between the sections of the raypath to see if compression and/or rarefaction regions occur; as in a classical Co-rotating Interaction Region (CIR) described in chapter 1 of this thesis; or if there is a possibility of shear occurring. Canals (2002) developed this method and looked briefly at some preliminary case studies which were also considered in this investigation of compression and interaction between streams of solar wind at in-situ distances.

In this chapter, the approach of mapping the IPS observations outward is extended to consider most of the potential interaction observations in the 10 year period of the EISCAT IPS data between 1994 and 2003 inclusive, along with a 2002 extremely long-baseline observation of an interaction region (Bisi *et al.*, 2005) described briefly in this chapter and in full in chapter 6 of this thesis. The approach has moved away from a case study by case study description to a look at the overall interaction within the solar wind, with example case studies of a CIR and a shear layer detection in the IPS data. Coronal Mass Ejections (CMEs) which can also cause intermediate velocities and compression/shock regions on a much shorter-lived time-scale (Canals, 2002) are not included in this study, only relatively long-lived phenomenon are studied. These data are summarised in tables after the example case study of each of the phenomenon investigated in this chapter.

4.1 Interaction regions in general

The importance of this approach of mapping the IPS raypaths out to the in-situ distances is that it provides a much better indication of the region of interaction in the raypath and thus the distance from the Sun. It therefore provides a much more robust way of looking at how CIRs and other forms of long-lived interaction develop than that shown in Breen *et al.* (1996b, 1997a, 1998). Provided that interaction can be found in the ray-

path, high frequency IPS measurements, from for example the EISCAT system (as used here), can be used to detect the early formation of compression regions or shear between fast and slow streams. As IPS measurements are sensitive to the approximate square of the electron density, they have a much greater sensitivity to changes in solar wind than for example, white-light measurements such as those by the Solar Mass Ejection Imager (SMEI) instrument. IPS measurements should therefore be able to detect compression regions closer-in to the Sun than other techniques that are available at present.

Intermediate velocities have been seen in Ulysses data (e.g. while transiting through stream transitions) and in EISCAT IPS data for many years (e.g. Breen *et al.*, 1997b; Forsyth & Gosling, 2001). Interaction regions occur in the solar wind due to a fast wind being carried under the slow wind from the rotation of the Sun and this is mostly characterised by intermediate velocities. This is most-common when a non-polar coronal hole has formed or when there is an equatorward extension of a polar coronal hole. This type of interaction is commonly known as a co-rotating interaction region since it is caused by the rotation of the Sun and the difference in spiral angles of each of the streams of solar wind due to their respective different velocities. The slow wind has a much tighter spiral than the fast wind since it does not travel as far from the Sun in a the same amount of time as the fast wind while the Sun rotates at a constant rate. In a similar way, shear layers between streams are caused where the fast stream is "sliding" past the slow stream at an adjacent latitude (but not the same latitude as is the case with CIRs). This is not interaction per se, but interaction is possible along the shear itself on the stream-stream boundary and can lead again to intermediate velocities being detected. This is particularly the case in IPS observations where there is a large proportion of the raypath passing through the boundary region between the shearing streams.

4.1.1 Data selection

The initial filtering of the data, starting with well over 2000 IPS observations to search through, was completed by looking at the first stage of data analysis. This stage gives

a view of the auto- and cross-correlation spectra (as described in detail in chapter 3) for signs of intermediate velocities and/or more than one stream in the raypath that is quite close to the velocity of the dominant stream crossing the IPS raypath. In other words, cases where there is no clear single stream or clear non-interacting fast and slow streams. Cases that were thought to contain more than one stream, one of which being an intermediate velocity stream, i.e. having a mid-velocity plane-of-sky value between $400\,\mathrm{km\,s^{-1}}$ and $600\,\mathrm{km\,s^{-1}}$, were also selected as possible CIR/shear layer cases from the data between 1994 and 2003 inclusive. At this stage, around 325 IPS observations were identified as fulfilling these criteria. In addition to this, cases where the same source or a source at a similar latitude and/or distance was observed around the same time as these 325 or so observations were also considered.

The next stage was to look more closely at the data and to remove those observations that were possible CME candidates including those that showed signs of not remaining in the weak scattering regime (described in chapter 2). A closer look at the shape of the cross-correlation functions was undertaken to check for observations that were showing signs of intermediate velocity, but not showing more than one stream, i.e. not having any asymmetry in the shape of the cross-correlation function. These too were removed from the list of possible cases to be investigated. An intermediate velocity observation of a single stream will not be able to show compression/rarefaction or shear when mapped out to in-situ distances since there is only a single stream velocity in the IPS observation. Therefore, different regions of the raypath will not overlap when mapped to in-situ distances since the whole raypath would be mapped at a constant velocity. Observations that still displayed signs of noise after the noise filtering in the first stage of data analysis was undertaken were also eliminated from the investigation. This then left around 300 observations of “clean” data that showed signs of intermediate velocity with the possibility of there being more than one stream, and which had in some cases a repeated (or several repeated) and/or similar observation(s) around the same time and/or position as the main identified possible interaction/shear IPS observation. This is more than can be

completely covered in a single Ph.D. thesis chapter and it should also be noted that during this investigation, some of the fast wind dominated IPS observations around the solar minimum were found to have structure within the fast wind (Bisi *et al.*, 2006). These were looked into as a separate study continuing on from this investigation and are discussed in chapter 5 of this thesis.

The next stage of the investigation was to fit the best cases (those deemed most-likely to show signs of compression/rarefaction/interaction and thus help to improve this method and avoiding those which have had substantial investigation previously) with the weak scattering model and then ballistically map out from the IPS distance the streams of the solar wind that crossed the IPS raypath at their fitted velocities to the Ulysses and Wind respective distances, after the use of white-light maps to constrain the stream boundaries along the IPS raypath as described in detail in chapter 3.

4.2 CIR development

As described in chapter 1, CIRs are familiar from spacecraft observations and are characterised in the main by a dense region of compression at the leading edge of the fast stream as it starts to interact and push into the trailing edge of the preceding slow stream. This compression can cause enhanced scintillation in an IPS observation of a CIR-formation region. At the trailing edge of the fast stream, a low density rarefaction region occurs where the flows diverge due to the following slow stream having a tighter spiral angle because of its lower velocity, and the fast stream seemingly pulling away from it in front. The degree of compression steepens as the angle of the respective stream angles gets greater, i.e. a greater difference in the velocities of the two interacting streams. At large distances from the Sun, shocks can develop at the leading edge of the fast stream, as described in chapter 1 of this thesis and in more detail in Forsyth & Gosling (2001). At the EISCAT IPS observation distances however (typically inside 120 $R_{\odot}$), the angle between the spirals is not as great as it is at the in-situ distances of spacecraft such as Ulysses (typ-

ically 1.4 AU-5.0 AU). Therefore, the effects are not as dramatic in IPS data since IPS observations generally reveal the onset of the compression region that can develop into a CIR near to and outside of 1 AU in cases such as these.

4.2.1 CIR case study

The CIR case study is taken from the dates 20000520 to 20000525 (inclusive) using the source 0318+164. These dates include the two preliminary case studies from 2000 carried out in Canals (2002) of 20000521 and 20000524 with this source. These are roughly equatorial observations based in the southern hemisphere ranging from -6.2° latitude at a P-Point distance of 29.7 $R_\odot$ on 20000520 to -1.3° latitude at a P-Point distance of 47.1 $R_\odot$ on 20000525. All six observations were taken off the East limb of the Sun during Carrington rotation 1963 and were mapped onto the Carrington rotation map from LASCO C2 data at 5 $R_\odot$. An example can be seen in terms of one of the middle observations, 20000522, in the combined map in figure 4.1. This displays the IPS raypath ballistically mapped; onto the white-light synoptic map as described in chapter 3 (top panel), to the distance of the Wind spacecraft from the Sun (middle panel), to the distance of the Ulysses spacecraft from the Sun (bottom panel). Also shown by the coloured strips in the figure are the radial velocity components of solar wind outflow measured by the Wind spacecraft (around 0° latitude in the middle panel) and by the Ulysses spacecraft (around -57° latitude in the bottom panel).

As can be seen in figure 4.1, when the observation is mapped out to the distance of the Wind spacecraft, it provides excellent correlation with the velocities detected by Wind and their positioning in latitude and longitude. Compression regions can be seen both at the distance of Wind and at the distance of Ulysses. It should be noted however, that in reality (contrary to what the maps show) the two streams would not overlap as they do here as two discrete streams since interaction would have taken place. The maps are clear illustrations however of if and where streams can interact and at what distances can

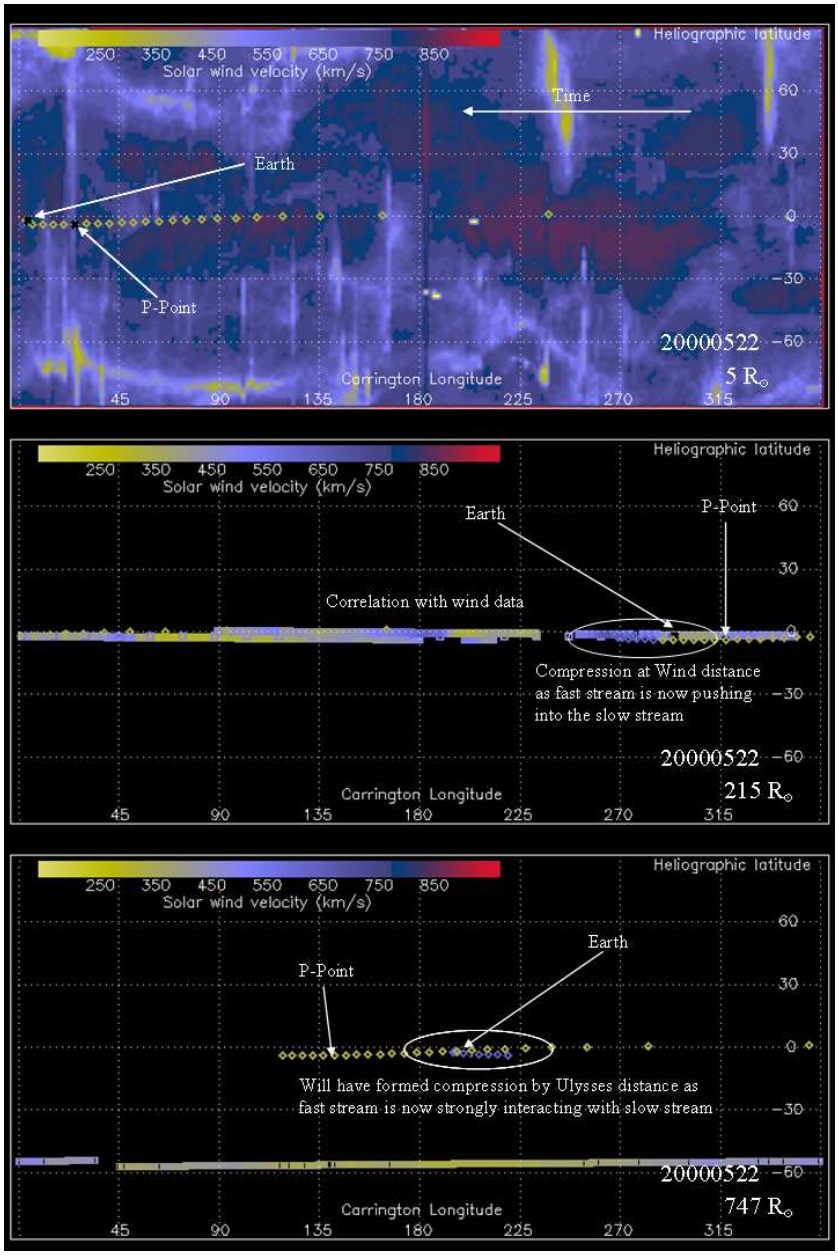

Figure 4.1: Observation of a CIR with source 0318+164 on 20000522 mapped down at IPS detected stream velocities onto the LASCO C2 white-light synoptic map in the top panel, and then mapped out from IPS distance out to the Wind (centre panel) and Ulysses (bottom panel) distances respectively.

the interaction expect to be seen.

Figures 4.2 and 4.3 show successively the six observations of 0318+164 through the dates 20000520 to 20000525 consecutively at a mapped distance to the Wind spacecraft. Marked on each of them are regions of compression, interaction and rarefaction. As

the days progress, IPS observations start by detecting both compression and rarefaction regions when mapped onto the Wind data at velocities comparable to those detected by Wind on 20000520. On 20000521 however, compression is no longer detected since the streams have evolved, but a rarefaction region is still seen. By 20000522, the rarefaction disappears and compression is once again detected - but this time at a different Longitude than before. This seems to suggest that there may be multiple stream interactions happening or that this is a long-lived event close to the Sun (in comparison with traditional CIRs outside of 1 AU). On all remaining days, 20000523 to 20000525 inclusive, the mapped IPS data continues to show good correlation with the velocities detected by the Wind spacecraft and also continues to observe compression at approximately the same position in the sky suggesting a long-lived structure of a CIR due to the compression of the streams and the length of the event.

Figures 4.4 and 4.5 show successively the six observations of 0318+164 through the dates 20000520 to 20000525 consecutively at a mapped distance to the Ulysses spacecraft. Marked on each of them are regions of compression, interaction, rarefaction, and cases where the fast stream is seen to move under the slow stream - which in reality is likely to mean strong compression at Ulysses distances or even shocks. As the days progress, IPS observations start by detecting movement of the fast stream under the slow stream when mapped onto the Ulysses data at their respective velocities. No direct comparison of velocities of the Ulysses spacecraft can be made since it does not achieve a latitude similar to that of the IPS observations on any of the six days of observing with source 0318+164. On 20000521 however, movement of the fast stream under the slow is no longer detected since the streams have evolved, but a large rarefaction region is seen. This is comparable to what occurs when this observation is mapped to the Wind spacecraft distance. By 20000522, the rarefaction disappears and compression is now detected (again as it was at the distance of Wind). By 20000523, movement of the fast stream can be seen under the slow once more, with strong compression and therefore in reality much interaction on 20000524 and again on 20000525. The mapped IPS data at

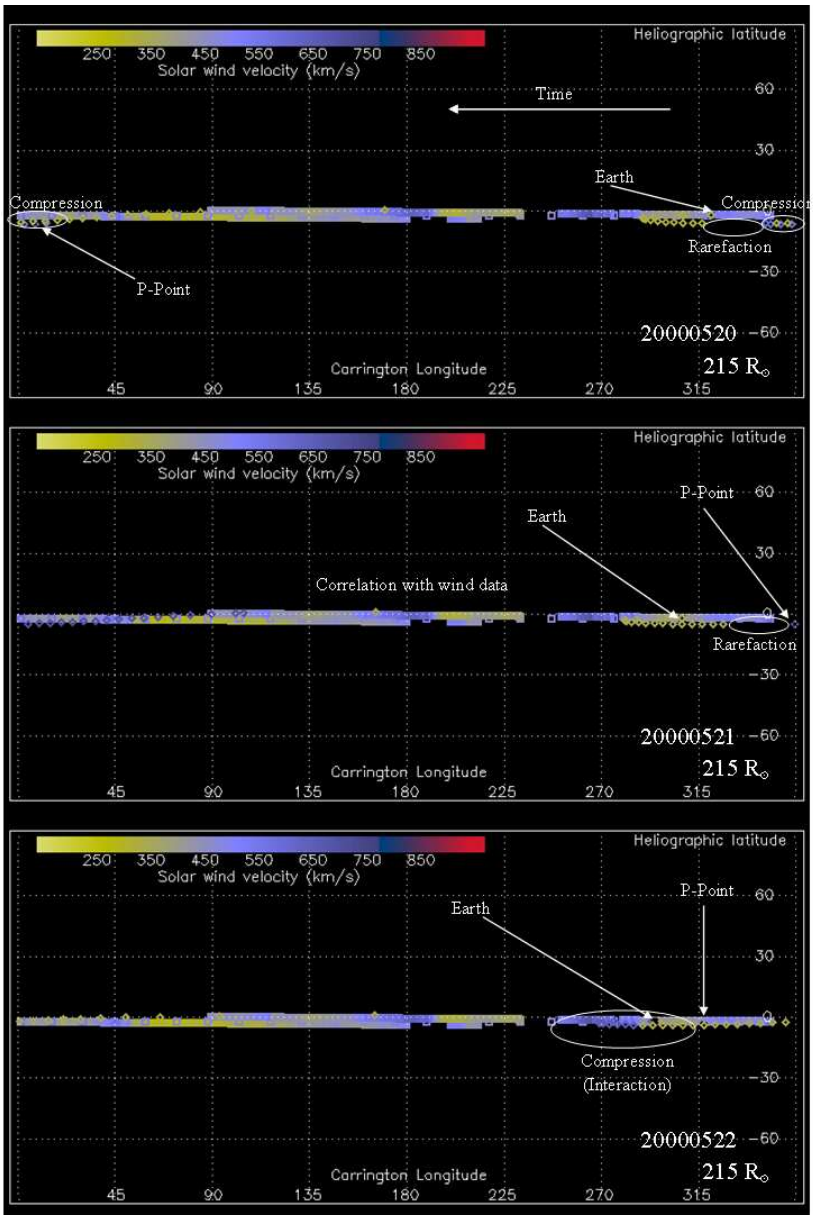

Figure 4.2: Figure showing the IPS raypath of 0318+164 mapped to the distance of the Wind spacecraft on dates (from top to bottom) 20000520 to 20000522 along with the Wind velocity data for Carrington rotation 1963. An explanation of the figure can be found in the text.

Ulysses distance continues to show good correlation with the features seen at the distance of Wind throughout this six day period suggesting that not only was this a long-lived event at Wind, the same event continued out to Ulysses distance and probably beyond as would be expected from a CIR since they are generally very large long-lived structures (e.g. Gosling *et al.*, 1978a; Forsyth & Gosling, 2001).

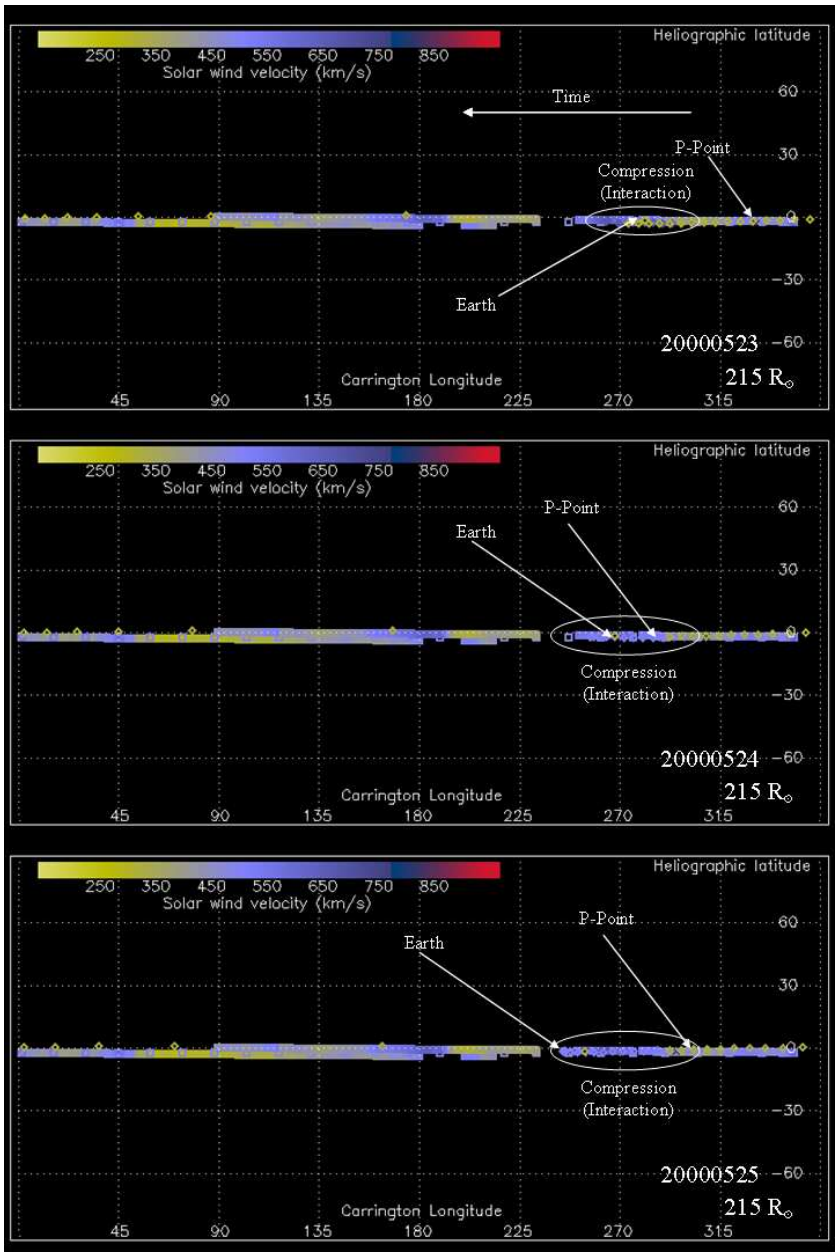

Figure 4.3: Figure showing the IPS raypath of 0318+164 mapped to the distance of the Wind spacecraft on dates (from top to bottom) 20000523 to 20000525 along with the Wind velocity data for Carrington rotation 1963. An explanation of the figure can be found in the text.

This case study of 0318+164 over the six days shows what has already been known for some time with respect the the scale and long-length of a CIR, but also shows how strongly a CIR can be picked up at IPS distances (in this case ~29 $R_\odot$-47 $R_\odot$) with intermediate/fast stream velocities ranging from 528 km s^{-1} to 716 km s^{-1}, and a more stable slow stream velocity range of 316 km s^{-1} to 363 km s^{-1}. Clear signs of compression and rarefaction

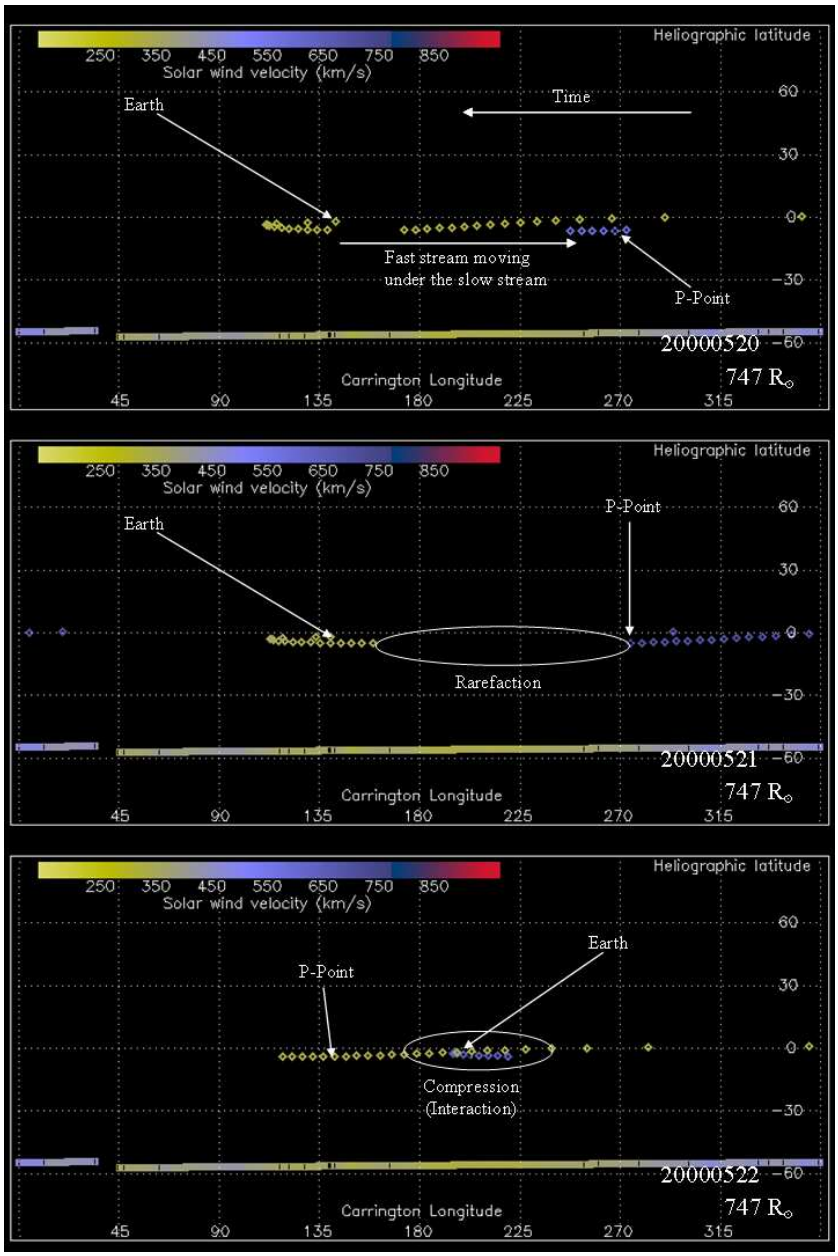

Figure 4.4: Figure showing the IPS raypath of 0318+164 mapped to the distance of the Ulysses spacecraft on dates (from top to bottom) 20000520 to 20000522 along with the Ulysses velocity data for Carrington rotation 1963. An explanation of the figure can be found in the text.

can be seen at both Wind and Ulysses distances as well as good correlation with velocity measurements of the respective spacecraft. The fast stream being carried under the slow stream is also seen at Ulysses distances in particular, but remembering that this is not a true representation since the fast and slow streams where this occurs will no longer exist at this distance as interaction would have taken place - a downfall of the mapping method

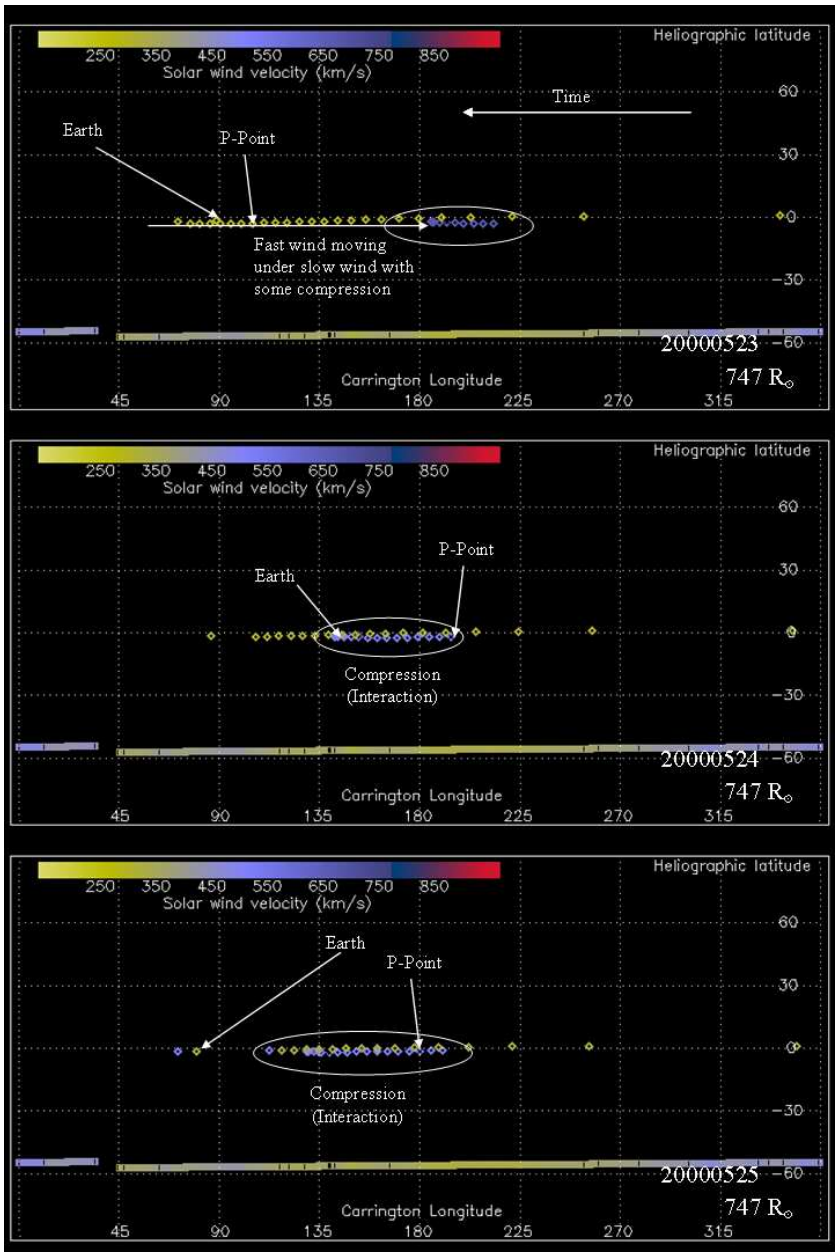

Figure 4.5: Figure showing the IPS raypath of 0318+164 mapped to the distance of the Ulysses spacecraft on dates (from top to bottom) 20000523 to 20000525 along with the Ulysses velocity data for Carrington rotation 1963. An explanation of the figure can be found in the text.

employed since it only allows the overlap and mixing of streams.

From this case study, it is easy to adopt this method and apply it to other cases where interaction is thought to occur between streams and look for these features at the mapped distances to discern whether or not an observation of interaction is that of a CIR.

4.2.2 CIR EISCAT IPS observations summary

The same method that was used for the case study was then applied to other possible CIR cases and the results of the investigation can be seen in table 4.1. This includes all the observations that were looked at in depth during this investigation. Also indicated in the table are those observations where comparison with in-situ data were possible in that they overlapped with it at a similar latitude and a similar same time-frame (the same Carrington rotation was generally used as the time-frame in line with the fact that synoptic maps also cover a single Carrington rotation). In-all, 31 separate observations of CIRs were detected in these IPS data that were mapped to in-situ distances.

4.3 Shear layers

Shear layers are characterised in the main by a region of two streams lying at a very shallow angle (close to parallel latitude) with quite often some interaction detected along the stream-stream boundary. In IPS data, a velocity gradient is often detected but there is no increase in scintillation since generally compression regions do not occur as they do in the case of CIRs. The flows merely slide passed each other by comparison to the compression and rarefaction that occurs in CIR-formation seen in IPS data.

4.3.1 Shear layer case study

The shear layer case study is taken from the dates 19960523 and 19960524 using the source 0431+206. This is a southern hemisphere observation around -18° latitude at a P-Point distance around $25\,R_{\odot}$ on 19960523 and around -20° latitude at a P-Point distance around $21\,R_{\odot}$ on 19960524. Both observations were taken off the East limb of the Sun during Carrington rotation 1909 and were mapped onto the Carrington rotation map from LASCO C2 data at $5\,R_{\odot}$. This can be seen in the combined mapped figures 4.6 and 4.7 displaying the IPS raypath ballistically mapped onto the white-light map, to the distance of the Wind spacecraft along with the Wind velocity data, and to the distance of the Ulysses spacecraft along with the Ulysses velocity data.

EISCAT IPS CIR results						
Date	Source	vfast ($km\,s^{-1}$)	dvparf ($km\,s^{-1}$)	vslow ($km\,s^{-1}$)	dvpars ($km\,s^{-1}$)	Spacecraft Comparison
19950704	0738+177	578.9	126.4	349.9	39.7	None
19950709	0738+177	680.1	267.6	297.3	56.0	None
19990502	0137+331	602.0	4.1	358.0	59.2	None
19990502	0318+164	448.0	0.0	378.0	0.0	Wind
19990503	0137+331	582.2	109.7	414.2	80.7	None
19990503	0318+164	676.0	5.5	312.0	39.8	Wind
19990504	0318+164	682.0	0.0	319.0	0.0	Both
19990505	0318+164	759.0	446.0	326.0	100.9	Both
19990506	0318+164	800.0	0.0	367.0	116.7	Both
19990507	0312+123	800.0	0.0	384.0	67.0	Ulysses
19990510	0336+323	447.8	31.8	317.8	97.9	None
19990515	0319+415	632.0	128.7	289.0	86.7	None
20000514	0319+415	403.0	125.1	295.0	59.1	None
20000518	0321+123	532.0	51.6	288.0	0.0	Wind
20000519	0403+260	506.0	0.0	399.0	173.1	Wind
20000520	0318+164	605.0	73.2	341.0	100.8	Wind
20000521	0318+164	716.0	350.0	363.0	114.0	Wind
20000521	0403+260	555.0	119.8	194.0	61.3	None
20000522	0318+164	668.0	47.5	356.0	94.3	Wind
20000523	0318+164	682.0	135.3	316.0	67.1	Wind
20000523	0431+206	556.0	104.3	283.0	47.9	Wind
20000524	0318+164	529.0	116.0	336.0	21.5	Wind
20000525	0318+164	528.0	0.0	349.0	0.0	Wind
20000527	0432+416	499.0	130.0	365.0	0.0	None
20000907	1042+120	750.0	0.0	365.0	93.8	Wind
20000908	1042+120	435.0	49.8	184.0	66.6	Wind
20000909	1042+120	697.0	163.9	290.0	60.0	Wind
20000910	1150-003	412.0	0.0	316.0	170.6	Wind
20000911	1150-003	423.0	54.5	163.0	19.7	Wind
20010523	0431+206	728.0	0.0	253.0	100.7	Wind
20030430	0318+164	624.0	190.5	244.0	0.0	Wind

Table 4.1: Table showing a summary of the EISCAT IPS CIR results as estimated using the weak scattering model described in chapter 3 where in the same notation; vfast is the estimated velocity of the faster of the two streams, vslow is the estimate of the velocity of the slower of the two streams, and dvparf and dvpars are the estimates of the 'spread' in velocities of each of the respective streams. The spacecraft comparison column indicates whether there was any comparison with either the Wind or Ulysses spacecraft. Generally, where there was a comparison, the IPS velocity results were in-agreement with the spacecraft data.

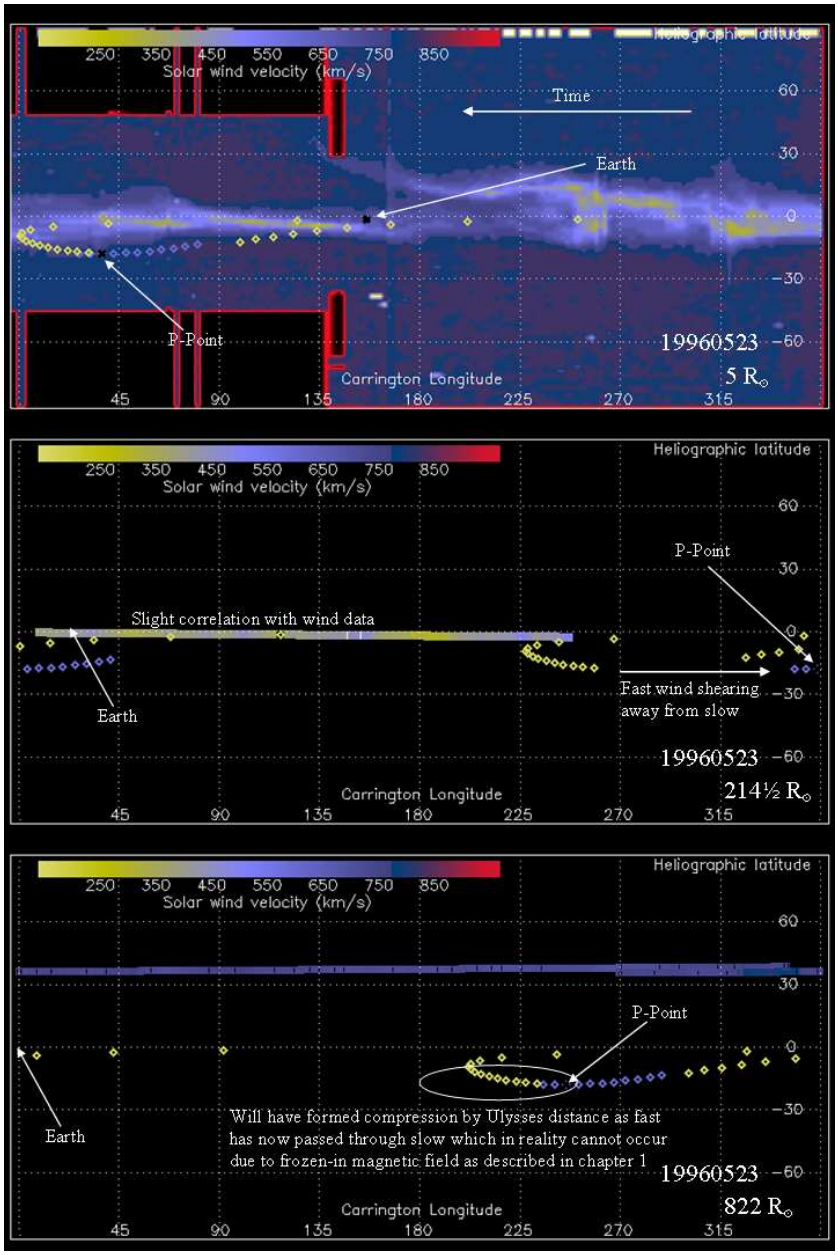

Figure 4.6: Observation of a shear layer with source 0431+206 on 19960523 mapped down at IPS detected stream velocities onto the LASCO C2 white-light synoptic map in the top panel, and then mapped out from IPS distance out to the Wind (centre panel) and Ulysses (bottom panel) distances respectively.

The first day of the two consecutive observations (19960523) has a much greater velocity difference between the streams compared with the second day, and so by the time the streams reach the distance of the Ulysses spacecraft they show signs of compression as the fast has seemingly passed through the slow (which in reality cannot happen because

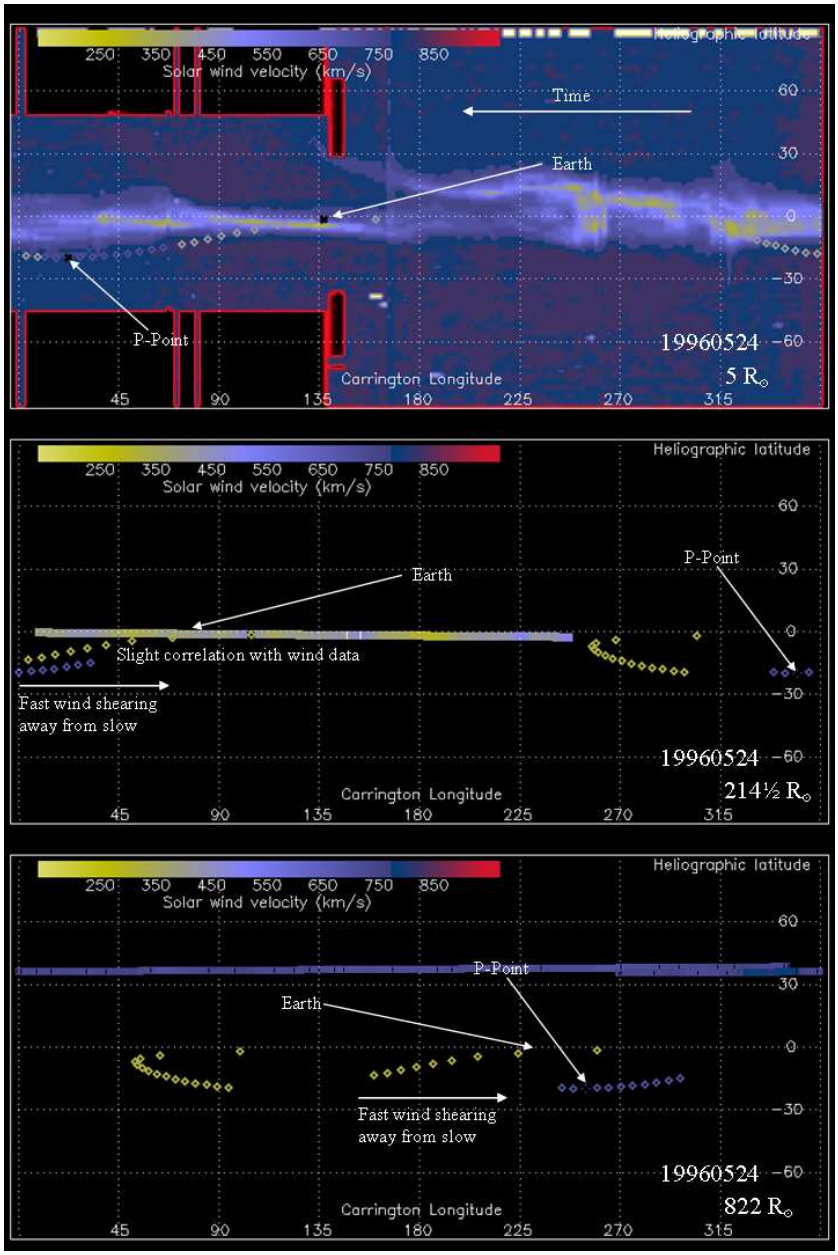

Figure 4.7: Observation of a shear layer with source 0431+206 on 19960524 mapped down at IPS detected stream velocities onto the LASCO C2 white-light synoptic map in the top panel, and then mapped out from IPS distance out to the Wind (centre panel) and Ulysses (bottom panel) distances respectively.

of the "frozen-in" magnetic fields) due to the large difference in Parker spirals. It is likely that by Ulysses distance some sort of interaction would have occurred and the shear may have even started to build into a CIR, although the stream angle may be a little too shallow for this to have occurred - without in-situ data at these latitudes and distance it is difficult

to ascertain exactly what may happen.

The second day of the observation of this source (19960524) shows a faster fast stream with a slow to intermediate velocity second stream. The P-Point of the observation is a little closer-in to the Sun and a little further South in latitude. It has also moved along by a few degrees in longitude from that of the previous day making it lie a little less in the slowest areas of the streamer belt as can be seen from the comparison with the white-light map. Since the slower of the two streams is rather higher in velocity than on the previous day, the spiral angle is not so tightly wound and therefore by the distance of the Ulysses spacecraft it will not have formed compression as on the previous day's observation, but shear is clearly seen.

The small amounts of comparison achieved with the Wind velocity data reveal that velocities for the ends of the raypath are very similar, and where the raypath moves South away from the Wind data where the shear is being detected, the Wind data shows signs of a slow to intermediate velocity around equatorial regions. This is consistent with where the slow to intermediate velocity stream in IPS data on the second day of observing 0431+206 is being detected when mapped to Wind distance but lying just South of the Wind data.

Overall, with the shape of the streamer belt and the positioning of the IPS raypath (particularly that of the central fast stream), this case study over a two day period displays good signs of shear between the streams of solar wind as they evolve out to in-situ distances. Unfortunately, due to the positioning of the source from one day to the next (as with all the cases of shear investigated here which were seen in more than one single observation), it is not possible to work out the latitudinal thickness of this shear as was carried out in Breen *et al.* (1999) using source 1229+020 with other 1996 observations where the source moved through the shear in a latitudinal direction with each consecutive observation. However, this method does provide a solid way of finding cases of shear within the solar wind at IPS distances and in looking at how these develop by in-situ observation

distances.

From this case study, it is easy to adopt this method and apply it to other cases where some interaction is thought to occur between streams or it is thought that the raypath lies along a stream boundary and look for these features at the mapped distances to discern whether or not an observation is of a shear layer.

4.3.2 Shear layer EISCAT IPS observations summary

The same method as used for the case study was applied to other possible shear layer cases and the results of the investigation can be seen in table 4.2. This includes all the observations that were looked at in depth during this investigation. Also indicated, are those where comparison with in-situ data were possible (as with the CIR detections). In all, 21 observations of shear in this investigation were detected in the IPS data when mapped out to in-situ distances. This combining of white-light, IPS, and in-situ data with the method described provides a much improved way at getting information from the IPS data and discerning whether or not a particular observation is that of a shear layer. Many of the observations displayed at least some correlation with spacecraft data and in the most-part were consistent at similar latitudes as shown in the case study example.

4.4 Extremely long-baseline observation

Recent developments in the IPS observing technique have included the use of much more widely separated antennas with separations up to 2000 km in the parallel baseline with EISCAT and the Multi-Element Radio Linked Interferometer Network (MERLIN) based in the United Kingdom (UK) as described in papers by Bisi *et al.* (2005) and Breen *et al.* (2006); and in depth in chapter 6 of this thesis. The difference between time lags for solar wind speed increases as antenna separation increases, improving velocity resolution.

EISCAT IPS shear layer results						
Date	Source	vfast ($km\,s^{-1}$)	dvparf ($km\,s^{-1}$)	vslow ($km\,s^{-1}$)	dvpars ($km\,s^{-1}$)	Spacecraft Comparison
19950709	0741+271	712.0	142.9	447.0	314.0	Ulysses
19950710	0735+331	696.0	147.2	232.0	106.8	Both
19950719	0735+331	786.0	274.8	325.0	0.0	Wind
19960523	0431+206	616.0	172.0	180.0	53.6	Wind
19960524	0431+206	729.0	98.0	429.0	15.7	Wind
19960525	0521+166	690.0	110.7	325.0	0.0	Wind
19960529	0403+260	661.0	239.2	165.0	24.2	Both
19990502	0242+110	742.0	312.8	311.0	171.5	Ulysses
19990502	0321+123	480.0	4.0	338.0	3.2	Ulysses
19990503	0242+110	748.6	316.4	352.9	41.7	Both
19990503	0312+123	638.0	119.5	344.0	42.5	Ulysses
19990508	0321+123	600.0	120.0	306.0	170.9	Both
19990509	0321+123	733.0	310.4	202.0	78.6	Both
19990514	0433+053	555.5	10.8	230.7	0.0	None
19990921	1008+075	620.0	114.6	259.0	32.4	Wind
20000517	0432+416	454.0	170.3	238.0	175.2	Wind
20000519	0321+123	619.0	0.0	393.0	0.0	None
20000520	0403+260	511.0	61.3	365.0	213.0	None
20000526	0319+415	424.0	145.8	234.0	48.9	None
20000911	1120+143	379.0	45.0	295.0	120.6	Wind
20000912	1120+143	397.0	75.9	287.0	167.7	Wind

Table 4.2: Table showing a summary of the EISCAT IPS Shear Layer results as estimated using the weak scattering model described in chapter 3 where in the same notation; vfast is the estimated velocity of the faster of the two streams, vslow is the estimate of the velocity of the slower of the two streams, and dvparf and dvpars are the estimates of the 'spread' in velocities of each of the respective streams. The spacecraft comparison column indicates whether there was any comparison with either the Wind or Ulysses spacecraft. Generally, where there was a comparison, the IPS velocity results were in-agreement with the spacecraft data.

One observation from 20020515 produced a correlation function that showed an intermediate velocity with signs of interaction between two solar wind streams due to its large degree of off-radial (meridional) flow - described in detail in chapter 6 of this thesis and first noted in Bisi *et al.* (2005).

The intermediate velocity IPS observation from 2002, figure 4.8 and repeated as figure 6.3 in chapter 6, displays a clear north-ward deflection of the solar wind outflow. This is considered to be arising from interaction above the leading edge of the coronal hole and could be signs of a CIR or shear layer forming. Further discussions of the observation can be found in chapter 6 of this thesis, where the technique and usage of extremely long-baseline observations is fully described and the data are shown.

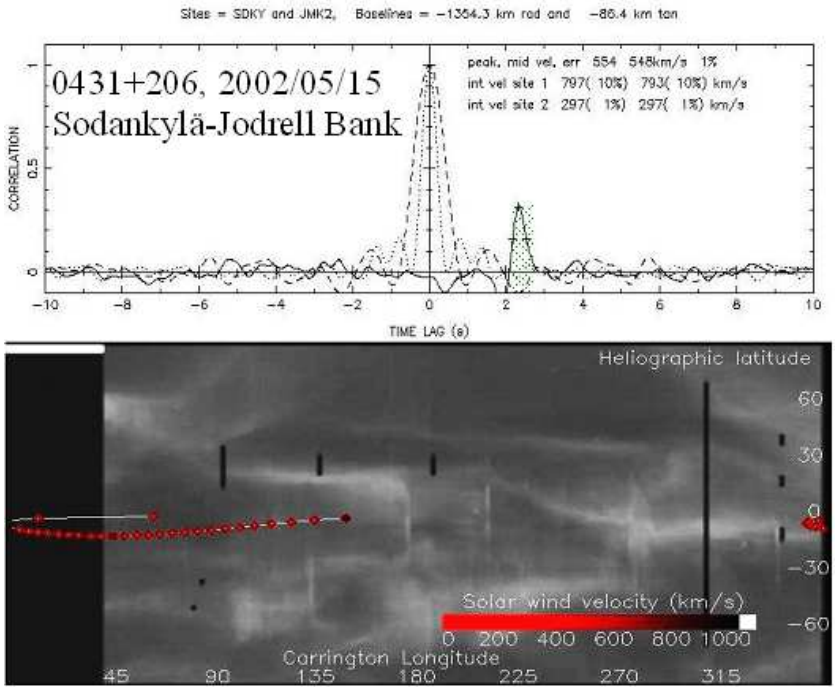

Figure 4.8: Sodankylä-Jodrell Bank observation of 0431+206 on 20020515, example correlation functions and the raypath mapped onto a 5 $R_{\odot}$ SOHO|LASCO East limb synoptic map or Carrington rotation 1989.

4.5 Intermediate velocity EISCAT IPS observations summary

After looking at these data, they clearly illustrate that CIRs and shear layers represent the two extremes of the same phenomenon caused by interaction along the boundary layers between fast and slow streams of the solar wind (Gosling *et al.*, 1978a; Gosling, 1996; Gosling & J.Pizzo, 1999). They quite often depend on the angle between the two respective streams. The closer the angle to a longitudinal line, the more likely it is to form a CIR and the closer the angle to a latitudinal line, the more likely it is to form a shear layer in general. It is difficult to discern between the two without mapping outward since no discernible pattern of velocities or velocity variations comes from either of the two lists.

In terms of the cases where comparison with spacecraft data were possible, good correlation was found between the mapped IPS raypaths and the hourly averaged in-situ velocity measurements over a Carrington rotation. This can be seen especially in the CIR case study given here of successive observations with source 0318+164 over a period of six days from 20000520 to 20000525 inclusive.

The extremely long-baseline observation shows what can be considered to be a "deflection layer" where-by the solar wind is being deflected strongly in a non-radial north-ward meridional direction. This could lead to a "convergence layer" with the slow outflow of solar wind just North of the equator (and hence just North of the interaction) where the deflected stream and slow wind outflow would interact further. However, additional observations by this method are needed of interaction regions to develop this possibility further, which unfortunately relies a little on luck since the extremely long-baseline campaigns are limited to just a few days per year due to the difficulties in obtaining observing time on the very busy system of MERLIN. Further discussion of this case is carried out in chapter 6 of this thesis.

Chapter 5

Two-mode structure of the fast solar wind?

At solar minimum, the solar wind is highly bimodal, characterised by low-density fast flow from large polar coronal holes and high-density slow flow from above the equatorial streamer belt. At solar maximum however, the situation is more complex. The heliosphere is dominated by slow wind with narrow streams of faster flow occurring at any latitude. When observed at 1 AU these streams are generally slower than the polar fast streams observed by Ulysses at solar minimum. Results of flow from the boundary regions of coronal holes using IPS data from EISCAT suggest that the slower "fast" stream velocities seen in-situ at solar maximum may result from the combination of two different physical processes - fast wind from boundary regions being intrinsically slower, and the flow from narrow holes being disproportionately affected by interaction on stream boundaries. This chapter presents a thorough analysis of the previous solar minimum data which was carried out, looking at over 500 different IPS observations around the solar minimum period 1994-1998, together with a limited number of observations made during the approach to solar minimum in 2004.

5.1 Introduction

Throughout the discussions in this chapter, it is defined that the "polar crown flow" is the central region of the polar fast streams (as seen in interplanetary space) and "flank flow" is the region of fast flow between this crown outflow and the equator-ward boundary of the fast stream.

Ulysses observations from the first polar pass (1994-1996) revealed the existence of a latitudinal gradient in the fast wind speed across the polar regions, with the highest velocities measured at the highest latitudes (Phillips *et al.*, 1995; Goldstein *et al.*, 1996; Woch *et al.*, 1997; McComas *et al.*, 2000; Habbal & Woo, 2001). The boundary between the fast and slow outflow measured by Ulysses was located at about $\pm 20°$ around the heliographic equator (Woch *et al.*, 1997).

The most commonly accepted view of the fast wind places its origin within polar coronal holes, at the center of the supergranular cells (Dupree *et al.*, 1996), or at the boundaries of supergranular cells (Hassler *et al.*, 1999). This view then requires a super-radial expansion of the boundaries of the polar coronal holes with radial distance, allowing the fast wind to occupy a significant volume of the heliosphere at solar minimum. However, using white-light, radio ranging and ultraviolet spectroscopic observations in the inner corona, Woo and Habbal (1997) and Habbal and Woo (2001) suggested that the fast wind originates in the quiet Sun as well as in the polar coronal holes, and that the outflow is predominantly radial. In the latter scenario, the fast solar wind from the quiet Sun would be expected to be marginally slower and slightly denser than the outflow from the polar coronal hole.

In this chapter, the use of IPS data from EISCAT (Rishbeth & Williams, 1985; Wannberg *et al.*, 2002) taken during the last solar minimum (1994 through to 1997) supplemented by the Ulysses|SWOOPS (Solar Wind Observations Over the Poles of the Sun), (Bame *et al.*, 1992) instrument, observations from LASCO (Large Angle Spectroscopic COron-

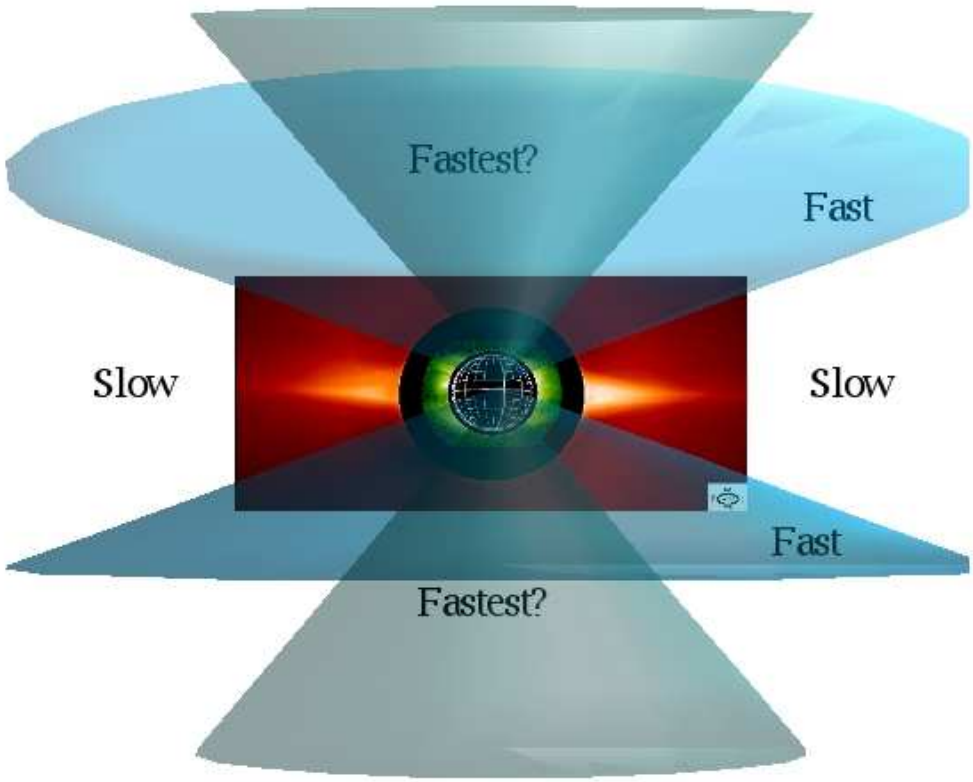

Figure 5.1: Figure showing what a two-mode fast solar wind may look like; with the fastest flow coming from above the coronal holes as seen in Yohhok/SOHO X-ray/EUV data, fast flow coming from above the region of coronal hole seen in Mauna Loa/SOHO white-light data (not including the overlap with the X-ray/EUV data); and the slow flow originating above the streamer belt (again as seen in Mauna Loa/SOHO data). The images here are taken from the SOHO|EIT (green) and SOHO|LASCO (red) instruments with funnels (cones) of what the outflow for each stream may look like.

agraph), (Brueckner *et al.*, 1995) and EIT (Extreme ultra-violet Imaging Telescope) (Delaboudiniere *et al.*, 1995), instruments on SOHO (SOlar and Heliospheric Observatory), the Mauna Loa Mk III coronagraph (Fisher *et al.*, 1981), and the Yohkoh (Ogawara, 1987; Ogawara *et al.*, 1991)|SXT (Soft X-ray Telescope), (Acton *et al.*, 1989) instrument to investigate whether there is evidence of a two-mode structure within the fast solar wind, as originally proposed by Woo and Habbal (1997). Figure 5.1 summarises the overall picture which is being investigated throughout this chapter.

5.2 Initial case study

The study described in this chapter was originally prompted by the results of an EISCAT observation of 0741+271 above the North polar coronal hole on 11 July 1995 as seen in figure 5.2 showing the IPS raypath mapped back (as described in chapter 3) onto the Mauna Loa MkIII white-light map with both the white-light and X-ray coronal hole boundaries marked and the correlation functions for the observation. The source was observed with the EISCAT telescopes of Sodankylä in Finland and Kiruna in Sweden. The distance of the point of closest approach (P-Point) from the Sun was 25.9 $R_\odot$ and the observation commenced at 0336UT. Upon fitting the data (as described in chapter 3 and later in this chapter), it was found that the observation was best represented not by fast and slow flow, but by a two-mode fast wind. The best-fit velocities of each of the streams were 748 km s^{-1} for the faster higher latitude stream, and 686 km s^{-1} for the lower latitude fast stream. To fit the lower fast stream, the spread in velocities required was considerable. This was because the sfit analysis program (weak scattering model) can only fit two components of solar wind velocity so that a small amount of slow solar wind will be present in the low latitude tail of the slower fast wind component. In the best-fit obtained, the narrow "true fast" stream extended 30° on either side of the point of closest approach of the raypath to the Sun, with a slightly slower "quiet Sun" or neighboring stream occupying the remainder of the raypath.

The IPS data were mapped out (as described in chapter 3) to the in-situ distance of wind at 213.9 $R_\odot$ and Ulysses at 402 $R_\odot$, in figures 5.3 and 5.4 respectively. The two streams were plotted at their respective velocities and so cause a slight overlap on one side of the fastest of the two streams, a slight compression, and a slight gap on the other side of the fastest stream, a slight rarefaction. This is more noticeable at Ulysses distance since Ulysses is further out from the Sun, but in this case, it is not an important feature since this study does not concern compression regions as it is looking at a possible bi-modal nature of the fast solar wind. The importance of this observation is the fact that there are two fast streams, and neither of which can be considered as coming strictly from the polar

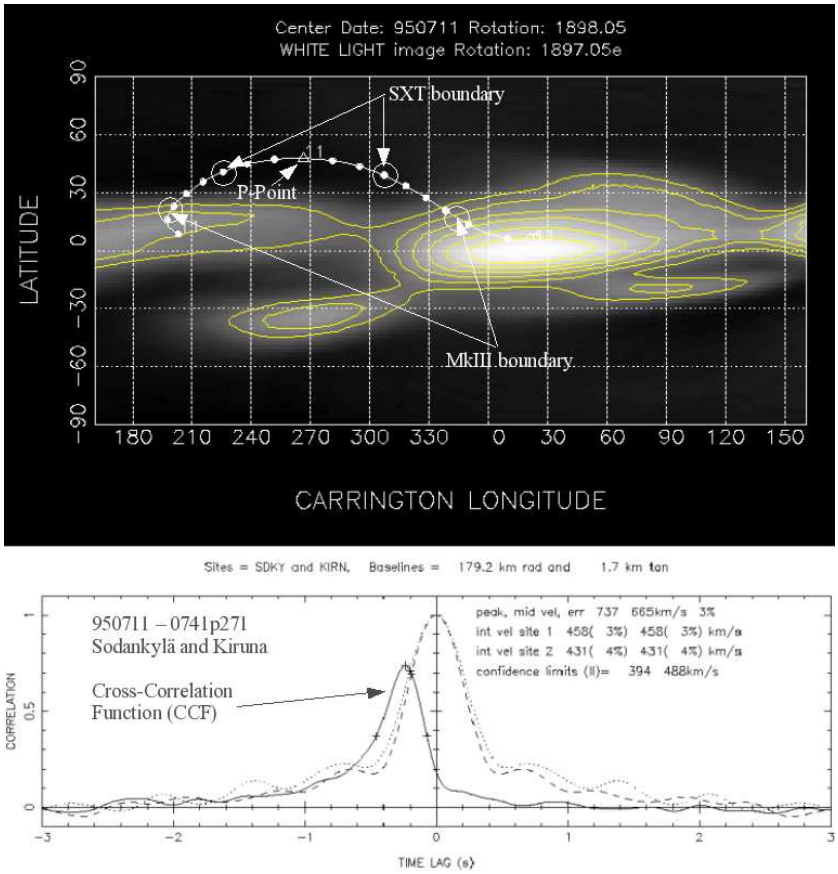

Figure 5.2: The upper part shows a white-light map of the East limb of the Sun, Carrington Rotations 1897-1898 centred on 19950711, constructed using data taken from the Mauna Loa MkIII Coronagraph at 1.7 $R_{\odot}$ with the IPS raypath mapped onto it and both SXT and MkIII coronal hole boundaries circled as well as the P-Point, the point of closest approach of the IPS raypath to the Sun in the plane of the sky. The lower part shows the Cross-Correlation Function of the Sodankylä and Kiruna sites on 19950711 with source 0741+271.

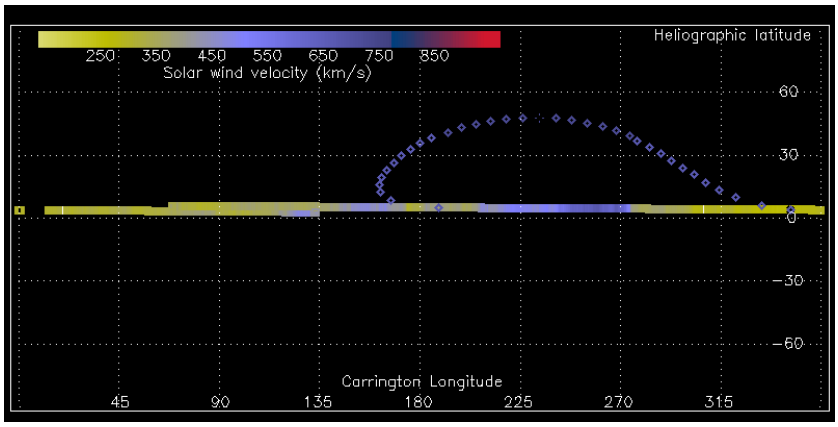

Figure 5.3: IPS data for 0741+271 on 11 July 1995 (19950711) mapped out to Wind's distance from the Sun with the in-situ hourly-averaged radial velocity data as measured by Wind.

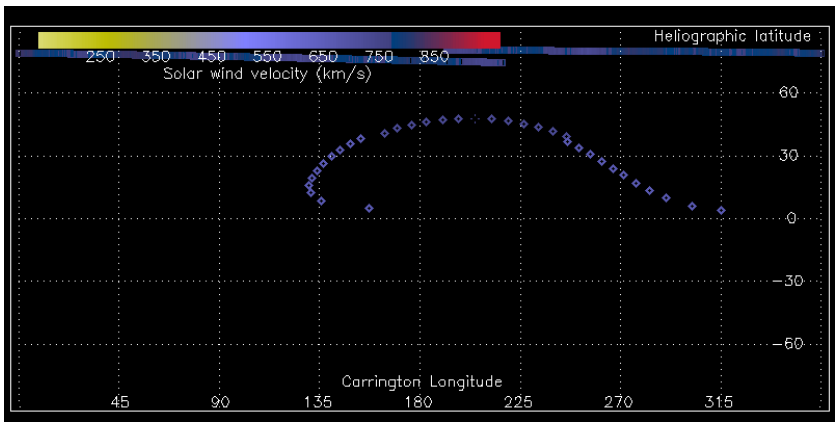

Figure 5.4: IPS data for 0741+271 on 11 July 1995 (19950711) mapped out to Ulysses' distance from the Sun with the in-situ hourly-averaged radial velocity data as measured by Ulysses.

coronal hole. A similar picture was obtained previously when Ulysses was travelling from equatorial regions to higher latitudes; it saw a steady increase in the velocity of the fast solar wind with increasing latitude northward toward the pole from the equator.

The IPS data suggests more than one fast speed stream in the raypath for this case, but further investigation is needed. The faster of the two streams in the central part of the raypath is at a higher latitude than the slower stream either side of it in the raypath. This configuration of faster fast stream with increasing latitude is consistent with the view of the origins of the fast solar wind as discussed in Woo & Habbal (1997a); Habbal *et al.* (1997).

5.3 Data selection

In this study, it was deemed important to consider only low-noise, high-latitude data from fast-wind dominated observations of simple isolated radio sources. Therefore, the criteria for selecting observations described by Canals *et al.* (2002) was adopted, in which only data from observations at elevation angles of more than 10° of isolated point-like sources were considered. Also required was that more than 85% of the scintillation detected in these observations had to come from regions of the raypath overlying white-light coronal holes.

The majority of the IPS observations discussed in this chapter were made between 1994 and 1997 using the EISCAT radio telescopes and a single extremely long-baseline observation combining data taken at 1420 MHz by EISCAT and MERLIN telescopes in the northern Scandinavia and the UK respectively (Bisi *et al.*, 2005; Breen *et al.*, 2006) is discussed later in this chapter and in the next chapter of this thesis.

The Ulysses data used here are hourly-averaged SWOOPS ions radial velocity data taken during the first polar pass of the Sun. These data were from the mid- to high-latitude southern and northern polar passes where the solar wind velocity did not dip below 600 km s^{-1} for each hourly-averaged data-point used, thus eliminating interaction regions and periods of large variations in velocity seen at the slow to fast wind transition in the Ulysses velocity data.

5.4 Data analysis

Woo & Habbal (1997a) suggested that a small step in density seen in the Ulysses data indicated the presence of two modes of fast wind, with the fastest (and least dense) emerging radially from the polar coronal hole and a second, slightly slower and denser stream emerging from the quiet Sun.

The regions of the IPS raypaths overlying the polar coronal holes were estimated by ballistically projecting the raypath down onto a white-light map constructed from either Mauna Loa MkIII data or, when available, from SOHO|LASCO observations (as described in chapter 3). These boundaries were used as constraints in fitting the observations using a bimodal weak-scattering model (Coles, 1996; Klinglesmith, 1997) in which the two components of flow were taken to be "fast" (overlying the coronal hole) and "slow" (overlying the bright white-light corona) as previously discussed again in chapter 3. The results of these fits were taken to represent the null-hypothesis result, in which the fast solar wind was best represented by a single stream with some finite variation in flow speed. Next, in order to determine whether the observations could be better represented using a two-mode fast wind, it was assumed that the fast wind was divided into two components - a "fastest" wind occupying the portion of the raypath which lay above the polar coronal hole seen in Yohkoh|SXT synoptic maps (or, when available, the coronal hole seen in synoptic maps derived from SOHO|EIT 195 Å observations of disc centre) and a second, "flanking" stream which occupied the remainder of the region above the coronal hole seen in the white-light maps. Finally, the "fast" and "faster" fit was repeated with the boundaries of the "faster" stream set at between 10° pole-ward of the EUV coronal hole boundary and 10° equator-ward, varied in 5° steps. The quality of fit to these data using the different stream boundaries was judged by comparing the reduced-chi-squared (χ^2_ν) parameter for the fits. An example of this can be seen from the observation of 1120+143 on 19950907 in figure 5.5 where the IPS raypath has been projected back onto a synoptic map created from Mauna Loa MkIII data in this case and has the stream boundaries for both fitting cases marked on there.

The weak scattering model (as described in detail in chapter 3) for fitting these data assumes that all the scintillation comes from a single point source in the centre of the beam (Coles, 1996). Structured or multiple sources in the beam will give rise to superpositions of scintillation patterns which, at present, cannot be fitted in a manner which is not misleading. The sources used for the main (85%+) and reserve cases (70%-85%)

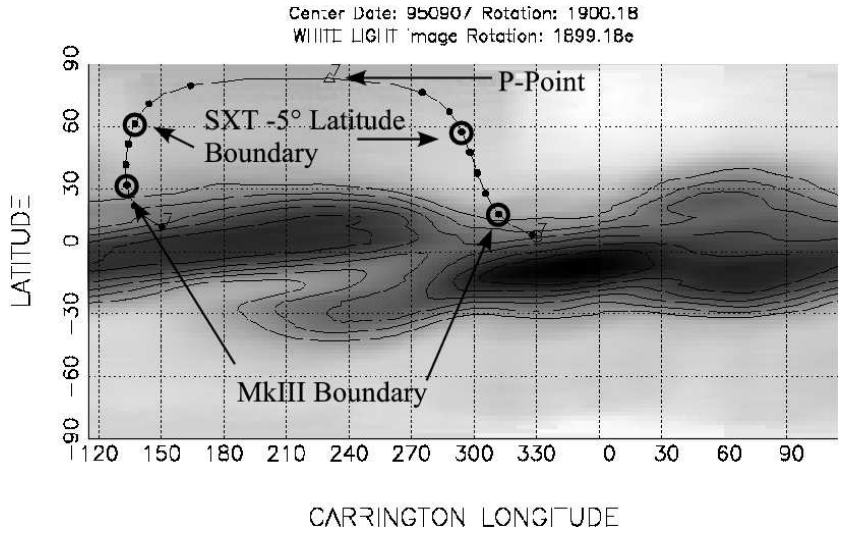

Figure 5.5: A white-light map of the East limb of the Sun, Carrington Rotations 1889-1900 centred on 19950907, constructed using data taken from the Mauna Loa MkIII Coronagraph at 1.7 $R_\odot$ with the IPS raypath of 1120+143 mapped onto it and both SXT -5° latitude and MkIII coronal hole boundaries circled as well as the P-Point, the point of closest approach of the IPS raypath to the Sun in the plane of the sky.

are all based on those found as being suitable compact IPS sources in the investigation carried out in Canals (2002), based on the variation of source structure with baseline at 21 cm wavelength set out in http://www.aoc.nrao.edu/~gtaylor/csource.html (the VLA master calibrator list).

For the scintillation to be strong enough for the signal spectrum to be clearly resolved but not so strong as to start to come into the strong scattering regime in the fast solar wind, only observations for which the point of closest approach of the raypath to the Sun lay between 15 $R_\odot$ and 120 $R_\odot$ were considered. In the past, this has proven to be the best range when considering mid- to high-latitude fast solar wind observations. This eliminated possible distortion of the results by the effects of strong scattering.

In order to detect small variations in the fast solar wind structure, it is necessary to eliminate observations containing a significant amount of slow wind. This was done using a two-stage selection process. In the first stage, any observation in which less than 30° of the raypath around the point of closest approach to the Sun overlaying the coronal hole

was eliminated. This provided a quick way of eliminating observations containing a large proportion of slow solar wind. The list of observations was then refined by calculating the proportion of scintillation being generated in the region of the raypath which overlay the coronal hole. Only observations in which more than 85% of the scintillation came from above the coronal hole were considered for the main study. As discussed in section 2, the slow wind was assumed to produce 3.5 times more scintillation per unit path-length than the fast wind in this calculation - this gave us considerable confidence that we were indeed eliminating observations which contained a significant proportion of slow wind. A second, reserve, list of observations in which between 70% and 85% of the scintillation was likely to have been produced in the fast wind was also prepared.

The criteria were applied to all EISCAT IPS observations taken between 1994 and 2002 - typically over 250 observations per year. Only observations from near to solar minimum (1995-1997) were considered and of these, 160 of which met the initial criteria (source structure, distance and the initial test for fast wind dominance), and of these, 11 satisfied the criteria for clearly fast-dominated observations of isolated, point-like sources, while a further 11 satisfied the criteria for the reserve list.

After analysis of the observations which satisfied the criteria for the primary list, a further stage of selection was applied to the reserve list. It was determined that the latitude of the point of closest approach of the raypath to the Sun should not lie below 65° heliographic latitude. This ensured that observations contained a high proportion of high-latitude fast wind data and offset to some degree the effects of the higher proportion of slow wind in the tails of the raypaths accepted in the reserve list. After applying all criteria and eliminating data which contained detectable levels of interference, eight cases remained, seven main and one reserve. Due to the scattering model having a large number of variables it leads to a possibility of over-fitting the IPS observations. This can be dealt with by analysing separate intervals on an IPS observation lasting for more than 15 minutes such as the case of 0521+166 on 19960608 (figure 5.6) allowing more parameters to be fitted

to it since this reduces the effect of baseline rotation and giving ten auto-correlation functions and five cross-correlation functions to fit as opposed to two and one respectively if this were fit all at once.

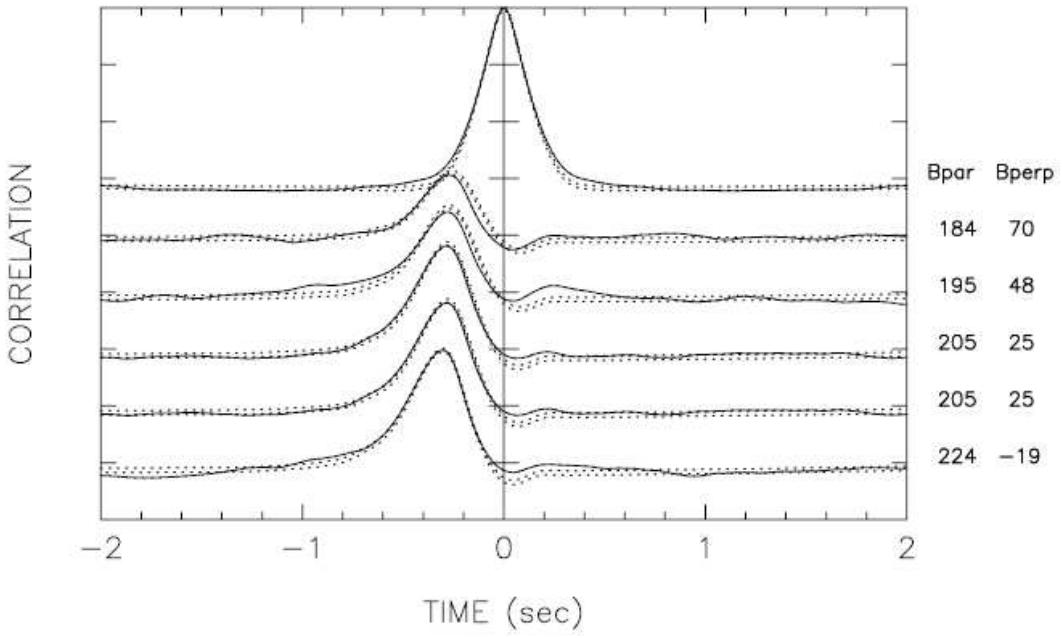

Figure 5.6: Plot to show the fitting of an extended IPS observation to demonstrate that the IPS data are not over-fitted. Bpar and Bperp stands for the parallel and perpendicular baselines of the IPS observation respectively. Plot construction courtesy of W. A. Coles of UCSD.

5.5 Results

Both EISCAT IPS observations and Ulysses|SWOOPS data were analysed as part of this investigation into the structure of the fast solar wind.

5.5.1 EISCAT IPS data

Additional information for interpreting these data came from SOHO|LASCO observations: The raypath for the observations was ballistically projected onto Carrington rota-

tion maps produced by LASCO C2 and representing coronal white-light intensity at $5\,R_{\odot}$. In these maps, dark areas represent coronal holes and bright regions are associated with streamers. Although a similar method was adopted for the Mauna Loa MkIII synoptic maps, the Yohkoh|SXT synoptic maps and the SOHO|EIT synoptic maps, the assumption of a simple ballistic trajectory for the solar wind will break down close to the Sun, increasing the degree of uncertainty in projecting the raypaths down to heights lower than $5\,R_{\odot}$. Hence the mapping was limited to the white-light data and around the X-ray/EUV data.

For this study it was important to use only observations which were clearly fast dominated - with no more than 15% of the scintillation detected coming from slow streams. To identify these observations we calculated the contribution to the overall scintillation pattern coming from regions above the white-light coronal hole (identified with fast wind) and from above the bright white-light corona (identified with slow wind, as in Coles (1996)). In this analysis the density variations in the slow wind were taken to be 3.5 times greater than those in the fast wind - this is likely to be an over-estimate, as EISCAT observations suggest that the density variations in the slow wind are normally 2-3 times greater than those in the fast wind over the distance range considered in this study (Fallows *et al.*, 2002b), but we considered it was important to select only fast-dominated observations even at the expense of eliminating some borderline cases.

As discussed in earlier, the observations were first fitted as a two-mode wind containing a fast and a slow stream, with the boundaries between fast and slow flows estimated by projecting the raypath down onto a map of white-light intensities in the corona. These data were then fitted a second time as a two-mode fast wind, taking the boundaries between the fast modes from synoptic maps of soft X-ray or EUV emission. Figure 5.7 shows an example of each of the types of fit that can be accomplished with the weak scattering model with one of the observations, 1120+143 on 19950907, as used earlier when showing the selection of boundaries. From the top, the first shows the data fitted as a traditional two-

mode fast and slow wind, the second shows the data fitted as a single fast stream, the third shows the data fitted by a two-mode fast stream with equal velocity weighting and the last shows the data fitted by a two-mode fast stream weighted by a small amount for the “fast” stream. Further details can be seen in the caption to the figure.

Due to the greater uncertainties in mapping back closer-in to the Sun to the X-ray and EUV data and in order to see if a relationship exists between any boundary within the fast wind and the lower corona, the boundary was first taken as the X-ray/EUV coronal hole and then varied in latitude in 5° steps from -10° to +10° of the X-ray/EUV coronal hole boundary. The fit with the lowest χ_{ν}^{2} parameter closest to unity was taken to be the most accurate representation of the solar wind structure in the observation.

Of the eight remaining observations that met all of the criteria for a clear fast dominated flow, seven of them were best-fitted using a bi-modal fast wind.

The IPS results are summarised in table 5.1, with the best-fitted results shown in bold-type. In the majority of cases, the fast stream data were best represented by two modes of fast wind, the faster of which being at higher latitudes.

The boundary between the two modes of fast wind was always set at or within 10° of the X-ray/EUV coronal hole boundary but a no more-specific pattern emerged for its relationship with this boundary. We therefore consider it important to compare these results with the one and only available set of high latitude in-situ solar wind data recorded, the SWOOPS measurements made by the Ulysses spacecraft while making its first polar pass at solar minimum.

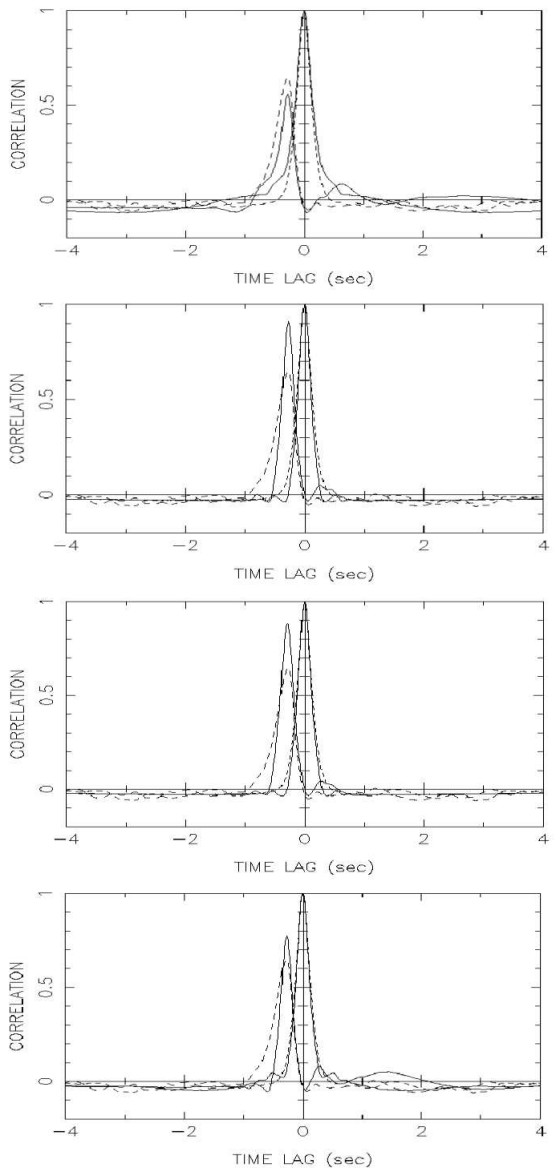

Figure 5.7: An example of different types of model that can be considered with the weak scattering program (sfit) of one of the observations, 1120+143 on 19950907. All parameters were set as default values so this is not a true fitting, but is instead an example of how the modelled correlation functions vary with different assumptions of solar wind conditions. From the top: The first shows the data fitted as a traditional two-mode fast and slow wind with the boundaries through the raypath set at ±50° and the weighting set to 5.3, vfast = 700 km s^{-1}, vslow = 300 km s^{-1} and no parallel or perpendicular velocities; the second shows the data fitted as a single fast stream with vfast = 700 km s^{-1} and no parallel or perpendicular velocities; the third shows the data fitted by a two-mode fast stream with equal velocity weighting with the boundaries through the raypath set at ±30° with vfast = 850 km s^{-1} (faster), vslow = 700 km s^{-1} (fast) and no parallel or perpendicular velocities; and the last (bottom) shows the data fitted by a two-mode fast stream with a weighting of 5.3 for the "fast" stream with the boundaries through the raypath set at ±50° with vfast = 850 km s^{-1} (faster), vslow = 700 km s^{-1} (fast) and no parallel or perpendicular velocities. When properly fitting the data however, all variables are able to be modified by setting them or by fitting them using the weak scattering model.

IPS RESULTS											
Observations		χ^2_ν for IPS boundaries						IPS Analysis Details			
Date	Source	White-light χ^2_ν	X-ray/ EUV -10°	X-ray/ EUV -5°	X-ray/ EUV	X-ray/ EUV +5°	X-ray/ EUV +10°	θ_{in} Lat. of best-fit	θ_{out} Lat. of best-fit	Lat. of P-Point	χ^2_ν close to 1
950714	0741+312	2.53	2.40	2.99	4.04	2.63	**0.94**	64.06	74.33	82.23	**0.94**
950906	1120+143	2.94	9.36	3.56	3.36	**2.90**	N/A	68.87	71.99	77.19	**2.90**
950907	1120+143	6.63	2.26	**1.99**	2.96	2.69	N/A	57.33	61.3	82.96	**1.99**
950908	1120+143	3.25	0.71	0.83	1.22	**0.90**	N/A	57.97	57.02	87.85	**0.90**
960529	0336+323	6.10	5.65	**4.46**	8.50	N/A	N/A	49.67	54.79	58.91	**4.46**
960608	0521+166	7.41	7.29	6.89	7.00	**6.32**	N/A	-72.06	-49.43	-72.06	**6.32**
960609	0521+166	8.04	7.24	**5.81**	6.98	8.07	8.18	-61.54	-65.57	-78.62	**5.81**
960817	0954+177	**2.88**	2.97	3.84	3.96	5.00	11.37	26.95	52.72	85.06	**2.88**

Table 5.1: Summary of the IPS data of the two-mode fast wind study, the X-ray/EUV boundaries are in 5° steps in latitude.

5.5.2 Ulysses|SWOOPS in-situ data

The Ulysses|SWOOPS ions hourly-averaged data were "binned" (averaged further) for approximately every 100 data points (100 hours) and then fitted with polynomials via a least-squares fitting method of orders 1 to 6. A second approach used a bimodal linear fit (i.e. straight line with a change in gradient) with the break-point between the two linear fits set to a range of latitudes from 75° N/S to 10° from the equator-ward boundary of the fast wind (where the Ulysses hourly averaged data no longer dipped below 600 km s^{-1}). The χ^2_ν value was used as the measure of the goodness of fit. These data were split into four different sections, the increasing latitude part of the southern polar pass, the decreasing latitude part of the southern polar pass, the increasing latitude part of the northern polar pass and the decreasing latitude part of the northern polar pass. In order to restrict the study to fast wind, the low-latitude cut-off point, as described earlier, in each case was when the solar wind velocity never dipped below 600 km s^{-1} in any hourly averaged data point before the "binning" process. These data appeared to be best represented by the bi-linear fit in three out of the four segments and a linear fit in one out of the four segments as shown in tables 5.2 and 5.3, and in figures 5.8, 5.9, 5.10 and 5.11. There was no clear

Ulysses|SWOOPS Results				
Type/Order of fit	South increasing latitude	South decreasing latitude	North increasing latitude	North decreasing latitude
Straight-line	2.77866	1.00748	**0.48211**	1.13374
Two-stage gradient	**2.36277**	**1.00580**	0.46569	**1.06449**
X^2 parabola	2.42265	1.02292	0.47697	1.10716
X^3 parabola	2.39792	1.05332	0.49470	1.11038
X^4 parabola	2.42291	1.14123	0.47549	1.14463
X^5 parabola	2.44963	1.03524	0.48553	1.13722
X^6 parabola	2.47625	1.07227	0.55003	1.14732

Table 5.2: Summary of Ulysses|SWOOPS ions analysis, the lowest/appropriate χ^2_ν value closest to unity are in bold.

relationship between the latitude at which the gradient changed, in those cases where it did change, and the latitude of the coronal hole boundary seen in X-ray or EUV emission during the same Carrington Rotation. It should also be noted that in those cases where a bi-linear fit gave the lowest χ^2_ν value closest to unity in table 5.2, the improvement of fit gained was generally very small. It should also be noted that in the increasing latitude northern pole case, the χ^2_ν value is always over-fitted which is why the straight-line linear fit is the most appropriate in this case. The only clearly significant result indicated a single fast wind with higher velocities at higher latitudes, which is in good agreement with the results of McComas *et al.* (2000).

Comparisons of the two-mode fast IPS best-fitted data and SWOOPS ion velocity data can be seen in figures 5.12, 5.13, 5.14 and 5.15 in respect of latitude and distance from the Sun. However, it should be noted that these observations were taken at different times and are in no-way direct comparisons but can be used to get the general picture of the two different data-sets. The green Ulysses data represent the North pole radial component of velocity data of increasing latitude portion of the first polar pass and the purple Ulysses data represent the South pole radial component of velocity data of decreasing latitude portion of the first polar pass as these were the two most-significant portions of the Ulysses data that fitted. In figure 5.13, the dark blue data points are those of the “fast”

Ulysses|SWOOPS Results				
Variable	South increasing latitude	South decreasing latitude	North increasing latitude	North decreasing latitude
Latitude of change in gradient	(-52.95 +2.58/ -1.50)°	(-72.48 +0.48/ -0.93)°	Straight-line	(+31.94 +1.95/ -1.04)°
Date of change in gradient	16/02/94: 1994, 46.60	30/10/94: 1994, 302.23	N/A	11/07/96: 1996, 192.48
Carrington rotation during change in gradient	1879	1888	N/A	1911
Days of year for the Carrington rotation	1994: 37.96 to 65.29	1994: 283.24 to 310.53	N/A	1996: 180.70 to 207.90
Latitude of SXT coronal hole	60±10°	50±10°	50±10°	50±10°
Latitude of EIT coronal hole	Not available	Not available	Not available	60±10°
χ^2_ν of fit	2.362770	1.005800	0.482111	1.064490
Nu	94	26	27	89
Significance Level	$\ll 0.001$	~ 0.450	> 0.990	~ 0.300
Summary	No clear fit	Weak evidence for a bi-modal fast wind	Strong evidence for a single fast wind	Weak evidence for a bi-modal fast wind

Table 5.3: Summary of Ulysses|SWOOPS ions best-fit analysis for the two-mode fast wind study.

velocity IPS solar wind fitted values and the red data points are those of the "faster" velocity IPS solar wind fitted values. In figures 5.14 and 5.15, the dark blue data point with a ∘ in it represents the IPS observation of 0741+312 on 19950714. The light brown data point with a □ in it represents the IPS observation of 1120+143 on 19950906. The royal blue data point with a ⋄ in it represents the IPS observation of 1120+143 on 19950907. The dark lilac data point with a ▽ in it represents the IPS observation of 1120+143 on 19950908. The scarlet red data point with a △ in it represents the IPS observation of 0336+323 on 19960529. The dark green data point with a ◁ in it represents the IPS observation of 0521+166 on 19960608. The dark gray data point with a ▷ in it represents the IPS observation of 0521+166 on 19960609.

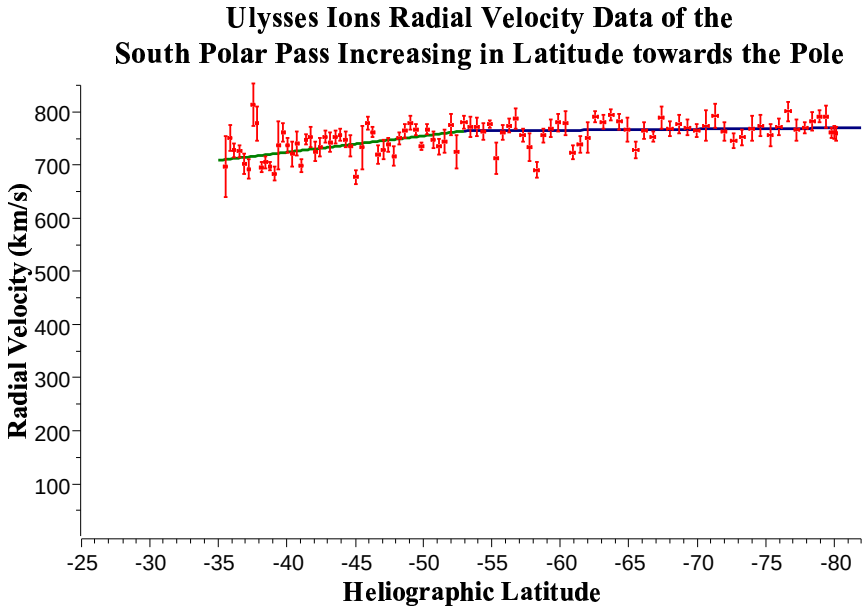

Figure 5.8: Plot of averaged Ulysses ions radial velocity showing the portion of the first polar pass where the spacecraft is approaching the South pole of the Sun from Jupiter and is increasing in negative latitude when doing so. The two lines represent the "best-fit" determined by the χ^2_ν fit to the binned data showing that a change in gradient of velocity with latitude fits these data best. The latitude and χ^2_ν fit values can be seen in table 5.3.

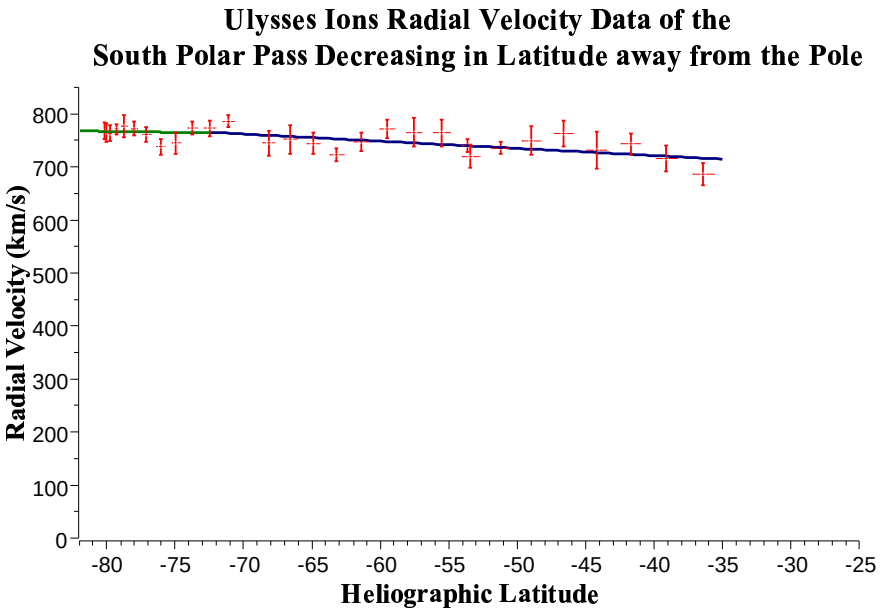

Figure 5.9: Same as for figure 5.8 but this is showing the portion of the first polar pass where the spacecraft is approaching the equator from the South pole of the Sun and is decreasing in negative latitude when doing so.

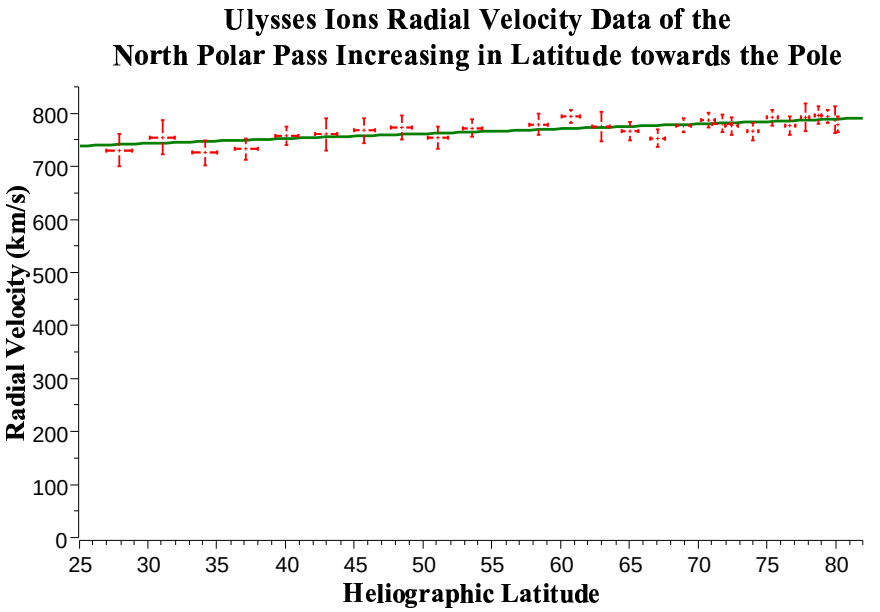

Figure 5.10: Same as for figure 5.8 but this is showing the portion of the first polar pass where the spacecraft is approaching the North pole of the Sun from the equator and is increasing in positive latitude when doing so. This time fitted best as a single straight-line.

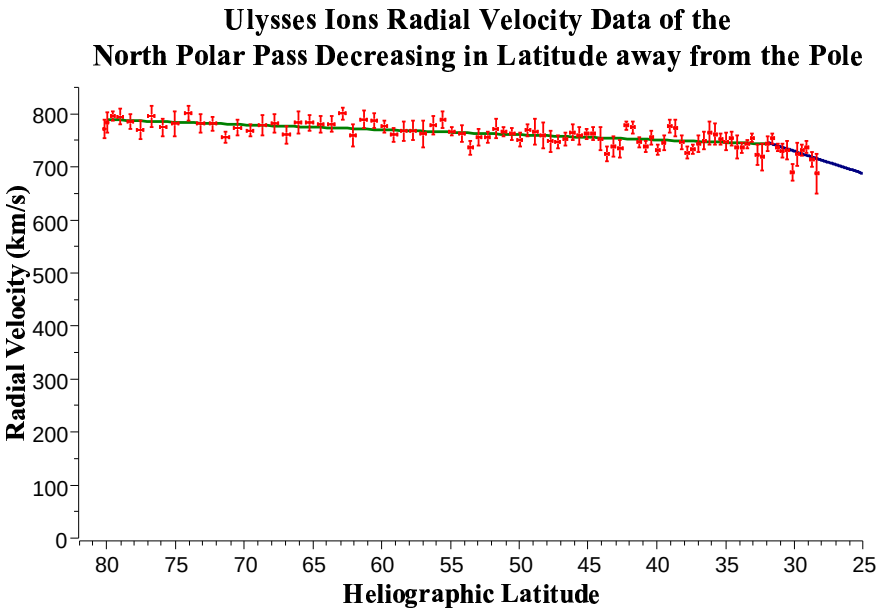

Figure 5.11: Same as for figure 5.8 but this is showing the portion of the first polar pass where the spacecraft is travelling out from the Sun toward Jupiter and is decreasing in positive latitude when doing so.

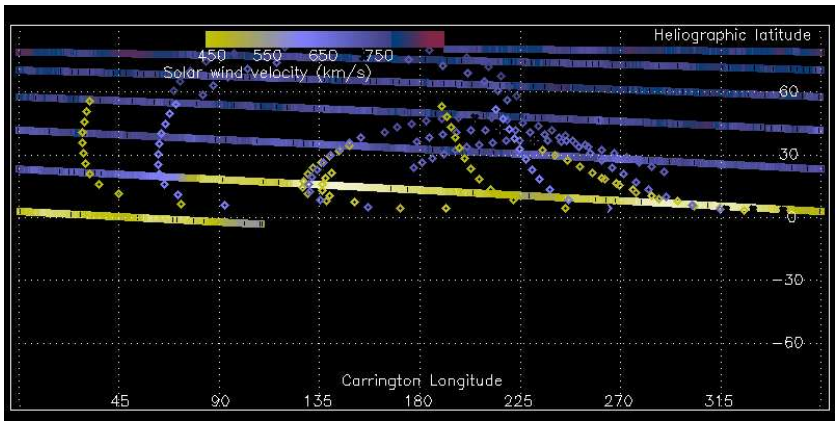

Figure 5.12: Figure showing a comparison in latitude and velocity of the fitted IPS data mapped to the SWOOPS data from the two-mode fast solar wind investigation around the same time-period.

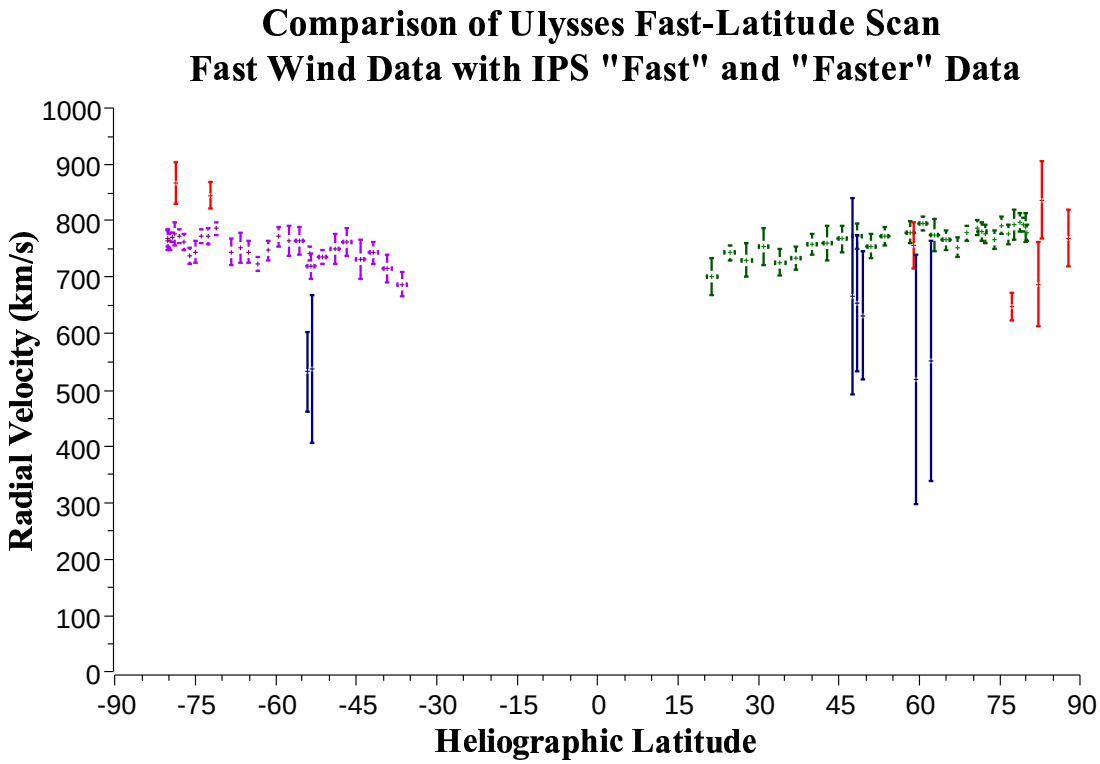

Figure 5.13: Figure showing the IPS “fast” (navy blue) and “faster” (red) stream fitted velocity values as a rough comparison to the values of the two most-significantly fitted Ulysses SWOOPS ions radial velocity binned data with latitude. The axis is decreasing in latitude away from the South pole (on the left) toward the equator (purple) and increasing in latitude away from the equator toward the North pole (green). The error bar on the IPS values is a measure of the range of velocities to the fitted value and although the fitted value is at the centre of the error bar, due to inabilities of the fitting routines, this may not necessarily be the case, i.e. it could be that the range of velocities (the error bar) is not symmetric about the velocity value but there is no-way of knowing this with the current fitting routines.

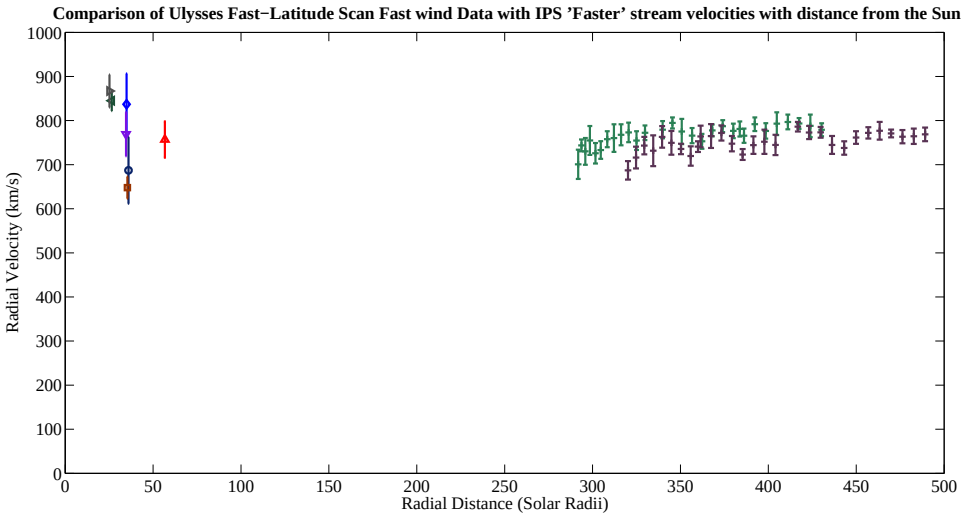

Figure 5.14: Figure showing the IPS "faster" stream fitted velocity values as a rough comparison to the values of the Ulysses SWOOPS ions radial velocity binned data with distance from the Sun. The error bar on the IPS values is a measure of the range of velocities to the fitted value and although the fitted value is at the centre of the error bar, due to inabilities of the fitting routines, this may not necessarily be the case, i.e. it could be that the range of velocities (the error bar) is not symmetric about the velocity value but there is no-way of knowing this with the current IPS analysis fitting routines.

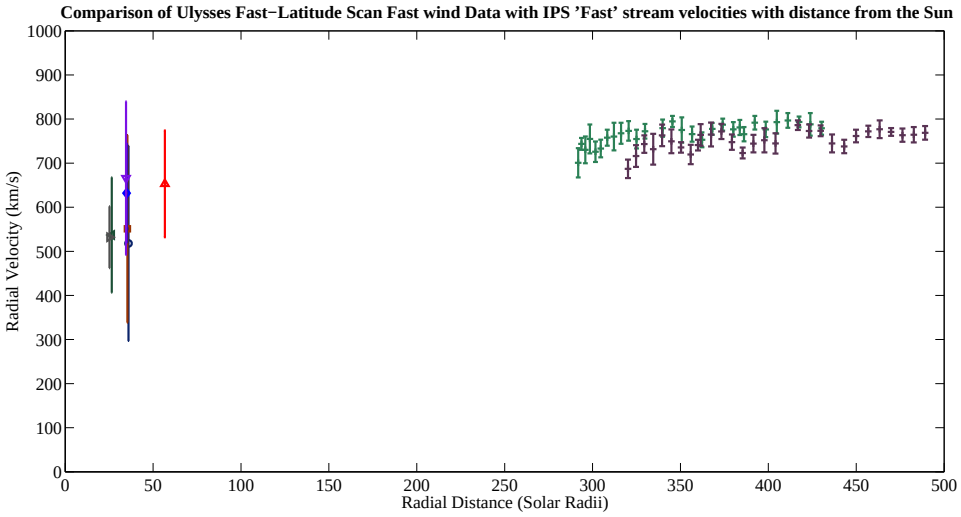

Figure 5.15: Same as in figure 5.14 but for the "fast" stream fitted velocity values of the IPS data.

5.5.3 Extremely long-baseline observation

As described in the previous chapter, further developments in the IPS observing technique have included the use of much more widely separated antennas. Separations up to 2000 km in the parallel baseline can be obtained with EISCAT and the Multi-Element Radio Linked Interferometer Network (MERLIN), as described in Bisi *et al.* (2005); Breen *et al.* (2006), and in the chapter 6 of this thesis. One observation from 20040512, produced a correlation function that showed two clear fast wind peaks and is shown in figure 6.4 of chapter 6.

This observation strongly suggests the presence of two distinct fast components and can be interpreted in two ways:

- It could represent a region of fast flow from above the polar coronal hole at the crown with a velocity of around 780 $\mathrm{km\,s^{-1}}$ and slower flow above the quiet Sun with a velocity of around 670 $\mathrm{km\,s^{-1}}$;

or

- The observation shows fast flow from above the whole of the white-light coronal hole with a velocity of around 825 $\mathrm{km\,s^{-1}}$ and slower flow above the equator-ward extension of the polar coronal hole with a velocity of about 675 $\mathrm{km\,s^{-1}}$. The outflow from equator-ward extensions of coronal holes is generally accepted to be slower than that from large polar holes (e.g. Kojima *et al.*, 2004) and the geometry of the observation (discussed in Breen *et al.*, 2006) does suggest that this might be the most likely source of the slower component. In this case, the transition from the flow above the large polar hole and that from the narrow equator-ward extension would be fairly abrupt, leading to the appearance of two discrete fast components of flow.

This result does not necessarily confirm the existence of a fast wind made up of two distinct components with different sources, but together with the EISCAT observations

described earlier, it does provide convincing evidence of non-uniformity in the fast solar wind to a greater degree than is seen in the Ulysses|SWOOPS data.

5.6 Discussion

The results from IPS and in-situ measurements described in this chapter provide evidence for a change in character of the solar wind between the polar crown and the equator-ward flanks of the fast wind, but IPS suggests a two-mode fast solar wind much more strongly that in-situ. The polar fast wind is faster and appears to vary little with latitude whereas the wind above the lower latitude regions of the white-light coronal hole shows a more marked decrease in velocity with decreasing latitude. These results are generally consistent with the Woo and Habbal proposals. However, the in-situ results suggest a continuous distribution of solar wind speeds rather than two distinct modes.

All of the observations which fitted best as a two-mode fast solar wind (with the exception of 0336+323 on 19960529 which was at 66.7 $R_\odot$) had P-Points between 25 $R_\odot$ and 36 $R_\odot$ from the Sun, and the one case that fitted best as fast and slow had a P-Point of 17.8 $R_\odot$. There does not seem to be a relationship with distance from the Sun at present at IPS distances. This may be because the majority of observations here are within an 11 $R_\odot$ band.

Together with the super-radial expansion of the fast wind first detected by Moran (1998), and recently confirmed by extremely long-baseline observations by Bisi *et al.* (2005); Breen *et al.* (2006) and in a forthcoming paper, these data are more consistent with the standard model of fast solar wind emergence in which flow from the EUV coronal hole subsequently over-expands to lower latitudes and does not flow purely radial. The extremely long-baseline observation of 20040512 does suggest two distinct modes of fast wind. However, in this case, the raypath extended from above the polar hole into a region above an equator-ward extension of the northern polar hole. Therefore, it is proposed that

the greater densities present above the low-latitude part of the coronal hole lead to the observation being dominated primarily by high-latitude, low density flow from across the raypath near the point of closest approach, and secondly, by slightly slower higher density flow from deep within the equatorial extension of the coronal hole.

The results reported in this chapter do not unambiguously distinguish between two different models of the fast wind structure. They do however, point to a difference in character between the polar fast wind and that of lower latitudes above the flanks of the white-light coronal hole.

5.7 Two-mode fast solar wind summary

The results presented in this chapter provide a useful test of the alternative models of the fast wind internal structure. They reveal a difference in character between the flow found in interplanetary space above the polar crown and that found above the flanks of the white-light coronal hole (particularly in the IPS data), though probably not a sudden transition from one type of flow to another. Within the fast solar wind itself, the latitudinal gradient in velocity in the polar crown stream is considerably shallower than that seen in the equator-ward flanks of the fast stream. The results suggest that (within the limits imposed by uncertainties in the IPS results and scatter in the Ulysses data) it is possible to assume a constant velocity over the polar crown. This is not the case at the flanks of the fast stream, where we see a significant decrease in velocity at lower latitudes. The results of the Ulysses spacecraft gave a mixed-representation by a bi-linear model and a linear fit, but this cannot be regarded as confirmation that a change in gradient since it could be the case that there is an inhomogeneity in the turbulence that damps out between IPS distance (typically $\sim 50\,R_{\odot}$) and the typical distance of Ulysses (over 10 times that), only that there is a difference in character between the polar stream and the flanks of the fast wind.

It is suggested that the flow observed above the centres of the polar coronal holes should be regarded as the archetypal fast wind. The change in latitudinal gradient in velocity observed in interplanetary space at latitudes near to those of the boundaries of the X-ray coronal holes may indicate an internal boundary within the fast wind or may simply be the signature of a more gradual change in solar wind properties. The presence of two distinct fast velocities in the EISCAT-MERLIN result strongly suggests a difference in character between the high-latitude fast wind (found above the polar coronal hole) and the outflow from the equator-ward extension of the polar hole, and it is likely that this difference also applies to flow above the centres of polar coronal holes and regions near their equator-ward boundaries.

Chapter 6

Meridional flow of solar wind streams and extremely long-baseline observations

This chapter describes research into the large-scale structure of the solar wind in general and in-particular, evidence (if any) of meridional flow of the solar wind. It builds on work previously carried out by Moran (1998) and by Bisi *et al.* (2005). The time lag for maximum cross-correlation can be used to estimate the outflow speed of the irregularities producing the scintillation (as described in chapter 3). The ability of the observation to resolve streams of solar wind with differing velocities increases as the radial separation in the plane of sky of the raypaths (the parallel baseline) increases, though as the irregularity pattern is evolving in time any increase in parallel baseline will lead to a decrease in the degree of correlation (Klinglesmith, 1997; Moran *et al.*, 1998) as described in chapter 2.

The highest degree of correlation will be observed when the irregularity patterns drifting across the raypaths are most alike; that is, when the separation of the raypaths in the plane of the sky is parallel to the plane-of-sky projection of the solar wind outflow. If the outflow is not purely radial then maximum correlation will be observed for a non-zero perpendicular baseline (Moran, 1998). In this way, extended IPS observations can be

used to detect meridional velocities in the solar wind (e.g. Breen *et al.*, 1996b; Moran *et al.*, 1998; Bisi *et al.*, 2005).

6.1 Extremely long-baseline observations

The extremely long-baselines (up to 2000 km) available between EISCAT and MERLIN allow different solar wind streams crossing the IPS raypath (and also the direction of flow) to be determined with much greater accuracy than was previously possible during earlier experiments. These included the EISCAT-only baselines which are only available up to 390 km (as discussed in detail in chapter 3).

6.1.1 Introduction

The accuracy of solar wind velocity estimates are greatly improved as the separation of the antennas projected into the plane of the sky used to sample the scintillation pattern is increased. The time lag for maximum correlation also increases as a result, i.e. increasing the parallel baseline. As this happens, the ability to resolve two different solar wind speeds across the raypath improves (e.g. Grall, 1995; Coles, 1995; Grall *et al.*, 1996; Klinglesmith, 1997). However, the irregularity pattern giving rise to the IPS will also be evolving with time. This means that the degree of correlation between the scintillations observed at the two different sites will be decreased as the parallel baseline is increased.

Until the early 1990s, two-site IPS measurements were typically taken with parallel baselines of around 100 km - 150 km (as described in chapter 3 of this thesis). However, in 1993 a series of observations at 933.5 MHz using EISCAT were undertaken to support the measurements taken on the first polar pass by the Ulysses spacecraft. The geometry required for these observations forced the use of much longer parallel baselines than had previously been used. The baselines were in excess of 300 km and unexpectedly gave good correlations between the scintillation patterns observed at the two sites (Breen *et al.*, 1996b). In addition, the improved sensitivity of the measurements to differing veloci-

ties of solar wind meant that fast and slow streams across the raypath could be clearly distinguished. The respective contributions of each of the streams appeared as two distinct peaks (fast and slow) in the correlation functions (Grall, 1995; Coles, 1996). Rao *et al.* (1995) combined measurements from the GMRT and Ootacamund radio telescopes, which operated at 327 MHz, giving a parallel baseline of 560 km. Again, a good correlation between the scintillation patterns between the sites was observed. Moran *et al.* (1998) considered the relationship between maximum cross-correlation of the scintillation patterns recorded at the EISCAT sites and the parallel baseline length showing that the rate at which the degree of correlation fell away with increasing parallel baseline was best represented by a Gaussian curve.

6.1.2 Methodology

The observations discussed in this chapter combine measurements of IPS from MERLIN and EISCAT of the 2002, 2004 and 2005 observing campaigns. The results presented show that correlation between the scintillation patterns detected at receiving sites separated by up to 2000 km not only exist, but can be used to provide information on solar wind speed, direction of flow (off-radial), and the large-scale velocity structure of the solar wind. Remembering that IPS observations are sensitive only to the component of solar wind velocity perpendicular to the raypath, the simple estimates of solar wind speed taken from the time lag for maximum correlation include a degree of "foreshortening" (e.g Coles, 1996). These "plane-of-sky" speeds are therefore lower than the true radial outflow speed and so have to be corrected.

In previous cases where this method has been employed (e.g. Breen *et al.*, 1996b, 1999), correction for this effect and determination of other solar wind parameters were undertaken by fitting these data using a weak-scattering model (as in the previous two chapters of this thesis). As it was not immediately apparent that some of the assumptions made in this model would remain valid when time lags for maximum correlation approached or even exceeded an 8 s time lag, no attempt was made to model these data in the investiga-

tion in this chapter with the exception of the EISCAT-only observations from 2005 used as a comparison. The particular assumption that the temporal evolution of the irregularity pattern could be adequately modelled throughout the time duration for the density variations to pass over one site and then the next. Instead, estimates of the path-integrated plane-of-sky speed of the solar wind directly from the time lag for maximum correlations were acquired and then used to estimate the outflow speed by determining the probable location of regions of fast and slow flow in the raypath (by projecting the raypath down onto SOHO|LASCO maps of white-light intensity in the corona or those of the EIT instrument - again as in the previous two chapters of this thesis), assuming a 1:3 scintillation index rating between fast and slow wind (Fallows *et al.*, 2002b) and solving the path-integration problem across the region of the raypath immersed in each stream. The reason for choosing a weighting of 3 in this chapter as opposed to 3.5 used previously in this thesis is that with this particular IPS technique, the slow contribution is not going to get mixed in with that of the fast since each stream is separated by a longer time lag due to the increased baseline length and so there is not a need to be quite so conservative with the weightings. Also, lessening this criterion can be justified due to the limited number of extremely long-baseline observations.

The approach of estimating the velocity of solar wind from the time lag does have some limitations however. The most important of these is that a finite spread in solar wind speeds across the stream considered will introduce a skew of the correlation function to shorter time lags, leading in turn to an over-estimate of the plane-of-sky speed (e.g. Breen *et al.*, 1996b). The plane-of-sky speeds used here with the radial outflow speeds deduced from them (as quoted) are therefore likely to be over-estimates of the true solar wind speeds.

As in Breen *et al.* (2006), the over-estimates of velocity are considered acceptable as the purpose of this chapter is to show that extremely long-baseline IPS observations could be used to estimate solar wind speeds and that the ability of the observation to resolve

regions of flow with different outflow speeds was greatly improved by comparing results from different pairs of sites from the EISCAT and MERLIN observing systems along with detecting the off-radial flow of the solar wind. The application of the weak-scattering model to extremely long-baseline observations and its use to estimate true solar wind speeds will be discussed in the next chapter as part of further work since there was no longer any time left within the time frame of this thesis to carry out a thorough analysis using the weak scattering model and investigating its suitability and capability with the extremely long unprecedented baselines.

6.1.2.1 Observing at different frequencies (dual-frequency observations)

As discussed briefly in chapter 2 of this thesis and more thoroughly in Fallows *et al.* (2006), it is possible to obtain meaningful results from two observing sites that are operating at different frequencies. These are still obtainable even over the very long-baselines of the ESR to the EISCAT mainland sites at frequencies of 500 MHz, 928 MHz and 1420 MHz; and also the extremely long-baseline observations between EISCAT and MERLIN sites with the Tromsø antenna recording at 928 MHz and all others at 1420 MHz. Fallows *et al.* (2006) shows by comparing these dual-frequency observations with single-frequency observations, the results agree and generate velocities for the solar wind streams that are very similar for similar baselines, and cuts, through the solar wind, i.e. for when looking at similar parts of (and along similar direction through) the solar wind. Results combining data from MERLIN (at 1420 MHz) and the EISCAT antenna of Tomsø (at 928 MHz) are therefore included in this chapter.

6.2 Observations

The results presented in this chapter were obtained from measurements that took place on 15 May 2002 (20020515) and 12 May 2004 (20040512) as discussed in Bisi *et al.* (2005); and from 13 and 14 May 2005 (20050513 and 20050514) as discussed in Breen *et al.* (2006). The telescopes used were the Jodrell Bank MkII and the Cambridge tele-

scope of MERLIN (both receiving on a 10 MHz bandwidth centred on 1420 MHz), the Kiruna and Sodankylä telescopes of EISCAT, receiving over a 7 MHz band centred on 1420 MHz and the Tromsø telescope of EISCAT, receiving on a 5 MHz band centred on 928 MHz. The 2002 observations were intended to determine whether significant correlation existed between scintillation patterns recorded at such widely-separated sites, i.e. with parallel baselines of up to 2000 km. Once this was established, more extensive programmes of observation were developed in 2004 as discussed in Bisi *et al.* (2005), and later in 2005 as discussed in Breen *et al.* (2006). The length of the observations (over an hour in each case) were designed to allow the IPS baselines to rotate through the radial direction in the plane-of-sky for each EISCAT-MERLIN antenna pair. The baseline as viewed in the sky plane is defined with two components, the parallel baseline, B_{Par}, in the radial direction; and the perpendicular baseline, B_{Perp}, in the meridional direction as seen in figure 6.1. The baselines for the various combinations of receiving sites are set out later in this chapter, which also includes a summary of the calculated radial velocities of the flow(s) as estimated directly from the time lag for maximum correlation and the parallel baseline for the observation and then corrected into the radial direction. The periods of observation were compared with the SOHO|LASCO lists of coronal mass ejections (CMEs); http://cdaw.gsfc.nasa.gov/CME_list/ and http://lasco-www.nrl.navy.mil/cmelist.html. None of the CMEs listed were likely to have crossed the IPS raypath within 3 hours of the period of observation.

6.2.1 Comparison of EISCAT and MERLIN data

After matching the times for the data series from the different telescopes, these data were analysed using a 20 minute running window advanced by 5 minutes in each successive analysis to give a set of spectra and cross-correlation functions at 5 minute intervals. Correlation functions and their associated spectra were therefore obtained for over-lapping 20 minute intervals centred at 5 minutes apart for the whole observing period of each of

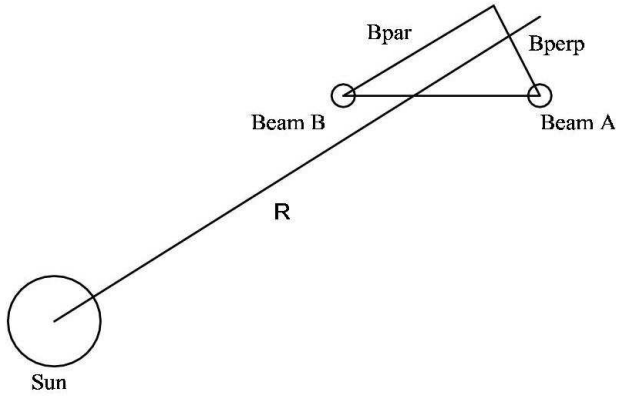

Figure 6.1: Diagram showing the parallel and perpendicular components of an IPS observation relative to the radial outflow of solar wind as if looking from the radio source (perpendicular to the page) toward the two IPS antennas labelled as Beam A and Beam B. Beam A and Beam B are representative of of the raypath from each of the two IPS receivers. Correlation of the signal received at each of the sites is greatest when the parallel baseline lies across the direction of flow of the solar wind - if the solar wind flows in a purely radial direction, then maximum correlation will be achieved when B_{Par} lies parallel to the line R (which represents a purely radial outflow with B_{Perp} in the Meridional direction).

(Breen *et al.*, 2002c)

the observations. The very long time lags for maximum correlation present in these data at the time of analysis for this thesis proved difficult to fit using the weak scattering scattering model, so instead the time lag(s) of peak(s) in the cross-correlation functions was used to estimate the solar wind velocity(s) across the line-of-sight, as described earlier in this chapter. The ratio of parallel and perpendicular baselines (in the plane of the sky) for which maximum cross-correlation was observed was used to determine the meridional angle of outflow, assuming that when the baseline lies parallel to the solar wind flow in the sky plane the correlation is maximised.

Additional information for interpreting the data came from SOHO|LASCO observations where the raypath for each observation was ballistically projected down on to Carrington rotation maps produced by LASCO C2 representing coronal white-light intensity (as described in chapter 3 and used extensively in chapters 4 and 5). The IPS raypaths in this investigation were mapped to $5\,R_{\odot}$ onto the synoptic maps, with dark areas in the map taken to represent source regions of high-speed flow and bright regions as lying below

streams of slow wind as described in chapter 3 of this thesis.

6.2.2 May 2002 observations

In the 2002 observations, the strong mid-high-latitude source 0319+415 was observed at a heliographic latitude of 60° N and at heliocentric distance of 83 $R_\odot$. An example of the correlation functions and the raypath mapped onto a SOHO|LASCO C2 white-light map can be seen in figure 6.2.

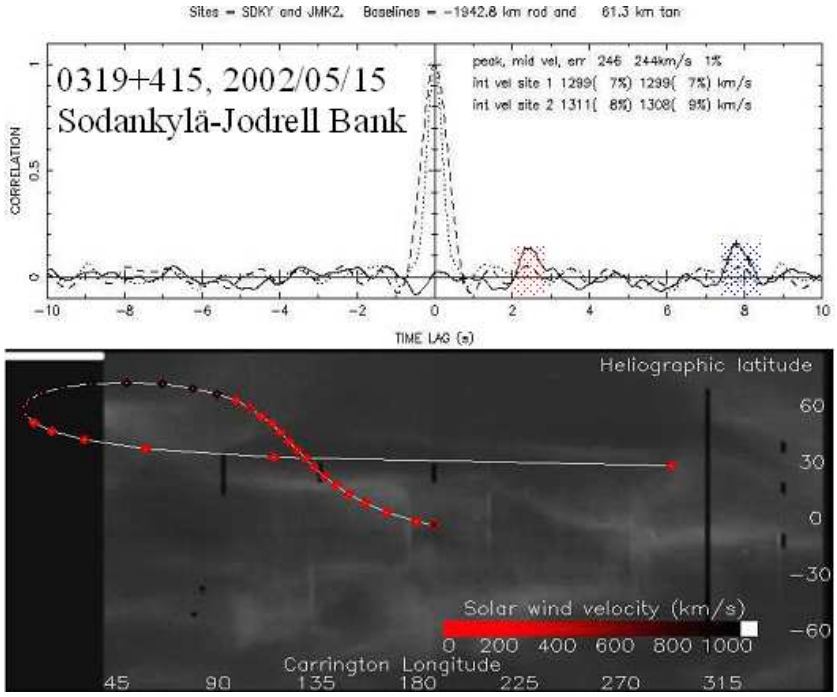

Figure 6.2: Sodankylä-Jodrell Bank observation of 0319+415 on 20020515, example correlation functions and the raypath mapped onto a 5 $R_\odot$ SOHO|LASCO synoptic map of the East limb for Carrington rotation 1989.

The source 0431+206 was observed just South of the helio-equator at 12° S and 56 $R_\odot$ from the Sun. An example of the correlation functions and the raypath mapped onto a SOHO|LASCO C2 white-light map can be seen in figure 6.3. Both sources were observed for 60 minutes and the parallel baselines ranged from 1285 km between Jodrell Bank and Sodankylä at 0600 UT for 0431+206 to 1981 km between Cambridge and Sodankylä at 1435 UT for 0319+415.

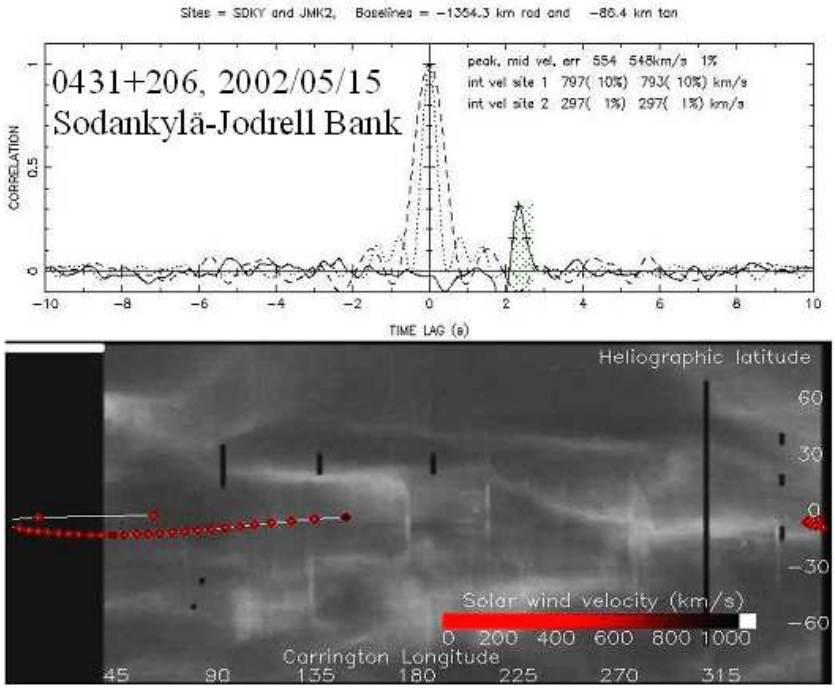

Figure 6.3: Sodankylä-Jodrell Bank observation of 0431+206 on 20020515, example correlation functions and the raypath mapped onto a 5 $R_\odot$ SOHO|LASCO synoptic map of the East limb for Carrington rotation 1989.

The observation of 0319+415 started at 1400 UT and produced several baselines with correlations of up to ~14% for both the fast and slow streams of solar wind detected along the raypath with time lags of ~2.4 s for the fast stream and ~8 s for the slow stream. Although these correlations are low, they are consistent with multiple baselines of different sites from each of the EISCAT and MERLIN systems of telescopes. This strongly suggests that these correlations are real and represent the motion of the small-scale irregularities in the solar wind. The range of velocity estimates can be found in table 6.1. The velocity measurements are consistent with what may be expected from the configuration of the corona below the raypath, with the fast wind emerging from the high-latitude coronal hole and its equator-ward extension. It was noticeable in all correlations between the different baseline combinations that B_{Perp} was significantly different from zero. This means that the solar wind detected was not flowing in a purely radial direction. This was originally described in preliminary studies with EISCAT-only baselines in Moran (1998);

Moran *et al.* (1998).

The observation of 0431+206 started at 0600 UT and produced several baselines with correlations of up to ~38% for what appears to be a region of possible interaction just South of the helio-equator over an equatorial coronal hole as seen from the mapping of the IPS raypath onto the synoptic map in figure 6.3. The correlations produced a large B_{Perp} suggested a large off-radial flow in the meridional direction and velocities were of an intermediate nature, consistent with those expected for an interaction region (e.g. Canals, 2002) or for flow above coronal hole boundary layers (e.g. Breen *et al.*, 1999). Again, the range of velocity estimates can be found in table 6.1.

6.2.3 May 2004 observations

The 2004 observations concentrated on 0319+415, which then lay at 56° N, 85 $R_{\odot}$ off the East limb of the Sun. An example of the correlation functions and the raypath mapped onto an SOHO|EIT synoptic map can be seen in figure 6.4. Since this was a case for a two-mode fast solar wind, the SOHO|EIT synoptic map mapping is shown here in place of the SOHO|LASCO map.

The parallel baselines ranged from 1824 km with Jodrell Bank and Kiruna to 1975 km between the Cambridge and Sodankylä sites. The observation, as in 2002, was for an hour in duration. The raypath for the observation lay mainly above a dark coronal hole in white-light data and so was mapped onto an EUV synoptic map from SOHO|EIT as seen in figure 6.4. The reasoning for this was to look for the possibility that a two-mode fast solar wind was being observed as described in the investigation carried out in chapter 5 of this thesis. However, as the solar magnetic equator was considerably tilted (and twisted) during the spring of 2004, the distance of the raypath into the coronal hole varied and was dependent on the IPS baseline used (which in turn depends on the combination of sites cross-correlated). The correlation functions (an example of which is given in figure 6.4) showed a clear peak at a time lag of 2.47 s to 2.71 s. This corresponded to

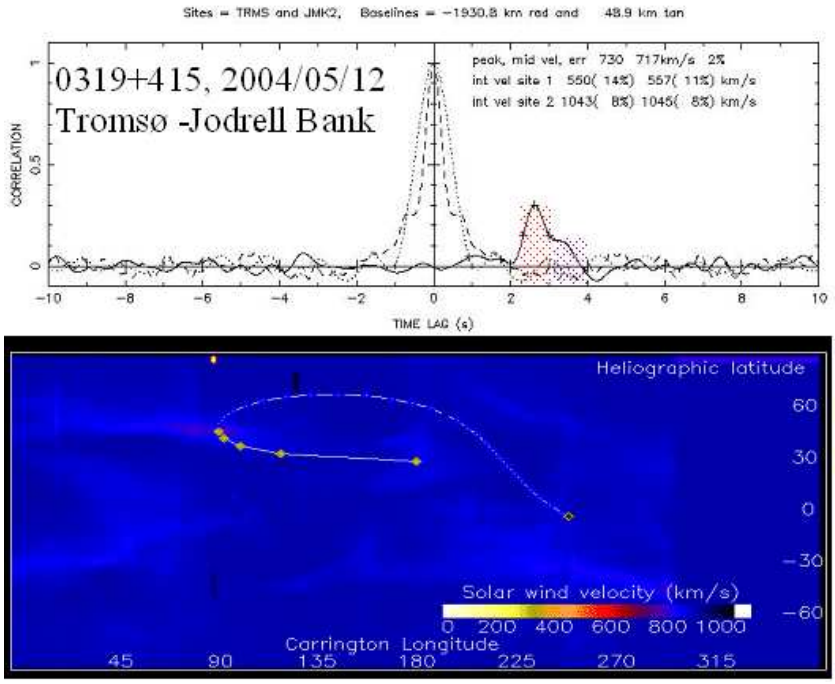

Figure 6.4: Tromsø-Jodrell Bank observation of 0319+415 on 20040512, example cross-correlation and the raypath mapped onto an SOHO|EIT synoptic map of the East limb for Carrington rotation 2016.

radial velocity estimates of 834 km s^{-1} to 848 km s^{-1}. In addition to this, the correlation functions for Jodrell Bank-Sodankylä, Jodrell Bank-Tromsø and Cambridge-Sodankylä baselines showed a second (lower) peak in the correlation function at time lags of 3.20 s to 3.48 s. This was corresponding to radial velocity estimates of 617 km s^{-1} to 669 km s^{-1}. Ulysses in-situ measurements (e.g. Riley *et al.*, 1997; Woch *et al.*, 1997; McComas *et al.*, 2000) have shown that the solar wind speed over the polar crown is higher than that above the equator-ward edges of polar coronal holes (and as found in IPS data in Bisi *et al.* (2006) and the previous chapter of this thesis suggesting a possible two-mode fast solar wind), while there have long been suggestions (e.g. Nolte *et al.*, 1976; Kojima *et al.*, 2004) that the outflow above narrow equatorial coronal holes may be slower than that of those found above the polar crown. The range of velocity estimates can be found in table 6.1.

6.2.4 May 2005 observations

On dates 20050513 and 20050514, 0319+415 was again observed. The point of closest approach to the Sun of the raypath for the observation lay at a heliocentric distance of around 83 $R_\odot$, and at a latitude of around 58° off the East limb of the Sun. As in 2004, the coronal configuration was still rather complex for so late in the solar cycle. A twisted streamer belt configuration was still being observed by the SOHO|LASCO C2 instrument as seen in figure 6.5 which also includes the 20050514 observation ballistically mapped down on to it. The raypaths for the observations lay mostly above the northern polar coronal hole, but some contributions from slow wind could be expected due to its positioning in the corona. The May 2005 observations were analysed very similarly to those from 2002 and 2004. However, the window was advanced with 10 minute "snapshots" and 5 minutes intervals, instead of the 20 minute snapshots used for the 2002 and 2004 data. This is because the maximum correlations were generally greater when a shorter "snapshot" was used. A reason postulated for this could be that the solar wind detected along the raypath's of the telescopes was evolving more quickly with time than it was in the 2002 and 2004 observations and the effects of de-correlation by the changing geometry were more significant than the reduction in quality of data obtained on a shorter integration interval. This meant that the solar wind observing geometry was more varied after 20 minutes in 2005 than it was after the same about of time in 2002 or 2004 and thus reduced the amount of correlation for a 20 minute period of analysis. The range of the parallel baselines was from 1874 km to 1985 km for the 20050513 observation, and from 1828 km to 2007 km for the 20050514 observation.

The cross-correlation functions for observations made on 20050513, and up until 1410UT on 20050514, show a consistent peak at 2.39 s to 2.80 s. This corresponds to plane-of-sky speeds of 708 $km\,s^{-1}$ to 803 $km\,s^{-1}$, with most observation intervals suggesting plane-of-sky speeds $\sim$730 $km\,s^{-1}$ to $\sim$770 $km\,s^{-1}$. In addition, some observations showed a secondary peak which had corresponding plane-of-sky speeds of 484 $km\,s^{-1}$ to 600 $km\,s^{-1}$. If these two peaks are associated with outflow from higher- and lower-latitude regions of

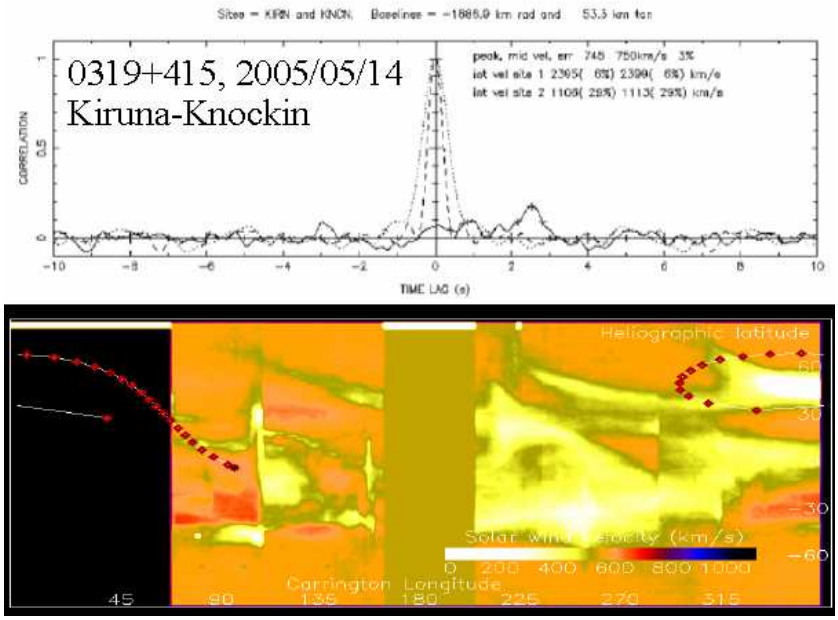

Figure 6.5: Kiruna-Knockin observation of 0319+415 on 20050514, example cross-correlation and the raypath mapped onto a 5 $R_\odot$ SOHO|LASCO synoptic map of the East limb for Carrington rotation 2029

the polar coronal hole, then they imply solar wind speeds of 743 km s^{-1} to 846 km s^{-1} for the highest-latitude flow, and then 677 km s^{-1} to 747 km s^{-1} for lower-latitude fast flow. Some intermediate flow was also detected due to the positioning of the IPS raypath. It should be noted however, that the likely positions of fast stream boundaries assumed in this analysis can only be considered as rough estimates due to a gap in SOHO|LASCO coverage as can be clearly seen in figure 6.5. The range of velocity estimates can be found in table 6.2.

The results from the observations on 20050514 were very similar to those from 20050513 up until 1410UT as previously described. After this time, a sharp change in the time lag for maximum cross-correlation was seen and is likely to be caused by the passage of an interplanetary magnetic cloud. This cloud is most-probably associated with the solar eruption and radio-burst pattern between 1630UT and 1710UT on 20050513 as mentioned in chapter 1 and discussed fully in Jones *et al.* (2006a).

6.2.4.1 EISCAT-only observations - May 2005

Observations of 0319+415 using the Kiruna and Sodankylä antennas of EISCAT (equating to parallel baselines ~161 km) showed a 56% to 64% correlation at time lags of around 0.25 s to 0.27 s. These time lags in-turn correspond to plane-of-sky speeds of 600 km s^{-1} to 639 km s^{-1}. This velocity range is in-between the two velocities that were detected in the extremely long-baseline observations between EISCAT and MERLIN. If the stream which appears as fast wind in the shorter-baseline EISCAT-only observations extended across both the "fast" and "intermediate" components seen in the extremely long-baseline observations, then this would correspond to outflow speeds of around 690 km s^{-1} to 734 km s^{-1}. Upon fitting the EISCAT-only observations with a weak scattering model (as described in chapter 3 and used extensively in the two previous results chapters), it was indicated that an outflow velocity of 809 km s^{-1} was present. The solar wind also had a spread in velocity of 120 km s^{-1} in the fast wind. The 400 km s^{-1} stream detected had a spread of just 20 km s^{-1} in the slow wind. This implies that the true solar wind speeds lay approximately in the range 749 km s^{-1} to 869 km s^{-1} for fast wind, and 390 km s^{-1} to 410 km s^{-1} for the slow from the EISCAT-only results. These results are consistent with the extremely long-baseline observations of the high-latitude fast wind and suggest that the EISCAT-MERLIN observations are capable of resolving the high- and low-latitude components of the fast wind separately (as in the 2004 data also), while the EISCAT-only observations see the outflow as a single intermediate/fast stream with a large spread in the velocity of the stream. As in the case of the 2004 observations, the extremely long-baseline observations did not detect the slow outflow seen in the EISCAT-only data (Breen *et al.*, 2006).

6.3 Discussion

The solar wind velocities seen in these observations from EISCAT and MERLIN in 2002, 2004 and 2005 are highly consistent across completely independent combinations of antennas; see tables 6.1 and 6.2. This is strong evidence that these correlations are indeed

real and can provide accurate information on solar wind outflow speed. In addition, all the observations show signs of solar wind off-radial flow with fast wind being predominantly equator-ward, interaction regions being deflected, slow wind showing some signs of a pole-ward flow, and variability during the transit of an interplanetary magnetic cloud.

As described here in terms of the 2005 data and also in Breen *et al.* (2006), the 2002, 2004 and 2005 campaigns where the EISCAT-only baselines were available of the same source on the same day as those of the EISCAT-MERLIN baselines, the velocities are consistent across both experiments. There are two interesting differences however:

- The first of the differences is that several of the EISCAT-MERLIN baselines show secondary fast peaks (consistent with the greater velocity resolution from the longer baselines used) in the cross-correlation functions, indicating the presence of a second, slightly slower component of flow than that of the main peak. The EISCAT observations however, show a "fast" peak only, which is generally an intermediate velocity estimate between the two components that are seen in the extremely long-baseline observations. This is evidence of a significant spread in velocities for the 2004 extended observation. These results (as discussed in the previous chapter in terms of a two-mode fast solar wind) suggest that there is genuinely a difference in character between the fast wind above polar coronal holes and that above the equator-ward extensions of these holes. Several studies using Ulysses data have shown that fast wind from lower latitudes is slightly denser than the outflow from the polar crown (e.g. Woch *et al.*, 1997), so the roughly density-squared dependence variation of IPS production would lead to a greater bias toward lower-latitude regions of the "flanks" of the fast stream and therefore to the slowest regions. This would then result in observations appearing to contain two discrete components of fast wind.

- The second difference between the results from the EISCAT-MERLIN and EISCAT-only observations is that the former only detected slow wind outflow in 2004 when a substantial proportion of the raypath lay above a bright corona. The latter though,

always showed some evidence of slow flow across the IPS raypath. It is not immediately apparent why the extremely long-baseline observations do not show the slow component that is seen in the EISCAT results, but the hypothesis is that an explanation may lie in slight differences in meridional (north-south) velocity between the fast and slow components due to a non-radial outflow. It was suggested in Breen *et al.* (1996b) that the cross-correlation between the scintillation patterns observed at the two sites should be at a maximum if the projection on the plane of the sky of the baseline between the receiving sites was parallel to the projection onto the plane of the sky of the solar wind outflow. This approach was later used by Moran *et al.* (1998); Bisi *et al.* (2005) and in this chapter to detect non-radial flow in the solar wind. As the parallel baseline increases, so does the sensitivity of the observation to meridional flow direction improve (since increasingly large changes in perpendicular baseline are required to produce the same angular deviation). If there is a slight difference in meridional direction between the fast and slow components then this could provide an explanation as to why the extremely long-baseline observations do not detect the slow flow seen on shorter baselines of EISCAT-only. An alternative explanation is that the irregularity pattern in the slow wind did not remain coherent over the time it took to drift from the raypath of one of the telescopes to the raypath of the other, so did not give rise to a feature in the correlation function since this feature would have petered-out during that time. This is possible, but appears doubtful in light of the clear slow wind correlation peaks seen in 2002. At present, the directional explanation appears more convincing.

6.3.1 Velocities

The main results of this investigation can be seen in the table in tables 6.1 and 6.2. The outflow speeds inferred from these observations for fast flow are rather higher than those detected by Ulysses during its first (solar minimum) polar pass. Although they are not significantly greater than those seen in earlier IPS results (e.g. Breen *et al.*, 1999).

Summary of EISCAT-MERLIN 2002 and 2004 IPS observations							
Date	**Source**	**Stream**	**Sites (ME)**	**Radial Velocity Range ($km\,s^{-1}$)**	**Radial Velocity Average ($km\,s^{-1}$)**	**Meridional* Angle (°)**	**Meridional* Velocity ($km\,s^{-1}$)**
20020515	0319+415	Fast	JK	825-858	841	0.7	10.2
20020515	0319+415	Fast	JS	800-818	810	0.8	11.0
20020515	0319+415	Fast	CS	823-829	826	2.0	28.3
20020515	0319+415	Slow	JK	318-328	324	-1.7	-9.5
20020515	0319+415	Slow	JS	323-325	324	-0.7	-4.0
20020515	0319+415	Slow	CS	307-327	321	-4.5	-25.6
20020515	0431+206	Int.	JK	586-603	595	-11.5	-120.2
20020515	0431+206	Int.	JS	620-650	641	-6.5	-71.1
20040512	0319+415	Faster	JK	830-848	845	1.4	20.1
20040512	0319+415	Faster	JS	840-841	841	3.3	47.3
20040512	0319+415	Faster	JT	833-843	840	0.9	13.5
20040512	0319+415	Faster	CK	839-840	840	0.8	11.9
20040512	0319+415	Faster	CS	834-843	840	0.7	10.9
20040512	0319+415	Fast	JS	658	658	3.7	42.0
20040512	0319+415	Fast	JT	617-655	642	-7.2	-0.6
20040512	0319+415	Fast	CS	669	669	3.2	37.0

Table 6.1: Summary of velocities and meridional angles of the observations from the 2002 and 2004 extremely long-baseline IPS campaigns. The Sites (ME) column are the MERLIN-EISCAT sites where the MERLIN sites are first and are Cambridge (C), Jodrell Bank (J) and Knockin (K), and the EISCAT sites are second and are Kiruna (K), Sodankylä (S) and Tromsø (T). Int. is for an intermediate stream detection on 20020515 with Jodrell-Kiruna and Jodrell-Sodankylä.

* Where maximum cross-correlation occurs for each baseline combination (may be more than one occasion); negative meridional angle/velocity is in the north-ward meridional off-radial direction.

Summary of EISCAT-MERLIN 2005 IPS observations							
Date	**Source**	**Stream**	**Sites (ME)**	**Radial Velocity Range ($km\,s^{-1}$)**	**Radial Velocity Average ($km\,s^{-1}$)**	**Merid-ional* Angle (°)**	**Merid-ional* Velocity ($km\,s^{-1}$)**
20050513	0319+415	Faster	JK	756-772	764	1.2/-0/1	15.7/-1.8
20050513	0319+415	Faster	JT	776-846	804	1.0/-0.3	14.0/-3.6
20050513	0319+415	Faster	JS	770-774	772	1.6	21.1
20050513	0319+415	Faster	KK	791-827	804	0.5	7.2
20050513	0319+415	Faster	CK	743-805	787	2.2	31.4
20050513	0319+415	Faster	CS	747-922	814	1.9	25.6
20050513	0319+415	Faster	CT	782-810	793	1.0	13.7
20050513	0319+415	Fast	JS	732	732	2.5	31.7
20050513	0319+415	Fast	JT	700-747	722	1.9	24.7
20050513	0319+415	Fast	CK	677	677	2.9	34.1
20050513	0319+415	Fast	CT	719-743	731	0.5	6.2
20050513	0319+415	Fast	KS	690-734	712	-7.3/5.5	-93.2/66.6
20050513	0319+415	Int.	CS	593-593	593	2.6	26.5
20050514	0319+415	Faster	KK	763-772	766	1.6	22.2
20050514	0319+415	Faster	CS	743	743	0.5	7.0
20050514	0319+415	Fastest	KK	1432-1433	1433	0.5	11.8
20050514	0319+415	Fastest	KS	1485-1495	1488	-2.2/-3.5	-55.8/-91.0
20050514	0319+415	Fastest	JS	1463-1497	1479	-2.6	-67.6
20050514	0319+415	Fastest	CK	1474-1493	1484	-9.1	-133.6
20050514	0319+415	Fastest	CS	1425	1425	0.5	11.2
20050514	0319+415	Fast	KK	1246-1336	1292	-3.6	-82.1
20050514	0319+415	Fast	KS	989-1230	1143	1.7	28.8
20050514	0319+415	Fast	JS	1208-1258	1232	1.2	26.0
20050514	0319+415	Fast	JK	1323-1373	1348	-4.2	-97.3
20050514	0319+415	Fast	CS	1214-1337	1279	-3.6	-84.5

Table 6.2: Summary of velocities and meridional angles of the observations from the 2005 extremely long-baseline IPS campaigns. The Sites (ME) column are the MERLIN-EISCAT sites where the MERLIN sites are first and are Cambridge (C), Jodrell Bank (J) and Knockin (K), and the EISCAT sites are second and are Kiruna (K), Sodankylä (S) and Tromsø (T). Int. is for an intermediate stream detection on 20050513 with Cambridge-Sodankylä. The faster stream is so-called as it was over a high-latitude portion of the IPS raypath, and the fastest and fast streams are so-called as the velocities across the high- and mid-latitude portions of the IPS raypath during the crossing of an interplanetary magnetic cloud.

* Where maximum cross-correlation occurs for each baseline combination (may be more than one occasion); negative meridional angle/velocity is in the north-ward meridional off-radial direction.

There are two possible explanations for this: That the use of time lag for maximum cross-correlation to determine the plane-of-sky speed introduces a potential bias to higher speeds; or that the irregularities themselves may be moving faster than the background solar wind bulk flow. It is intended at Aberystwyth to investigate both of these possibilities in the not too distant future with continued IPS campaigns of 2006 and again planned for 2007.

The observation of 0319+415 on 20020515, figure 6.2, was of a high northern latitude source. The observations showed clear fast and slow peaks on all available baselines. Significant correlation was observed at time lags of up to 8 s. Velocities of the fast stream on all baselines used were between 800 km s^{-1} and 858 km s^{-1}. Velocities of the slow stream on all baselines used were between 307 km s^{-1} and 328 km s^{-1}.

The observation of 0431+206 on 20020515, figure 6.3, was of a source just South of the helio-equator. The raypath lies along the boundary of an equatorial coronal hole. Observations showed intermediate velocity flow with velocities on all baselines used between 586 km s^{-1} and 650 km s^{-1}.

The observation of 0319+415 on 20040512, figure 6.4, was of a high northern latitude source. It displayed clear signs of a two-component fast wind, probably corresponding to polar crown and flank coronal holes. Velocities on all baselines were between 834 km s^{-1} and 848 km s^{-1} for the polar crown coronal hole and between 617 km s^{-1} and 655 km s^{-1} for the mid-latitude coronal hole.

The observations of 0319+415 on 20050513, figure 6.5, and also on 20050514, were of a high northern latitude source and up until 1410UT on 20050514 displayed signs of a two-component fast wind and an intermediate velocity from the one end of the raypath going into the equatorial streamer at the Earth end of the raypath. Velocities on all extremely long-baselines between 743 km s^{-1} and 846 km s^{-1} for the higher latitude fast solar wind,

677 km s^{-1} to 747 km s^{-1} for the lower latitude fast solar wind, and between 586 km s^{-1} and 650 km s^{-1} for the intermediate flow toward the equatorial streamer belt.

6.3.2 Meridional flow

The maximum cross-correlation is not necessarily observed for a zero B_{Perp}. Maximum cross-correlation for a non-zero B_{Perp} indicates that the plane of sky projection of the solar wind velocity is not precisely radial. To find the off-radial angle, the B_{Par} and B_{Perp} must be corrected for the movement of the Earth using the respective equations developed by B. J. Rickett of UCSD in equations 6.1 and 6.2, where θ_{source} is the heliocentric latitude of the source. From this, the meridional angle, $\theta_{meridional}$, and henceforth the meridional velocity, $V_{meridional}$, can be calculated using equations 6.3 and 6.4 respectively.

$$B_{Par}(corrected) = B_{Par}(raw) + (V_{Earth} \times \sin \theta_{source}) \tag{6.1}$$

$$B_{Perp}(corrected) = B_{Perp}(raw) + (V_{Earth} \times \cos \theta_{source}) \tag{6.2}$$

$$\theta_{meridional} = \arctan \left(\frac{B_{Perp}(corrected)}{|B_{Par}(corrected)|} \right) \tag{6.3}$$

$$V_{meridional} = V_{radial} \times \sin \theta_{meridional} \tag{6.4}$$

In the following plots (as in tables 6.1 and 6.2, the MERLIN-EISCAT sites are defined by letters where the MERLIN sites are first and are Cambridge (C), Jodrell Bank (J) and Knockin (K); and the EISCAT sites are second and are Kiruna (K), Sodankylä (S) and Tromsø (T). For example, KK represents the baselines between the Knockin and Kiruna baselines.

The fast stream observations from 2002, figure 6.6, show evidence of a small equator-ward flow of around 1° to 2° in the most-part.

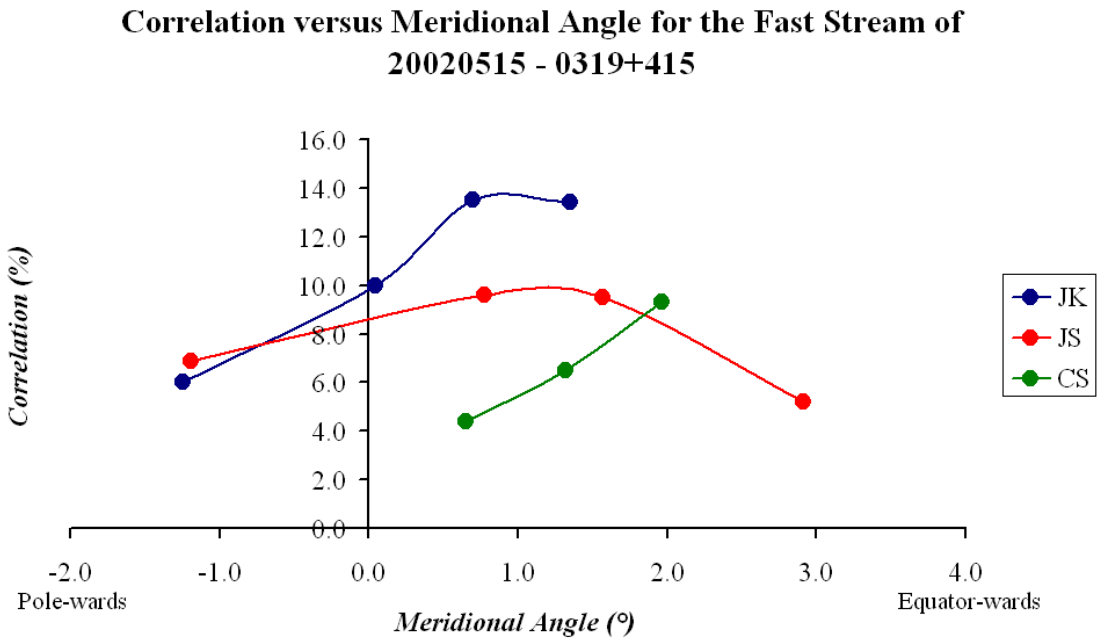

Figure 6.6: EISCAT-MERLIN off-radial angle results from the fast solar wind stream of the extremely long-baseline observations of 0319+415 on 20020515.

The slow wind observations from 2002, figure 6.7, show some evidence of a small pole-ward deviation. At present, it is not certain if this represents the effects of stream-stream interaction or a genuine expansion of the slow solar wind. The pole-ward direction is between 1° and 4° in the most-part.

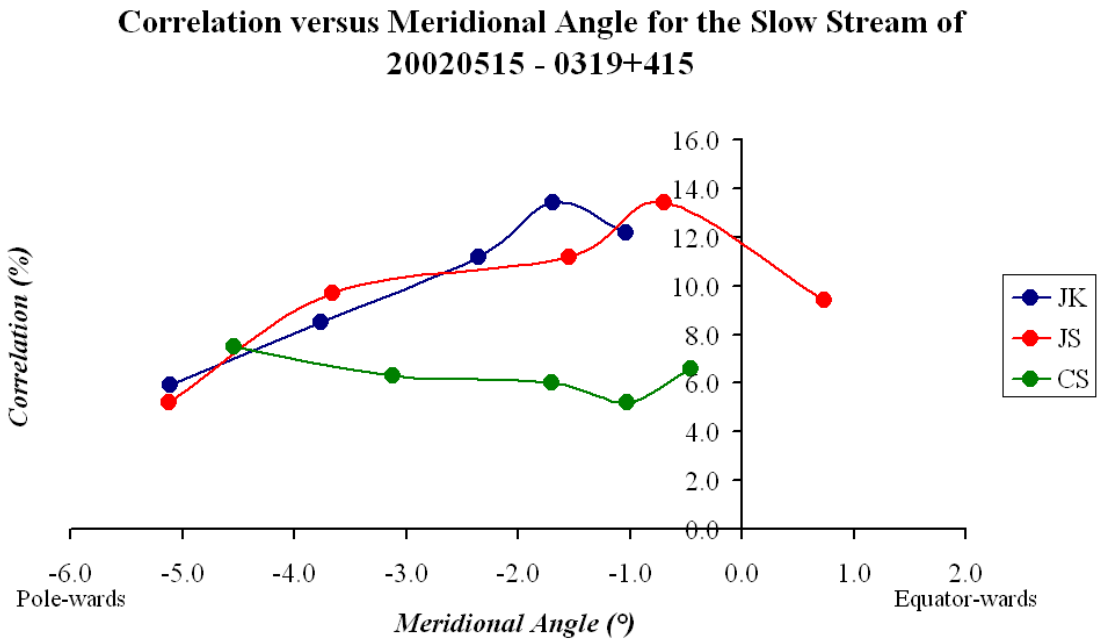

Figure 6.7: EISCAT-MERLIN off-radial angle results from the slow solar wind stream of the extremely long-baseline observations of 0319+415 on 20020515.

The intermediate velocity observations from 2002, figure 6.8, display a clear north-ward deflection of the outflow. The interpretation of this is that it is arising from interaction above the leading edge of the coronal hole as can be seen from the configuration of the corona with the IPS raypath overlaying it in figure 6.2. The north-ward meridional flow is between 6° and 8° in Jodrell-Sodankylä observations, and around 11.5° for the Jodrell-Kiruna observations.

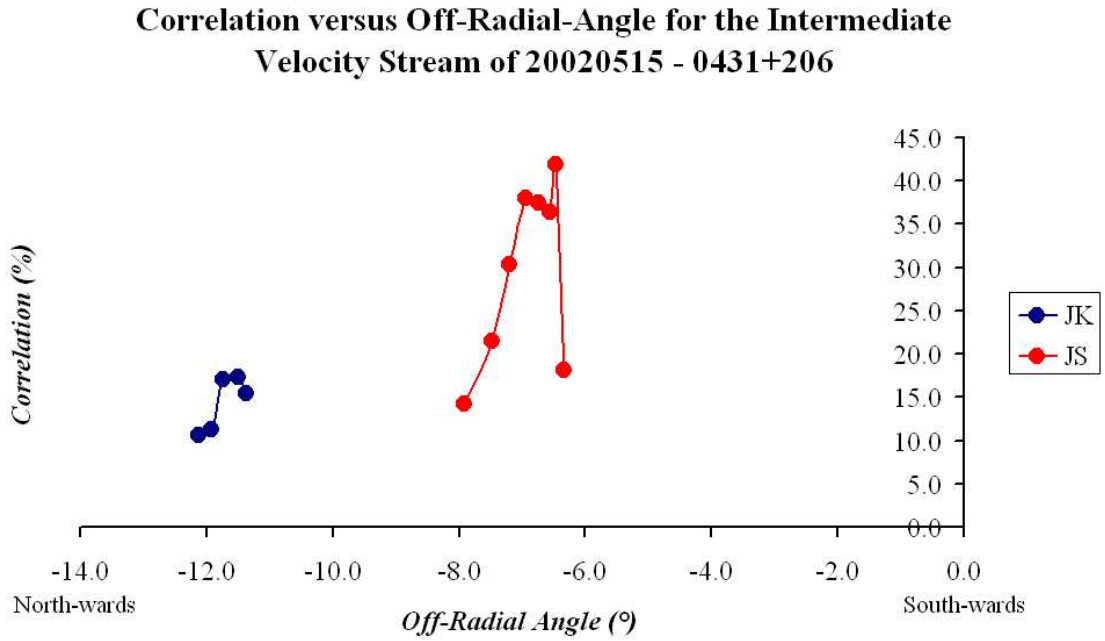

Figure 6.8: EISCAT-MERLIN off-radial angle results from the intermediate solar wind stream detected in the extremely long-baseline observations of 0431+206 on 20020515.

The polar crown fast wind observations from 2004, figure 6.9, also show a small equator-ward flow of between 1° and 2° in the most-part. This is comparable to those seen in 2002, and in the shorter EISCAT baselines reported in Moran *et al.* (1998).

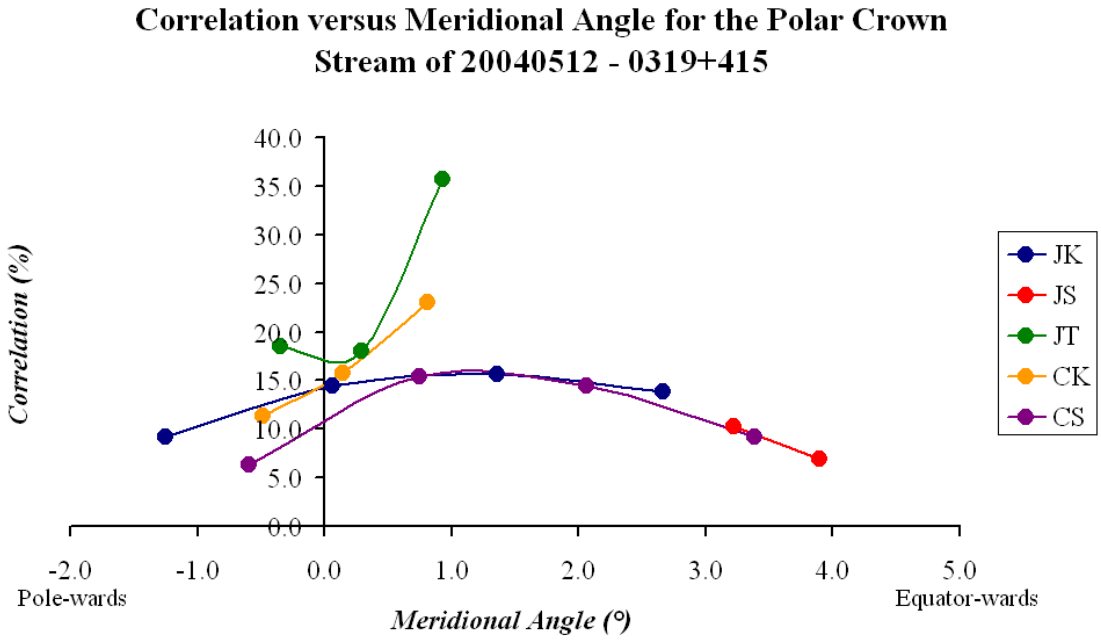

Figure 6.9: EISCAT-MERLIN off-radial angle results from the polar coronal hole fast solar wind stream of the extremely long-baseline observations of 0319+415 on 20040512.

The mid-latitude fast solar wind stream observations from 2004, figure 6.10, show some evidence of an equator-ward deviation between 3° and 4°- although this stream was not clearly resolved in enough baseline combinations to determine the precise degree of super-radial expansion and some radial/very close to radial expansion also being detected in the Jodrell-Tromsø observations.

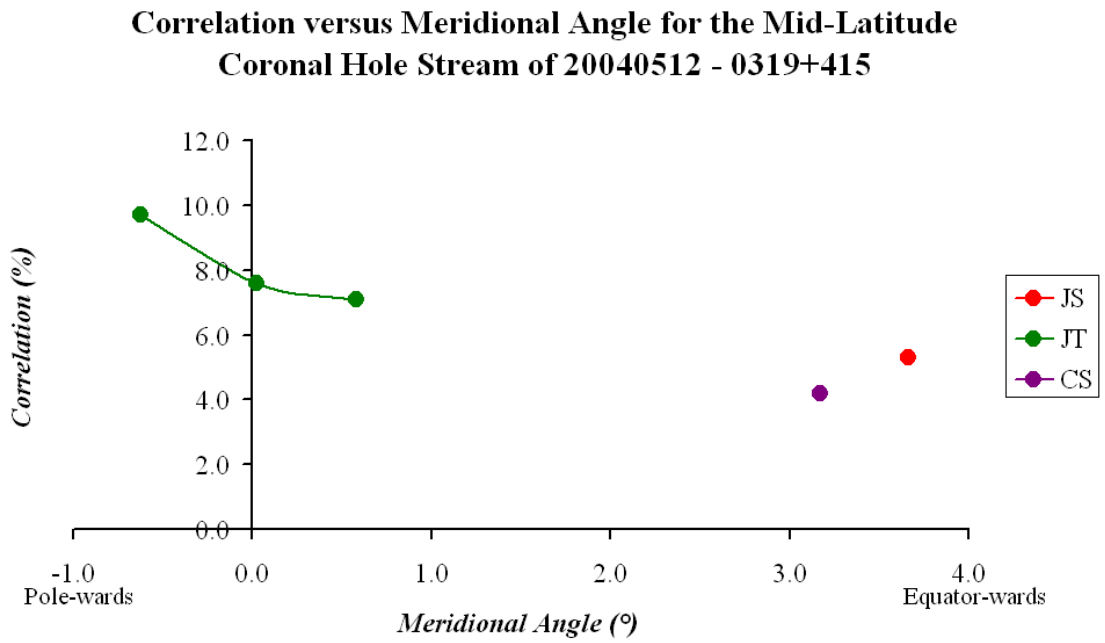

Figure 6.10: EISCAT-MERLIN off-radial angle results from the mid-latitude coronal hole fast solar wind stream of the extremely long-baseline observations of 0319+415 on 20040512.

The higher latitude faster wind observations from 2005 before 1410UT on 20050514, figures 6.11 and 6.12, also show a significant and consistent equator-ward flow. The degree of meridional flow in the equator-ward direction is between 0.5° and 3° in the most-part. This is again comparable to those seen in 2002, to those of 2004, and also those detected in the shorter EISCAT baselines as were reported in Moran *et al.* (1998).

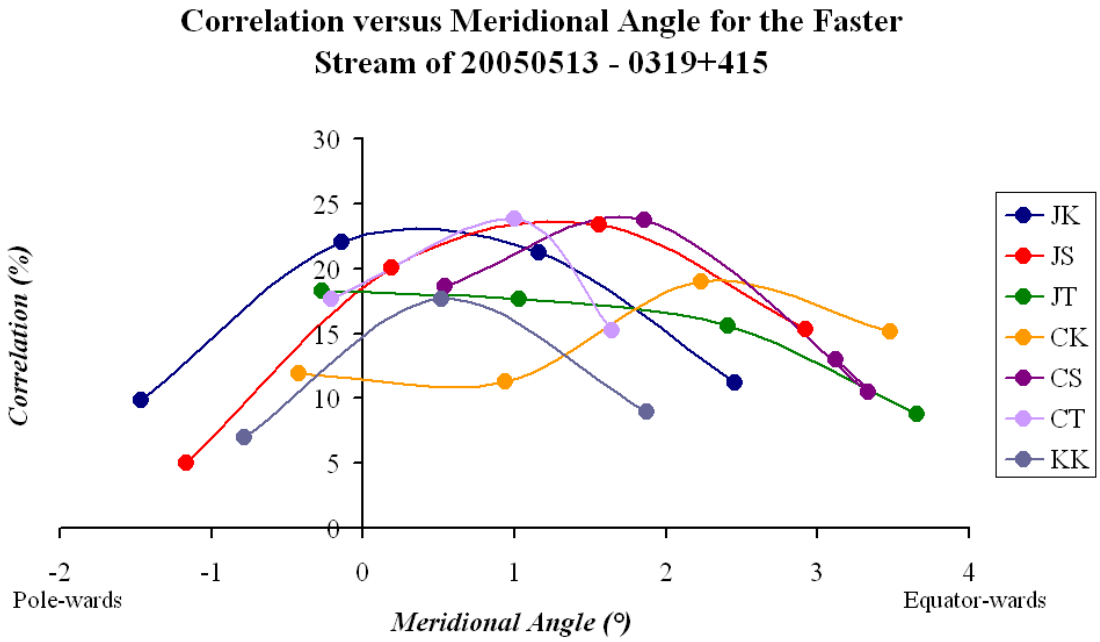

Figure 6.11: EISCAT-MERLIN off-radial angle results from the higher latitude faster solar wind stream of the extremely long-baseline observations of 0319+415 on 20040513.

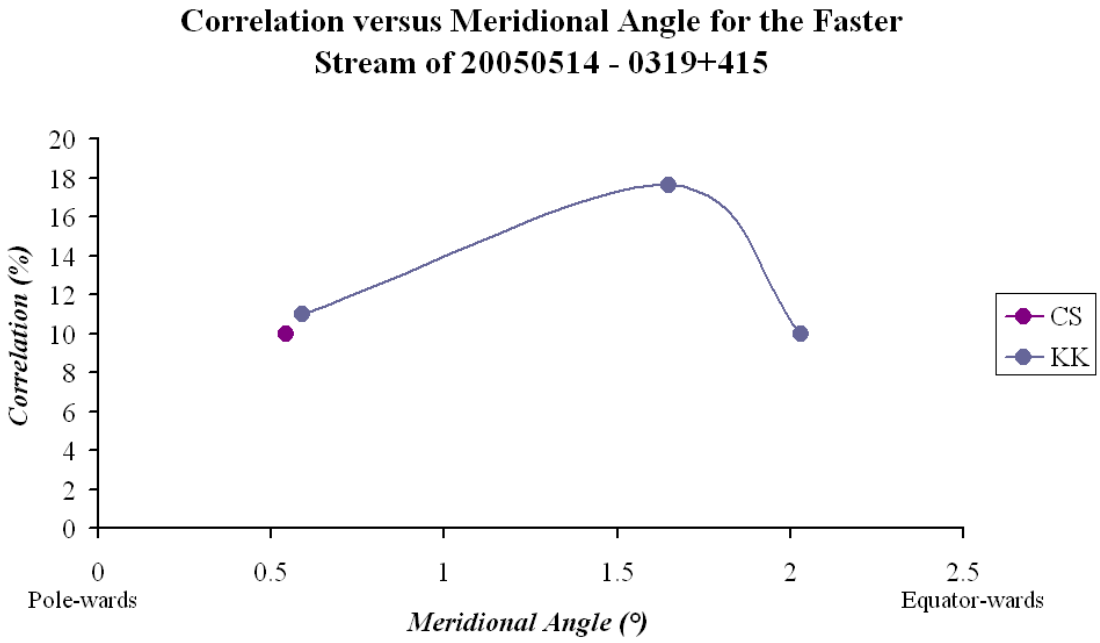

Figure 6.12: EISCAT-MERLIN off-radial angle results from the higher latitude faster solar wind stream of the extremely long-baseline observations of 0319+415 on 20040514 up until 1410UT.

The lower latitude 2005 fast wind observations from 20050513, figure 6.13, also show a significant and consistent equator-ward flow. The degree of meridional flow in the equator-ward direction is between 0.5° and 3° in the most-part with a hint of pole-ward flow in two of the observations. This result is still comparable to the two-mode fast wind detected in 2004, but to a lesser extreme in terms of the equator-ward values.

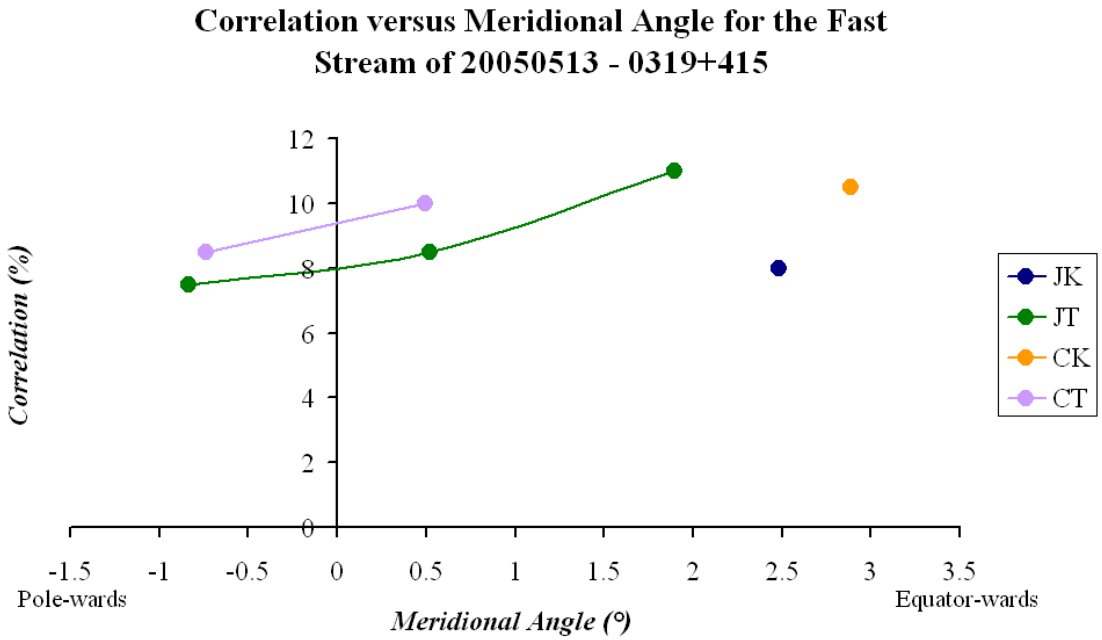

Figure 6.13: EISCAT-MERLIN off-radial angle results from the lower latitude fast solar wind stream of the extremely long-baseline observations of 0319+415 on 20040513.

The intermediate velocity 2005 solar wind observations on 20050513, figure 6.14, show an equator-ward flow to a greater extent. The degree of meridional flow in the equator-ward direction is between 2.5° and 4° . However, with only two observations of this in total, no solid result can feasibly be obtained.

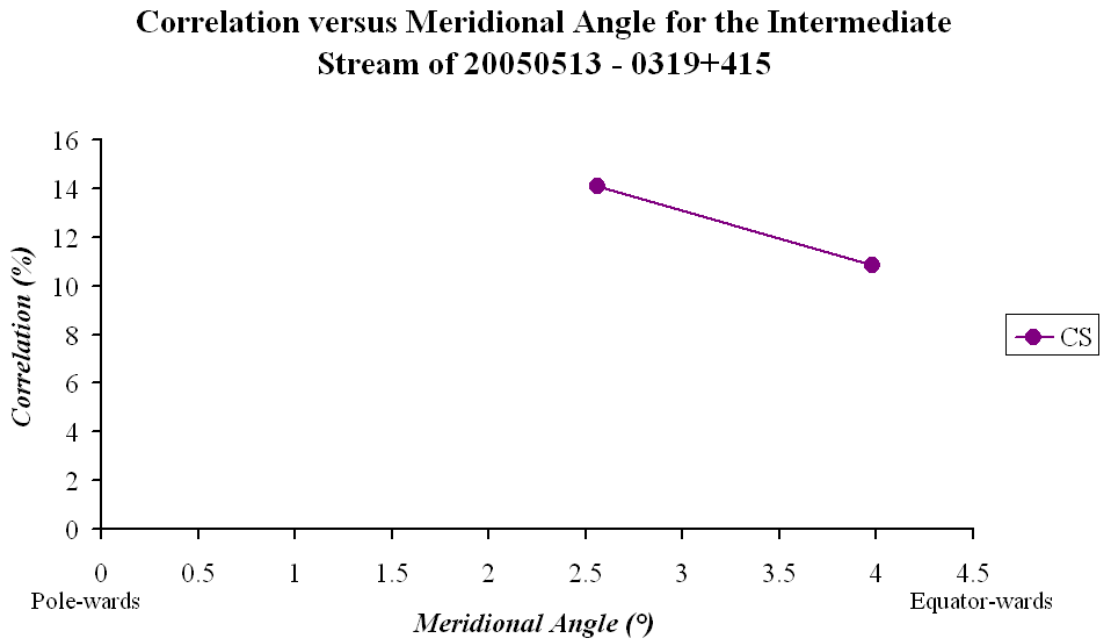

Figure 6.14: EISCAT-MERLIN off-radial angle results from the intermediate velocity solar wind of the extremely long-baseline observations of 0319+415 on 20040513.

The fastest wind observations of 2005 from 1410UT on 20050514, figures 6.15, show a significant variation of meridional flow between 4° pole-ward and 4° equator-ward in the most-part, with some extreme observations around 10° pole-ward. It should be noted that the higher-value correlations are generally in the pole-ward direction. This variation is thought to be caused by an interplanetary magnetic cloud transiting the observations.

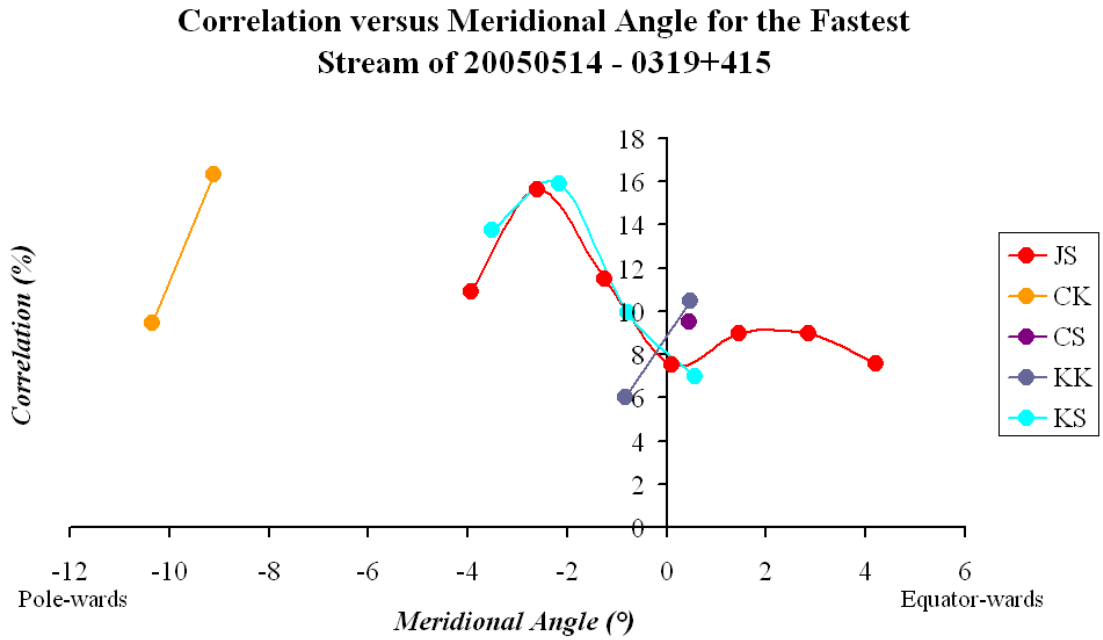

Figure 6.15: EISCAT-MERLIN off-radial angle results from the fastest solar wind velocity detected of the extremely long-baseline observations of 0319+415 on 20040514 from 1410UT onward.

The other 2005 fast wind observations from 1410UT on 20050514, figures 6.16, again show a significant variation of meridional flow. These observations show it to be between 4° pole-ward and 2° equator-ward in the most-part with the largest of the correlation values. It should be noted that the higher-value correlations in this case are both pole-ward and equator-ward. This variation is thought to be cause due to an interplanetary magnetic cloud transiting the observations.

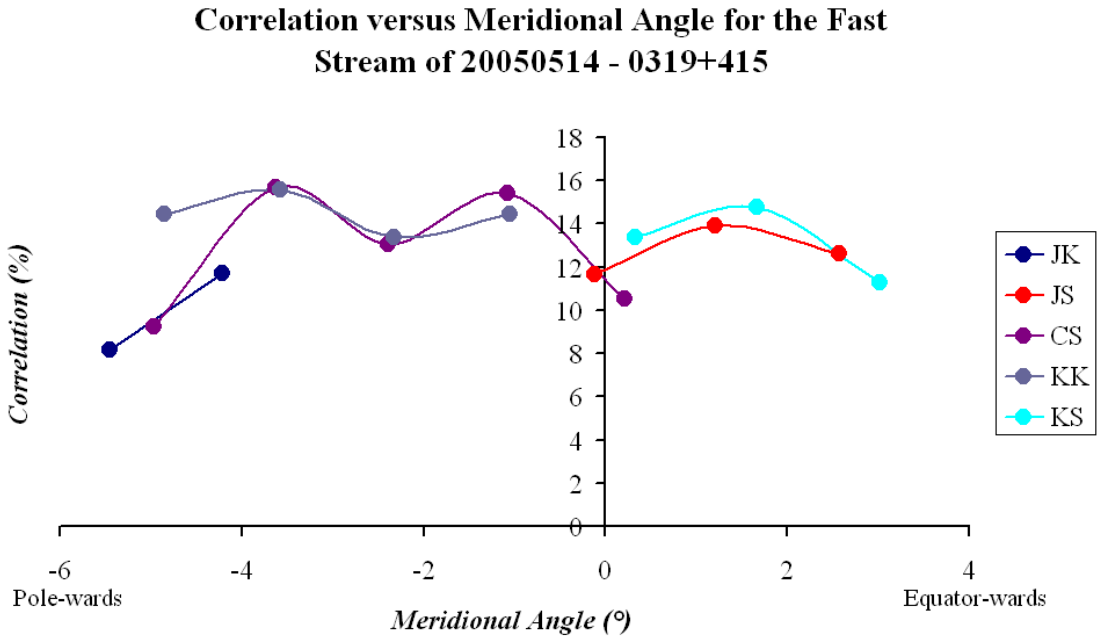

Figure 6.16: EISCAT-MERLIN off-radial angle results from the slower fast solar wind velocity detected of the extremely long-baseline observations of 0319+415 on 20040514 from 1410UT onward. It is likely that this arises from internal structure within the magnetic cloud, but as the event was Earth-directed, white-light information from the SOHO spacecraft gives nothing useful on the internal structure so it is not really known what is going on within the magnetic cloud.

6.4 Extremely long-baseline observations summary

The observations discussed here are the longest baseline IPS measurements to-date. The results include the first detections of two discrete modes of fast solar wind, with the faster outflow most probably originating toward the crown of the polar coronal hole and the slightly slower component in the equator-ward extension of the hole in 2004, and similarly for the two fast wind velocities detected in the 2005 data up until 1410UT on 20050514.

The 2002, 2004 and 2005 observations have also yielded the best estimates of solar wind direction to-date, showing a small (~1-2°) but significant equator-ward component of flow in the fast wind, suggesting a slight over-expansion to lower latitudes even at heliocentric distances of 80 $R_{\odot}$.

The slow wind observations suggest there may be some degree of pole-ward over-expansion, but at present it is not certain whether this arises from a genuine over-expansion of the slow wind or from the geometry of the Sun's coronal holes and streamer belt during May 2002, which could lead to weak interaction deflecting the flow in a north-ward direction. If however, the slow wind is indeed expanding off-radially toward the pole and with the off-radial flow of the fast wind being in an equator-ward direction, this could lead to the formation of a "convergence layer". This would be a convergence of the fast and slow wind at the boundary between the two and not the same as the convergence layer as discussed at the end of chapter 4 of this thesis. This type of convergence may form a radially outward flowing stream of an intermediate velocity.

An observation of flow above the boundary of a low-latitude coronal hole in 2002 certainly showed significant (~6-7°) north-ward deflection of the flow, with the characteristics of the stream (intermediate velocity with relatively little variation in outflow speed) being consistent with a developing interaction region. The possibility of this too forming a "convergence layer" is discussed at the end of chapter 4.

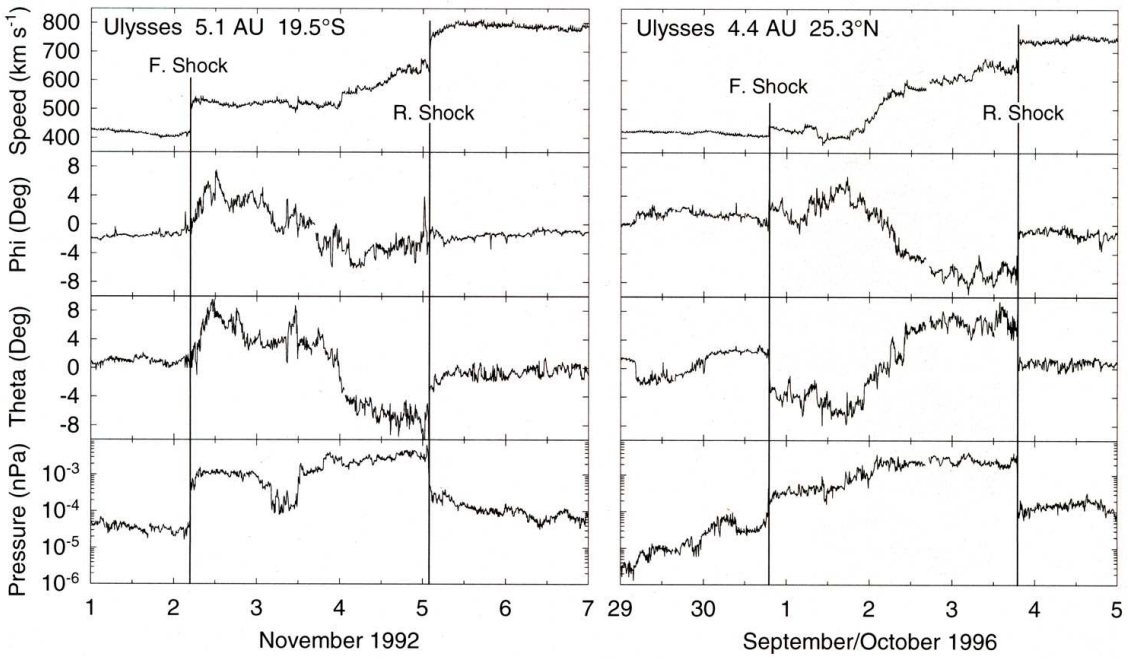

Figure 6.17: Examples of two cases of CIRs from Ulysses data. The case on the left is a southern hemisphere observation and the case on the right is a northern hemisphere observation. The parameters plotted are those (from the top panel down) of the solar wind speed, azimuthal flow angle, meridional flow angle, and proton pressure. It is the meridional flow angle which is of interest here since it is of a similar degree to that which has been detected in the intermediate velocity IPS observation in 2002 much closer-in to the Sun.

(Gosling *et al.*, 1995b, 1997, taken from Forsyth & Gosling 2001)

Looking at Ulysses data examples of two CIR detections - one in November 1992 and the other in September/October 1996 (Forsyth & Gosling, 2001) seen in figure 6.17 - off-radial deflections of the solar wind are seen in regions that are downstream of both the forward and reverse shocks remembering that a spacecraft observes the downstream region of a reverse shock before that of the upstream region (Forsyth & Gosling, 2001). Looking at the southern hemisphere example from 1992 (since the IPS observation was also South of the helio-equator although not quite to the same extent), after the forward shock is detected, there is an equator-ward (north-ward) meridional flow detected in the Ulysses velocity data. This is followed by a switch to a pole-ward (south-ward) meridional flow being detected downstream of the reverse shock. The IPS observation has similar meridional off-radial flow angles as those detected by Ulysses in 1992 following the forward shock. Although off-radial flow to this extent at Ulysses distances is well es-

tablished (Gosling *et al.*, 1993a), it comes as a surprise that a similar degree of off-radial flow in the meridional direction is detected coming from a region of interaction much closer to the Sun at IPS observing distances. This gives a strong insight into how soon off-radial flow can occur and how quickly interaction regions can develop.

It is not yet possible to give any pattern with distance from the Sun or with hemisphere since the only successful non-northern hemisphere observation so far using the extremely long-baseline technique was of an interaction region just South of the helio-equator in May of 2002 with 0431+206. Many more observations are needed before a pattern can be established if one were to exist.

The observations of an interplanetary magnetic cloud transiting through the IPS observations from 1410UT on 20050514 show high velocities of what are probably two different fast streams and a large degree of off-radial flow in the meridional direction. This direction of this flow is highly variable for both ranges of velocity detected - more so for the fastest of the two streams. This is the first detection to-date of such variable meridional flow using extremely long-baseline IPS observations of an interplanetary magnetic cloud.

Chapter 7

Conclusions and future work

This chapter discusses the aims, conclusions, and the possibilities of future improvement of the work carried out in this thesis on the large-scale structure of the solar wind.

7.1 Overall Conclusions

This thesis set out to look at the large-scale structure of the solar wind in the inner heliosphere. This was accomplished in various ways. Firstly, a re-analysis of around 10 years of EISCAT IPS data was undertaken and the data were then mapped to in-situ distances; adopting the method applied to preliminary case studies by Canals (2002). From this, discoveries of CIR formation and shear layers were made and the ability to distinguish between the two forms of interaction detected in IPS data discussed. This investigation lead to the possibility of there being structure within the fast solar wind due to one of the initial possible CIR candidates investigated showing a better fit with a two-mode fast solar wind rather than a fast and slow, or fast and intermediate flows. This lead to the complete re-analysis of the data from the previous solar minimum fast wind dominated IPS observations to investigate this possibility of a two-mode fast solar wind. Finally, the direction of flow of solar wind was investigated through the development of the method of extremely long-baseline IPS; combining data from EISCAT and MERLIN to achieve better velocity resolution and directional information than had previously been

obtained. The results show that meridional flow is common in the solar wind with the fast stream consistently displaying an over-expansion in an equator-ward direction; the possibility of pole-ward flow in the slow wind (although further observations are necessary to confirm this); but either or both pole-ward and equator-ward could be apparent in regions of interaction and during a passage of magnetic clouds. This reveals that the solar wind is seemingly flowing outward from the Sun in a non-radial fashion much closer-in than previously detected with off-radial (meridional) flow for fast, slow, and interacting streams.

7.1.1 Boundary regions between fast and slow streams in the solar wind

The results of this investigation confirm that CIRs and shear layers represent the two extremes of the same phenomenon which are caused by interaction along the boundary layers between fast and slow streams of solar wind (Gosling *et al.*, 1978a). However, it is very difficult to discern between the two without mapping outward since no discernible pattern of velocities or velocity variations comes from either of the two lists. Some observations previously interpreted as CIRs have now been shown to be cases of shear between the streams. In terms of the cases where comparison of the IPS observations with spacecraft data were possible, an overall good correlation was found between the mapped IPS raypaths and the hourly averaged in-situ velocity measurements over a period of one Carrington rotation of in-situ data.

The extremely long-baseline observation of a region of interaction in 2002 (Bisi *et al.*, 2005) shows what can be considered to be a “deflection layer”. This is where the solar wind is being deflected strongly in a non-radial north-ward meridional direction (as discussed in chapter 6). It is known that off-radial flow in the North-South direction above and below CIRs at large distances from the Sun can occur (Gosling *et al.*, 1993a, 1997), but it comes as a surprise that it has developed inside the orbit of Venus. This deflection in the IPS data could lead to a “convergence layer” with the slow outflow of solar wind

just North of the equator (and hence just North of the region of interaction) allowing for possible additional interaction to occur further out from the Sun. However, future observations of interaction regions using this method are needed to develop this hypothesis further - which unfortunately will rely a little on luck. This is because the extremely long-baseline campaigns are limited to just a few days per year due to the difficulties in obtaining observing time on the very busy and over-subscribed MERLIN system. However, this may be helped by recent talks with the Rutherford-Appleton Laboratory (RAL) to obtain usage time on their 25 metre Chilbolton radio telescope which is also suitable for making IPS measurements.

In addition to this, the Sun is now coming to solar minimum from looking at recent SOHO|LASCO images and is starting to look very much like it did in 1996 during the first Whole Sun Month campaign. Now, with a really well established method, these conditions provide a perfect opportunity for it to be applied to new data when looking at interaction in the solar wind and together with extremely long-baseline observations, it could provide a perfect opportunity for measuring the direction of flow throughout interaction regions as they form and develop thoughout IPS observations of that region.

7.1.2 Two-mode structure of the fast solar wind?

The aim of this investigation was to research the possibilities of there being structure within the fast solar wind around the previous solar minimum after an initial case study revealed a possibility of there being a two-mode fast solar wind. After a complete search through the data of suitable fast wind observation sources from the time near to and during the previous solar minimum, and analysis of those cases using the weak scattering model (as described in chapter 3), it was found that there were eight remaining candidates from an initial 300+. Of these eight, seven seemed to fit best using a two-mode fast model rather than the traditional fast and slow model of solar wind outflow.

Additional information as a method of comparison was used from the only source avail-

able at this time with in-situ velocity measurements of the solar wind out of the ecliptic plane, i.e. those from the Ulysses spacecraft. The analysis of the Ulysses data provided mixed conclusions of there being a continuous gradient in the fast solar wind outflow (as was found by e.g. McComas *et al.*, 2000) to there being a two-stage gradient with no possibility of pinning down the latitude of where this change occurs. In-situ data did however provide strong evidence of a continuous gradient in fast solar wind velocity rather than two distinct modes of fast flow.

In addition to this, an extremely long-baseline observation from 2004 showing what seems to be a two-mode fast wind, along with a similar (but less conclusive result due to the eruptive event on 20050513) result from the 2005 extremely long-baseline observations. It is now clear that a thorough analysis of the current solar minimum data are needed to further investigate this phenomenon and try to resolve in a more concrete fashion whether or not this structure seen in the fast solar wind IPS data are indeed real as present results seem to suggest.

Overall, there is fairly strong (but inconclusive) evidence of a possible two-mode fast stream in IPS data, but not in the Ulysses data. This could be caused by the streams smoothing-out with distance from the Sun since a large amount of evolution can take place in the structure of the solar wind from where it is detected using the technique of IPS to where it is measured at the in-situ distances of for example, the Ulysses spacecraft (~1.4 AU to ~5 AU). Further high-latitude fast wind dominated observations are necessary (along with further extremely long-baseline observations) to establish more clearly what the structure within the fast solar wind is.

7.1.3 Meridional flow of solar wind streams and extremely long-baseline observations

The 2002, 2004 and 2005 observations have yielded the best estimates of solar wind direction and are also the longest baseline IPS measurements to-date. They display a

small (~1-2°) but significant equator-ward component of flow in the fast wind, suggesting a slight over-expansion to lower latitudes - even at heliocentric distances of 80 $R_{\odot}$. The results include the first detections of two discrete modes of fast solar wind, with the faster outflow most probably originating toward the crown of the polar coronal hole and the slightly slower component in the equator-ward extension of the hole in 2004, and similarly for the two fast wind velocities detected in the 2005 data up until 1410UT on 20050514. The slow wind observations suggest a similar and possibly greater pole-ward expansion. However, it is not certain at present whether this arises from a genuine over-expansion of the slow wind or from the geometry of the Sun's coronal holes and streamer belt during May 2002, which could lead to weak interaction deflecting the flow in a north-ward direction.

However, if the slow wind is flowing radially or expanding toward the pole (and with the off-radial flow of the fast wind being in an equator-ward direction), then a "convergence layer" could be formed on the boundary. This would be a convergence of the fast and slow wind at the boundary between the two streams. This type of convergence could produce a radially outward flowing stream of perhaps an intermediate velocity as a result of the two non-radially flowing streams creating a narrow shear layer. This would be narrower than if everything was outwardly-propagating in a radial direction with a steep velocity gradient across it. A boundary layer between fast and slow flow of a low-latitude coronal hole in 2002 certainly showed significant (~6-7°) north-ward deflection of the flow. The characteristics of the stream being an intermediate velocity with relatively little variation in outflow speed is consistent with a developing interaction region. This too has the possibility of forming a "convergence layer", but on this occasion with the slow flow which seems to be coming from just North of the equator. This extremely long-baseline observation could also be considered to show a "deflection layer" where-by the solar wind is being deflected strongly in a non-radial north-ward meridional direction.

Presently, it is not possible to extract any pattern in terms of distance from the Sun or

with hemisphere. This is because the observations to date have been of the northern-hemisphere in the fast wind covering a narrow distance range from the Sun. Extremely long-baseline observations of the fast wind using southern hemisphere sources were successfully undertaken in June 2006 - these are however too late to be included in this thesis but will certainly be used in future developments of this work.

The direction of meridional flow detected in the extremely long-baseline observation of 20050514 from 1410UT onward shows a flow that is highly variable for both ranges of the two streams of velocity detected. This is more so for the fastest of the two streams. The observations is the first detection to-date of such variable meridional flow using extremely long-baseline IPS observations of an interplanetary magnetic cloud.

Further development and ability of getting more results from the extremely long-baseline technique will only be accomplished when many more observations can take place and when the weak scattering model can produce successful results from the data - this is hopefully going to be achieved with the 2006 extremely long-baseline observing campaigns that took place in May and June of 2006.

7.2 Future opportunities based on the outcomes of this thesis

The large-scale structure of the solar wind as it emerges from the inner corona differs significantly from that observed at 1 AU. The effects of interaction between streams of solar wind with different velocities and between transients and the background solar wind combine to produce significant evolution in 3-dimensional structure. Recent studies using extremely long-baseline IPS experiments and from previous solar minimum solar wind EISCAT IPS data have shown that the fast solar wind above the polar crown differs in character from the flow at the flanks of polar holes or of equatorial coronal holes. The extremely long-baseline observations indicate that the fast wind expands super-radially

toward the equatorial plane by 1° to 3° at interplanetary distances inside of 1 AU. Future observations will be used to determine how the degree of meridional expansion varies with distance into the polar hole and also with heliocentric distance. This will then feed into modelling studies of solar wind expansion and instabilities, which will then hopefully allow a determination of whether this over-expansion is carried over from the early stages of solar wind formation (original super-radial expansion) or whether it is driven by developing instabilities within the fast solar wind. The science questions to be addressed by this further study are:

- What is the origin of the equator-ward expansion of the fast solar wind seen in interplanetary space?
- How does the meridional flow of solar wind streams affect where cases of interaction end up at in terms of latitude?
- How does the off-radial flow and the fast wind structure vary with coronal hole size and position on the "surface" of the Sun?

Another factor to be considered is that of the picture of the solar wind flow and structure in the southern hemisphere as compared to the northern hemisphere. Are there any discernible differences, or is there a symmetry with the north? The same can be said for off the West limb of the Sun - are there any differences from the East limb? If there are differences in either of these cases, how and why are they there?

Overall, there is an obvious urgent need for further extremely long-baseline observations and to compare these in a similar method as was undertaken in Moran (1998) in terms of the modelling of the data and also to incorporate this into the mapping so that streams can be mapped taking account of meridional flow, i.e. changes in latitude as they travel out-ward from the Sun. There is also a need to look more at patterns with distance/time/latitude and fully incorporate the ESR in terms of very long-baseline observations (~950 km for parallel baseline) to make the most of this form of IPS as well as the two "new" possible telescopes. If it is found that streams of non-radial flow around

regions of interaction onset where IPS observations detect two streams at these distances but a single intermediate velocity is being detected further from the Sun at present in-situ distances, what is the possibility of this intermediate velocity being due to the convergence and therefore smoothing out of the two streams detected in IPS. This may be a similar situation for the detections of the two-mode fast solar wind in IPS data, but not seen to such an extent in the in-situ Ulysses data much further out from the Sun than that of the IPS data.

Preliminary testing of the latest generation of the weak scattering model (sfit) with the extremely long-baseline observations has proved hopeful. A quick analysis of the two-mode fast solar wind detection in the extremely long-baseline results of 20040512 with 0319+415 using the Jodrell Bank MkII and Kiruna telescopes have yielded solar wind velocities of $740\,\mathrm{km\,s^{-1}}$ and $573\,\mathrm{km\,s^{-1}}$ for the "faster" and "fast" stream detections respectively and with respective variations in velocity of $25\,\mathrm{km\,s^{-1}}$ and $416\,\mathrm{km\,s^{-1}}$. This is the first time the "fast" velocity has been detected in this combination of baselines. It should be noted though, the very large variation in the "fast" stream and little variation in the "faster" stream suggests that there may be something happening in the fast stream - possibly interaction with the surrounding streamer belt of the mid-latitude coronal hole from which the "fast" stream is detected. As a comparison with the non-sfit velocity values for these sets of observations, the "faster" stream was found to have radial velocities in the range of $830\,\mathrm{km\,s^{-1}}$ to $848\,\mathrm{km\,s^{-1}}$, while the "fast" stream was found to have velocities in the range of $617\,\mathrm{km\,s^{-1}}$ to $669\,\mathrm{km\,s^{-1}}$ across all baseline combinations. This means that the sfit velocity values are lower than the velocities measured using the method described in chapter 6, but this is as expected for reasons also explained in that chapter. Much more careful work is needed in getting the weak scattering model to successfully fit data from extremely long-baseline configurations.

7.3 The future for IPS in Europe

The number of extremely long-baseline observations have been restricted thus far by the limited amount of observing time available on the over-subscribed MERLIN system. However, from Spring 2007, it is hoped that the Aberystwyth Group will have access to the Chilbolton (CFARR - Chilbolton Facilities for Atmospheric and Radio Research) telescope (pictured in figure 7.1) as part of their collaboration with RAL (as stated earlier). This telescope is capable of observations around or near to 1420 MHz and is of a similar specification to that of the Knockin MERLIN telescope, and so is capable of IPS observations. In addition to this, it is hopeful that use of the proposed 32 metre radio telescope at Birr Castle in Ireland (Eire) can be used for the extremely long-baseline IPS experiment once it has been built in the next few years.

Figure 7.1: RAL's Chilbolton radio telescope as viewed from above.
(Taken from http://www.cclrc.ac.uk/Activities/Gallery/ChilboltonAerial0604.jpg, June 2006)

Integration of IPS data with STEREO|HI data will help to resolve small-scale structure in the solar wind and thus gain a better picture of the large-scale heliosphere through 3D reconstruction of extremely long-baseline observations. An analysis package for com-

bining the IPS and HI data is already underway at Aberystwyth with a hope of testing it in the 2007-2008 IPS campaigns and to make full use of it by the 2009 IPS observing campaign(s). It is electron density information from STEREO that can be incorporated into the IPS data and give a better picture of the different density structures along the IPS raypath which at present, is not possible as there are no data available.

IPS observations will be attempted around, in, and near to the planetary magnetosphere of Mercury; and around and near to the planet Venus; in the hope of looking at how these planets effect the solar wind. Similarities/differences between the two very different planets (e.g. magnetosphere 'v' atmosphere respectively) will also be investigated.

LOFAR (LOw Frequency ARray)/MWA (Mileura Widefield Array)/LoSKA (Low frequency Square Kilometre Array) systems that are about to come online, or will hopefully be coming online in the not too-distant future, may be capable of imagery of velocity structures in the solar wind as well as electron density measurements that could prove very beneficial to IPS observations in the same way as those of the STEREO|HI instruments.

Publication List

Jones, R. A., A. R. Breen, R. A. Fallows and M. M. Bisi, *The fast solar wind in the acceleration region: Observational constraints from interplanetary scintillation measurements*, SOHO 15 Conference Proceedings, ESA Publications Division on CDROM SP-575, Pages 176-179, December 2004

Bisi, M. M., A. R. Breen, R. A. Fallows, P. Thomasson, C. A. Jordan, R. A. Jones and G. Wannberg, *Combined EISCAT/ESR/MERLIN Interplanetary Scintillation Observations of the Solar Wind*, Solar Wind 11-SOHO 16 Conference Proceedings, 2005, ESA Publications Division on CDROM SP-592, Pages 593-596, September 2005

Jones, R. A., A. R. Breen, R. A. Fallows, M. M. Bisi, P. Thomasson, G. Wannberg and C. A. Jordan, *The solar eruption of May 13 2005: EISCAT and MERLIN observations of a coronal radio burst*, in press, Annales Geophysicae, 2006

Breen, A. R., R. A. Fallows, M. M. Bisi, P. Thomasson, C. A. Jordan, G. Wannberg and R. A. Jones, *Extremely long-baseline Interplanetary Scintillation measurements of Solar Wind velocity*, in press, Journal of Geophysical Research, 2006

Bisi, M. M., A. R. Breen, S. R. Habbal, R. A. Fallows and R. A. Jones, *Large-scale structure of the fast solar wind*, submitted in January 2006 for the Journal of Geophysical Research

Fallows, R. A., A. R. Breen, M. M. Bisi, R. A. Jones and G. Wannberg, *Dual-Frequency Interplanetary Scintillation Observations of the Solar Wind*, in press, Geophysical Research Letters, 2006.

Jones, R. A., A. R. Breen, A. Canals, R. A. Fallows, M. M. Bisi and G. Lawrence, *Interaction between coronal mass ejections and the solar wind*, submitted in May 2006 for the Journal of Geophysical Research.

Bibliography

Acton, L. W., M. Bruner, W. Brown, J. Lemen, T. Hirayama, S. Tsuneta, T. Watanabe & Y. Ogawara, The Solar-A Soft X-Ray Telescope Experiment, *Advances in Space Research*, **8**(11), pages 93–99, 1989.

Armstrong, J. W. & W. A. Coles, Analysis of three-station interplanetary scintillation data, *Journal of Geophysical Research*, **77**, pages 4602–4610, 1972a.

Armstrong, J. W., W. A. Coles & B. J. Rickett, Observations of strong interplanetary scintillation at 74 Megahertz, *Journal of Geophysical Research*, **77**(16), pages 2739–2743, 1972b.

Aschwanden, M. J., *Physics of the Solar Corona: An introduction*, Springer-Praxis Books in geophysical sciences, 2004.

Axford, W. I. & J. F. McKenzie, The Solar Wind, in J. R. Jokipii, C. P. Sonett & M. S. Giampapa, editors, *Cosmic Winds and the Heliosphere*, University of Arizona Press, 1997.

Bame, S. J., D. J. McComas, B. L. Barraclough, J. L. Phillips, K. J. Sofaly, J. C. Chavez, B. E. Goldstein & R. K. Sakurai, The Ulysses solar wind plasma experiment, *Astronomy and Astrophysics Suppliment*, **92**(2), page 237, 1992.

Biermann, L., Cometenschweifen und solare korpuskularstrahlung, *Zs. F. Astrophys.*, **29**, pages 274–286, 1951.

Biermann, L., Solar corpuscular radiation and the interplanetary gas, *Observatory*, **77**, pages 109–110, 1957.

Bisi, M. M., A. R. Breen, R. A. Fallows, P. Thomasson, R. A. Jones & G. Wannberg, Combined EISCAT/ESR/MERLIN Interplanetary Scintillation Observations of the Solar Wind, in *ESA SP-592: Solar Wind 11/SOHO 16, Connecting Sun and Heliosphere*, pages 593–596, European Space Agency, 2005.

Bisi, M. M., A. R. Breen, S. R. Habbal, R. A. Fallows & R. A. Jones, Large-scale Structure of the Fast Solar Wind, *Submitted to the Journal of Geophysical Research, January*, 2006.

Bourgois, G., W. A. Coles, G. Daigne, J. Silen, T. Turunen & P. J. Williams, Measurements of the solar wind velocity with EISCAT., *Astronomy and Astrophysics*, **144**, pages 452–462, 1985.

Brandt, J. C., Historical Introduction and Summary, in *Introduction to the Solar Wind*, pages 3–17, W. H. Freeman and co., 1970a.

Brandt, J. C., Ground based methods of observation, in *Introduction to the Solar Wind*, pages 103–117, W. H. Freeman and co., 1970b.

Breen, A. R., W. A. Coles, R. Grall, U. P. Løvhaug, J. Markkanen, H. Misawa & P. J. S. Williams, EISCAT measurements of interplanetary scintillation, *Journal of Atmospheric and Terrestrial Physics*, **58**, pages 507–519, 1996b.

Breen, A. R., W. A. Coles, R. R. Grall, M. T. Klinglesmith, J. Markkanen, P. J. Moran, B. Tegid & P. J. S. Williams, Eiscat measurements of the solar wind, *Annales Geophysicae*, **14**, pages 1235–1245, 1996c.

Breen, A. R., R. A. Fallows, M. M. Bisi, P. Thomasson, C. A. Jordan, G. Wannberg & R. A. Jones, Extremely long-baseline Interplanetary Scintillation measurements of Solar Wind velocity, *in press, Journal of Geophysical Research*, 2006.

Breen, A. R., Z. Mikic, J. A. Linker, A. J. Lazarus, B. J. Thompson, D. A. Biesecker, P. J. Moran, C. A. Varley, P. J. S. Williams & A. Lecinski, Interplanetary scintillation measurements of the solar wind during Whole Sun Month: Comparisons with coronal and in situ observations, *Journal of Geophysical Research*, **104**, pages 9847–9870, 1999.

Breen, A. R., P. J. Moran, C. A. Varley, W. P. Wilkinson & P. J. S. Williams, EISCAT measurements of the solar wind: Observations of interaction regions, *Physics and Chemistry of Earth*, **22**(5), pages 387–390, 1997b.

Breen, A. R., P. J. Moran, C. A. Varley, W. P. Wilkinson, P. J. S. Williams, W. A. Coles, A. Lecinski & J. Markkanen, Interplanetary scintillation observations of interaction regions in the solar wind, *Annales Geophysicae*, **16**, pages 1265–1282, 1998.

Breen, A. R., P. J. Moran, C. A. Varley, P. J. S. Williams, W. A. Coles, R. R. Grall, M. T. Klinglesmith & J. Markkanen, EISCAT measurements of interaction regions in the solar wind, *Advances in Space Research*, **20**, pages 27–+, 1997a.

Breen, A. R., S. J. Tappin, C. A. Jorden, P. Thomasson, P. J. Moran, R. A. Fallows, A. Canals & P. J. S. Williams, Simultaneous interplanetary Scintillation and Optical measurements of the acceleration of the Slow Solar Wind., *Annales Geophysicae*, **18**, pages 995–1002, 2000b.

Breen, A. R., P. Thomasson, C. A. Jordan, S. J. Tappin, R. A. Fallows, A. Canals & P. J. Moran, Slow and fast solar wind acceleration near solar maximum, *Advances in Space Research*, **30**, pages 433–436, 2002c.

Brueckner, G. E., Solar wind research with the Large Angle Spectroscopic Coronagraph (LASCO) experiment onboard the Solar and Heliospheric Observatory (SOHO) satellite, in *Solar Wind Conference*, 1995.

Brueckner, G. E., R. A. Howard, M. J. Koomen, C. M. Korendyke, D. J. Michels, J. D. Moses, D. G. Socker, K. P. Dere, P. L. Lamy, A. Llebaria, M. V. Bout, R. Schwenn, G. M. Simnett, D. K. Bedford & C. J. Eyles, The Large Angle Spectroscopic Coronagraph (LASCO), *Solar Physics*, **162**, pages 357–402, 1995.

Canals, A., *Interplanetary Scintillation Studies of the Solar Wind during the Rising Phase of the Solar Cycle*, Ph.D. Thesis, The University of Wales, Aberystwyth, 2002.

Canals, A., A. R. Breen, L. Ofman, P. J. Moran & R. A. Fallows, Estimating random transverse velocities in the fast solar wind from EISCAT Interplanetary Scintillation measurements, *Annales Geophysicae*, **20**, pages 1265–1277, 2002.

Cohen, M. H., E. J. Gundermann, H. E. Hardebeck & L. E. Sharp, Interplanetary Scintillations. II. Observations, *Astrophysical Journal*, **147**(2), pages 449–466, 1967.

Coles, W. A., Interplanetary Scintillation Observations of the High-Latitude Solar Wind, *Space Science Reviews*, **72**, pages 211–222, 1995.

Coles, W. A., A bimodal model of the solar wind speed, *Astrophysics and Space Science*, **243(1)**, pages 87–96, 1996.

Coles, W. A. & R. Esser, An observational limit to the amplitude of Alfven waves in the solar wind and comparison with an acceleration model, *Journal of Geophysical Research*, **97**, pages 19 139–+, 1992.

Coles, W. A. & J. K. Harmon, Interplanetary Scintillation Measurements of the Electron Density Power Spectrum in the Solar Wind, *Journal of Geophysical Research*, **83**(A4), pages 1413–1420, 1978.

Coles, W. A. & J. K. Harmon, Propagation observations of the solar wind near the sun, *Astrophysical Journal*, **337**, pages 1023–1034, 1989.

Coles, W. A. & B. J. Rickett, IPS observations of the solar wind speed out of the ecliptic, *Journal of Geophysical Research*, **81**, pages 4797–4799, 1976.

Coles, W. A., B. J. Rickett, V. H. Rumsey, J. J. Kaufman, D. G. Turley, S. Ananthakrishnan, J. W. Armstrong, J. K. Harmon, S. L. Scott & D. G. Sime, Solar cycle changes in the polar solar wind, *Nature*, **286**, pages 239–241, 1980.

Delaboudiniere, J. P., G. E. Artzner, J. Brunaud, A. Gabriel, J. F. Hochedez, F. Millier, X. Y. Song, B. Au, K. P. Dere, R. A. Howard, R. Kreplin, D. J. Michels, J. D. Moses, J. M. Defise, C. Jamar, P. Rochus, J. P. Chauvineau, J. P. Marioge, R. C. Catura, J. R. Lemen, L. Shing, R. A. Stern, J. B. Gurman, W. M. eupert, A. Maucherat, F. Clette, P. Cugnon & E. L. van Dessel, EIT: Extreme-Ultraviolet Imaging Telescope for the SOHO Mission, *Solar Physics*, **162**, pages 291–312, 1995.

Dennison, P. A. & A. Hewish, The solar wind outside the plane of the ecliptic, *Nature*, **213**, pages 343–346, 1967.

Domingo, V., B. Fleck & A. I. Poland, SOHO: The Solar and Heliospheric Observatory, *Space Science Reviews*, **72**, pages 81–+, 1995.

Dupree, A. K., M. J. Penn & H. P. Jones, He i 10830 Angstrom Wing Asymmetry in Polar Coronal Holes: Evidence for Radial Outflows, *Astrophysical Journal*, **467**, pages L121+, 1996.

Ekers, R. D. & L. T. Little, The motion of the solar wind close to the sun, *Astronomy and Astrophysics*, **10**, pages 310–316, 1971.

Esser, R., O. Lie-Svendsen, R. Edgar & Y. Chen, Observational and theoretical constraints on the heating and acceleration of the fast solar wind, in M. Velli, R. Bruno, F. Malara & B. Bucci, editors, *AIP Conf. Proc. 679: Solar Wind Ten*, pages 249–254, 2003.

Eyles, C. J., G. M. Simnett, M. P. Cooke, B. V. Jackson, A. Buffington, P. P. Hick, N. R. Waltham, J. M. King, P. A. Anderson & P. E. Holladay, The Solar Mass Ejection Imager (Smei), *Solar Physics*, **217**, pages 319–347, 2003.

Fallows, R. A., *Studies of the Solar Wind Throughout a Solar Cycle*, Ph.D. Thesis, The University of Wales, Aberystwyth, 2001.

Fallows, R. A., A. R. Breen, M. M. Bisi, R. A. Jones & G. Wannberg, Dual-Frequency Interplanetary Scintillation Observations of the Solar Wind, *in press, Geophysical Research Letters*, 2006.

Fallows, R. A., P. J. S. Williams & A. R. Breen, EISCAT measurements of solar wind velocity and the associated level of interplanetary scintillation, *Annales Geophysicae*, **20**, pages 1279–1289, 2002b.

Fisher, R. R., SPARTAN 201-3: Coronagraphs, World Wide Web, 1995, http://umbra.nascom.nasa.gov/spartan/coronagraphs.html accessed 19 March 2006 at 16:55h GMT.

Fisher, R. R., R. H. Lee, R. M. MacQueen & A. I. Poland, New Mauna Loa Coronagraph Systems, *Appl. Op.*, **20**, pages 1094–1101, 1981.

Ford, M. S. & F. W. Menk, Coupling of the Sun's internal oscillations to the solar wind, World Wide Web (WARS2006 Proceedings), 2006, http://www.ips.gov.au/IPSHosted/NCRS/wars/wars2006/proceedings/final/h/ford.pdf accessed 29 March 2006 at 21:25h GMT.

Forsyth, R. J., A. Balogh & E. J. Smith, The underlying direction of the heliospheric magnetic field through the Ulysses first orbit, *Journal of Geophysical Research (Space Physics)*, **107**(A11), pages 19–1, 2002b.

Forsyth, R. J., A. Balogh, E. J. Smith, G. Jones & T. Horbury, The heliospheric magnetic field at solar maximum, in *COSPAR, Plenary Meeting*, 2002a.

Forsyth, R. J. & J. T. Gosling, *Corotating and transient structures in the heliosphere*, pages 107–166, The heliosphere near solar minimum. The Ulysses perspective / André Balogh, Richard G. Marsden and Edward J. Smith (eds.). Springer-Praxis Books in Astrophysics and Astronomy. London: Springer. ISBN 1-85233-204-2, 2001.

Galloway, D. J. & N. O. Weiss, Convection and magnetic fields in stars, *Astrophysical Journal*, **243**, pages 945–953, 1981.

Goldstein, B. E., M. Neugebauer, J. L. Phillips, S. Bame, J. T. Gosling, D. McComas, Y.-M. Wang, N. R. Sheeley & S. T. Suess, ULYSSES plasma parameters: latitudinal, radial, and temporal variations., *Astronomy and Astrophysics*, **316**, pages 296–303, 1996.

Gopalswamy, N., *Solar and Space Weather Radio Physics: Current Status and Future Developments*, volume 314 of *Astrophysics and Space Science Library*, chapter 15 - Interplanetary Radio Bursts, pages 305–333, Kluwer Academic Publishers, 2004, ISBN 1-4020-2813-X.

Gosling, J. T., Corotating and Transient Solar Wind Flows in Three Dimensions, *Annual Review of Astronomy and Astrophysics*, **34**, pages 35–73, 1996.

Gosling, J. T., Coronal Mass Ejections: An Overview, in N. Crooker, J. A. Joselyn & J. Feynman, editors, *Coronal Mass Ejections*, Geophysical Monograph Series, chapter 1, pages 9–16, American Geophysical Union, 1999, ISBN 0-87590-081-X, including IUGG Volumes, Maurice Ewing Volumes, and Mineral Physics Volumes.

Gosling, J. T., J. R. Asbridge, S. J. Bame & W. C. Feldman, Solar wind stream interfaces, *Journal of Geophysical Research*, **83**, pages 1401–1412, 1978a.

Gosling, J. T., S. J. Bame, W. C. Feldman, D. J. McComas, P. Riley, B. E. Goldstein & M. Neugebauer, The northern edge of the band of solar wind variability: Ulysses at ˜4.5AU, *Geophysical Research Letters*, **24**, pages 309–312, 1997.

Gosling, J. T., S. J. Bame, D. J. McComas, J. L. Phillips, V. J. Pizzo, B. E. Goldstein & M. Neugebauer, Latitudinal variation of solar wind corotating stream interaction regions: ULYSSES, *Geophysical Research Letters*, **20**, pages 2789–2792, 1993a.

Gosling, J. T., S. J. Bame, D. J. McComas, J. L. Phillips, V. J. Pizzo, B. E. Goldstein & M. Neugebauer, Solar Wind Corotating Stream Interaction Regions Out of the Ecliptic Plane: ULYSSES, *Space Science Reviews*, **72**, pages 99–+, 1995b.

Gosling, J. T., A. J. Hundhausen, V. Pizzo & J. R. A. V. 3, Compressions and rarefaction in the solar wind, *Journal of Geophysical Research*, **77**, pages 5442–5454, 1972.

Gosling, J. T. & V. J.Pizzo, Formation and Evolution of Corotating Interaction Regions and their Three Dimensional Structure, *Space Science Reviews*, **89**, pages 21–52, 1999.

Grall, R. R., *Remote Sensing Observations of the Solar Wind Near the Sun*, Ph.D. Thesis, University of California, San Diego, 1995.

Grall, R. R., W. A. Coles, M. T. Klingesmith, A. R. Breen, P. J. S. Williams, J. Markkanen & R. Esser, Rapid acceleration of the polar solar wind, *Nature*, **379**, 1996.

Habbal, S. R. & R. Woo, Connecting the Sun and the Solar Wind: Comparison of the latitudinal profiles of coronal and Ulysses measurements of the fast wind, *The Astrophysical Journal*, **549**, pages L253–L256, 2001.

Habbal, S. R., R. Woo, R. O'Neal, J. Kohl, G. Noci & C. Korendyke, Origins of the slow and the ubiquitous fast solar wind, *The Astrophysical Journal*, **489**, pages L103–L106, 1997.

Harrison, R. A., C. J. Davis & C. J. Eyles, The STEREO heliospheric imager: how to detect CMEs in the heliosphere, *Advances in Space Research*, **36**, pages 1512–1523, 2005.

Hassler, D. M., I. E. Dammasch, P. Lemaire, P. Brekke, W. Curdt, H. E. Mason, J. C. Vial & K. Wilhelm, Solar wind outflow and the chromospheric magnetic network, *Science*, **283**, pages 810–+, 1999.

Hewish, A., The irregular structure of the outer regions of the solar corona, *Proceedings of the Royal Society*, **A 238**, pages 238–251, 1955.

Hewish, A., A user's guide to scintillation, *Journal of Atmospheric and Terrestrial Physics*, **51**(9/10), pages 743–750, 1989.

Hewish, A. & S. E. Okoye, Evidence for an Unusual Source of High Radio Brightness Temperature in the Crab Nebula, *Nature*, **207**, pages 59–+, 1965.

Hewish, A., P. F. Scott & D. Wills, Interplanetary scintillations of small diameter radio sources, *Nature*, **203**, pages 1214–1217, 1964.

Hey, J. S., *The Radio Universe*, Pergamon Press, third edition edition, 1983, first Edition - 1971, Second Edition 1975, Third Edition - 1983.

Hundhousen, A. J., An Introduction, in N. Crooker, J. A. Joselyn & J. Feynman, editors, *Coronal Mass Ejections*, Geophysical Monograph Series, chapter 1, pages 1–7, American Geophysical Union, 1999, ISBN 0-87590-081-X, including IUGG Volumes, Maurice Ewing Volumes, and Mineral Physics Volumes.

Jackson, B. V., HELIOS photometer measurement of in-situ density enhancements, *Advances in Space Research*, **6**, pages 307–310, 1986.

Jackson, B. V., A. Buffington, P. Hick, Y. Yu & D. Webb, The Pertinence of Three-Dimensional Solar Mass Ejection Imager (SMEI) Solar Wind Analysis to Ulysses Observations, 2005, Presentation at the Solar Wind 11-SOHO 16 Meeting.

Jones, R. A., A. R. Breen, R. A. Fallows & M. M. Bisi, The Fast Solar Wind in the Acceleration Region: Observational Constraints from Interplanetary Scintillation Measurements, in R. W. Walsh, J. Ireland, D. Danesy & B. Fleck, editors, *ESA SP-575: SOHO 15 Coronal Heating*, pages 176–+, 2004.

Jones, R. A., A. R. Breen, R. A. Fallows, M. M. Bisi, P. Thomasson, G. Wannberg & C. A. Jordan, The solar erruption of May 13 2005: EISCAT and MERLIN observations of a coronal radio burst, *in press, Annales Geophysicae*, 2006a.

Kaiser, M. L., The STEREO mission: an overview, *Advances in Space Research*, **36**, pages 1483–1488, 2005.

Klinglesmith, M., *The Polar Solar Wind from 2.5 to 40 Solar Radii: Results of Intensity Scintillation Measurements*, Ph.D. Thesis, University of California, San Diego (UCSD), 1997.

Kojima, M., A. R. Breen, K. Fujiki, K. Hayashi, T. Ohmi & M. Tokumaru, Fast solar wind after the rapid acceleration, *Journal of Geophysical Research (Space Physics)*, **109**(A18), page 4103, 2004.

Kojima, M. & T. Kakinuma, Solar cycle evolution of solar wind speed structure between 1973 and 1985 observed with the interplanetary scintillation method, *Journal of Geophysical Research*, **92**, pages 7269–7279, 1987.

Krieger, A. S. & A. F. Timothy, A coronal hole and its identification as the source of a high velocity solar wind stream, *Solar Physics*, **29**, pages 505–525, 1973.

Lang, K. R., *The Cambridge Encyclopedia of the Sun*, Cambridge University Press, 2001, ISBN 0-521-78093-4.

Leighton, R. B., R. W. Noyes & G. W. Simon, Velocity fields in the solar atmosphere. I. Preliminary report, *Astrophysical Journal*, **135**, pages 474–499, 1962.

Li, X., Acceleration of the Fast Solar Wind through Minor Ions, in H. Lacoste, editor, *ESA SP-547: SOHO 13 Waves, Oscillations and Small-Scale Transients Events in the Solar Atmosphere: Joint View from SOHO and TRACE*, pages 369–+, 2004.

Malbet, F., High angular resolution coronography for adaptive optics., *Astronomy and Astrophysics*, **115**, pages 161–+, 1996.

Massey, W., *Measuring Intensity Scintillations at the Very Long Baseline Array (VLBA) to Probe the solar Wind*, Ph.D. Thesis, The University of California, San Diego, 1998.

Maxwell, J. C., *Treatise on Electricity and Magnetism*, Oxford, 1873.

McComas, D. J., B. L. Barraclough, H. O. Funsten, J. T. Gosling, E. Santiago-Munoz, R. M. Skoug, B. E. Goldstein, M. Neugebauer, P. Riley & A. Balogh, Solar wind observations over Ulysses' first polar orbit, *Journal of Geophysical Research*, **105**(A5), pages 10 419–10 433, 2000.

McComas, D. J., P. Riley, J. T. Gosling, A. Balogh & R. Forsyth, Ulysses' rapid crossing of the coronal hole boundary, *Journal of Geophysicae Research*, **103, A2**, pages 1955–1967, 1998a.

McKenzie, J. F., M. Banaszkiewicz & W. I. Axford, Acceleration of the high speed solar wind., *Astronomy and Astrophysics*, **303**, pages L45–L48, 1995.

Moran, P. J., *Interplanetary Scintillation Measurements of the Solar Wind using EISCAT*, Ph.D. Thesis, The University of Wales, Aberystwyth, 1998.

Moran, P. J., A. R. Breen, W. A. Coles, R. Grall, M. T. Klinglesmith, J. Markkanen, C. A. Varley & P. J. S. Williams, Eiscat measurements of the solar wind: measurements of fast and slow streams, *Physics and Chemistry of Earth*, **22**(5), pages 389–392, 1997.

Moran, P. J., A. R. Breen, C. A. Varley, P. J. S. Williams, W. P. Wilkinson & J. Markkanen, Measurements of the direction of the solar wind using interplanetary scintillation, *Annales Geophysicae*, **16**, pages 1259–1264, 1998.

Neugebauer, M. & C. W. Snyder, The Mission of Mariner II: Preliminary observations, *Science*, **138**, pages 1095–1097, 1962.

Neugebauer, M. & C. W. Snyder, Mariner 2 observations of the solar wind, *Journal of Geophysical Research*, **71**, pages 4469–4484, 1966.

Neugebauer, M. & R. von Steiger, The Solar Wind, in J. A. M. Bleeker, J. Geiss & M. C. E. Huber, editors, *The Century of Space Science*, chapter 47, pages 1115–1140, Kluwer Academic Publishers, 2003.

Neupert, W. M. & V. Pizzo, Solar Coronal Holes as Sources of Recurrent Geomagnetic Disturbances, *Bulletin of the American Astronomical Society*, **6**, pages 292–+, 1974.

Nicolson, I., *The Sun*, Mitchell Beazley Publishers, 1982, ISBN 0-85533-311-1.

Nolte, J. T., A. S. Krieger, A. F. Timothy, R. E. Gold, E. C. Roelof, G. Vaiana, A. J. Lazarus, J. D. Sullivan & P. S. McIntosh, Coronal holes as sources of solar wind, *Solar Physics*, **46**, pages 303–322, 1976.

Ofman, L. & J. M. Davila, Solar wind acceleration by large-amplitude nonlinear waves: Parametric study, *Journal of Geophysical Research*, **103**, pages 23 677–23 690, 1998.

Ogawara, Y., The SOLAR-A Mission, *Solar Physics*, **113**, pages 361–370, 1987.

Ogawara, Y., T. Takano, T. Kato, T. Kosugi, S. Tsunta, T. Watanabe, I. Kondo & Y. Uchida, The Solar-A Mission: An Overview, *Solar Physics*, **136**, pages 1–16, 1991, kluwer Academic Publishers - Printed in Belgium.

Parker, E. N., Dynamics of interplanetary gas and magnetic fields, *Astrophysical Journal*, **128**, pages 664–685, 1958.

Parker, E. N., *Interplanetary Dynamic Processes*, Interscience Publishers, New York, 1963.

Phillips, J. L., A. Balogh, S. J. Bame, B. E. Goldstein, J. T. Gosling, J. T. Hoeksema, D. J. McComas, M. Neugebauer, N. R. Sheeley & Y. M. Wang, ULYSSES at 50 deg south: Constant immersion in the high-speed solar wind, *Geophysical Research Letters*, **21**, pages 1105–1108, 1994.

Phillips, J. L., S. J. Bame, W. C. Feldman, B. E. Goldstein, J. T. Gosling, C. M. Hammond, D. J. McComas, M. Neugebauer, E. E. Scime & S. T. Suess, ULYSSES Solar Wind Plasma Observations at High Southerly Latitudes, *Science*, **268**, pages 1030–+, 1995.

Phillips, K. J. H., *Guide to the Sun*, Cambridge University Press, 1992, ISBN 0-521-39788-X.

Rao, A. P., S. Ananthakrishnan, V. Balasubramanian & W. A. Coles, Very long baseline IPS observations of the solar wind speed in the fast polar streams, in *Solar Wind Conference*, pages 94–+, 1995.

Reiff, P. H., The Use and Misuse of Statistical Analyses, in R. L. Carovillano & J. M. Forbes, editors, *ASSL Vol. 104: Solar-Terrestrial Physics: Principles and Theoretical Foundations*, pages 493–+, 1983.

Rickett, B., IPS observations of the solar wind velocity and microscale density irregularities in the inner solar wind, in *Solar Wind Seven Colloquium*, pages 255–258, 1992.

Rickett, B. J. & W. A. Coles, Evolution of the solar wind structure over a solar cycle - Interplanetary scintillation velocity measurements compared with coronal observations, *Journal of Geophysical Research*, **96**, pages 1717–1736, 1991.

Riley, P., S. J. Bame, B. L. Barraclough, W. C. Feldman, J. T. Gosling, G. W. Hoogeveen, D. J. McComas, J. L. Phillips, B. E. Goldstein & M. Neugebauer, ULYSSES solar wind plama observations at high latitudes, *Advances in Space Research*, **20**, pages 15–+, 1997.

Rishbeth, H. & P. J. S. Williams, Ionospheric Radar: the system and its early results, *Monthly Notices of the Royal Astronomical Society*, **26**, pages 478–512, 1985.

Russell, C. T., A Brief History of Solar Terrestrial Physics, in M. G. Kivelson & C. T. Russell, editors, *Introduction to Space Physics*, chapter 1, pages 1–26, Cambridge University Press, 1995, ISBN 0-521-45714-9.

Salpeter, E. E., Interplanetary Scintillations. I. Theory, *The Astrophysical Journal*, **147**, pages 433–+, 1967.

Scherer, P. H., R. S. Bogart, R. I. Bush, J. T. Hoeksema, A. G. Kosovichev, J. Schou, W. Rosenberg, L. Springer, T. D. Tarbell, A. Title, C. J. Wolfson, I. Zayer & M. E. Team, The Solar Oscillations Investigation - Michelson Doppler Imager, *Solar Physics*, **162**, pages 129–188, 1995.

Schwenn, R., Radial gradients in solar wind plasma, Technical report, Max-Planck-Inst. fuer Physik und Astrophysik, Garching (Germany, F.R.)., 1974.

Schwenn, R., Large-scale structure of the interplanetary medium, in R. Schwenn & E. Marsch, editors, *Physics of the Inner Heliosphere II, Waves and Turbulence*, pages 98–181, Springer-Verlag, 1990, ISBN 0-387-52083-X.

Scott, S. L., W. A. Coles & G. Bourgois, Solar wind observations near the sun using interplanetary scintillation, *Astronomy and Astrophysics*, **123**, pages 207–215, 1983.

Snyder, C. W. & M. Neugebauer, Interplanetary Solar-Wind Measurements by Mariner II, in C. C. Chang & S. S. Huang, editors, *ASSL Volume 3: Plasma Space Science*, pages 67–+, 1965.

Thomasson, P., MERLIN, *Quarterly Journal of the Royal Astronomical Society*, **27**, pages 413–431, 1986.

Thompson, S. J., *OSCA, an Optimised Stellar Coronagraph for Adaptive Optics*, Ph.D. Thesis, University College London, University of London, 2004.

Uscinski, B. J., The elements of wave propagation in radom media, New York: McGraw-Hill, 1977.

Wang, Y.-M., N. R. S. Jr., R. A. Howard, J. R. Kraemer, N. B. Rich, M. D. Andrews, G. E. Brueckner, K. P. Dere, M. J. Koomen, C. M. Korendyke, D. J. Michels, J. D. Moses, S. E. Paswaters, D. G. Socker, D. Wang, P. L. Lamy, A. Llebaria, D. Vibert, R. Schwenn & G. M. Simnett, Origin and Evolution of Coronal Streamer Structure during the 1996 Minimum Activity Phase, *Astrophysical Journal*, **485**, pages 875–+, 1997.

Wannberg, G., L.-G. Vanhainen, A. Westman, A. R. Breen & P. J. S. Williams, The new 1420 MHz dual polarisation interplanetary scintillation (IPS) facility at EISCAT, in *Conference Proceedings*, Union of Radio Scientists (URSI), 2002.

Wannberg, G., I. Wolf, L.-G. Vanhainen, K. Koskenniemi, J. Rttger, M. Postila, J. Markkanen, R.Jacobsen, A. Stenberg, R. Larsen, S. Eliassen, S. Heck & A. Huuskonen, The EISCAT Svalbard Radar, a case study in modern incoherent scatter radar system design, *Radio Science*, **32**, pages 2283–2307, 1997.

Wenzel, F. P., R. G. Marsden, D. E. Page & E. J. Smith, The ULYSSES Mission, *Astronomy and Astrophysics Supplement Series*, **92**, pages 207–+, 1992.

Woch, J., W. I. Axford, U. Mall, B. Wilken, S. Livi, J. Geiss, G. Gloeckler & R. J. Forsyth, SWICS/ULYSSES Observations: The Three-Dimensional Structure of the Heliosphere during Solar Minimum, in *Solar Wind Papers*, Max-Planck-Institut Für Aeronomie, 1997.

Woo, R. & S. R. Habbal, Extension of coronal structure into interplanetary space, *Geophysical Research Letters*, **24**(10), pages 1159–1162, 1997a.

Worster, C., Outer Solar Atmosphere and Heliosphere, World Wide Web, 1998, http://www.hao.ucar.edu/public/asr/asr98/osah/osah.html accessed 12 January 2005 at 15:15h GMT.